

DISSERTATION

SIMULTANEOUS TRAPPING OF ^{85}Rb & ^{87}Rb IN A FAR OFF RESONANT TRAP

Submitted by

Anthony R Gorges

Department of Physics

In partial fulfillment of the requirements

For the Degree of Doctor of Philosophy

Colorado State University

Fort Collins, Colorado

Spring 2010

COLORADO STATE UNIVERSITY

February 26, 2010

WE HEREBY RECOMMEND THAT THE DISSERTATION PREPARED UNDER OUR SUPERVISION BY ANTHONY GORGES ENTITLED SIMULTANEOUS TRAPPING OF ^{85}Rb & ^{87}Rb IN A FAR OFF RESONANT TRAP BE ACCEPTED AS FULFILLING IN PART REQUIREMENTS FOR THE DEGREE OF DOCTOR OF PHILOSOPHY.

Committee on Graduate work

Richard Eykholt

Robert Leisure

Mario Marconi

Advisor: Jacob Roberts

Department Chair: Dieter Hochheimer

ABSTRACT OF THESIS

SIMULTANEOUS TRAPPING OF ^{85}Rb & ^{87}Rb IN A FAR OFF RESONANT TRAP

The experiments described in this thesis were focused on the physics of simultaneous trapping of ^{85}Rb and ^{87}Rb into a Far Off Resonant Trap (FORT), with a view towards the implementation of a non-evaporative cooling scheme. Atoms were first trapped in a Magneto Optical Trap (MOT) and from there loaded into the FORT. We investigated the effects of loading the FORT from a MOT vs. an optical molasses; observing that the molasses significantly improved the trapped atom number. The ultimate number of atoms trapped is determined by a balance between efficient laser cooling into the FORT and light-assisted collisional losses from the FORT. We have studied and measured the loss rates associated with light-assisted collisions for our FORT, measuring both heteronuclear and homonuclear collisions. It was discovered that induced long range dipole-dipole interactions between ^{85}Rb and ^{87}Rb have a significant impact on FORT loading. This interaction interferes with the loading into the trap and thus limits the number of atoms which can be trapped in the FORT under simultaneous load conditions. Despite this limitation, all required experimental parameters for our future measurements have been met. In addition to these FORT studies, we have found a technique which can successfully mitigate the effects of reabsorption in optically thick clouds, which is a limitation to the ultimate temperature an atom cloud will reach during

light-based cooling. Planned future measurements for this project include the creation of a variable aspect ratio FORT; along with investigating collision assisted Zeeman cooling.

Anthony Robert Gorges
Department of Physics
Colorado State University
Fort Collins, CO 80523
Spring 2010

Acknowledgement

The work presented in this thesis was made possible by the contributions of several people. I would like to take the time to thank those whom have helped both myself and the research presented in this thesis.

None of the work here would have been possible without the guidance and work from my advisor, Dr. Jacob Roberts. I was given an opportunity to learn many aspects of scientific research thanks to Dr. Roberts. One of the smartest people I've had the pleasure of meeting, and one of great patience; I was able to learn and grow as a scientist under his tutelage. Jake is an excellent scientist, he was always willing to take the time to help me in my research and understanding. Additionally, he always provided a positive environment which further helped those of us in the lab in all aspects of the experiment; from machining and electronics to theory and data analysis. Without Jake's expert guidance, I would not have progressed as much as I did. Thus, for everything that Jake had provided to me while I worked as his graduate student, I am forever grateful.

Much of the work I have done could not have happened without the diligence and work of other graduate students in the lab. Ansel Foxley contributed heavily to the early work including the construction of experimental apparatuses. While he did not stay long in the lab, I appreciate the help that he granted me. I'd also like to acknowledge Mathew Hamilton for all his efforts he gave to the lab and to our experiments. He contributed significantly to the experiment in construction, data acquisition, and data analysis. His efforts allowed me to progress efficiently through the experiments presented in this

thesis. I am very grateful for the assistance he provided me during the course of my PhD research. I wish him well as he finishes his own experiments with Collision Assisted Zeeman cooling.

The lab was aided greatly by undergraduates, and I'd like to take the time to thank some of those who have helped with the experiments. Christopher Ryan worked in the lab when I first started in Jake's group, and thanks to his efforts we were able to construct preliminary equipment such as lasers and electronics. Because of his efforts, we were able to get to the preliminary stages of the experiment quickly. I am grateful for the time he committed to the lab and his ability to efficiently and effectively aid in the many aspects of the experiments.

David French was another exceptional undergraduate whose work contributed greatly to my own research. His ingenuity in the lab, mechanical mindset, and creative problem solving skills were essential in finishing our work with MOT and progressing through our work with the FORT. If we had a problem with light contamination of our measurements, he was always there with cardboard in hand to solve the problem in a few minutes. When we had heating issues from the CO₂ laser chiller, he found a car radiator that simply latched onto the side and deposited the heat into the recirculating water. He was able to quickly understand both the mechanics and physics of the experiment. His skills in the lab and the machine shop were invaluable to my work. Without his help, I could not have completed much of my research on the time scale that I was able to achieve. Dave was also great to just work with, there was rarely a dull moment with him around. I greatly appreciate the aid and friendship that he lent me during his time in our lab. I wish him well as he finishes up his own PhD work at the University of Michigan.

Michael DeAngelo was also instrumental in the research, particularly for the light assisted loss FORT experiments. He was responsible for generating the excited-state spaghetti plots I used in my experiments. Mike had a real knack for the theory and math for the experiments and is an exceptionally bright man. His attitude and enthusiasm for the work made Mike very easy to work with and I am grateful for the time and work he put into the experiment.

Many people outside the lab contributed to my success as well. Most notably, I'd like to acknowledge Dennis Agosta and Kevin Smith. They never lost faith in me, even when I myself had doubts. They always encouraged me to move forward and supported me in everything I did. Graduate school would not have been the same place if not for Dennis and Kevin. Whether it be school work, research, or just relaxing they have always been there and continue to do so to this day. If not for their help and friendship, I doubt I would have ever stuck it through long enough to finish my PhD. I also would not have experienced the great cheese fiasco, whether or not that was a good thing. While we have started to go our separate ways, I'll never forget the support and friendship from Dennis and Kevin. They were always able to cheer me up and to help me move forward in my endeavors. Thus from the bottom of my heart I thank Dennis and Kevin for everything they gave to me.

Finally, I'd like to thank all my friends and family. Through their love, support, and understanding I was able to accomplish my goals. Their guidance and encouragement was essential to my success and I am very grateful for all the love and support I received.

Table of Contents

Chapter 1: Introduction.....	1
1.0 Background.....	1
1.1 Overview.....	4
1.1.1 Laser cooling and trapping of atoms (Chapter 2).....	5
1.1.2 Experimental apparatus (Chapter 3).....	6
1.1.3 Suppression of reabsorption in ultracold gases (Chapter 4).....	8
1.1.4 Homonuclear loading and optimization of the FORT (Chapter 5).....	10
1.1.5 Light-assisted collisional loss (Chapter 6).....	11
1.1.6 Collisional induced decoherence (Chapter 7).....	13
1.1.7 Heteronuclear loading of the FORT (Chapter 8).....	14
1.1.8 Collision assisted Zeeman cooling (Chapter 9).....	15
1.2 Summary.....	16
Chapter 2: Trapping Ultracold Atoms in Light Traps.....	18
2.1 The making of a MOT.....	18
2.1.1 Doppler cooling.....	23
2.1.2 Cooling below the Doppler limit.....	29
2.1.3 Trapping in space.....	34
2.1.4 Loading into MOT.....	39
2.2 The optical dipole trap.....	40
2.2.1 Loading into the FORT.....	44
Chapter 3: Experimental Equipment.....	57
3.1 Diode lasers.....	58
3.1.1 Diffraction grating control of diode frequency.....	61
3.1.2 Temperature stabilization of diode lasers.....	67
3.1.3 Frequency calibration and servo of diode lasers.....	70
3.1.4 Cooling and hyperfine repump laser intensity control.....	76
3.2 Computer control of the experiment.....	78
3.2.1 The Labview experiment control program.....	80
3.2.2 Imaging software.....	85
3.3 Data collection.....	86
3.3.1 Absorption imaging techniques.....	88
3.3.2 The probe laser imaging system.....	91
3.4 The Far Off Resonant Trap.....	94
3.4.1 Alignment of the Far Off Resonant Trap.....	97

3.4.2 CO ₂ beam characterization.....	98
3.5 Vacuum chamber, light fields, and magnetic gradient.....	100
3.5.1 Bootstrapping, normal vacuum operation and getter operation.....	108
3.5.2 Baking the system.....	110
3.6 Conclusion.....	115
 Chapter 4: Suppression of Reabsorption in Ultracold Gases via Modulation of Light... 118	
4.1 Reabsorption in optically thick clouds.....	118
4.1.1 The reabsorption processes.....	122
4.2 Reabsorption rate calculations.....	125
4.3 Measurements of the reabsorption reduction.....	139
4.3.1 The experimental setup.....	140
4.4 Experimental results.....	144
4.4.1 Experimental conclusions.....	151
 Chapter 5: Homonuclear Loading Measurements and Optimizations of the Loading of a Far Off Resonant Optical Trap..... 155	
5.1 Parameters of the FORT load.....	156
5.1.1 Experimental measurement of load rate and loss rate.....	161
5.2 Experimental setup and conditions.....	165
5.2.1 MOT loading.....	166
5.2.2 Molasses loading.....	173
5.3 Data and results.....	176
5.3.1 MOT Load.....	176
5.3.2 Molasses load.....	179
5.3.3 Data variation.....	179
5.3.4 Data analysis.....	181
5.4 FORT loading sequence.....	186
5.5 Conclusion.....	189
 Chapter 6: Light Assisted Collisional Loss in a ^{85/87} Rb Ultracold Optical Trap..... 193	
6.1 Effect of collisions in ultracold atom dynamics.....	195
6.2 Experimental conditions and equipment.....	206
6.3 Data and analysis.....	209
6.4 Models.....	215
6.5 Mixed potentials.....	222
6.5.1 Saturation effects.....	225
 Chapter 7: Collisional Disruption During Shallow Optical Trap Loading in an Ultracold Mixture of ⁸⁵ Rb/ ⁸⁷ Rb..... 230	
7.1 Effective laser cooling and coherence.....	232
7.1.1 Known collisions.....	233
7.2 Experimental conditions and setup.....	236

7.2.1	Load rate reduction experimental setup.....	237
7.2.2	Data analysis for load rate reduction data.....	238
7.2.3	Optical pumping rate change experimental setup.....	242
7.2.4	Hyperfine state distribution measurement.....	246
7.3	FORT load disruption.....	248
7.3.1	Collision induced decoherence.....	248
7.3.2	Dipole-dipole interaction and wave-packet splitting.....	252
7.4	Discussion of results and conclusion.....	255
7.4.1	Summary.....	260
Chapter 8: Determination of $^{85}\text{Rb}/^{87}\text{Rb}$ simultaneous Far Off Resonant Load Rates and Loss Coefficients.....		263
8.1	Modeling the FORT load.....	264
8.2	Load and loss rate measurements.....	266
8.2.1	FORT loading analyzed under simple assumptions.....	267
8.2.2	FORT loading with variable load and loss rates.....	275
8.3	Using the model to predict FORT load.....	282
Chapter 9: Review and Future Measurements.....		285
9.1	Review.....	285
9.2	Future work.....	292
9.2.1	The variable aspect ratio trap.....	292
9.2.2	Collision assisted Zeeman Cooling.....	295
9.3	Conclusion.....	300

Chapter 1

Introduction

1.0 Background

The experiments presented in this thesis were all in some way concerned with the effects of light interaction with ultracold atoms. The concept of light interaction with atoms has been around for some time, starting from the earliest days of spectroscopic measurements [1]. Spectroscopy has been employed to determine properties of atoms or molecules. For example, measuring spectral lines can be used to determine energy levels of atomic or molecular systems. The natural linewidth of these lines yields information about the excited-state lifetime. Doppler measurements yield information about the velocity distribution of a gas of atoms and can be used to calculate the temperature of the atoms. Examining the hyperfine structure of spectral lines tells us about the interaction of the nuclear spin of an atom with that of the electron spin of the atom. While these are just a few examples of the use of spectroscopy, there are many others; though it is not the goal of this thesis to give a full history on the subject.

At the heart of the light-atom interactions studied in this thesis is the absorption and subsequent emission of a photon by an atom. A photon of energy $h\nu$ can be absorbed by an atom if the energy is sufficiently close to the energy difference between two of the atom's states. This absorption and emission can be manipulated in meaningful ways so as to affect an atom's properties (velocity, internal state, etc.). Until the advent of laser cooling, the primary focus of light-atom interaction has been on manipulating the internal

states of atoms. After the advent of laser cooling, though, an enormous amount of research has focused on controlling not only the internal but external states of atoms. For instance, in Doppler cooling, counter-propagating light is overlapped onto a gas of atoms. The light is purposefully detuned to the red (lower energy) of an atom's resonant transition. As the atom moves through the light field, it "sees" a difference in energy of the two beams depending on the direction of travel. The beam the atom is moving towards will appear higher in energy due to the Doppler shift, and thus closer in resonance. The converse is true for the beam the atom is moving away from. As a result, the atom will tend to absorb more photons from the beam it is moving towards. Since light carries with it momentum, this preferred scattering direction causes a net loss of kinetic energy from the atom (spontaneous emission is relied on to carry away the entropy). This form of cooling forms the base of laser cooling and trapping [2]. Doppler cooling is discussed in depth in Chapter 2.1.1.

Likewise, light can be used to confine atoms to a space. This process is similar to Doppler cooling wherein atoms are made to scatter light in a preferential treatment. In systems such as Magneto-Optical Traps (MOT) [3, 4], a magnetic gradient is applied to the atoms that allow the exploitation of the Zeeman effect to produce a spatially confining force. Because the Zeeman effect removes the degeneracy of the m_F energy levels, the magnetic gradient is used to shift the atom into resonance with the laser light with respect to the $B=0$ point. An atom not at the center of the magnetic gradient (where $B=0$) will preferentially scatter light which will "push" it back to the center. In this way, a spatial force is created on the atom through the interaction of a photon. The spatial force is used in conjunction with Doppler cooling to create a trapped ultracold atom

cloud. The spatial confinement of the atoms for a MOT is discussed in further detail in Chapter 2.1.3.

While many forms of light interaction with atoms rely on the scattering of photons by the atoms, light can influence atoms without spontaneous scattering. Such is the case of the Far-off resonance trap (FORT). A FORT consists of a focused laser beam that is far detuned from the resonant transitions of the atom being trapped, which means that atom scattering of FORT photons is negligibly low. FORTs create an effectively conservative potential and belong to a class of ultracold atom traps known as optical dipole traps [5, 6]. As the name implies, the optical dipole trap takes advantage of the interaction of light with an atom's dipole. A light field can induce a dipole in an atom, and that induced dipole is proportional to the electric field of the applied light. That induced dipole can then interact with electric field of the applied light. The potential which is created from this interaction is equal to the atom's dipole dotted into the electric field of the applied light. Thus the potential is proportional to the intensity of the light. In its simplest configuration, a FORT is created by focusing down a laser, thus creating an intensity gradient. Since the potential is proportional to the intensity, the atoms are attracted to the area of highest intensity (for red detuned lasers).

Another way to understand the source of the confining potential in a FORT is through the AC Stark shift. When an atom is subjected to a red detuned light, the interaction of the light field and the atom causes the ground-state energy of the atom to be lowered, (the AC Stark shift [7]). The AC Stark shift is dependent upon the intensity of the light illuminating the atom; the higher the intensity, the greater the effect. As such, areas of greater intensity will result in a lower ground-state energy of the atom and again

atoms are attracted to the area of highest intensity. While the trap depth of the optical dipole is lower than that of the MOT, the tightly confining potential created by it can significantly increase the density of trapped atoms. An additional advantage specifically with FORTs is that since its so far detuned, it will not significantly contribute to heating of the cloud. The optical dipole trap is discussed in depth in Chapter 2.2.

As an aside, there are other forms of traps which take advantage of electromagnetic interactions to cool and/or trap atoms. A common trap, which has been well utilized especially in the creation of Bose-Einstein Condensates (BEC) is the magnetic trap [8]. This introduction was not meant to be comprehensive, but rather touch on topics most relevant for the experiments presented in later chapters.

1.1 Overview

When I first joined the group, there was no established experimental apparatus. In order to perform any of the experiments which were ultimately investigated, the apparatus had to first be constructed. This had the added benefit of allowing me to be involved with the construction of many pieces of the apparatus itself. Much of the experimental apparatus was made in house, including electronics, magnetic coils, diode laser set up, programs, etc.

The ultimate goal when we began was to investigate a non-evaporative cooling scheme using collisions between ^{87}Rb and ^{85}Rb held in a FORT. The idea behind the cooling scheme is to encourage m_F changing collisions between the two isotopes in such a way as to convert kinetic energy into internal energy of the atom, and then remove that internal energy via photon scattering. However, the examination of this cooling scheme is left for future experiments, the results of which will likely be very interesting. If the

cooling scheme can be proven to work well, it can aid other experiments such as those which use BECs. Currently, the main method of obtaining a BEC is through the use of evaporative cooling, a method which innately requires a significant number loss. If atoms can be cooled further than the standard pure optical means (Doppler cooling and sub-Doppler cooling), the number of atoms in BECs can conceivably be increased. Moreover, a non-evaporative cooling technique can widen the range of experimental parameters under which experiments requiring cooling can be performed.

1.1.1 Laser cooling and trapping of atoms (Chapter 2). The predominant trap used to cool and trap neutral atoms at this time is the MOT. The MOT is also the starting point for loading our FORT as well. Integral to the MOT is the laser cooling of atoms which comes in the form of both Doppler and sub-Doppler cooling [9-11]. Doppler cooling was discussed in brief above. It relies on the Doppler shift to shift the frequency of a red detuned beam (as seen by the atom) closer into resonance for the beam the atom travels towards and further out of resonance for the beam it's moving away from. The result of this atom-photon interaction is a viscous force which opposes the motion of the atom. This viscous force then can cool the atom.

The process of sub-Doppler cooling is a similar premise built around atom-photon interactions which oppose the motion of the atom. There are two forms of sub-Doppler cooling, Sisyphus and Induced orientation cooling [12, 13]. In Induced orientation cooling, two circularly polarized beams are counter-propagated. The polarization field which results is a linear polarization that rotates its axis of polarization in space in a helical pattern. As an atom moves through this field, it seeks to come to a ground state spin distribution that is in equilibrium with the local polarization direction. Because of

the Clebsh-Gordon coefficients of the various transitions through which this can happen, the atom ends up scattering on average more photons from the beam it is traveling towards than the one it is traveling away from. In this aspect, Induced orientation cooling is similar to that of Doppler cooling, though is more efficient and able to realize a lower temperature limit. In an actual system, such as the 6-beam MOT used in our experiments (3 beams each of which are retroreflected) the polarization field present is very complex. But the result is that both forms of sub-Doppler cooling are naturally present, which explains why in early experiments the measured MOT temperatures were lower than that which could be expected from just Doppler cooling [14]. Sub-Doppler cooling is discussed in depth in Chapter 2.1.2.

Trapping in space utilizes interactions between atom and photons to produce a space varying force. For the experiments presented in this thesis, the traps used were the FORT and the MOT. The MOT exploits the Zeeman effect to produce a space varying force. The FORT utilizes dipole interaction with the trap light field to produce a space varying force. Both of these methods were briefly discussed above in the introduction. A more detailed discussion of both these traps is discussed in Chapter 2.1.3 for MOT trapping and Chapter 2.2 for FORT trapping.

1.1.2 Experimental apparatus (Chapter 3). The majority of the apparatus hardware was built in lab, including the external cavities of the lasers which supply the MOT laser field. These lasers had to be constructed and controlled to produce the proper frequency of light necessary to create a MOT. The lasers used in our experiment were standard diode lasers. We construct an external feedback cavity for the diodes using a feedback grating in the Littrow configuration. This feedback cavity allows the diode to be

tuned to the proper frequency by adjusting the angle of incidence with the diffraction grating. The feedback system allows these lasers to operate single mode and to be tuned a few GHz continuously [15, 16]. The diode lasers and diffraction grating control is covered in Chapter 3.1 and 3.1.1 respectively.

There was some considerable electronics required to control the diode lasers as well. For stable running, the diode had to be temperature controlled. Fluctuations in the diode laser temperature will manifest itself as fluctuations in the diode laser frequency. As trapping and cooling of atoms requires precise control of the laser frequency, the temperature must be controlled. The electronics for the temperature control were also created in lab and discussed in Chapter 3.1.2. And as precise frequency control is necessary, the diode lasers must be calibrated to known frequencies so that they may be properly set. To accomplish this, a saturation absorption signal is utilized to reference the lasers to the transition frequencies of the Rb isotope we wish to trap, which provides the absolute frequency calibration. A Dichroic-Atomic-Vapor Laser Lock (DAVLL) is used to provide a linear signal to which the diode laser can be locked [17]. This acts as a servo to keep the laser on transition along with calibration for detuning the lasers a specific amount. Both devices used to calibrate and control the diode output frequency were built in lab as well. The calibration of the diodes is discussed further in Chapter 3.1.3.

In addition to the electronics which control the diode laser, a computer program made in Labview controls the execution of a data sequence. In this way, we can reliably and reproducibly change timing, isotopes trapped, imaging, etc. While laser set points are set by hand, the Labview program controls a series of TTLs which activate specific set points so that the laser frequency can be varied during the course of a data sequence

reliably. This program too was made in lab and is discussed in further detail in chapter 3.2.

Also controlled by the Labview program was the imaging system. This system consisted of a laser diode constructed and controlled through the standards means (explained in brief above and in detail in Chapter 3), tuned to be on resonance with either the ^{85}Rb or ^{87}Rb isotope. Then standard absorption imaging techniques are used to image the atoms. These images are recorded on a CCD camera and a series of programs are utilized to store and analyze the images. Absorption imaging is covered in Chapter 3.3.1. The remainder of Chapter 3 talks in depth on the other devices necessary for the experiment which include the vacuum chamber (made offsite), the anti-Helmholtz coils, and the CO_2 beam use to make the FORT.

1.1.3 Suppression of reabsorption in ultracold gases (Chapter 4). While photon-atom interactions have been discussed as a mechanism by which atoms can be cooled, there are also interactions which lead to heating of the atom cloud. One such process is known as reabsorption. Cooling atoms through photon interactions takes advantage of the spontaneous decay to carry away the entropy (in essence the emitted photon is more energetic than the absorbed). Problems arise when the ultracold gas cloud becomes optically thick. In the case of optically thick clouds, the spontaneously emitted photon will be increasingly likely to scatter off another atom in the cloud before escaping. These spontaneously emitted photons are emitted in random direction and polarization, so there's no cooling effect from these additional scatterers. Instead, the net effect of the reabsorption of spontaneously emitted photons in ultracold gases is a heating effect, ultimately limiting the efficiency of laser cooling (and optical pumping). These

limitations due to reabsorption have been observed experimentally in studies showing a decrease in laser cooling efficiency with increasing optical depth [18-22].

The reabsorption process which is most familiar to ultracold atom systems has two components to it. There is a one-photon and a two-photon process which composes the overall reabsorption. The most basic form of reabsorption is the one-photon process. Here, a photon is spontaneously emitted, but if the optical depth of the cloud is too great, that photon will not escape the cloud. Instead, it will be reabsorbed by another atom in the cloud. Since the spontaneously photon is emitted in random direction and polarization, it can yield photon recoils with the atom which can induce heat or it can depolarize the atom with respect to the cooling laser field which can negatively impact optical pumping. The one-photon reabsorption process is perhaps the easiest one to mitigate as the rate of the rescattering is detuning dependent. Increasing the detuning leads to lower reabsorption rates.

The two-photon reabsorption process is harder to deal with. That is because this is a Raman process in which a pump photon (i.e. a photon from whatever laser light is illuminating the cloud) and scattered photon drive the atom into a ground-state with different momentum. Over multiple reabsorption events, this can lead to momentum diffusion, and thus results in the heating of the cloud. Unlike the one-photon process which can be mitigated through detuning, the two-photon process is more resilient to detuning effects. Essentially the pump photons and spontaneously scattered photons will be of the same frequency, and changes in detuning will not affect this relationship. Therefore, the two-photon Raman process can still occur even at higher detunings. To mitigate this process, the coherence of the two-photon reabsorption process must be

disrupted in some way. We were able to achieve such a disruption experimentally through altering the frequency spectrum and spatial pattern of the illuminating light. Reduction of reabsorption will improve any optically-based cooling technique. The investigation of this photon-atom interaction is discussed in detail in Chapter 4.

1.1.4 Homonuclear loading and optimization of the FORT (Chapter 5). The cooling scheme we wish to implement requires collisions between ^{85}Rb and ^{87}Rb held in a trap which will not cause heating to the atom cloud. Thus a FORT is employed to fulfill that purpose. Since the FORT is a conservative potential and is relatively shallow in our experimental setup ($\sim 120\ \mu\text{K}$), the load of the FORT is dependent upon sub-Doppler cooling efficiently reducing atoms' velocities while the atoms traverse the FORT volume. In addition, collisions between atoms being trapped or background gas can cause loss out from the trap. Thus, the ultimate number of atoms that can be loaded into the FORT is a balance between a load rate and a loss rate of atoms from the FORT. The loss mechanism out of the FORT is dominated almost exclusively by atoms in the trap colliding with each other. In particular, two-body light-assisted collisions form the dominant loss mechanism.

In examining the FORT load, we wished to find the experimental sequence through which we can maximize the number of atoms into the FORT. We examined load rates and loss rates under various parameters to construct the ideal conditions under which we can load the FORT. The homonuclear characterization of the FORT load is covered in Chapter 5. As part of these studies we investigated two FORT loading regimes. The first was to load the FORT directly from the MOT, referred to as MOT loading. In MOT loading, the MOT is detuned to create a compressed MOT (CMOT)

and the FORT is turned on. The CMOT stage is left on for the duration of the FORT load, and the load rate and losses are measured. The second form of loading investigated was molasses loading. Here the MOT is turned off during the FORT load, accomplished by turning off the anti-Helmholtz (AH) field at the start of the FORT load. The laser cooling light is left on creating an optical molasses. Since there is no longer an AH field, there is no spatial confinement of the atoms. The advantage of the optical molasses is that the detuning used for an optical molasses is much larger than that for the CMOT. It was found that both molasses and MOT loading can obtain similar load rates into the FORT. However, due to the increased detuning for the molasses, the loss rates for the molasses load are considerably smaller than that for MOT loading.

1.1.5 Light Assisted Collisional Loss (Chapter 6). As mentioned in the previous section, light-assisted collisions are the dominant loss mechanism out of the FORT. These collisions are another example of photon-atom interactions. These collisions occur between atoms illuminated in a near resonant light field, and have been the subject of investigation since the beginning of laser cooling [23-25].

Atoms interact with one another at long ranges through dipole-dipole interactions. The light-assisted collisions we are concerned with focus on an atom pair that is initially in the ground-state (S+S). The atom pair can absorb a near resonant photon and be promoted to an excited-state (S+P) potential. Quantum indeterminacy leads to an inability to distinguish which atom of the pair was excited, and so the atoms can be excited to states that consist of each individual atom being in an S+P state superposition. In such a superposition, there is a non-zero dipole present. On these

excited-state potentials, then, the slope of the potential is significantly steeper than the ground-state due to the interaction of the atom dipoles.

A process known as radiative decay can produce loss from the system once the atoms have been excited to these potentials. Essentially, an atom pair on the excited-state potential will accelerate along the potential. After some time, the atom pair will emit a spontaneous photon to fall back to the ground-state. But since the atom pair had moved on the excited-state potential, there is an energy difference between the absorbed and emitted photon, with the typical case being that the emitted photon has a lower frequency than the excitation photon. The difference in the energy is given to the atom pair in the form of kinetic energy. If the kinetic energy is large enough, it can eject the atom pair from the trap; thus leading to loss.

The ability to trap a heteronuclear mixture of ^{85}Rb and ^{87}Rb into a FORT presented an opportunity to study these types of collisions in a way that had not been done before. In general, the excited-state potentials involved in light-assisted collisions contain considerable structure and exhibit both repulsive and attractive features. However, in our investigation we were able to study many different excited-state potentials including those which were either purely repulsive or purely attractive. Thus we were able to measure the light-assisted loss rates as a function of different characteristics of the excited-state potential. It was found through the course of our study that potentials which exhibited stronger repulsive characteristics had lower loss rates than those which exhibited stronger attractive characteristics.

This form of atom-photon interaction has negative effects with respect to keeping atoms in the FORT, which will be necessary in the implementation of the proposed

cooling scheme. At the very least, these collisions needed to be quantified so that we can account for the losses that could be induced from our trap under normal load conditions. At best, we could find a combination of hyperfine state distributions which would mitigate the loss caused by light-assisted collisions. It was found that the light-assisted loss rates were heavily dependent upon their hyperfine state of the colliding pair. For instance, an atom pair with both in the lower hyperfine ground-state produced the least amount of loss during the FORT loading process. By optically pumping the atoms into their lower states as much as possible some mitigation of the light-induced collisional loss was achieved. These collisions and their measurements are discussed in detail in Chapter 6.

1.1.6 Collision induced decoherence (Chapter 7). In the course of studying heteronuclear loading of the FORT, we encountered a surprising result. When loading both isotopes into the trap, the maximum number of each isotope was significantly lower than under homonuclear conditions. While some decrease is expected due to light-assisted collisions, the measured collision rates could not account for the overall decrease in the observed number. This was surprising since the resonant transitions of ^{85}Rb and ^{87}Rb are detuned from each other by several hundred natural linewidths – thus the presence of laser light resonant with one of the isotopes should have little impact on the other. This large detuning should isolate the system from cross-isotope disruptions of laser cooling and loss outside of light-assisted collisions.

During the course of the investigation, we began to focus the impact of the presence of one isotope on the other's hyperfine state distribution. The FORT used in our experiments was a shallow FORT, with a trap depth of $\sim 120\ \mu\text{K}$. Since the FORT is a

conservative potential, there is a strong dependence upon the hyperfine state distribution to efficiently sub-Doppler cool the atoms as they cross the FORT trap volume. A disruption to this hyperfine state distribution would manifest itself as a reduction of the load rate, and thus would yield fewer trapped atoms. In particular, our system was very sensitive to the coherence of the atoms with respect to the laser light field as we load our FORT from a molasses whose cooling light is detuned by 10-20 natural linewidths from resonance. Because of the relatively large detuning, incoherent scattering is not sufficient to produce efficient sub-Doppler cooling and coherent two-photon scattering is a crucial part of the sub-Doppler cooling. If the presence of one isotope decreased the coherence of the other, the sub-Doppler cooling will become less efficient.

It was found during the course of the evaluation that indeed the presence of one isotope, despite being far detuned, could affect the hyperfine state distribution of the other. Coherent scattering re-established the proper hyperfine state distributions so there was never a total destruction of the loading of the FORT. However, decoherence inducing collisions can disrupt the overall efficiency of sub-Doppler cooling. These forms of collisions manifested themselves as an overall load rate reduction which was measured as a max number reduction. This mechanism is detailed in Chapter 7.

1.1.7 Heteronuclear loading of the FORT (Chapter 8). With light-assisted collisions and collision inducing decoherence in mind, we sought to fully describe the FORT loading for both isotopes under standard experimental conditions. The hope was to describe the system well enough to give us a convenient “knob” which we could tune (pump and hyperfine laser power, detuning, etc.) the number of each isotope in the FORT to meet our experimental needs. We used the standard load equations and assumptions

normally made for FORT loading [7] as a model for our load. The standard assumptions are an independent load rate($R(t)$ only varying with time, not dependent upon atom number or hyperfine state distribution) and independent hyperfine state distribution (the hyperfine state distribution is set through optical pumping and not dependent upon the numbers of ^{85}Rb and ^{87}Rb).

While we knew the assumptions were not true given our earlier results discussed in chapter 7, we did not have a comprehensive model for the changes in hyperfine state distribution and the disruption of the load rate and so it was unclear how relevant this physics would be in describing the overall heteronuclear loading of the FORT. During the investigation of the dual loading, we started with all the assumptions listed above and found that the data observed loading was inconsistent with our model. As such, the assumptions were relaxed one at a time to try to obtain better agreement with measured results and to quantify the system. Ultimately, we found that the physics described in chapter 7 had to be taken into account in order to create a realistic description of the heteronuclear loading of the FORT. Chapter 8 covers the discussion of these measurements and the results.

1.1.8 Collision assisted Zeeman cooling (Chapter 9). The sympathetic cooling scheme we ultimately wish to measure is that of collision assisted Zeeman (CAZ) cooling. This experiment will be conducted in the future and thus is only dealt with briefly in this thesis. This collision relies on m_F changing spin-exchange collisions between the isotopes [26] combined with optical pumping to create a closed cooling cycle. Thus, photon-atom interactions play a large role in completing the cooling cycle. Losses due to photon-atom interactions such as reabsorption or light-assisted collisions

need to be accounted for and minimized. A non-evaporative cooling scheme which can cool below the limits of sub-Doppler cooling has long been desired. One such application of this cooling scheme would be for the more efficient creation of Bose-Einstein condensates (BEC). Currently the main method of achieving BEC transition temperatures is through the use of evaporative cooling [8-29]. This method throws away the vast majority of atoms in order to achieve the necessary temperature. Increased cooling below that of sub-Doppler cooling can, at the very least, result in less atoms being thrown away during evaporative cooling. Chapter 9 covers in brief the proposed experiment and discussion of CAZ cooling.

1.2 Summary

The previous summaries outline the new physics discovered through the work described in this thesis. In all of these experiments, unexpected behaviors were discovered in systems that consisted of, essentially, nearly motionless atoms with sharp atomic resonances being illuminated by narrowband laser light. The role of quantum coherence was often an important facet of understanding the results of these measurements. In seemingly simple systems, there is still a wealth of discoveries that can be made.

References for Chapter 1

- ¹ Wolfgang Demtroder, *Laser Spectroscopy*, 2nd Ed. (Springer-Verlag Berlin Heidelberg, New York, 1981)
- ² Harold J. Metcalf and Peter van der Straten, *Laser Cooling and Trapping*. Springer-Verlag New York, Inc. New York City, 1999
- ³ E. Raab, M. Prentiss, A. Cable, S. Chu, and D. Pritchard, *Phys. Rev. Lett.* **59**, 2631 (1987)
- ⁴ Carl Wieman, Gwen Flowers, and Sarah Gilbert, *Am. J. Phys.* **63**, 317 (1995)
- ⁵ S. Chu, J. Bjorkholm, A. Ashkin, and A. Cable, *Phys. Rev. Lett.* **57**, 314 (1986)
- ⁶ A. Ashkin, *Phys. Rev. Lett.* **40**, 729 (1978)
- ⁷ S. J. M. Kuppens *et. al.*, *Phys. Rev. A* **62**, 013406 (2000)
- ⁸ Jacob L. Roberts PhD thesis, University of Colorado (2001)
- ⁹ Steven Chu, *Rev. Mod. Phys.* **70**, 685 (1998)
- ¹⁰ Claude N Cohen-Tannoudji, *Rev. Mod. Phys.* **70**, 707 (1998)
- ¹¹ William D. Phillips, *Rev. Mod. Phys.* **70**, 721 (1998)
- ¹² Harold J. Metcalf and Peter van der Straten, *Phys. Rep.* **244**, 204 (1994)

-
- ¹³ J. Dalibard and C. Cohen-Tannoudji, *J. Opt. Soc. Am. B* **6**, 2023 (1989)
- ¹⁴ P. Lett *et al.*, *Phys. Rev. Lett.* **61**, 169 (1988)
- ¹⁵ C. J. Hawthorn, K. P. Weber, and R. E. Scholten, *Rev. Sci. Instrum.* **72**, 4477 (2001)
- ¹⁶ A. Q. Liu, X. M. Zgang, D. Y. Tang, and C. Lu, *Appl. Phys. Lett.* **85**, 3684 (2004)
- ¹⁷ Kristan L. Corwin *et. at.*, *Appl. Opt.* **37**, 3295 (1998)
- ¹⁸ D. J. Han, M. T. DePue, and D. S. Weiss, *Phys Rev. A* **63**, 023405 (2001).
- ¹⁹ V. Vuletic, C. Chin, A. J. Kerman, and S.Chu, *Phys. Rev. Lett.* **81**, 5768 (1998).
- ²⁰ H. Perrin *et al.*, *Europhys. Lett.* **46**, 141 (1999).
- ²¹ A. J. Kerman, V. Vuletic, C. Chin, and S. Chu, *Phys. Rev. Lett.* **84**, 439 (2000).
- ²² D. Boiron, A. Michaud, A. Lemonde, Y. Castin, C. Salomon, S. Weyers, K. Szymaniec, L. Cagnet, and A. Clairon, *Phys. Rev. A* **53**, R3734 (1996).
- ²³ M. Prentiss *et al.*, *Opt. Lett.* **13**, 452 (1988)
- ²⁴ L. Marcassa *et al.*, *Phys. Rev. A* **47**, R4563 (1993)
- ²⁵ D. Sesko, T. Walker, C. Monroe, A. Gallagher, and C. Wieman, *Phys. Rev. Lett.* **63**, 961 (1989)
- ²⁶ G. Ferrari, *Eur. Phys. J. D* **13**, 67 (2001)
- ²⁷ M. H. Anderson, J. P. Ensher, M. R. Matthews, C. E. Wieman, and E. A. Cornell, *Science* **269**, 198 (1995)
- ²⁸ K. B. Davis *et. al.*, *Phys. Rev. Lett.* **75**, 3969 (1995)
- ²⁹ K. B. Davis, M. -O. Mewes, and W. Ketterle, *Appl. Phys. B* **60**, 155 (1995)

Chapter 2

Trapping Ultracold Atoms in Light Traps

In this chapter, the basics of laser cooling and trapping will be discussed. The experiments presented in this thesis used two basic types of traps; the Magneto Optical Trap (MOT) and the Optical Dipole Trap. The particular form of dipole trap used for these experiments is known as a Far Off Resonant Trap (FORT). While both of these traps confine atoms, they do so through different mechanisms. Those mechanisms and the basics of laser cooling will be covered in this chapter.

2.1 The Making of a MOT

The Magneto Optical Trap (MOT) is a robust and often used trap used for the capture and cooling of neutral atoms. The first experiments which realized the capture of atoms in a MOT were performed on sodium and were reported in 1987 [1]. David Pritchard, Steven Chu and co-workers were able to capture 10^7 atoms with a reported effective trap depth of 0.4 K. Since then numbers, densities, and temperatures have been greatly improved and many neutral species have been successfully trapped in MOTs. MOTs themselves have been well studied and the procedures and apparatuses necessary for the creation of them are well known [2]. In many systems, including experiments presented in this thesis, the MOT provides the initial trapping and cooling of atoms. Other traps are loaded from the MOT, such as loading into an optical dipole trap [3, 4, 5]. The characteristics of a MOT allow it to capture and cool atoms effectively. A MOT has a large trap depth, especially when compared to many types of optical trap. A larger trap

volume allows for a large number of atoms to be captured effectively through strong radiative forces [6]. It is very robust; there is a large parameter space in which the MOT will work. This allows for easy implementation.

The MOT used in the experiments for this thesis was a retroreflected MOT. Instead of using 6 independent beams, 3 beams are used with each beam reflected back into the chamber to produce the appropriate overlapping trapping light field. The MOT is not intensely sensitive to the overlap of the beams, nor is it sensitive to precise settings of polarization (though the polarizations must be set at least roughly correctly to establish cooling and trapping). As an illustration of this robustness, at one point we accidentally exchanged a retroreflection waveplate for a beam splitter. Even with the beam splitter in place instead of the proper waveplate, a MOT was achieved; thus demonstrating the robust nature of the MOT.

The methodology for creating MOTs is now well known [7] and 100's of experiments have been done using MOTs in some form. Many dynamics of MOTs and techniques for using MOTs are known and published. In all the work presented in this thesis, the work was either done directly in the MOT, or the MOT was used as an initial trap. In the latter case, the MOT was then overlapped with a Far Off Resonant Trap (FORT) which was then loaded directly from the MOT. In this chapter, I will focus on the dynamics behind Magneto-Optical and Far Off Resonant trapping while chapter 3 will focus on the fabrication of the experimental apparatus itself.

While MOTs have been used to trap a wide variety of elements, the work presented in this thesis focused solely on two species of Rubidium, ^{85}Rb and ^{87}Rb . We were able to trap ^{85}Rb and ^{87}Rb both individually and simultaneously. Many of the loss

and cooling mechanisms present in ultracold trapping are related to the internal structure of the atoms themselves. Thus, by using differing species it becomes possible to probe different collisions and other properties of the atoms. In fact, the first reported simultaneous trapping of different species in a MOT was an $^{85}\text{Rb}/^{87}\text{Rb}$ MOT [8]. Collisions in an ultracold, heteronuclear gas have been the subject of many experiments since then [9, 10]. Of particular interest in heteronuclear ultracold traps is photoassociation [11] which is commonly studied in terms of creation of molecules [12] as a tool to study the fundamental properties of bond formation and energies. However, the process of light assisted collisions can also lead to losses from both MOTs and FORTs during trap loading as well (see Chapter 6). Heteronuclear trapping can also allow for alternate optical pumping schemes through sympathetic cooling between the differing species [13]. In fact, one of the future projects of the group is to ultimately use a heteronuclear loaded FORT in order to attempt an all optical, sympathetic cooling mechanism based on the Zeeman effect.

In order to create a heteronuclear trap, each species required its own set of lasers; each isotope needed two lasers which consisted of a trapping laser and a hyperfine repump laser (defined in Fig. 2.1). This is because ^{85}Rb and ^{87}Rb have different atomic structures and thus different hyperfine splittings, resulting in the frequency necessary to excite the proper cooling transitions for the two isotopes being different. ^{87}Rb has a nuclear spin $I=3/2$ and ^{85}Rb has a nuclear spin $I=5/2$. Since both isotopes of Rb have a non-zero nuclear spin; both exhibit hyperfine structure in their ground and excited states, though the splitting between their respective hyperfine levels is different. The hyperfine levels are denoted by F , which is the total angular momentum of an atom ($F=I+J$, where J

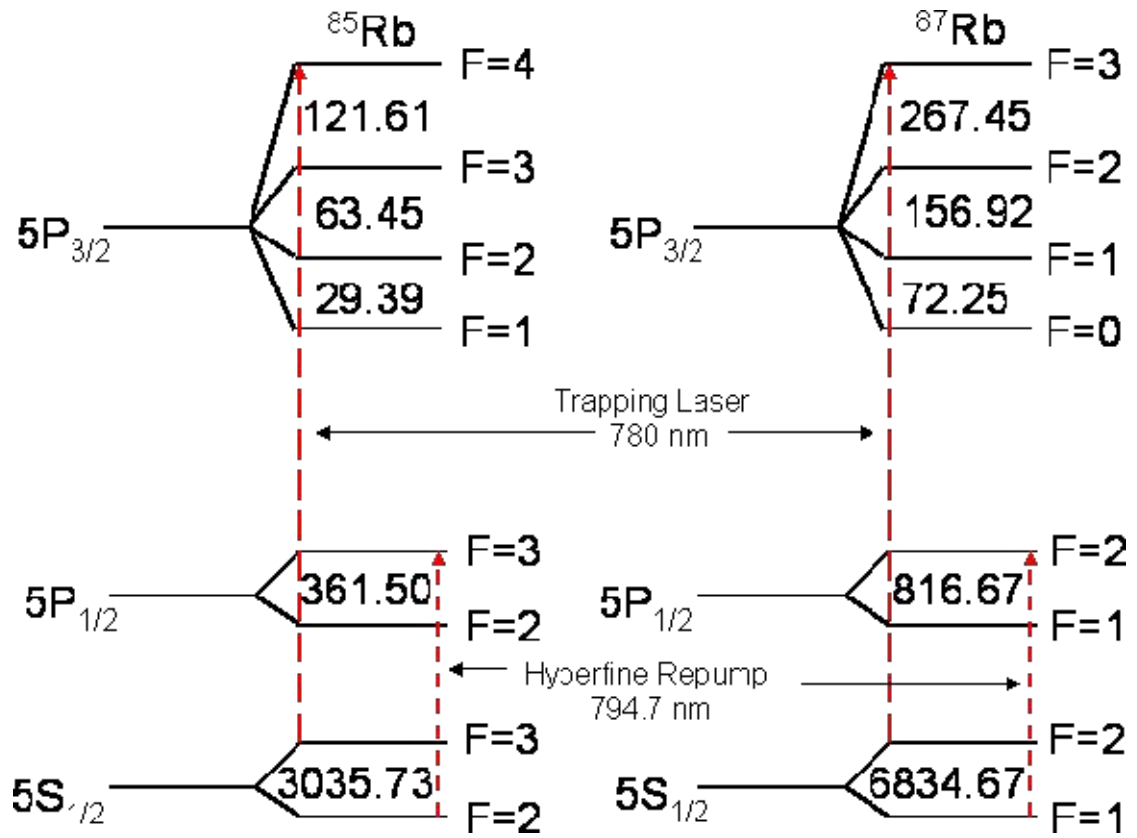


Figure 2.1 Hyperfine structure for both ^{85}Rb and ^{87}Rb of their ground states and first excited P-states. All splitting frequencies are given in MHz. The cycling transition (trapping laser) and hyperfine repump transitions are labeled above. The D2 line for both isotopes is 780 nm, $5S_{1/2}$ to $5P_{3/2}$ transition. The D1 line for both isotopes is the 794.7 nm, $5S_{1/2}$ to $5P_{1/2}$ transition. All listed splittings in this figure were calculated from [14].

is the total angular momentum of the valence electron, $L+S$ in standard LS coupling). The beams from all four lasers were overlapped and propagated into the chamber to create the trapping light field and to ensure that both MOTs could be overlapped in space. This overlap is important in subsequent FORT loading. To maximize the number of each isotope into the FORT both MOTs must be overlapped with the FORT volume and hence each other.

Fig 2.1 shows the hyperfine structure for both ^{85}Rb and ^{87}Rb in addition to labeling the specific transitions used in the cooling and trapping of ^{85}Rb and ^{87}Rb . In the experiments presented both the D2 (780 nm) and D1 (794.7 nm) lines were used in order to trap and cool the Rb. While the specific mechanisms to cool and trap atoms are discussed in detail below, trapping and cooling require scattering of many photons by the atoms. The main cycling transition is the $F=3$ (2) to $F'=4$ (3) transition on the D2 line for ^{85}Rb (^{87}Rb). Here primes (F') denote excited states. While the predominant scattering will be from the cycling transition, there is a non-zero probability of making an off resonant transition. For example, for ^{85}Rb the primary off resonant transition would be from the $F=3$ ground state to the $F'=3$ excited state on the D2 line. The selection rule of $\Delta F=0, \pm 1$ prohibits a transition from the $F'=4$ excited state to the $F=2$ ground state, but if an off resonant transition occurs it then becomes possible for the atom on the $F'=3$ excited state to decay to the $F=2$ ground state. This breaks the scattering cycle and that atom becomes “dark” with respect to the main cooling light. In order to keep the cooling cycle going, there has to be a hyperfine repump laser to get the atoms back to the $F=3$ ground state. We accomplished this by pumping on the D1 line. In general, the hyperfine repump merely has to be able to move atoms from the lower hyperfine ground

state to the upper hyperfine ground state and this can be accomplished on the D2 line too. For our system we have chosen the hyperfine repump to operate on the D1 line. For example, ^{85}Rb is repumped on the D1 $F=2$ to $F'=3$ transition. Thus atoms which make an off resonant transition and end up in the $F=2$ ground state now are pumped to the $F'=3$ excited state where they will eventually make a transition back down to the $F=3$ ground state where it will once again be visible to the cycling laser.

The cooling of the atoms with laser light requires many atom-photon scattering events, which is why it is important to prevent population build up in the dark state. There are a few different types of cooling which occur in a MOT. The differing cooling mechanisms are discussed in this chapter. The primary cooling mechanism in a MOT is Doppler cooling. However, other sub-Doppler cooling mechanisms are present as well. It is the Doppler cooling which dominates at first by capturing the larger number, faster atoms and cooling them. Once the atoms are cooled enough that sub-Doppler mechanisms take over and achieve temperatures much lower than the Doppler limit.

2.1.1 Doppler Cooling. As mentioned above, in laser cooling and trapping using the MOT technique Doppler cooling is the process by which the majority of the cooling is accomplished. It's a relatively simple mechanism to understand, yet is a powerful and robust tool in laser cooling and trapping of atoms. In essence Doppler cooling works through velocity-dependent photon scattering wherein an atom will absorb a photon which has been Doppler shifted due to its velocity and then spontaneously emit a photon to return to the ground state. The rate at which an atom scatters photons is given by:

$$R = \frac{\gamma}{2} \left(\frac{I / I_{sat}}{1 + I / I_{sat} + 4 \left(\frac{\delta}{\gamma} \right)^2} \right) \quad (2.1)$$

where γ is the inverse of the excited state lifetime (τ); for Rb $\gamma=2\pi*5.98$ MHz. I_{sat} is the saturation intensity and is given by $(\pi\hbar c)/(3\lambda^3\tau)$ and is about 1.6 mW/cm^2 for Rb (this value is for the strongest transition in Rb assuming fully polarized atoms with optimally polarized light). I is the intensity of the cycling beam, and $\delta=2\pi\Delta$ (where Δ is the detuning of the laser off of the transition in Hz). Equation 2.1 is a scattering rate for an atom at rest in a light field. In general when discussing cooling forces for an atom moving through a light field, there is an additional velocity-dependent term included; ω_D . The resulting change in equation 2.1 is that δ goes to $\delta-\omega_D$ (where $\omega_D = -\vec{k} \cdot \vec{v}$, the frequency shift due to the Doppler effect). There is a maximum value of R in equation 2.1 when the lasers are tuned directly on transition ($\delta-\omega_D=0$). The scattering rate then decreases with increasing non-zero detuning. It is the detuning sensitivity of the scattering rate which allows for Doppler cooling. Figure 2.2 shows a simple 1-D representation of the Doppler cooling process. Atoms in the chamber are not stationary, and thus in a light field composed of counter-propagating beams they see Doppler shifts in the frequency of the light due to their velocity. With counter-propagating beams, an atom moving in the light field will see beam it's traveling toward shifted higher in frequency (blue shifted) while the beam it's traveling away from will appear lower in frequency (red shifted). Choosing an appropriate detuning can take advantage of the Doppler effect and detuning sensitive scattering rate to slow down the atom. Figure 2.2 illustrates this by detuning the cycling laser to the red of the transition. With this

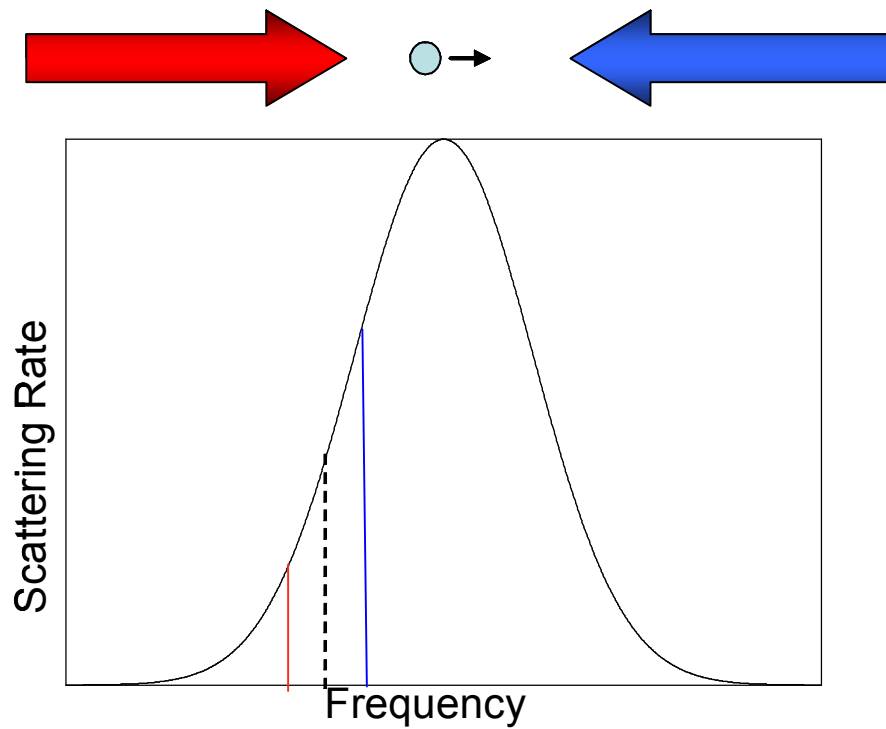


Figure 2.2 Scattering rate vs frequency illustration for an absorption of a photon by an atom. If a laser is detuned to the red (lower frequency) of the peak scattering rate (0 detuning) in the lab frame, the Doppler will cause an atom to preferentially scatter from the beam it is moving towards. As the atom moves towards a beam, it sees the frequency blue shifted and thus closer into resonance with its transition frequency. Conversely, the beam it is moving away from is red shifted, and is seen as being even further out of resonance. Because of this, the atom will scatter on average more photons from the beam it is traveling towards

selection of detuning, an atom in the laser field will see the beam it's traveling toward shifted higher in frequency and closer to resonance, conversely the beam the atom is traveling away from sees that beam shifted further out of resonance from the transition. The result is that on average the atom will scatter photons from the beam it's traveling towards more than it will scatter photons from the beam it is traveling away from.

This preferential scattering of photons opposite of the atoms direction of motion is what enables the cooling of the atoms in the cloud. A photon has a momentum of $\hbar k$ (k being the wave number of the laser light $2\pi/\lambda$) that is conserved in a scattering event with an atom. An atom which absorbs a photon receives a momentum kick of $\hbar k / m$ in the direction of the laser beam where m is the mass of the atom. By setting the conditions so that the atom absorbs more photons from the beam it is traveling towards, the net result is that the atom feels a force opposing its motion and thus slows down. There is, of course, spontaneous emission of a photon once the atom has absorbed a photon out of the laserfield. This spontaneous emission, however, is in a random direction. So over the course of many scattering events, the net momentum delivered to the atom from the spontaneous emission is zero. The average force imparted on the atoms from these momentum kicks is given by:

$$F = \frac{\hbar k \gamma}{2} \left(\frac{I / I_{sat}}{1 + I / I_{sat} + 4 \left(\frac{\delta - kv}{\gamma} \right)^2} - \frac{I / I_{sat}}{1 + I / I_{sat} + 4 \left(\frac{\delta + kv}{\gamma} \right)^2} \right) \quad (2.2)$$

where $k=2\pi/\lambda$ (λ is the wavelength of the trapping light, 780 nm for Rb). Figure 2.3 depicts the Doppler force exerted on an atom as a function of atom velocity. Values of $I/I_{sat}=2$ and a detuning of -10 MHz were taken to construct the graph.

Figure 2.3 shows one of the limitations to Doppler cooling which comes through in the velocity dependence of the force. An atom with large enough velocity will not feel significant force and thus will not be cooled. Doppler cooling only works effectively on atoms which have an initially slow enough velocity. More importantly, there is an ultimate limit to which Doppler cooling can cool. This is known as the Doppler limit and is given by $T_d = \hbar \gamma / 2k_B$; 141.41 μK for Rb. This limit is caused by statistical heating caused by the laser [15]. While earlier it was mentioned that over many scattering events, the momentum recoil caused by spontaneous emission was zero, because each rescatter has a momentum associated with it from the emitted photon the averaged emission does not have a zero effect. Each recoil will cause movement in a random direction, creating a random walk for an atom's motion. This is easily envisioned by considering an atom at rest. If a light field is applied the atom will begin to move around due to the spontaneous motion. While the average velocity will be zero, the instantaneous is not. This statistical heating caused by the absorption and emission of photons then leads to the ultimate limit on temperature able to be reached by pure Doppler cooling.

Doppler cooling, and in fact sub-Doppler cooling, exists in what is known as an optical molasses. The optical molasses is simply a red detuned laser field with no spatially confining force. The optical molasses applies a significant damping force to the atoms, which causes the atoms to quickly slow down. At its maximum ($v=8$ m/s from figure 2.3) the damping force produces an acceleration on the Rb atoms of about 70,000 m/s^2 . This equates to a sub-millisecond time constant for the cooling. Very quickly, these atoms then reach their equilibrium state and the motion of the atoms is similar then

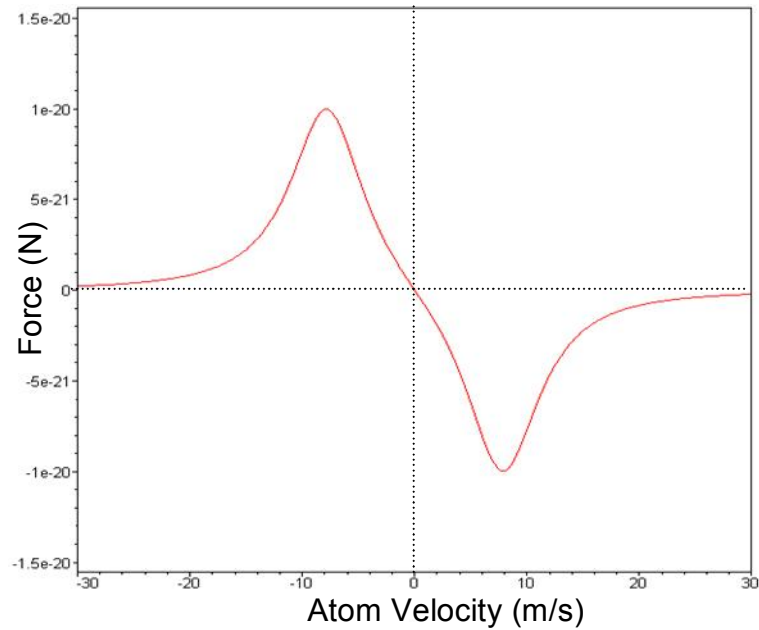


Figure 2.3 The calculated force on a atom from Doppler cooling as a function of atom velocity. $I/I_{\text{sat}} = 2$ and $\delta = -10$ MHz, a typical MOT load detuning for our experimental conditions. The force starts out from 0 m/s increasing as the Doppler effect is velocity sensitive. However, at some point the atoms move so fast that they will not be able to scatter enough photons to be effectively cooled and trapped. As such, around 30 m/s the force due to the Doppler effect goes to zero.

to Brownian motion [15]. While the first experiments with an optical molasses was consistent with that predicted through Doppler cooling [16]; in subsequent experiments with optical molasses, it was found that the temperature reached was actually well below that predicted through Doppler cooling [17]. Ultimately, this discovery led to the development of a new theory of cooling which is capable of reaching temperatures which are well below the Doppler limit [18].

2.1.2 Cooling below the Doppler limit. In the early experiments of laser cooling and trapping, measurements of optical molasses quickly discovered that the temperature to which atoms were being cooled to were well below that of the predicted Doppler limit. NIST performed one of the earlier experiments, trapping Na which has a Doppler limit of 240 μK . Surprisingly, the results of their experiment indicated the temperature of their Na cloud to be around 40 μK [17]. As such, it became apparent that there was another mechanism at work allowing for sub-Doppler cooling inherent to the optical molasses. There were several mechanics which were discovered to have the ability to cool below the Doppler limit, but two which are most applicable to our system collectively known as polarization gradient cooling [7,18]. The two types of polarization gradient cooling schemes rely on spatially varying polarization orientations. The discussion for polarization gradient cooling will be restricted to 1-D with the polarization field generated by a pair of counter-propagating beams of differing polarization. Induced orientation cooling uses $\sigma^+ - \sigma^-$ polarization, while Sisyphus cooling employs a $\text{lin} \perp \text{lin}$ orientation.

Induced orientation cooling consists of two counter-propagating circularly polarized beams of different handedness which are overlapped. In general, one can write

the positive frequency component of the total electric field from the counter propagating beams (along z axis) as

$$E(z) = E_o \varepsilon \exp(ikz) + E'_o \varepsilon' \exp(-ikz). \quad (2.3)$$

E_o, E'_o being the amplitudes of the beams and $\varepsilon, \varepsilon'$ being the polarizations. For induced orientation cooling ($\sigma^+ - \sigma^-$), the polarizations are given by [18]

$$\begin{aligned} \varepsilon &= -\frac{1}{\sqrt{2}}(e_x + ie_y) \\ \varepsilon' &= \frac{1}{\sqrt{2}}(e_x - ie_y) \end{aligned} \quad (2.4)$$

The overlapping of these two polarizations creates a polarization field which keeps the same ellipticity but rotates in space. For example, for the case in which $E_o = E'_o$ (as is the case for experimental MOT conditions such as our own) the polarization field is linear in which the axis of polarization rotates in a helix as an atom moves along the z direction. Since the light is linearly polarized, it will drive $\Delta m=0$ transitions; additionally, due to the difference in Clebsh-Gordan coefficients, after many scattering events atoms at rest will see a population build up predominately in the $m_F=0$ sublevel and this build up is symmetric across the m_F sublevels. The sample system shown in figure 2.4 shows the Clebsh-Gordan coefficients. However, an atom which happens to be moving in this field sees a space dependent variation in the axis of polarization in the light field. This rotation breaks the symmetry found in the $v=0$ case. As a result the populations in the individual m_F sublevels becomes dependent upon the value kv and the population build up is no longer symmetric. This is due to an imbalance in the m-state population pumping rates caused by the atoms' motion through the rotating polarization field. The end result is similar to Doppler cooling; the atom is more likely to scatter

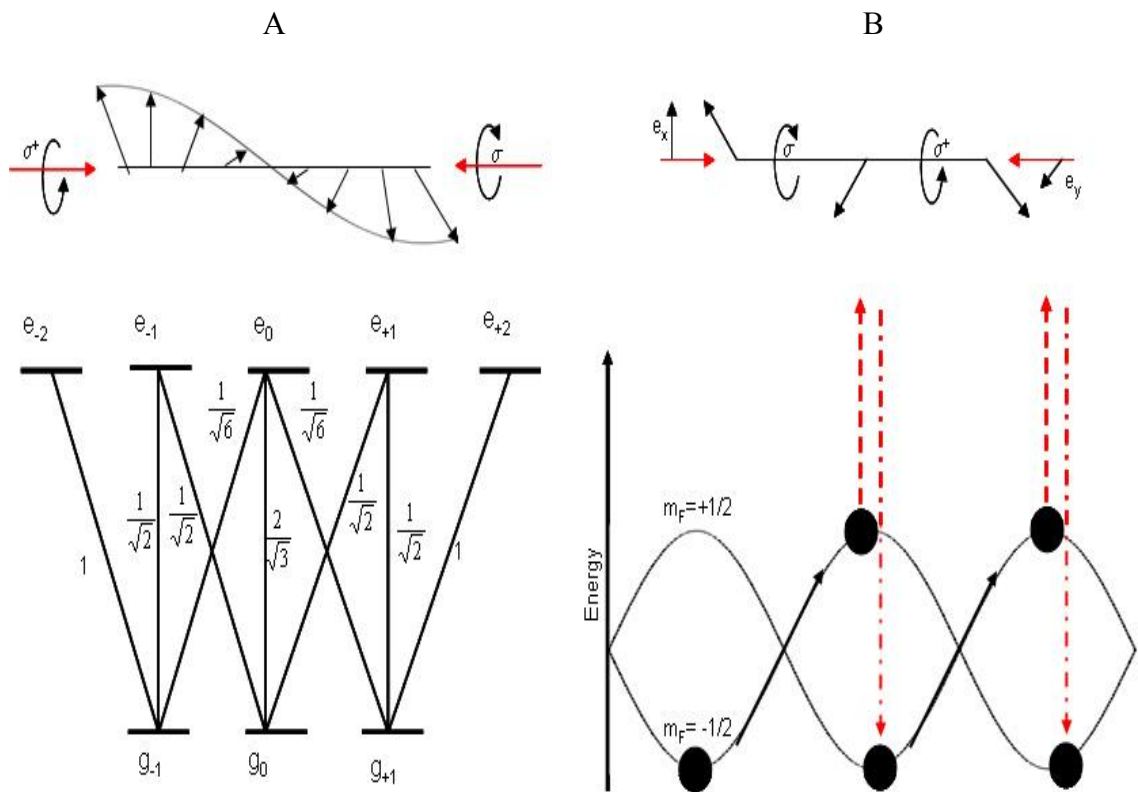


Fig 2.4 polarization gradients from A) $\sigma^+ - \sigma^-$ configuration and B) $\text{lin} \perp \text{lin}$ configuration. The top two illustrations show the polarization change with position, the bottom illustrations deal with the dynamics of each style of sub-Doppler cooling. Bottom A) shows the atomic structure for a simple $F = 1$ to $F'=2$ transition with Clebsch-Gordan coefficients for a stationary atom. Bottom B) illustrates the mechanism behind Sisyphus cooling where an atom climbs a potential hill and absorbs a photon at the top. Through spontaneous emission, the atom falls down to the lower ground state and starts the process over again.

atoms from the beam it is traveling into than it is to scatter photons from the beam it is traveling away from. Over many scattering events this leads to a net loss of momentum of the atom. Induced orientation cooling is more efficient than Doppler cooling and has a lower temperature limit (around the one photon recoil limit).

Sisyphus cooling (or lin \perp lin) works by a different mechanism. For Sisyphus cooling, the light field overlapped is linear (for example)

$$\begin{aligned}\varepsilon &= e_x \\ \varepsilon' &= e_y\end{aligned}\tag{2.5}$$

The result is a polarization field which switches polarization every $\lambda/8$. That is to say if the field starts linear at $z=0$, it will be circular (σ^-) at $z=\lambda/8$, linear again at $z=\lambda/4$, back to circular with the opposite handedness (σ^+) at $z=3\lambda/8$, back to linear at $z=\lambda/2$, etc.

Because the polarization varies with distance, the light shifts of the magnetic sub-states are also dependent upon position. Depending on where an atom is in the polarization field will determine which ground state is preferentially trapped. In the σ^- field, $\Delta m_F=-1$ transitions are pumped whereas in the σ^+ field $\Delta m_F=+1$ transitions are pumped. In the linear field $\Delta m_F=0$ transitions are pumped. Thus the ground state energies are shifted and position dependent. This energy shift is depicted in Fig 2.4 (b) for an example $J_g=1/2$ atom. As opposed to induced orientation cooling which relied on differential light shifts due to atoms moving in a polarization field. The differential light shifts utilized by Sisyphus cooling are present innately from the overlap of the linear beams.

As an atom moves through the polarization field, it sees the energy of the ground state which it is in oscillate with distance. As the atom climbs a potential hill, it gives up kinetic energy and thus at the peaks of the “hills” it is moving slower. As it moves down

the other side, the opposite is true. Thus an atom moving through such a field spends more of its time at the top of the potential peaks where it is moving the slowest. Since more time is spent here by the atom, on average the atom will absorb a photon from the light field at this point. Additionally, the Clebsh-Gordan coefficients are favorable for an absorption and subsequent state change at these points. Once in the excited state two things can happen. It can either go through a stimulated or spontaneous emission event in which it drops back down to the same ground state from which it originated from. In this case, the atom just continues down the potential slope and no energy has been lost. Or it can undergo a spontaneous emission event in which it drops down to a different ground state than the one from which it started. In this case, as depicted in Figure 2.4 (b), the photon which must be emitted to get to the lower ground state must be “bluer” than the one absorbed. The kinetic energy the atom gave up to climb the potential hill is radiated away by the spontaneously emitted photon and the atom has overall lost energy. Now in the lower ground state, the atom can repeat the process by giving up kinetic energy in order to once again climb the curve. This continual uphill movement and radiation to the lower ground state is where this cooling scheme gained its name.

While the viscous force from the two types of polarization gradient cooling are different, the equilibrium temperatures are similar. For Sisyphus cooling, the equilibrium temperature is [18]

$$T \approx \frac{\hbar\Omega^2}{8k_B|\delta|}. \quad (2.6)$$

Wherein the equilibrium temperature for induced orientation cooling is [18]

$$T \approx \frac{29\hbar\Omega^2}{300k_B|\delta|}. \quad (2.7)$$

Both of these equilibrium temperatures are calculated in the limit of $\delta \gg \gamma$. However, while the temperature limit for polarization gradient cooling is lower than Doppler cooling, the capture velocity is a lot smaller. Figure 2.5 shows the forces due to polarization gradient cooling for both Sisyphus and induced orientation cooling. So while this process can cool well below the Doppler limit, the atoms need to be moving much slower than they need to be for Doppler cooling to have an effect. In general, Doppler cooling and polarization gradient cooling work in tandem. As an atom is Doppler cooled its velocity drops to a magnitude at which polarization gradient cooling can take over. In actual application of laser cooling wherein trapping beams are directed in 3-D, both forms of polarization gradient cooling are naturally present. As explained below, MOT trapping beams are circularly polarized, but an atom in motion won't necessarily be moving along the direction of just one beam. As such, the atom will see a complex polarization field will actually be subject to both forms of polarization gradient cooling.

2.1.3 Trapping in space. Both Doppler cooling and polarization gradient cooling are mechanisms which provide a viscous force to an atom's motion. While these processes can slow an atom's movement there is nothing inherent in either of these mechanisms which provides a spatial force. As such, a different scattering dynamic is needed to provide a space sensitive force on the atoms. Figure 2.6 demonstrates a 1-D model of just such a process by which atoms can be trapped in space. Similar to several mechanisms of laser cooling and trapping, MOT trapping works by creating a system of preferential scattering. Where as for cooling, the scattering is designed to be velocity dependent; MOT trapping is designed to be spatially dependent. For spatial confinement,

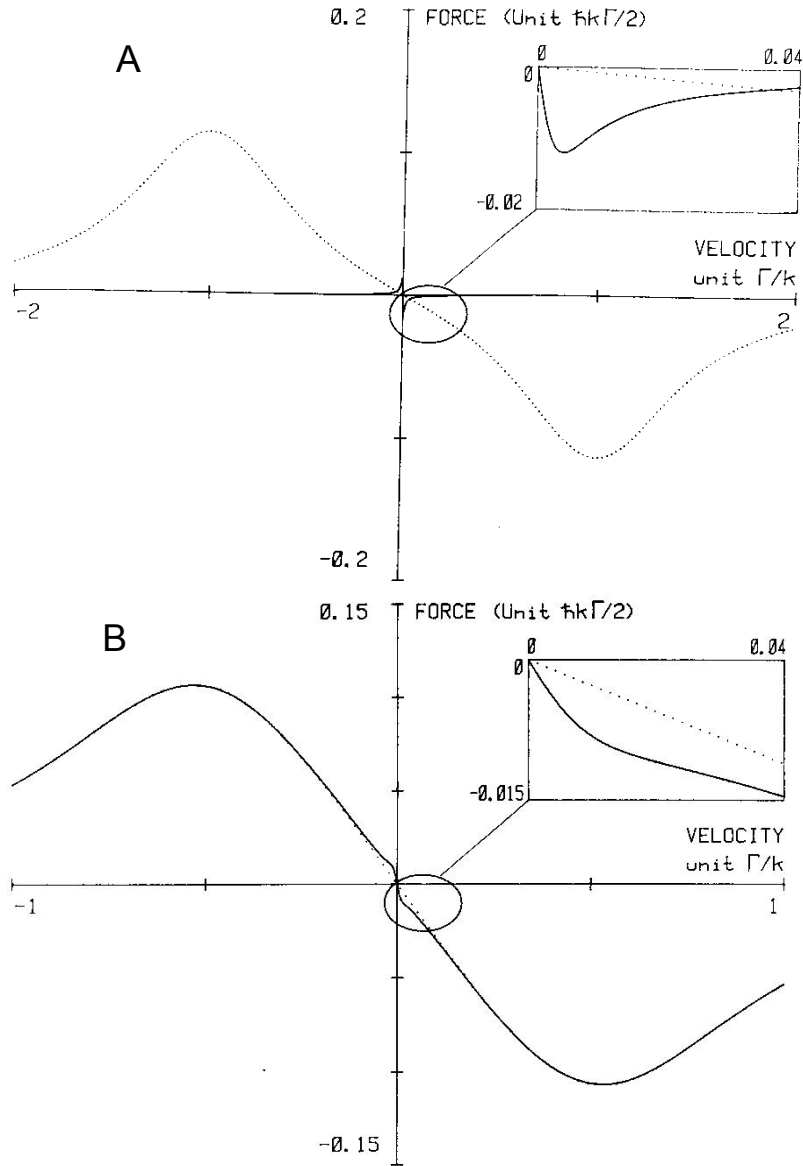


Figure 2.5 Figure A shows the variations with velocity of the force due to Sisyphus cooling. The dotted curve is the Doppler cooling, and the solid curve is Sisyphus cooling. Figure B shows the variations with velocity of the force due to induced orientation cooling. The dotted curve again shows the Doppler cooling and the solid curve induced orientation cooling. The inserts show the deviation from Doppler cooling, indicating that polarization gradient cooling has taken place. Both graphs are taken directly from [18].

the Zeeman effect is taken advantage of. The simplest of these structures for which MOT trapping will work is depicted in Figure 2.6. In this example transitions are driven from a ground state $J = 0$ to an excited state $J = 1$. In the excited state there are 3 magnetic sublevels $m = -1, 0, +1$. In the presence of a magnetic field, the energy degeneracy of these magnetic sublevels is broken and the magnetic sublevels become shifted through the Zeeman effect. The application of a linear, inhomogeneous magnetic field ($B(z) = A \cdot z$, where A is a constant) causes this shift in levels to become spatially dependent. Such a field is easily generated by a pair of anti-Helmholtz coils.

The trapping light for the MOT is composed of counter-propagating, circularly polarized beams of opposite handedness detuned to the red of the cycling transition. Again, $\Delta m = \pm 1$ transitions are driven by σ^\pm light. If we take a random point on the left side of Figure 2.6 ($z \neq 0$), where the $m = +1$ state has been shifted down in energy, we see that the $\Delta m = +1$ is shifted closer into resonance with the laser field. Hence, an atom here is more likely to absorb photons from the σ^+ beam; the opposite is true on the right side of the figure. Doppler cooling utilizes shifts in detuning with an atomic transition in a way which are sensitive to velocity. Likewise, the spatially confining force utilizes shifts in detuning which are sensitive to position. Since the detuning is dependent upon the Zeeman shift, the forces from this scattering are towards $z=0$ ($B=0$) [19], the center of the trap, where the Zeeman shift disappears. While figure 2.6 shows only the 1-D case for simplicity, the spatial confinement is easily expanded to 3-D. The only requirement for creating the spatially dependent force is a linearly changing B field and the proper polarization. The field requirements in 3-D are satisfied with a single anti-Helmholtz (AH) coil [20]. If the AH coils are oriented along the z -axis, there is obviously a

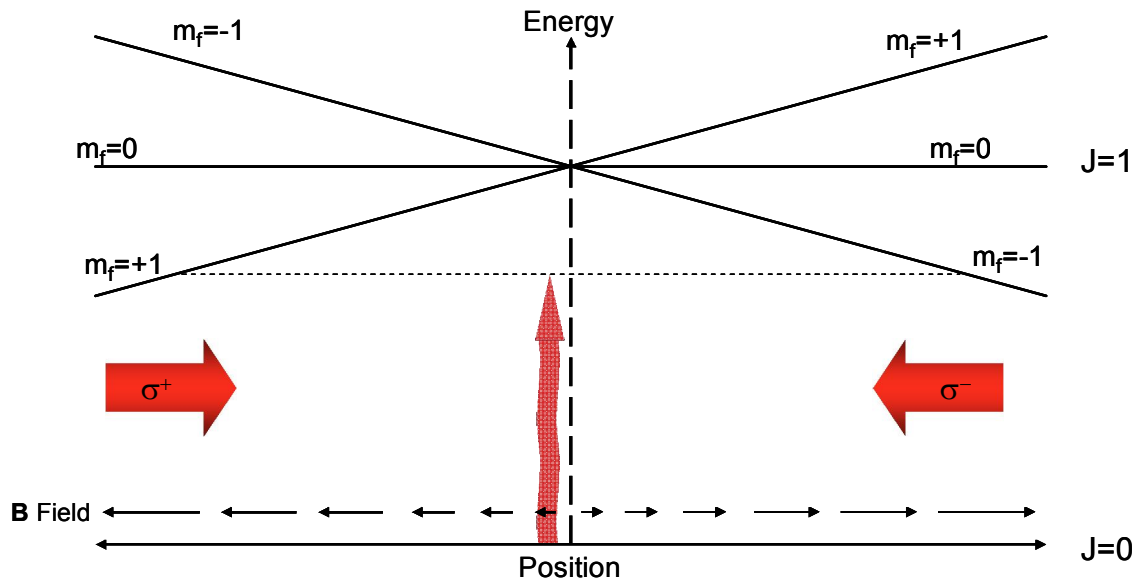


Figure 2.6 Set up for a MOT in 1-D. The arrows at the bottom indicate direction and relative strength of the magnetic field due to the anti-Helmholtz coils. The dashed line shows the detuning of the trapping laser, to the red of the transition. For the $F = 1$ state, the energy shift of the magnetic sublevels varies with the changing magnetic field. For instance, on the right side of the illustration, the $m_f = -1$ state is shifted closer into resonance with the light field. Thus transitions from the $F = 0$ $m_f = 0$ to $F = 1$ $m_f = -1$ are preferred and atoms on that side will be more likely to scatter σ^- light. Setting σ^- light to come in from the right to the left in the illustration will cause atoms on the right side to be pushed back towards the middle. The opposite is true on the left side of the illustration.

magnetic gradient along z. But this also creates a magnetic gradient in both x and y.

With just the one set of AH coils along the z-axis, symmetry says that the gradients in the x and y direction will be the same. Thus, the field gradients in the x and y direction can be found through

$$\begin{aligned}\vec{\nabla} \cdot \vec{B} = 0 &\rightarrow \frac{\partial B_x}{\partial x} + \frac{\partial B_y}{\partial y} + \frac{\partial B_z}{\partial z} = 0 \\ \frac{\partial B_x}{\partial x} &= \frac{\partial B_y}{\partial y} \\ \frac{1}{2} \frac{\partial B_z}{\partial z} &= -\frac{\partial B_x}{\partial x} = -\frac{\partial B_y}{\partial y}\end{aligned}\quad (2.8)$$

Since the magnetic field requirements are satisfied with a single set of AH coils, all that is necessary beyond that for 3-D trapping are 3 pairs of counter-propagating beams, with the 3 pairs being orthogonal to each other. This can be done in one of two ways. One is by using 6 separate beams and aligning them into the chamber properly to create 3 pairs of counter-propagating beams. The other way (as is the case with our system) is to use 3 separate beams which are aligned into the chamber and then retro-reflected back on themselves. These beams are used for both the cooling and spatial confinement. As an aside, while 6 beams are standard in most MOT setups, it is possible to construct a MOT with only 4 beams which are not counter-propagated [21].

The cycling transition lasers are used to drive these MOT transitions and Doppler cooling. The hyperfine repump lasers explained earlier in the chapter close the loop and prevent all the atoms in the trap from falling into the dark state. Thus the combination of the cycling and repump lasers, Doppler and polarization gradient cooling, and the Zeeman effect allow for the creation of an ultracold gas cloud centered at $B = 0$ in the

trap. These are the basics of creating a MOT. The equipment and design are discussed in Chapter 3.

2.1.4 Loading into MOT. The primary mechanism behind trapping into the MOT relies on the Doppler cooling of the Rb atoms in the vacuum chamber. This is because in order to be spatially confined the atoms have to be moving slow enough through the trap volume to be trapped; atoms moving too fast ($v_{\text{atom}} > v_{\text{capture}}$) through the trapping region will not be trapped. As stated above, the Doppler cooling mechanism requires atoms be moving slowly enough to scatter enough photons to feel a significant viscous force. This can be accomplished in many ways, but one of the most common and the one employed in these experiments is to load atoms from the low velocity tail of a Maxwell-Boltzman velocity distribution. In our system, we use Rb getters inside the vacuum chamber to provide Rb with just such a velocity distribution.

The getters provide a general background vapor of Rb in the vacuum chamber. This background vapor provides both the atoms which can be trapped into the MOT and also a cloud of atoms which are too energetic to be captured by Doppler cooling [22]. The energetic atoms are a source of loss from the trapped cloud through collisions with trapped atoms [23]. Thus there is a competition in the loading between the number of atoms available for capture and the collision rate between those atoms and the rest of the energetic atom vapor. The load rate from a vapor is given by

$$\dot{N} = R - N / \tau . \quad (2.9)$$

Where R is the load rate into the MOT (in general this is a function of many parameters including laser power, detuning, magnetic field gradient, etc.). N is the number of Rb atoms in the MOT and $1/\tau$ is the trap lifetime and dependent upon the conditions of the

background vapor and collisions with other species present in the chamber. The trap life time can be estimated. If Rb from the background is the dominant collision species then $1/\tau = n\sigma(3k_B T/m)^{1/2}$. Here, n is the density of Rb, σ is the cross section for the collision with an atom in the vapor which produces loss (which for Rb is approximately $2 * 10^{-13} \text{ cm}^2$), T is the temperature, and m is the mass of Rb [24]. The steady state number for the trapped atoms in a MOT is found to be $R\tau$. The ideal gas law ($PV=Nk_B T$) can be used to conveniently find the density as a function of pressure ($n = P/(k_B T)$), thus allowing for a relation between the lifetime of the MOT and the pressure in the vacuum chamber. Our experimental system contains only one vacuum chamber therefore, the experimental MOT is subjected to the full effects of loading and loss rate from background Rb vapor. However, other experiments have utilized a transfer of a MOT from one region to another in order to alleviate some of the loss out of a MOT due to collisions [25].

2.2 The Optical Dipole Trap

While MOTs are one of the most common forms of traps in laser cooling and trapping, there is a variety of other traps either used separately or in conjunction with the MOT. Magnetic traps are one such widely used traps. Often in the pursuit of Bose-Einstein condensation, magnetic traps are used as a final stage for evaporative cooling [24]. Another common trap, and one used in the experiments presented in this thesis, is the optical dipole trap, the simplest of which consists of a strongly focused Gaussian laser beam [26, 27]. As suggested by the name, an optical dipole trap takes advantage of an atom's dipole moment in order to trap atoms. The interaction between a laser's E field and an atom's electron induces a dipole (\mathbf{p}) in the atom. This induced dipole can then

interact with the E field from the laser to produce a potential. In the simplest of terms this induced dipole can be expressed as

$$\vec{p} = \alpha \vec{E}. \quad (2.10)$$

Where α is a polarizability constant. The potential (U_o) which is associated with this dipole is proportional to $-\vec{p} \cdot \vec{E}$ for a red detuned (laser frequency set below the atom's transition frequencies) optical dipole trap. Substituting equation 2.10 into this expression shows that $U_o \propto -\alpha E^2$, so the potential created through the interaction of the induced dipole and the laser field is proportional to E^2 . In other words, the potential is proportional to the intensity of a beam. In general, the potential created by the interaction of the induced dipole and the laser can be specified in terms of its detuning [28]

$$U_o = \frac{\hbar \delta}{2} \ln \left(1 + \frac{\Omega_1^2 / 2}{\delta^2 + (\gamma^2 / 4)} \right). \quad (2.11)$$

Where Ω_1 is the Rabi flopping frequency associated with the laser beam (both δ and γ are defined in equation 2.1). It is important to note that the expression for U_o in equation 2.11 is for a two level atom near resonance, and not applicable for the FORT used in the experiments. However, equation 2.11 suffices for an illustration of the trapping potential produced in a simplified atomic system. From equation 2.11 we can see that for red detuning ($\delta < 0$) the potential is attractive, at zero detuning the potential vanishes, and for blue detuning ($\delta > 0$) the potential become repulsive. Furthermore, if we write down the expression for the Rabi flopping frequency

$$\Omega^2 = \frac{\gamma^2}{2} \left(\frac{I}{I_{sat}} \right), \quad (2.12)$$

and substitute equation 2.12 into 2.11, we find the intensity dependency of the potential. The saturation intensity (I_{sat}) is defined in equation 2.1.

There are several advantages to using an optical dipole trap [26]. One such advantage is that the trapping potential is more tightly confining (in the radial direction) than that from a MOT. This allows for a higher density of atoms to be trapped than what can be achieved in a MOT. While some optical traps can cause strong scattering, employing a FORT alleviates problems associated with strong scattering [29]. (Another solution to the scattering problem is to use a blue detuned optical trap, wherein the atoms are attracted to points of minimal intensity instead of maximum [30].) An optical trap can be utilized to trap a wide variety of atoms, independent of the atom's spin state, and does not require a magnetic field. The large detuning inherent in a FORT leads to a very low spontaneous scattering rate as well as negligible photon recoil (which could lead to heating the cloud) [29].

Another property of an optical trap is that to create 3-D confinement, one only needs one trapping laser. The simplest optical trap, indeed the one used for the experiments presented in this thesis, is just a single beam which is focused to a minimum spot size [26] (for our system, the minimum spot size was $\sim 100 \mu\text{m}$). For red detuned optical traps, the intensity gradient from focusing the laser causes a force on the atoms towards the point of highest intensity. As demonstrated above discussion of the atom's dipole, it is the interaction of the atoms induced dipole with the electric field from the trapping laser which causes this force. Conceptually, there are AC Stark shifts in the ground state energy level of an atom in a light field which depend on the intensity of the laser light (as shown in equation 2.11) [31]. For red detuned optical traps, there is

lowering of the ground state energy of the atoms in the laser field which is dependent upon intensity; the higher the intensity the lower the ground state energy is shifted. This shift yields a force on that atoms give by

$$\mathbf{F} = -\nabla U = -\frac{\hbar\gamma^2}{8\delta I_s} \nabla \mathbf{I}. \quad (2.13)$$

Equation 2.13 again demonstrates the intensity dependency of the trapping force. The general form for the potential caused by the focusing of a Gaussian beam is given by [32]

$$U(r, z) = U_o \left(\frac{\exp[-2r^2 / \omega(z)^2]}{1 + (z / z_R)^2} \right). \quad (2.14)$$

For the FORT used in our experiments, $U_o = -\frac{\alpha I_o}{2c\epsilon_o} = -\frac{\alpha P}{c\epsilon_o \pi \omega_o^2}$ (α is the DC

polarizability of Rb, I_o is the full intensity of the FORT laser, P is the power of the FORT laser). Equation 2.14 describes a beam which propagates in the z direction. For a Gaussian beam, the waist size ($\omega(z)$) and the Rayleigh length (z_R) are

$$\begin{aligned} \omega(z) &= \omega_o \sqrt{1 + (z / z_R)^2} \\ z_R &= \frac{\pi \omega_o^2}{\lambda} \end{aligned} \quad (2.15)$$

Here, ω_o is the minimum waist size and λ is the wavelength of the optical trap laser. So for a red detuned optical trap, the minimum potential is at the point of maximum intensity. Thus by focusing a red detuned laser, atoms will feel an attractive force towards the minimum spot size where the intensity is the greatest. This creates a potential well, often approximated as a harmonic oscillator for FORTs, in which the atoms can be trapped. Atoms cooled into the trap which do not have sufficient kinetic energy to overcome the potential (i.e. $KE < U_o$) become trapped in the optical dipole trap.

Since the beam is focused in 3-D, it can trap in all directions with a single beam. The trap is not symmetric as the radial trapping will be much greater than the axial trapping for a single beam optical trap. Thus, these traps tend to be cigar shaped.

The low scattering rate of the FORT reduces the statistical heating which can occur in other traps which are closer to an atom's resonance. Large scattering rates from a trap's photons can cause noticeable recoil heating of the atoms in the trap. However, FORTs take advantage solely of the interaction of the atom's dipole and the laser's electric field and not a form of scattering (such as Doppler cooling in MOTs) [29]. For example, in Rb the main trap laser is at 780 nm, the repump at 795 nm, the FORT is 10.6 μm . The recoil heating and spontaneous scattering from the FORT light is negligible (~ 1 per 10,000 s). A FORT trap can be treated, therefore, as a conservative potential. One complication that can arise from this, however, is in trapping atoms into the FORT. As a FORT is a conservative potential, it cannot use its light to cool the atoms. While the confinement in a FORT is much stronger than that of a MOT, a FORT is shallower (~ 1 K for our MOT and 120 μK for our FORT). Since the FORT can not produce a damping force itself, atoms from the MOT (even those with small velocity, i.e $KE \ll 120 \mu\text{K}$) must be cooled into the FORT as they pass through the FORT volume. Therefore to load an optical dipole trap, cooling with additional light fields is required to trap the atoms into the FORT.

2.2.1 Loading into the FORT. There have been several techniques developed for loading a FORT or other optical traps. One way is to load an optical trap directly from an optical molasses. Some of the first observations of optically trapped atoms came from trapping out of the molasses [26, 31]. The first systems which loaded an optical

trap from a molasses could only load a very limited number of atoms (500-1300). However, refinements in loading procedure have greatly increased that number, and currently it is possible to routinely trap millions of atoms. An optical molasses has the light fields for Doppler and sub-Doppler cooling. However, since the anti-Helmholtz coils are not on during an optical molasses, there is no spatial force allowing the atoms to slowly expand. For a FORT, loading from an optical molasses is advantageous since it provides the additional cooling light required to trap the atoms into the FORT as they pass through the trap volume.

In general, the FORT homonuclear load can be modeled by

$$\frac{d}{dt}n = R(t) - \Gamma n - \beta n^2, \quad (2.16)$$

where n is the density of the trapped atoms, Γ is the single body loss rate, β is the two body loss rate, and $R(t)$ is the load rate. Initially in the loading of a FORT, the load is dominated by R , and can often be approximated as linear. However, as atoms begin to accumulate in the optical trap, the loss processes (represented by Γ and β) begin to become more pronounced and the number of atoms loaded into the optical trap slows down with time and eventually turns over. Figure 2.7 shows a sample graph for loading into our FORT. Γ is caused by such processes as heating dynamics, such that in each event only one atom is lost. Heating can occur from spontaneously scattered FORT photons, collisions with background gas atoms, etc. Due to the far detuning of our FORT laser, there is very little spontaneous scattering. Additionally, the vacuum inside the chamber is such that the scattering rate from background atoms is very small as well. Instead, it is the β term in equation 2.16 which represents the main loss channel from the FORT for our system. The two body loss rate is dominated by light assisted collisions

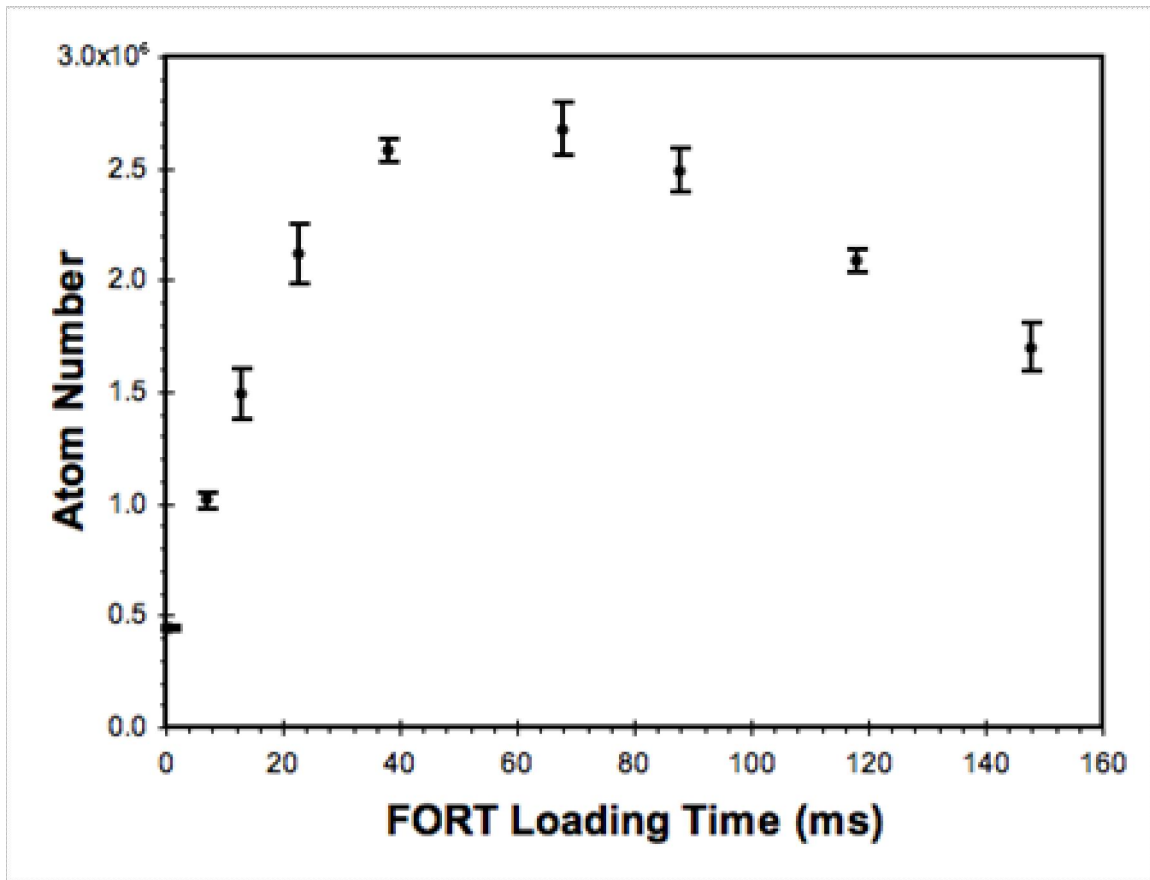


Figure 2.7: The number of atoms loaded into the FORT as a function of FORT loading time. In the first ~20 ms of the load, the number increases linearly with time (suggesting a constant load rate). However, once enough atoms begin to be loaded into the trap the loss mechanisms which are dominated by collisions begins to have a measurable effect and the rate at which atoms are loaded into the trap drops and eventually turns over. (See Chapter 5 for details).

[31]. Ground state hyperfine changing collisions, spin exchanging collisions, etc can also contribute to a two body loss rate. However, these mechanisms have an event rate which is two orders of magnitude smaller than our measured light assisted collision rates. Since for our system, the loss is dominated by the two body loss processes, often the Γ term can be ignored. The load rate and loss rates are affected by the intensity and detuning of both cycling and repump lasers. Thus finding the proper detuning, powers, and timings for each of the lasers is needed to maximize the number of atoms which can be loaded into the FORT.

When loading both ^{85}Rb and ^{87}Rb simultaneously into a FORT, cross species loss rates must be accounted for. The equations for heteronuclear loading are very similar to equation 2.16.

$$\begin{aligned}\frac{d}{dt}n_A &= R_A(t) - \beta'n_A n_B - \beta n_A^2 \\ \frac{d}{dt}n_B &= R_B(t) - \beta'n_A n_B - \beta n_B^2\end{aligned}\tag{2.17}$$

Since the two body collision losses dominate, the single body loss terms have been dropped from 2.17. The definitions are the same as for equation 2.16. The only new term is β' , which is the cross species two body loss term. While there are many qualitatively similar features between hetero- and homonuclear loading, the fact that two species are present at the same time greatly expands the complexity of the loading. The characterization of these terms and the optimization of heteronuclear FORT loading is discussed in detail in Chapter 5.

Our FORT loads typically produced millions of atoms trapped. We utilized a relatively large detuning from the cycling transition to optimize loading into the trap during the optical molasses, 120 MHz to the red of the ^{87}Rb cycling transition and 80

MHz to the red of the ^{85}Rb cycling transition produced the best results. However, for continued and consistent load numbers, a good overlap of FORT and MOT is required. Previous experiments document the necessity of overlap between optical trap and MOT to trap large number of atoms [31]. The procedure to overlap the MOT and the FORT is discussed in further detail in chapter 3.

Interestingly enough, we found that the optimum overlap of the FORT beam with the MOT was not to place the waist of the CO_2 beam in the middle of the MOT. Rather, larger number was obtained by slightly offsetting the waist of the FORT from the MOT. We theorize this is the case because of trap volume issues. While the force an atom feels is towards the maximum in intensity of the trap, the waist is rather small ($w_0 \sim 100 \mu\text{m}$) whereas further from the waist, the beam expands and there is a larger volume available to trap atoms. Thus the outer regions of the trap can capture more atoms due to its larger volume. The atoms once cooled into the FORT will then feel a force towards the center of the trap. Because the FORT is a conservative potential, the atoms will oscillate back and forth in the trap till their motion is damped by external light fields. Images of our FORT load were taken at very early times to see if this “sloshing” occurred. Indeed, images showed this back and forth movement of the atoms when they are first loaded into the trap. This “sloshing” is damped out due to collisions and trap anharmonicities in less than 100 ms. As such, standard data taking for atoms trapped in the FORT would be to hold atoms in the FORT for about 100 ms to approach equilibration and for the MOT atoms to have sufficient time to fall away so that atoms not trapped in FORT will not be imaged. As the trap was overlapped in the area which produced highest number, it seems

that the FORT employed in these experiments worked best when it could load atoms from the larger, less intense region of the FORT.

An important feature for continuous and optimal FORT loading was the quality of the MOT/FORT overlap. While we found it optimal to offset the center of the FORT slightly from the MOT, there still had to be a good overlap of the FORT volume with the MOT. The maximum number of atoms which can be loaded into the FORT is sensitive to this overlap. There are difficulties with alignment of the FORT, the major one being that the CO₂ beam is invisible and thus aligning the beam into the chamber is difficult. For aligning the FORT through the chamber, there is a periscope which can be used to walk the beam through and angle/position combination into the chamber, and a lens to focus the beam at the proper spot to be imaged onto the atoms by an internal lens. The goal of the alignment technique is to get close enough with the waist of the FORT beam to the MOT to load some atoms. Once an image can be taken of the FORT with some atoms, the number of atoms in the FORT can then be optimized through alignment. The alignment of the FORT is discussed in detail in Chapter 3.4.1.

Once the FORT is fully aligned, the trapping frequencies of the FORT need to be measured. The radial trap frequency (ω_r) was measured using parametric heating. This is accomplished through the use of the FORT acousto-optical modulator (AOM). An oscillating signal can be put up on the AOM RF and can cause the trap to oscillate in power. The parametric heating method of trap measurements is quite successful with a FORT, since atoms in the FORT are sensitive to the fluctuations caused by parametric heating [33, 34]. By using the AOM to sinusoidally modulate the power of the FORT, significant heating can be imparted to the trapped atoms when the modulation is twice the

trap frequency. The resonances from this method are actually predicted to occur at $2\omega_0/n$ where n is an integer and ω_0 is the trap frequency [35]. Therefore, resonances can be observed at sub-harmonics of ω_0 as well. There are systems where resonances from $n=1$ to 10 have been observed [33], though it takes especially strong excitations to be able to observe high n resonances. The $2\omega_0$ ($n=1$) resonance, however, is the easiest to observe and induces a large amount of heating into the cloud. Since such a large amount of heat is induced into the cloud at resonance one of the easiest variables to use to observe the resonance frequency is the size of the cloud. Since the size of the cloud is related to the temperature of the trapped atoms (see equation 2.22), significant heating of the cloud through a parametric excitation will cause a measurable increase in the size of the cloud.

The treatment of parametric heating can start with the simplest of harmonic oscillator equations, $\ddot{x} + \omega^2(t)x = 0$ [36]. Instead of a constant frequency ω_0 , the frequency is modulated parametrically with a frequency γ . For small modulation, we can write the oscillation of the system as

$$\omega^2(t) = \omega_0^2 [1 + h \cos(\gamma t)]. \quad (2.18)$$

Here ω_0 is the unperturbed oscillation frequency and h is positive and small ($0 < h \ll 1$).

The condition for resonance from this modulation was stated above as $2\omega_0/n$. The strongest resonance is for $n=1$, and the amplification coefficient (equation 2.19) can be found for this condition by considering $\gamma = 2\omega_0 + \varepsilon$, where $\varepsilon \ll \omega_0$.

$$s^2 = \frac{1}{4} \left[\left(\frac{1}{2} h \omega_0 \right)^2 - \varepsilon^2 \right] \quad (2.19)$$

In equation 2.19, s is the amplification coefficient, the condition for resonance of which is that s is real, which puts a range on ε over which resonance can be observed

$(-\frac{1}{2}h\omega_o < \varepsilon < \frac{1}{2}h\omega_o)$. In terms of our system, it is the range of modulation frequencies for which we will see additional heating to the cloud. This is just for the $2\omega_o$ resonance, in general the range of ε under which parametric excitation can be observed scales as h'' [36]. Since h is less than 1 (and positive), this relationship demonstrates why the $2\omega_o$ resonance is the easiest to observe, since it has the largest frequency modulation range which can be observed.

Figure 2.8 is a data set of just such a parametric excitation test. The size of the cloud is plotted vs. the modulation frequency used for the excitation. The $2\omega_o$ resonance is very clear in this test, though anything beyond $n=1$ was not observed in this test. However, it does demonstrate the dramatic change in temperature caused by the parametric heating of the atom cloud. Because this test relies on such large and easily measured changes, this method has proven to be an easy way to measure the radial trap frequency. There are other advantages of this sort of measurement of trap frequency. Since not all beams are truly $TEM_{0,0}$, this method can give a much better idea of trap strength than calculations. This was particularly necessary in the case of our FORT as our beam was significantly varied from a pure $TEM_{0,0}$ state, and had a $M^2 = 1.6$ (this is discussed in detail in Chapter 3). With this method, we found that the trap frequency in the radial direction for the FORT is $2\pi \times 450$ rad/s.

While in principle the axial direction can be measured using parametric heating, for our system we did not employ this method to measure the axial trap frequency. This is because the trapping in the axial direction is relatively weak; the trap frequency is rather small. Thus to impart the same amount of heat as that done for the radial direction it would take much longer to do so since the modulation frequency would be much lower

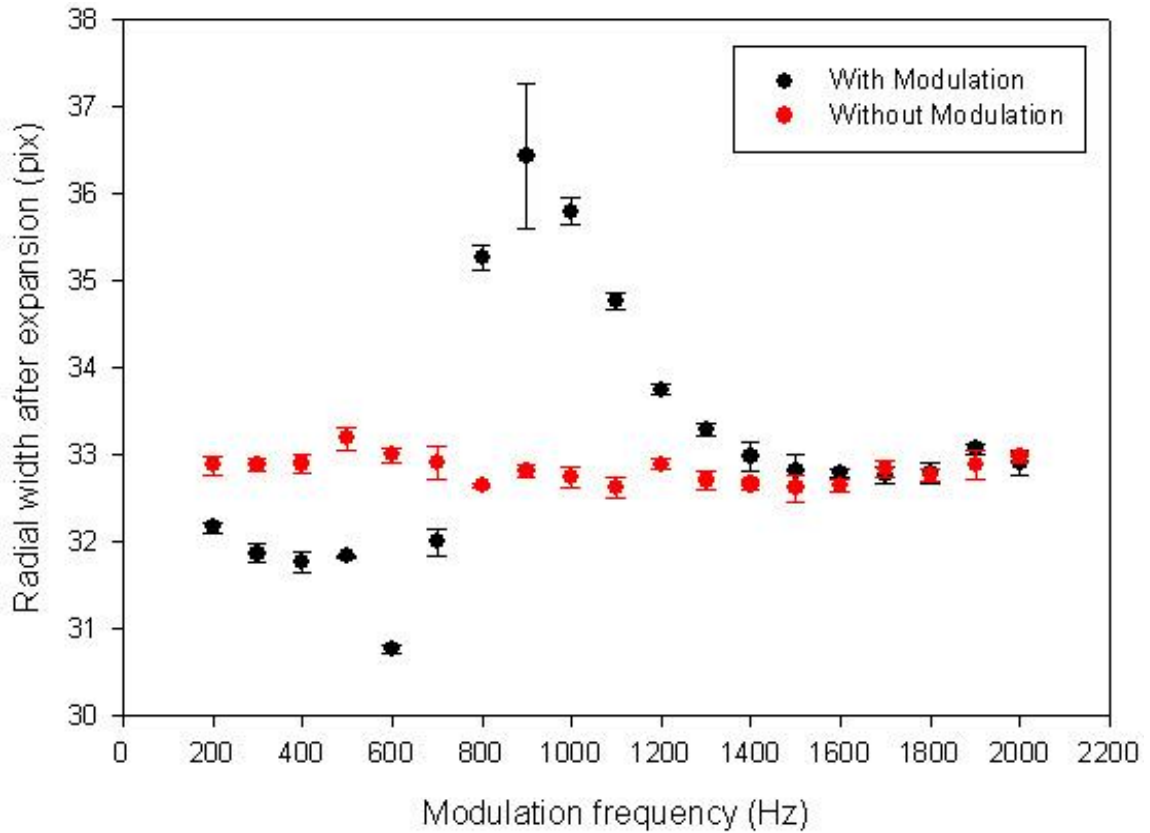


Figure 2.8 Parametric heating test for our FORT. Shown is the radial direction size as a function of modulation frequency. Circles are the width with the modulation, triangles are the widths without the modulation. Changes in the size due to modulation are observable. The size is given in pix, which is the size of the cloud in pixels of the CCD camera used in imaging. There is a clear resonance centered at about 900 Hz, which is indicative of significant heat being imparted to the cloud when the intensity of the trap is modulated at 900 Hz. This is the $2\omega_0$ resonance frequency, and it deviates from the size of the FORT without modulation measurably. This parametric heating test gives the frequency of the trap as $2\pi \times 450$ rad/s.

(several seconds). Instead, the axial trap frequency is calculated via atom temperature (measured by time of flight measurements) and size measurements.

For the derivation of the size of the cloud, a Maxwell-Boltzmann (MB) distribution was used. The MB distribution describes the number of atoms in a volume (dx^3) centered at some position \mathbf{x} with a velocity distribution (dv^3) centered at \mathbf{v} at some time t [24]. It is typically denoted by $f(\mathbf{x}, \mathbf{v}, t)$. The distribution for our system can be found in terms of our trap parameters [24]

$$f(\vec{x}, \vec{v}) = \frac{Nm^3 \omega_r^2 \omega_z}{8\pi^3 k_B^3 T^3} \exp\left[-\frac{mv^2}{2k_B T} - \frac{m}{2k_B T} (\omega_r^2 r^2 + \omega_z^2 z^2)\right]. \quad (2.20)$$

N is the number of atoms in the trap, m is the mass, and $\omega_{r(z)}$ are the trapping frequencies in the radial (axial) direction. Integrating 2.20 over all velocities will yield an equation for the density of the cloud as a function of position and is given by [24]

$$n(\vec{x}) = N\omega_r^2 \omega_z \left(\frac{m}{2\pi k_B T}\right)^{3/2} \exp\left[-\frac{m}{2k_B T} (\omega_r^2 r^2 + \omega_z^2 z^2)\right]$$

or

$$n(\vec{x}) = \frac{N}{(2\pi)^{3/2} \sigma_r^2 \sigma_z} \exp\left[-\frac{r^2}{2\sigma_r^2} - \frac{z^2}{2\sigma_z^2}\right] \quad (2.21)$$

The size of the atom cloud in the trap then comes from 2.21 and is defined as

$$\sigma_{oi} = \frac{1}{\omega_i} \sqrt{\frac{k_b T}{m}}. \quad (2.22)$$

Where $i = r$ or z (r being the radial direction with the axial direction being along the z axis), σ_{oi} is the initial width of the atom cloud before expansion, ω_i is the trap frequency in the direction of interest (in rad/sec). To measure the size of the cloud in the axial direction, we allowed the atoms to sit in the trap for several seconds. This was to allow the atoms to fully thermal equilibrium. The atoms were then released from the trap and

imaged using standard absorption imaging techniques (detailed in Chapter 3). There was a correction applied to the measurements of the axial length since the imaging beam is not perpendicular to the cloud. Rather, it makes a $\theta=50^\circ$ angle off normal in both the vertical and horizontal direction. As such, the measured length is not the actual length, but rather appears smaller. Thus the actual cloud size is

$$\sigma_z = \sqrt{\frac{\sigma_{zmeas}^2 - \sigma_r^2 (\cos(\Theta))^2}{(\sin(\Theta))^2}}. \quad (2.23)$$

Where σ_{zmeas} is the measured width in the axial direction (There is no necessary correction in the radial direction). Since the size of the cloud is imaged after a slight expansion time, the size of the cloud has to be corrected for to account for this expansion. Equation 2.24 gives the expression for the size of an atom cloud as a function of expansion time. Using this equation, σ_{oz} can be calculated and then through equation 2.22, the axial trap frequency (ω_z) can be extracted. The only other necessary piece of information for the calculation is the temperature of the cloud in the optical trap.

The temperature of the cloud is measured from time of flight measurement, and comes from the same set of data as the measurement of the axial trap depth. The radial widths are used for the calculation of the temperature, and unlike the axial widths require no significant correction to its measured size. When the atoms are released from the trap, the cloud expands since the atoms have a velocity ($v_{rms} = (k_B T/m)^{1/2}$). By measuring the cloud as it expands, we can calculate the initial temperature of the cloud by

$$\sigma_r(t) = \sqrt{\sigma_{or}^2 + \frac{k_B T}{m} t^2}. \quad (2.24)$$

In the treatment of the radial size, the initial trap width (σ_{or}) is very small, therefore we can neglect it in equation 2.24. However, in practice t is not known exactly. To account for this, we substitute $t \rightarrow t - t_o$ where t_o can be treated as a variable. For our system equation 2.24 becomes,

$$\sigma_r(t) = \sqrt{\frac{k_B T}{m} (t - t_o)^2} . \quad (2.25)$$

By measuring at two expansion points (t_1 and t_2), equation 2.25 can be simultaneously solved for T and t_o . Having calculated T and t_o , σ_{oz} can be calculated from,

$$\sigma_z(t) = \sqrt{\sigma_{oz}^2 + \frac{k_B T}{m} (t - t_o)^2} . \quad (2.26)$$

The calculated σ_{oz} and T can be plugged into equation 2.22 to extract the axial frequency. This method of measuring the axial trap volume is the easiest way to do so for a system similar to our. Optical lattices and other systems with strong axial confinement may employ other means such as parametric heating to measure the axial frequency. For our system, we measure our axial trap frequency $\omega_z = 2\pi \times 12$ rad/s. The fully thermally equilibrated cloud had a measured temperature of $T = 12$ μ K. A rule of thumb for the trap depth is that the temperature of the atoms in the trap are at 10% the trap depth, thus the trap depth of our FORT can be estimated to be 120 μ K.

References for Chapter II

- ¹ E. Raab, M. Prentiss, A. Cable, S. Chu, and D. Pritchard, Phys. Rev. Lett. **59**, 2631 (1987)
- ² Carl Wieman, Gwen Flowers, and Sarah Gilbert, Am. J. Phys. **63**, 317 (1995)
- ³ C.S. Adams, *et al.*, Phys. Rev. Lett **74**, 2631 (1995)
- ⁴ T. Takekoshi and R. J. Knize, Opt. Lett. **21**, 77 (1996)
- ⁵ D. Boiron, *et al.*, Phys. Rev. A **57**, R4106 (1998)
- ⁶ Harold J. Metcalf and Peter van der Straten, *Laser Cooling and Trapping*. Springer-Verlag New York, Inc. New York City, 1999
- ⁷ Harold J. Metcalf and Peter van der Straten, Phys. Rep. **244**, 204 (1994)

-
- ⁸ W. Suptitz, *et al.*, *Opt. Lett.* **19**, 1571 (1994)
- ⁹ M. S. Santos, *et al.*, *Phys. Rev. A* **52**, R4340 (1995)
- ¹⁰ James P. Shaffer, Witek Chalupczak, and N. P. Bigelow, *Phys. Rev. A* **60**, R3365 (1999)
- ¹¹ D. Wang, *et al.*, *Phys. Rev. Lett.* **93**, 243005 (2004)
- ¹² Y. B. Band and P. S. Julienne, *Phys. Rev. A* **51**, R4317 (1995)
- ¹³ D. J. Wineland, R. E. Drullinger, and F. L. Walls, *Phys. Rev. Lett.* **40**, 1639 (1978)
- ¹⁴ G. P. Barwood, P. Gill, and W. R. C. Rowley, *Appl. Phys. B* **53**, 142 (1991)
- ¹⁵ P.D Lett *et al.*, *J. Opt. Soc. Am. B* **6**, 2084 (1989)
- ¹⁶ S. Chu *et al.*, *Phys. Rev. Lett.* **55**, 48 (1985)
- ¹⁷ P. Lett *et al.*, *Phys. Rev. Lett.* **61**, 169 (1988)
- ¹⁸ J. Dalibard and C. Cohen-Tannoudji, *J. Opt. Soc. Am. B* **6**, 2023 (1989)
- ¹⁹ Harold Metcalf, *J. Opt. Soc. Am. B* **6**, 2206 (1989)
- ²⁰ T. Bergeman, G. Erez, and H. Metcalf, *Phys. Rev. A* **35**, 1535 (1987)
- ²¹ Matthieu Vangeleyn, Paul F. Griffin, Erling Riis, and Aidan S. Arnold, *Opt. Express* **17**, 13601 (2009)
- ²² C. Monroe, W. Swann, H. Robinson, and C. Wieman, *Phys. Rev. Lett.* **65**, 1571 (1990)
- ²³ John Weiner, Vanderlei S. Bagnato, Sergio Zilo, and Paul S. Julienne, *Rev. Mod. Phys.* **71**, 1 (1999)
- ²⁴ Jacob L. Roberts PhD thesis, University of Colorado (2001)
- ²⁵ C. J. Myatt, *et al.*, *Opt. Lett.* **21**, 290 (1996)
- ²⁶ S. Chu, J. Bjorkholm, A. Ashkin, and A. Cable, *Phys. Rev. Lett.* **57**, 314 (1986)
- ²⁷ A. Ashkin, *Phys. Rev. Lett.* **40**, 729 (1978)
- ²⁸ Claude Cohen-Tannoudji, Jacques Dupont-Roc, and Gilbert Grynberg, *Atom-Photon Interactions*. John Wiley and Sons Inc., New York, 1992, pp 378.
- ²⁹ J.D. Miller, R. A. Cline, and D. J. Heinzen, *Phys. Rev. A* **47**, R4567 (1993)
- ³⁰ N. Davidson *et. at.*, *Phys. Rev. Lett.* **74**, 1311 (1995)
- ³¹ S. J. M. Kuppens *et. al.*, *Phys. Rev. A* **62**, 013406 (2000)
- ³² Kristen Lee Corwin, PhD. Thesis, University of Colorado (1999)
- ³³ Jinwei Wu, Raymond Newell, Marc Hausmann, David Vieira, and Xinxin Zhao., *J. Appl. Phys* **100**, 054903 (2006)
- ³⁴ G. Roati, W. Jastrzebski, A. Simoni, G. Modugno, and M. Inguscio, *Phys. Rev. A* **63**, 052709 (2001)
- ³⁵ R. Jauregui, *Phys. Rev. A* **64**, 053408 (2001)
- ³⁶ L. D. Landau and E. M. Litshitz, *Mechanics*. Pergamon Press, Oxford (1976)

Chapter 3

Experimental Equipment

In the previous chapter, the dynamics of Magneto Optical Traps (MOTs) and Far Off Resonant Traps (FORTs) were discussed since these were the types of traps employed in the collecting of the data presented in this thesis. Along with the traps, a discussion of Doppler and sub-Doppler cooling was presented in some detail. These cooling mechanisms use the scattering of photons to oppose the motion of the atoms, ultimately causing the atoms to slow down and become colder. In addition to cooling atoms, the MOT uses photon scattering to create a spatially dependent force as well. By contrast, the FORT does not rely on photon scattering to produce a spatially dependent force, it uses light with an atom's dipole to confine atoms in a conservative potential. For the MOTs, FORT, and the associated laser cooling, laser light with particular characteristics is needed in order to create them.

Diode lasers are used to supply these light fields necessary for laser cooling and trapping. In order to trap and cool effectively, precise control of the lasers' frequency is required as the scattering rates are dependent upon the detuning of the laser. It is also necessary to be able to rapidly turn on and off the trapping and cooling light as needed. For the FORT, in addition to rapid turn on and off of the light, laser power, waist size, intensity gradient, and overlap with the MOT must be controlled as set. Both MOT and FORT require a vacuum as to limit collisions with "hot" background atoms. These background collisions can significantly impact trap density and number, thus all trapping

is conducted inside a vacuum chamber. Anti-Helmholtz coils are necessary to provide a magnetic gradient. This gradient is what allows for the spatially confining force necessary for the MOT.

In this chapter I will present the experimental equipment necessary for obtaining the MOT and FORT along with the imaging system necessary for recording the ultracold atoms. The designs of the necessary equipment, such as the diode lasers, vacuum chamber, magnetic fields, etc., are discussed in detail in this chapter. Also included are the electronics constructed for the control of the system and a description of the programs used to analyze and control the experiment. In addition, the absorptive imaging techniques used for imaging of the atoms are presented. Much of the equipment and programs used for the data presented in this thesis was constructed in-house. For example, electronics such as the lock boxes and temperature servos are non-commercial; made on site to fit our experimental set up.

3.1 Diode Lasers

The trap and hyperfine repump lasers operate at 780 nm and 795 nm respectively. We used laser diodes at these wavelengths to trap and cool atoms since laser diodes have several advantages over more complex laser systems [1]. One main advantage is that these lasers are easily obtainable. By happy coincidence the 780 nm diodes are used in optical drive devices like CD-Rom and DVD, while the repump diodes are actually 808 nm lasers used to pump Nd-YAG lasers. The 808 nm diodes are very easy to pull in wavelength, and thus can be made to operate at 795 nm. Diode lasers have the advantage of being relatively cheap (when compared to other laser systems), can be

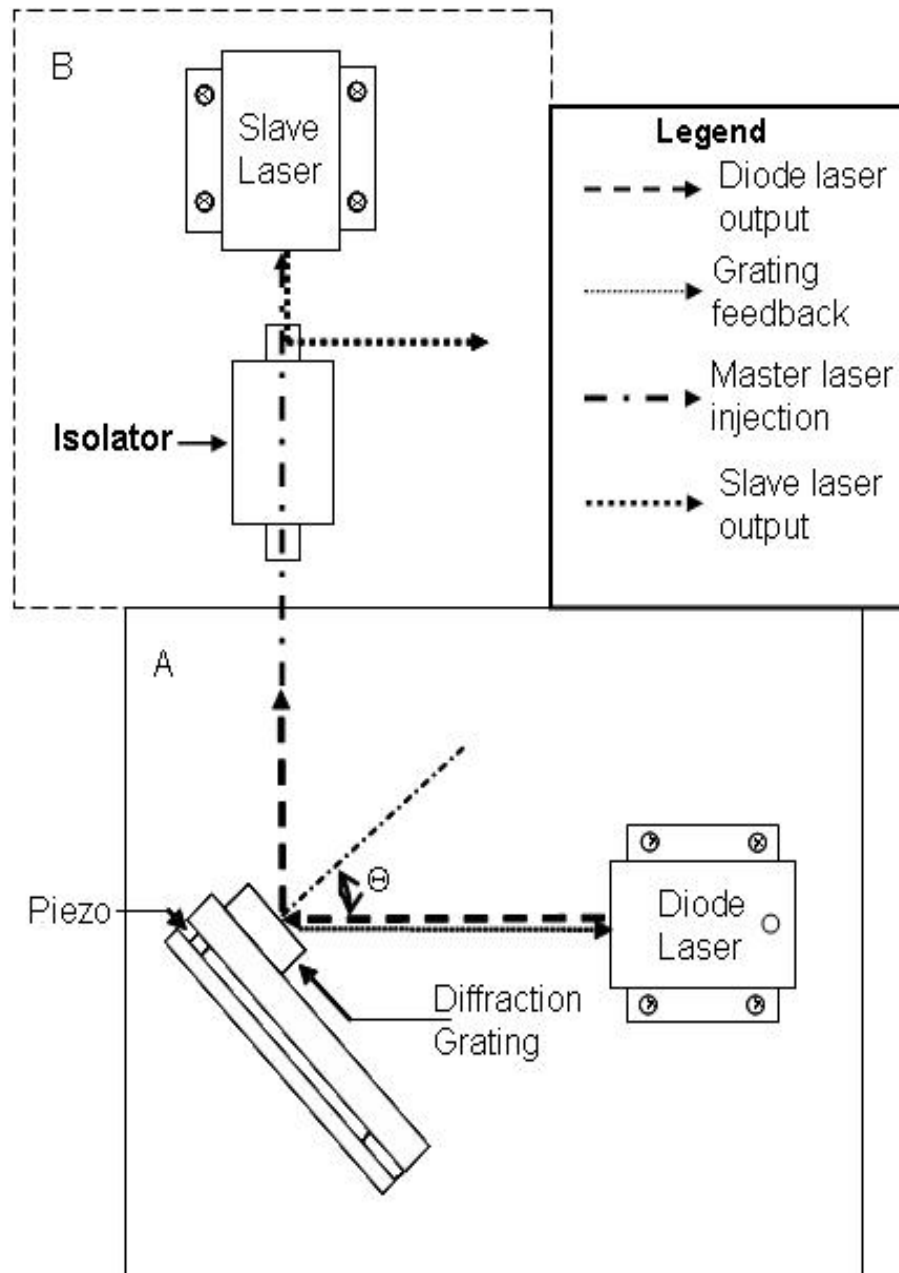


Figure 3.1 A is the standard diode laser configuration, showing the optical feedback for λ control. These lasers are used for the trapping, hyperfine repump, and imaging. The diode laser beam is collimated and the beam propagated towards a blazed diffraction grating. The angle Θ sets the wavelength through optical feedback, and Θ can be controlled precisely via the piezoelectric device behind the mount. B shows the extended master/slave set up, although necessary polarization optics for depicted beam path are not shown. In this extended configuration, output from A is used as an injection laser for the slave. In the upper right-hand corner a legend for the relevant beam paths is shown.

easily controlled, can be made compact so as not to take a lot of room on the optical table, and through proper servo and temperature control are rather stable [1]. Typically, diode lasers cannot reach the power output of other laser systems (such as the Ti-sapphire lasers which can put out ~ 500 mW CW), but they can still reach 10^3 's of I/I_{sat} for Rb for reasonable beam sizes, providing more than enough trapping power.

Through the implementation of a grating feedback system to form an external cavity (as illustrated in Figure 3.1 A and discussed in detail in section 3.1.1 below), these lasers can be made to operate single mode and tuned a few GHz continuously [2, 3] in our implementation. Some other experimental groups have obtained even larger tuning ranges in a compact design [4], in which they observe a 25 GHz continuous tuning range. While our tuning range was not quite that size, the few GHz we get from our diode laser system is sufficient to observe and scan continuously over the proper trapping and repump transitions individually. The particular scanning range is controlled by adjusting the diode laser current and temperature.

If power becomes an issue, as it was for us with ^{87}Rb for various reasons, the use of a simple master/slave system can boost the on-resonant power that can be obtained from one of these diode lasers. Such a master/slave system is depicted in figure 3.1 B. The first stage, the master laser, is exactly the same as before (figure 3.1 A). However, the output of that laser is then used as the master laser injection for another diode laser. Waveplates are necessary to couple the master laser through the isolator into the slave laser and to make use the slave laser beam is output appropriately from the isolator. Instead of using a blazed diffraction grating to provide feedback, the master laser is used to provide the feedback. In this way, part of the beam from the slave is not used as its

own feedback, and thus one can extract the full power of the slave laser while still allowing one to stabilize and control the frequency of the diode laser.

Thus laser diodes provide a cheap and convenient solution to laser cooling and trapping certain species. For our system we used Roithner Laser Technik ADL-78901TX diodes for our 780 nm diodes and Photonic DL-7141-035A diodes for our 795 diodes. While diode lasers offer much in the way of convenience, they are not without price. Controlling and setting a diode laser can be a hassle, and diode lasers are rather sensitive to the environmental conditions of the lab. Particularly troublesome can be a diode laser's dependence on lab temperature. The temperature regulation of the lab itself becomes important; if the temperature swing in the lab is too large the lasers will be unable to keep their transitions all day without physical grating tweaks or other adjustments. To offset this particular problem, which had plagued the lab for some time, eventually an external water cooled air conditioner was used. While a swing of a few degrees C in the day will not inhibit diode laser performance, swings of 6 degrees C or more certainly will.

3.1.1 Diffraction grating control of diode frequency. For our purposes, the most critical parameter of the trapping and cooling lasers that needs to be stabilized and controlled is the lasers' operating frequencies. One of the simplest geometries used to control a diode's frequency is the Littrow configuration; which is shown in figure 3.1 A. The Littrow configuration is an external cavity formed with a retroreflected beam from a blazed grating to provide feedback into the diode laser. The feedback is important in the stabilization and control of diode lasers. A free running diode laser (i.e. one with no cavity) can lase in several modes simultaneously due to the broad gain spectrum of the

diode laser itself. The result is a broad spectrum line width and power lost to frequencies unusable in the laser cooling and trapping of Rb. We observed in our system that even a small amount of laser power at the wrong frequency can lead to a serious loss of efficiency in laser cooling. The use of a Littrow external cavity laser has been used by many groups to help nearly eliminate this problem [5, 6, 7].

The grating determines the wavelength which is reflected back into the diode laser. This feedback lowers the losses of the feedback mode, resulting in an increase of the net round-trip gain of that mode. By significantly increasing the gain of one particular mode over all the other modes, the diode will operate with just that single longitudinal mode. As a result, more power is obtained at the feedback wavelength promoting single mode operation and lower threshold current.

In addition to the feedback from the grating, there are several other factors that influence the net gain of a particular wavelength in this diode laser configuration. The grating creates an optical cavity, which has a free spectral range (FSR) given by $c/(2L)$ where L is the length of the external cavity. As with the grating feedback, the wavelength which matches a resonant wavelength of the external cavity ($(2nL)/m$ where n is the index of refraction, air in our case, and m is the longitudinal mode number) experiences an increase in the round-trip gain for that wavelength. Another factor is the overall gain curve of the diode laser itself. This gain curve is intrinsic to the diode itself and is sensitive to temperature. Also temperature-dependent is the cavity which is formed by the physical parameters of the chip itself. The front and rear facets of the diode chip forms an optical cavity. This is why a diode laser can be free run (i.e. it can lase without an external laser cavity). As with the external cavity, the loss in the internal

cavity is minimized at resonant wavelengths of that cavity. Since the length of the internal cavity is dependent upon temperature, this becomes a way to control the frequency of the diode chip. The ultimate operating wavelength of the diode laser is set by the combination of all of these factors.

There are three main parameters that can be used to control the output of a diode laser; Θ (controlled by a voltage applied to the PZT shown in figure 3.1. A), temperature, and current. Small changes in the angle Θ shown in figure 3.1 A will change the wavelength that is fed back into the diode. In this way the feedback from the grating can be used to control the dominant wavelength emitted by the diode. For the Littrow configuration, the relationship between the angle Θ and the wavelength is simply

$$m\lambda = 2d \sin(\Theta). \quad (3.1)$$

Where m is the diffracted beam order (typically in most Littrow setups, the $m=-1$ beam provides the feedback into the diode laser), λ is the central wavelength (the wavelength fed back into the laser diode and thus the wavelength with the least amount of loss), and d is the grating ruling separation distance [8].

While the operating wavelength of the laser is determined primarily through the grating feedback, the precise wavelength is also influenced by the external cavity length. Since the external cavity resonances are sharp and closely spaced, the ultimate operating laser wavelength is the resonant wavelength of the external cavity with the most gain via feedback. As mentioned above, the free spectral range is approximately $c/(2L)$ where L is the length of the external cavity. Thus the amount by which a diode laser can be tuned is set through the cavity length and Θ . Both the free spectral range and Θ are controlled through the PZT. Because the two are not independent, this can lead to mode hops in the

laser's operating wavelength. Though with proper control and tuning of a laser diode, the mode hops will not cause significant interruption to the laser diode's performance.

Because of the sensitivity of the external cavity length, internal diode cavity length, and the diode gain curve to temperature, the temperature can be used to shift the resonant frequency of the diode and thus tune the laser to a transition via temperature. The diode laser current also influences the ultimate operating wavelength. Of course, the higher the current applied to the laser diode, the larger the output power and so in general high currents are desired. Higher currents lead to additional heating, however, altering the diode's frequency. By tuning the current and temperature the laser can be tuned to the desired transition. Current and temperature tuning were standard techniques in diode control before wide use of the external laser cavity with optical feedback was adopted [1].

In the initial construction of the laser diode boxes, the grating is initially set so that Θ is close to its ultimate operating position. To align the grating for optimal feedback, the first thing to be done is what is referred to as "flashing" the diode. The diode laser's current is adjusted till the laser is just below threshold. While there is spontaneously emitted light, the diode is not yet lasing. Then vertical angle of the grating is adjusted carefully by while observing the intensity of the laser beam, typically with an IR viewer. For our experiment, all the gratings were mounted on standard mirror mounts, and for the flash test the vertical adjustment of the mirror mount is used. When the grating is set so that the diffracted beam is fed back into the laser, the laser's output will suddenly increase. This is because of the fact that when the diffracted beam is fed back into the diode it reduces the loss for that wavelength and allows the diode to lase, thus

producing a very noticeable increase in the beams intensity. This produces a “flash” as one moves the vertical adjustment through this angle. By progressively decreasing the current of the diode and “flashing” the diode, the vertical angle can be set so that maximal feedback is delivered to the diode. Once the feedback is established, the frequency of the diode is set by adjusting the horizontal angle of the grating (this adjusts Θ from equation 3.1). The horizontal alignment knob of the mirror mount which the grating is attached to provides gross adjustment of the diodes frequency. The diode’s light is fed into an optical analyzer and the grating is adjusted till the central peak of the laser reaches the desired wavelength. Additionally, the optical analyzer will show if the diode is running in either single-mode or multimode. If the diode is running multimode, adjustments to the current and temperature can be made to ensure single-mode operation. The piezo depicted in Figure 3.1 A provides the fine angle control for the grating and can be used to precisely set the frequency of the diode laser to < 1 MHz precision.

Figure 3.2 contains the schematic for the current and piezo control used for frequency locking our lasers. One feature of the circuit is that it allows for the piezo to be “ramped” (PZT ramp) which allows the laser diode to scan over multiple transitions. A triangle wave signal is imputed into the circuit from the “Ramp In” BNC and outputs a triangle wave ramp signal from the “PZT out” BNC. This is the control ramp and this signal is sent to a high voltage amplifier (up to 50V was sufficient, 150 V was better) before being applied to the piezo shown in figure 3.1 A. This ramp signal causes the piezo to vibrate, altering the angle Θ and thus providing small changes to the output frequency. The circuit allows control over the amplitude of the ramp signal (Ramp gain) along with an offset bias voltage (PZT bias) through the use

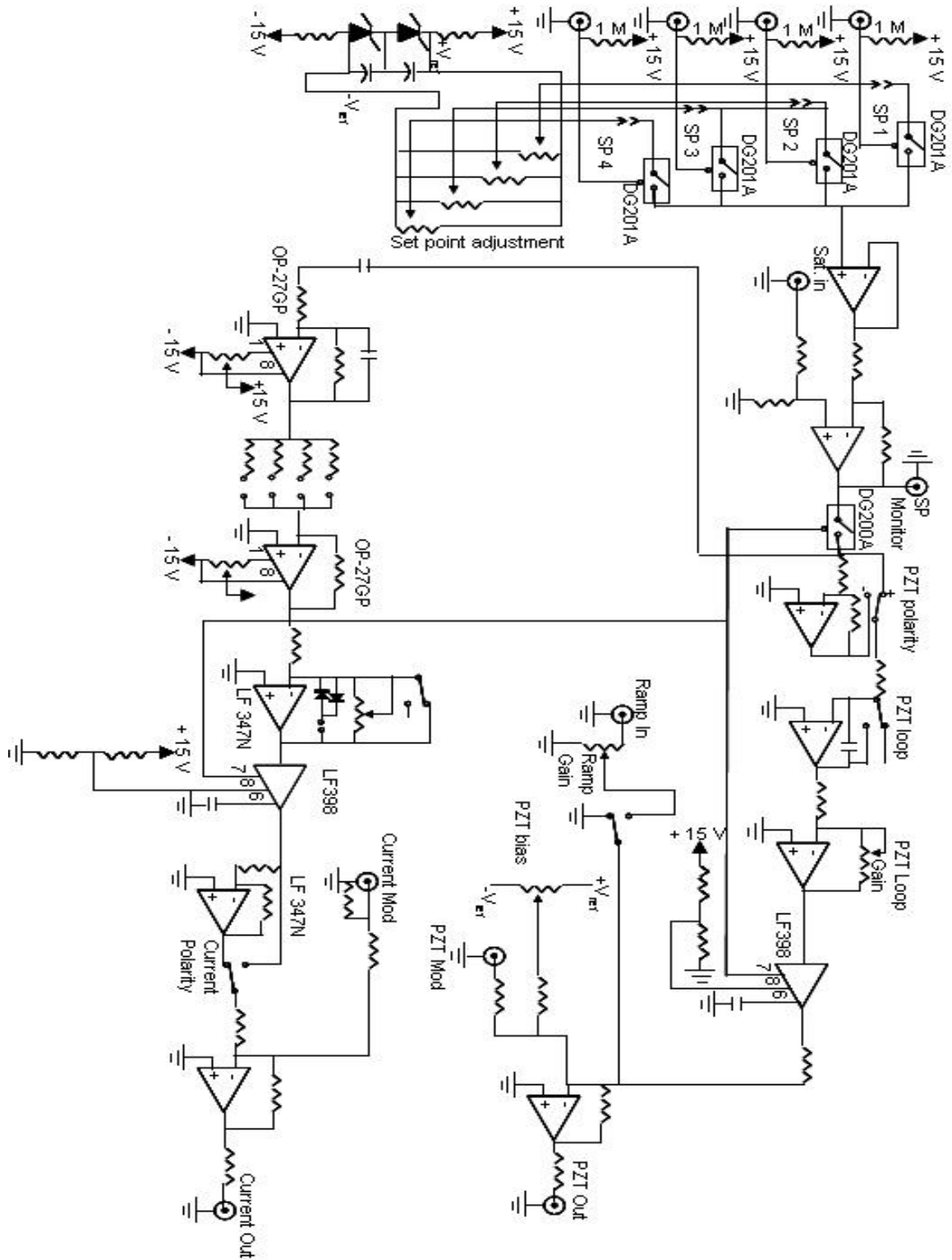


Fig 3.2 Schematic of the sidelock servo for the diode lasers. All op-amps not labeled are TL074. Design based on Jan Hall circuit from JILA [9]

of potentiometers (pots). When setting the laser's frequency for stable operation, the ramp is turned down to zero around the desired transition and the piezo offset allows for precise setting of the frequency. However, while the diode laser's frequency can be precisely controlled with the PZT bias, once set the frequency of the diode can wander due to environmental influences. Thus, the PZT voltage is servoed to keep the laser on transition. In addition to control over the piezo voltage, the current of the diode laser is servoed as well. The Current Out BNC shown in figure 3.2 allows the circuit to adjust the current as well as the piezo voltage in order to keep a diode on transition. The advantage to using current control is that it is very fast compared to the piezo, while the piezo can servo out longer drifts. The bandwidth of the current modulation is limited by the photodiode response time of our system, and thus can respond faster. The PZT bandwidth is about 100 Hz for our PZT's. The PZT control can adjust for slow drifts (<1 Hz), the current control is used for fast drifts. Thus for long term stable operations, we lock the laser frequency to a spectroscopic signal using the piezo and current servo system detailed in figure 3.2. The laser settings are rather stable with this servo and only require occasional calibration during the course of a day.

3.1.2 Temperature stabilization of diode lasers. While the Littrow diffraction configuration gives a simple and easily constructed set up to control the frequency of diode lasers, it is not enough to ensure single-mode tuning over Rb transitions. Diode lasers are particularly vulnerable to temperature which can affect both the frequency and the mode quality of the laser [1, 8]. For acceptable performance over long time periods, the temperature of the diode must be regulated. This is accomplished through use of a thermoelectric coupler (TEC) and servo circuit. A simple Peltier device transfers heat

across a junction in response to a current applied to the device. The diode sits on an aluminum plate, underneath which lies the TEC. On the other side of the TEC is a heat dump. For our experimental setup, the heat dump was a large block of aluminum; the laser diode assembly sat in thermal contact on top of this block. The TEC can transfer heat from the diode to the dump, and a servo is employed to regulate the current across the TEC. The laser diode rests in a small aluminum housing shown in figure 3.1 and a thermistor is placed in this housing so that it can accurately measure the temperature of the laser diode. This thermistor is used for feedback and control of the laser diode temperature. Figure 3.3 shows the schematic for the temperature control circuit.

Care has to be taken in order to select the proper resistors and capacitors in the circuit. If there is not enough gain near DC, the circuit cannot respond fast enough to keep the diode at the specified temperature. If there is too much gain at higher frequencies, the circuit will oscillate, causing swings in the diode's temperature and precise control of the output frequency will be impossible. An additional factor which may not be obvious is the degree of necessary lab temperature regulation. If the temperature in the lab fluctuates too greatly during the day, the temperature controller will not be enough to keep the diodes on their proper transition for the whole of the day. Thus long term drifts in the environment become important if those drifts exceed 4 or 5 degrees C. For our system, this relatively strong dependency on lab environment is rooted in the design of our laser boxes. The small aluminum housing for the diode is also where the thermistor is embedded. Since the thermistor is not in the exact location of the diode, temperature gradients can be established. Changes in these gradients as the lab

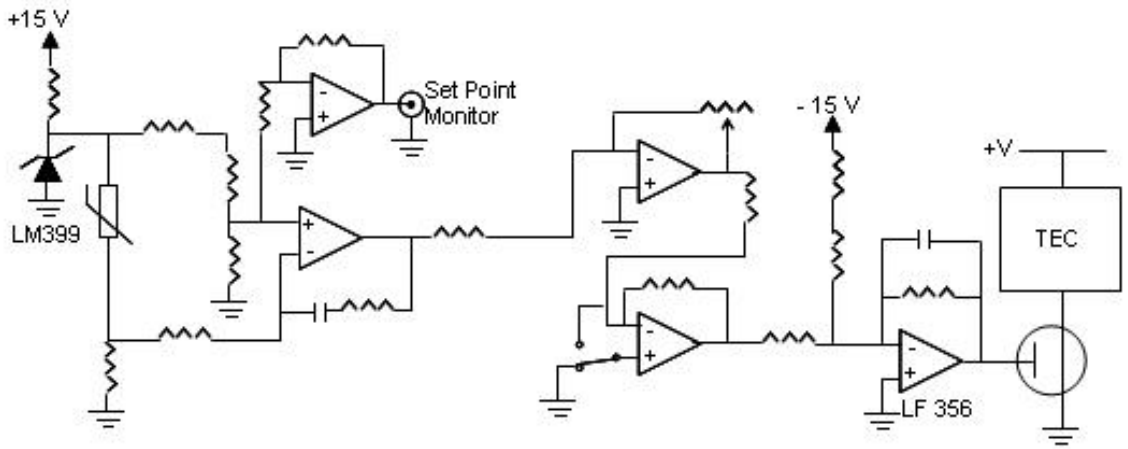


Figure 3.3 Temperature control circuit for the diode lasers. The circuit uses an LM399 as a stable voltage reference. A thermistor is implanted in the housing which holds the diode while the TEC sits underneath the diode. Gains and set points are set with the appropriate choice of resistors. As the thermal response for each laser is different, each laser system will have unique gain and set points to best serve the diode laser. The switch in the circuit on the +In pin of the second to last op-amp can switch the circuit between heating and cooling, but it cannot do both. As shown in the figure, the circuit is set to the cooling position. The current through the TEC is controlled with a field effect transistor (FET) and fed with an external power supply. All op-amps are TL074 unless otherwise specified.

temperature changes lead to different laser temperatures and thus drift in our laser frequency.

The temperature set point is chosen by characteristics of the individual diode laser, and thus varies from laser to laser. Generally speaking, colder is better for our diodes as it allows for the current to be increased while maintaining the same transition. Thus more power can be obtained at the desired frequency. However, due to mode hops and multimode operation, it is not always possible to cool significantly. Thus the set points are chosen for clean mode operation and power output. Additionally, a minimum of a few degrees C below room temperature is required for the servo to have a workable operating range.

3.1.3 Frequency calibration and servo of laser diodes. The temperature control of the diodes allows for the control of the diodes' output frequencies and ensures that the lasers can remain on the proper transitions throughout the day. The lasers then must be calibrated and locked onto the proper transition with the desired detuning necessary for the experiments. To set that output at the proper frequency and detuning, the actual frequency of the laser needs to be known, and a stable frequency reference is required. The reference used for our laser system is constructed through the use of a saturation absorption set up as depicted in the top of figure 3.4.

In saturation absorption spectroscopy, two beams are propagated through a Rb cell and overlapped onto photodiodes. The photodiodes are part of a simple subtraction circuit which displays the difference of the two beams. A saturating beam is counter-propagated and overlapped with one of the two beams in the Rb cell. Without the saturating beam, the signals from the two photodiodes will ideally cancel each other,

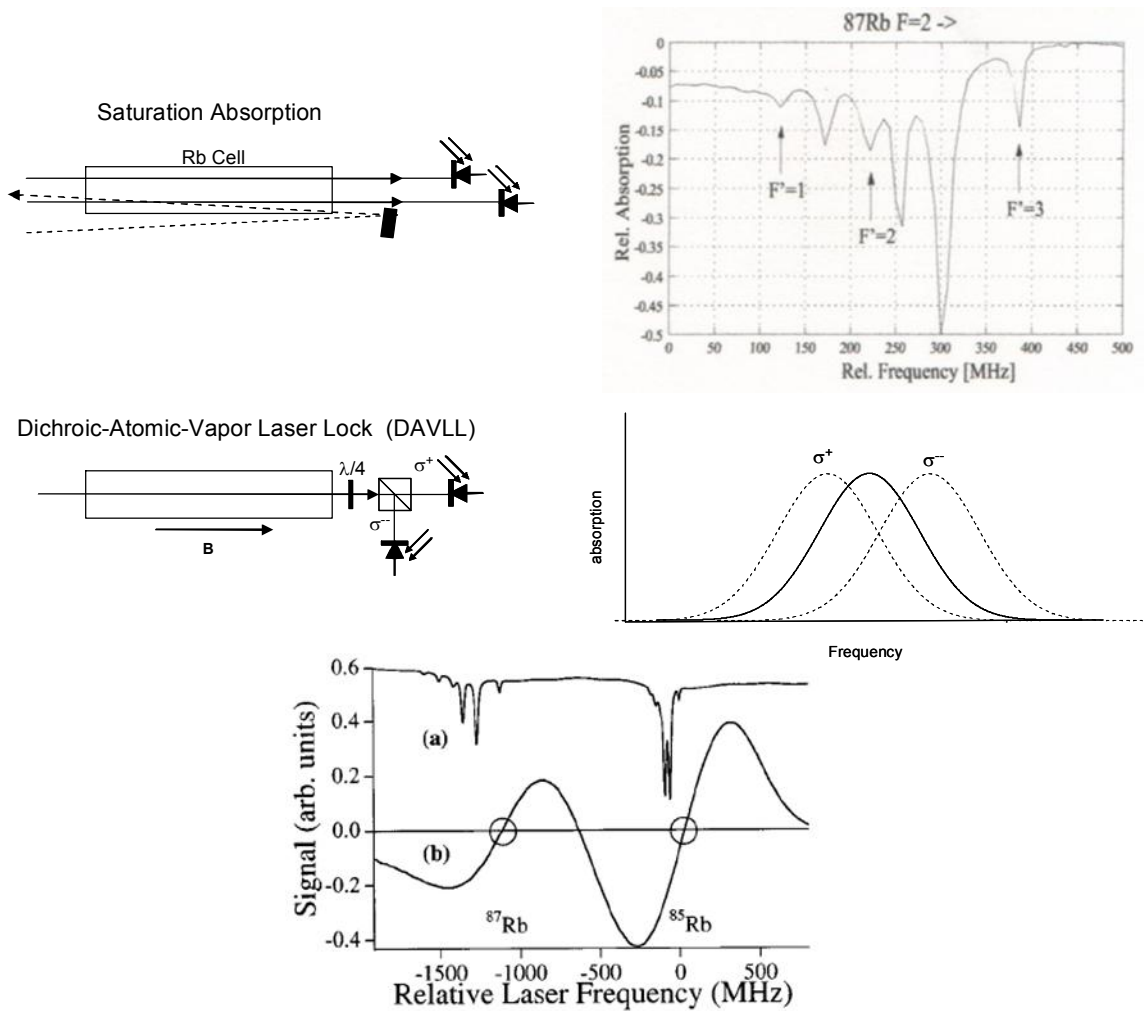


Figure 3.4 Saturation Absorption (top) and DAVLL (middle) set up for calibration of diode laser frequency. The dotted line for the Saturation set up depicts the counter-propagating saturation beam. Bottom picture displays both the saturation absorption and DAVLL signal for Rb. The bottom image was taken from [10]. The saturation absorption signal for ^{87}Rb was taken from [11].

giving a zero signal from the subtraction at all frequencies. With the saturation beam present, the subtraction should still be zero for most frequencies since the saturation beam is counter-propagated. Because the saturation beam is counter-propagated, the saturation beam will excite a different velocity class of atoms than the signal beam it is overlapped with due to Doppler-shifts and thus the subtracted signal would still be zero. However, when the frequency of the laser is on resonance with one of the Rb transitions, both the signal and saturation beam will excite the same atoms. The saturation beam causes a decrease in the absorption of the signal beam for these conditions, and thus the subtraction of the two signal beams yields dips in the signal. The top right illustration in figure 3.4 shows a standard saturation absorption signal in ^{87}Rb . While the saturation absorption signal clearly shows the transition frequencies, there are also present other dips in the absorption which do not correspond to an actual transition. These peaks are called crossover peaks and are present when multiple excited state hyperfine levels are available for a ground state atom. To understand the cross over we can consider a ground state atom which can be excited to one of two excited states with frequencies of ω_1 and ω_2 respectively. The resonance for the crossover peak occurs at $\omega_C = (\omega_1 + \omega_2)/2$ [12].

Since the signal beam and saturation beam are counter-propagating, at ω_C an atom moving in the glass cell will see one beam red shifted into resonance with the first excited state and the other beam blue shifted into resonance with the second excited state. As a result, we see a relatively large saturation absorption signal at the mean frequency of two coupled transitions [12]. Since these crossover peaks occur at exactly the mean value, they can be used for calibration.

By use of the saturation absorption signal, the lasers' frequency can be measured with sub-Doppler precision with respect to the atomic transitions of Rb. In principle, locking to this signal can be accomplished with either peak locking right on the tip of one of the saturation absorption dips or by side locking on the side of one of the peaks. Locking directly to the saturation absorption has the advantage of locking to a long-term stable reference. However, peak locking or side locking has relatively small capture range, and that makes the lasers susceptible to jumping out of lock due to vibration or electric noise. Side-locking is also sensitive to changes in the absorption lines, which will produce long-term drifts. For large frequency jumps, such as those necessary for loading our optical trap, peak locks are particularly problematic. This is because to jump frequency with a peak lock requires dithering the laser frequency, a lock-in amplifier, and an AOM to jump the laser frequency without losing frequency lock. What is preferred would be a linear signal over a broad frequency range, and that can be achieved by employing a Dichroic-Atomic-Vapor Laser Lock (DAVLL).

The DAVLL is a lock signal which takes advantage of the Zeeman shift in order to produce a linear voltage response over a broad frequency range [10]. The middle illustrations in figure 3.4 show the basic DAVLL setup. A single laser beam is directed through a Rb vapor cell. The cell itself is placed in a constant magnetic field, with typical field strengths on the order of a 100 G. The DAVLL signal is sensitive to temperature and needs to be regulated [13]. To regulate the temperature, the magnets which create the constant field and the Rb cell are enclosed in a copper or aluminum "oven" so that it can be temperature regulated. The laser beam which propagates through the DAVLL is linearly polarized and propagated along the magnetic field direction

($\vec{k} = k\hat{z}$). In the presence of a magnetic field ($\vec{B} = B\hat{z}$) the center frequency of the absorption spectrum can be shifted if the light is circularly polarized, as shown in the center graph of figure 3.4. Linearly polarized light can be thought of as a combination of σ^+ and σ^- polarizations, thus both positive and negative frequency shifts can affect a single linearly polarized beam. At the output of the DAVLL, a quarter waveplate converts the two circular polarizations into orthogonal linear polarizations. A polarizing beam splitting cube then separates these polarizations which are then overlapped onto photodiodes.

The curves in figure 3.4 show the standard absorption curves for Rb. Because a magnetic field lifts the degeneracy on the m_F energy levels, the resonant frequencies for each of the circularly polarizations are shifted. The solid curve shows the unshifted absorption curve, the dotted lines represent the absorption curve for both of the circular polarizations. Converting the two circular polarizations into orthogonal linear polarizations allows the separate polarizations to be separated via a polarization beam splitting cube. When the photodiode signals from these two polarizations are subtracted from each other, the DAVLL signal, which is shown in the bottom illustration of figure 3.4, is produced. This signal has a steep, linear slope over the frequency range of the transitions. This creates a reference to which the diode lasers can be locked. Dithering the current to the photodiodes is not required. Because of the large capture range, a larger tuning range is available and relatively large changes can be made to the laser frequency without fear of losing lock on the laser. Thus the DAVLL signal provides a reference to which the lasers can be locked that is far more robust than either peak or side

locking. The servo which utilizes the DAVLL signal can remain in lock over longer periods of time and is more stable against vibration and electronic noise.

While the DAVLL supplies a signal with a large capture range, the signal is sensitive to temperature and will drift in over time. Thus, the DAVLL signal must periodically be calibrated to a more stable frequency reference. A saturation absorption system allows for such a calibration of the DAVLL signal. So, in practice the saturated absorption signal provides a long-term, stable absolute frequency reference while the DAVLL allows for robust locking. The only disadvantage to using both a saturation absorption and DAVLL for locking of the lasers comes at the expense of space and mild cost. Both set ups require a finite amount of room, which on an optical table is valuable.

There are alternative techniques for locking multiple lasers in a way that allows for control of the lasers' frequency over several hundred MHz without each laser having an AOM. One such method involves beating different lasers' beams together on a fast photodiode. One laser with a saturation absorption and DAVLL assembly and the rest with just a DAVLL. One laser can be precisely set with good absolute accuracy, calibrated with its saturation absorption signal. The other lasers can then be referenced to the calibrated laser, removing the need for a saturation absorption setup for those lasers at the cost of one or more fast photodiodes and a frequency counter.

For all the work presented in this thesis we used both a DAVLL and saturation absorption for each laser, however. We require at minimum 5 diode laser systems on the optical table: a main cycling laser and hyperfine repump laser for each isotope plus a probe laser. The frequency separation between 780 nm (the main cycling laser) and 795 nm (hyperfine repump) is too large ($\sim 7 \cdot 10^{12}$ Hz) for the beat method, though.

Additionally, the frequency difference between the ^{85}Rb and ^{87}Rb transitions is enough to require very fast photodiodes (a few GHz). Thus for our system it was easiest and cheapest to construct full saturation absorption and DAVLL assemblies for each of our lasers.

The calibrated DAVLL signal for each laser is the error signal fed to the servo to lock the laser. The servo depicted by figure 3.2 locks the laser to the DAVLL signal through adjusting the PZT voltage (which corrects deviations with characteristic frequencies of DC to ~ 1 Hz) and the laser current (which corrects higher frequency deviations). The DAVLL signal voltage to which the laser is actually locked is specified through a set point. Our servos have four set points (SP 1-4) that can be set independently. The multiple set points allow for each laser's frequency to be jumped during the course of an experiment. This is necessary for work with Magneto Optical Traps (MOT) which requires different frequencies for loading, compressed MOT stages and molasses stages. The set points are selected via TTL signals. These signals are in turn set via the main Lab View code which controls the experiment. This system is discussed in the next section of this chapter.

3.1.4 Cooling and hyperfine repump laser intensity control. In addition to the frequency of the diodes, the diodes' light fields must also be controlled. Typical MOT and FORT sequences require that the intensity of the cooling and repump lights to be changed at specific times. One device used to control the light fields are shutters. The shutters are placed in the beam path for both the cooling and repump lasers of both isotopes. The shutters are a physical device which will either allow the laser beams to pass through or block them entirely. There is no intensity control with these devices

other than that. The shutters used in our experiment are Uniblitz LS6. Like the set points discussed above, the shutters are also controlled with TTL signals controlled by a Labview program (see Chapter 3.2). In order to shut off the light as quickly as possible, the laser beams are focused down with a lens. The shutters are placed at the minimum spot size of the beams. Since the area of the beams are small at that spot, the shutter can cut across the area faster and thus lead to faster turn off times and more stable reproducibility. The shutters can shut the beams off from the system within 100-300 μs . This value varies slightly between shutters and beam size and placement on the shutter can affect this value as well. The reproducibility of the shutter off time is about 10 μs . Turn on times (shutter opening as opposed to closing) can be different as well. However, the primary use of the shutters in our system was to shut light off at specific times, and thus we were more concerned with shut off times and reproducibility.

While the shutters can control the on/off of the diodes used for laser cooling and trapping, it is also necessary to have control over laser intensity. To accomplish this, we used acousto-optic modulators (AOMs) in the beam path of the hyperfine repump lasers. The main cooling lasers did not use AOMs as we needed all the power from the main cooling lasers. For the hyperfine repump lasers, the deflected beam was used for the repump beam. The intensity of this beam can then be controlled by the RF signal to the AOM from zero power to full power. The shutters for the hyperfine repump were in place to ensure that when we want the light off, it is shut off (there can be stray light that still gets through the optics even when the rf power is 0).

To goal of using the AOM rf is to be able to change the intensity of the hyperfine repump during the course of an experiment. To accomplish this, first an RF driver was

assembled. The AOM RF drivers for our set up were home built, and started with a voltage controlled oscillator. These devices put out a RF signal whose frequency can be adjusted by voltage. The majority of the AOMs that we use are 80 MHz AOMs, and thus the voltage control oscillators are set to be 80 MHz. In order to be able to change the AOM RF power during the experiment, thus changing the hyperfine power intensity, there are a couple of paths which can be accessed by the voltage control oscillator, controlled with TTLs. There is the full power path, which passes the signal to a pre-amplifier and then an amplifier out to the AOM. There are attenuation paths as well. We use either a voltage control attenuator, selectable, or fixed attenuators to produce the desired RF attenuation. Often times, an AOM RF driver can have multiple attenuation paths, one which has a fixed attenuation and one which passes through a variable attenuator which we can set externally as the experiment dictates. These different paths are controlled through RF switches which use TTL signals to activate. Thus with the appropriate choices of TTL signal, the proper AOM RF attenuation path can be selected. With this method, two or three attenuation paths can be made, controlled with Labview TTLs.

3.2 Computer Control of the Experiment

In order to have performed these experiments with magneto-optical traps and far off resonant traps, precise timing with up to sub-millisecond precision is needed over the whole of the system. Thus everything from laser light fields, laser detunings, magnetic fields, imaging systems, etc were controlled via computer. The heart of the computer control was a timing chip on a Viewpoint USA DIO-64 TTL board. It was these TTLs which provided all the triggers for experiment timing. The Labview program was set to

export a command to the board which was accurate at the .01 ms level with 32 TTL outputs. The board itself can handle ns timing and has 64 available TTL outputs, the Labview program can be changed to accommodate this. The TTL output from the board initiated every action taken during the experiment sequences. GPIB commands were occasionally used to set parameters of some devices such as a function generator or RF source. Other programs were necessary to establish the camera parameters. However, each device in the system was set to receive a TTL trigger to begin its operation. In this way we eliminated the problem of having to worry about differences in clock rates or unexpected delays between different elements in the experiment.

Running a particular experiment sequence thus required programming the sequence of TTL triggers on the timing board. Labview (LV) was chosen to be the main program used to set the TTL sequence. The front page interface of LV makes setting experiment parameter values and running the program rather simple, which is preferable for a high duty cycle program. Other programs were used to run necessary equipment in conjunction with the main LV control. Visual Basic (VB) was used to control the imaging program associated with the Princeton Instruments camera. While the TTL governed by the LV program controlled the trigger of the camera, the VB code handled the image processing and then displayed the optical density (OD) image used for all our analysis. Also, a Fortran program performed Gaussian fits to the OD images. From the fit values a wide variety of MOT and FORT characteristics could be calculated. The combination of all three of these programs provided the main software structure to the data collection and analysis.

3.2.1 The Labview experiment control program. The main program used for control over the experiment is a rather complicated Labview program. The goal of using the LV program is to use a single program which has control over the whole of the experiment which is easily adjustable to create desired experimental sequences and conditions. Each experimental sequence can be thought of as a series of steps which occur at specific times. At each of these steps something physical changed in the experiment such as: laser detuning changed, shutters which control laser light opened or closed, anti-Helmholtz coils turned on/off, probe laser firing, etc. The program must also be flexible enough to allow for multiple devices to be changed in each step. To change the state of any one device in the system, the TTL states of the DIO board must be changed at the desired time.

A significant complication arises from that fact that each device can have some delay time (i.e. a time delay between the receipt of its TTL change and the actual change in state). This varies between the individual devices in the experiment, and the program must be able to take into account the physical delays of the devices. If two devices need to turn off at the same time, say the anti-Helmholtz coils and one of the diode lasers for example, the program must be able to handle the delay time of each device so that they both turn off at the specified time in the experimental sequence. In any given experimental sequence, therefore, the numerous physical changes in the apparatus that occur over all the steps of the sequence translate into a required time TTL output pattern from the DIO board. It is the goal of the LV program to properly create this pattern and send it to the DIO board.

At its base is a subroutine which breaks down an array of T/F tables, associates a time with them, converts the output to hexadecimal, and then sends that output to the DIO board. The DIO board has an onboard clock chip that allows it to execute a list of commands for the output TTLs and their associated times. The T/F matrix input is where each step in the experiment is specified. There are 2 16xN matrixes which control 32 TTL outputs. For the experiments in this thesis, 32 TTLs were sufficient for control of the experiment, though the LV program itself should be easily upgraded to make full use of all 64 TTLs should it be necessary. In these matrices, rows are sequence steps, and columns are specific TTL outputs for the various devices. For every step in the experiment, there is a time associated with its row which is the base timestamp (labeled as “timestamp” in the LV program itself). The time stamp is an absolute scale starting from 0 and measured in ms, which can be set in .01 ms increments. The base timestamp is the initial timing for the experimental sequence run, listed in absolute time. In this way an overall matrix containing the appropriate TTL signals which go out to the experiment is constructed and associated with a time. Each step contains the complete specification of the DIO output for that step (i.e. the TTL state for every device at the associated time).

Since the time stamp is an absolute, if you wanted to change the timing of one row, you’d then have to change the timing of each subsequent row in order to preserve the same relative timing. This could prove dangerous in that whenever switching between conditions, one could have easily mistyped one of the many new values. To help alleviate this problem, an additional timing parameter called the “event delay” is utilized. The event delay will add a time to a specified row and that same time to any subsequent row automatically. The convenience of the event delay is that if one wanted

to delay or advance any given step in the experiment, they can do so with the event delay. The LV program will correct the timestamp of the sequence to account for the change, instead of changing each value in the base timestamp setting. Time can be added or subtracted so long as the subtraction doesn't cause the row to coincide with or happen before a previous row. In addition to the timestamp and event delay, one more correction is applied: a correction due to the delay associated with each device, as discussed above. Because there is delay in the triggering of a device, (e.g. a shutter), the times which the triggers are sent need to take this into account. These delays only need to be measured and input infrequently and thus won't be changed in the course of an experiment. The base timestamp + event delay + device delay are collectively referred to as the adjusted timestamp. The adjusted timestamp is the fully corrected time for the TTL triggers to be sent out to the device. Thus the T/F matrix, base timestamp, event delay, and device delay are the inputs to the LV program. The purpose of the LV program is then to construct the adjusted timestamp and associate each timestamp with the appropriate TTL settings.

The first thing the program must do in the run sequence is to properly associate the TTL state with the proper adjusted timestamp and prepare a hexadecimal code which can be output to the DIO board. The hexadecimal code is what is sent to the onboard chip of the DIO board, which tells it the adjusted timestamp and TTL states for each sequence step. The subroutine Multiport+delay 2-3.vi takes care of this, and so in the main program this subroutine can be called as a VI and the proper inputs attached; it will output the fully corrected hexadecimal output to the DIO board. The subroutine accomplishes this by first breaking down the whole of the output sequence, including

TTL matrix, the time stamp, the event delay, and the device delay, into single elements with its proper adjusted timestamp. With each element broken down and associated with a proper adjusted timestamp, an array of steps needs to be built back up. Essentially this step recreates the original T/F matrix but with the adjusted timestamp instead of the base timestamp. The elements go through a series of loops which sort and repack the elements, removing any line in the rebuilt array in which there are no TTL changes. In this way only times associated with TTL changes are converted into hexadecimal and passed on to the DIO board. This subroutine is the workhorse of the main Labview code which prepares the proper timing and TTL output to the DIO TTL board to the experiment. Once the hexadecimal code has been prepared, it's passed off to other subroutines which write to the board itself. The boardout.vi prepares the hexadecimal code for the DIO board which contains all the timing information stored in the onboard memory of the board. Other commands are handled through prepackaged subroutines such as the boardout.vi.

Much of the main Labview code has evolved alongside the experiments to become more adaptable and produce faster data taking rates. One such improvement is in the condition number. As stated, the main subroutine takes a matrix of a T/F array and associated times and corrections. At first the array had to be changed each time the experimental conditions had to change. Over the course of an entire experiment, however, this could lead to mistakes through not clicking the right T/F or entering incorrect values into the event delay, etc. Time between consecutive images can be quite short (sometime less than one minute). Thus often in the course of an experiment we are often quickly shifting through experimental sequences, which increases the chance of

making a mistake in inputting the values of the T/F array or event delay. To address this, the T/F array on the front page of the main Labview program is a 3-D matrix. In this manner, many pages of experimental condition can be loaded in before the start of an experiment. This is done with the event delay too, which is 2-D, a 1-D column with multiple pages. This allows for multiple time delays as well. The pages of the T/F array and event delay are linked together in a condition number, these condition numbers then allow for the storage of multiple experimental sequences on the front page of the LV code. Thus quickly shifting through experimental sequences is reduced to changing a single parameter. The first step in the main Labview program when run is to strip off the proper page and pass that along to the subroutine. The introduction of the event condition vastly increased data taking speed and reliability by ensuring that for each new experimental condition only a single number would have to change.

The remainder of the LV front page has many useful functions, though none requiring the depth of explanation needed for the subroutine and event delays and is mostly straight forward. There is a getter button and getter timestamp, the timestamp always has the top number at zero, the time below is the duration for which you want to run the getters for in ms. Initialize shutter allowed the shutters to be set in a specific configuration corresponding to which isotopes we wanted to load into the MOT; ^{87}Rb alone, ^{85}Rb alone, or both. The probe saturation absorption signal is run off of a deflected AOM beam, so a probe RF state control is included to allow the probe to be turned on outside the running of an experiment to allow for it to be set. There is a delete and clone option for conditions, which was used to clone any one page of the 3-D T/F array to any other page, and includes the event delays for the cloned page as well. This

eliminates having to re-enter an entire 2-D T/F array which could be quite cumbersome for long experiments. The LV program also has built in a sequence structure to allow for the easy accommodation of GPIB commands that can be used for various devices as dictated by the needs of the experiment. The GPIB commands configure the device before the experiment runs. Overall, the LV program lends itself to easy customization and upgrades.

3.2.2 Imaging software. The Labview program controls the whole of the data taking sequences, including the triggers to the camera which image the clouds. The imaging technique is discussed later in this chapter. Though Labview controls the triggers for the camera, it doesn't record the images. That is accomplished with a program called Winview, which came standard with our CCD camera (Roper Scientific model #7404-0001). The program sets up Winview to take accept a series of 4 images, which are triggered through TTL sequences to the camera. The only role Labview plays in the imaging sequence is to provide these TTLs. The first image is a clear out pulse, which clears the CCD array of any dark counts which could have accumulated. Next there is an image of the probe laser with the atoms present (Im1), an image of just the probe laser (Im2), and finally one with nothing turned on (Im3), which serves as a background measure. From these images the optical density (OD) of the atoms cloud can be calculated. The OD is a measure of the absorption length of the cloud and is proportional to the column density of the cloud [9]. In general, it can be found from the intensity of laser light which is transmitted through the cloud,

$$I = I_o \exp(-OD). \quad (3.2)$$

I is the transmitted intensity and I_o is the incident intensity. The absorptive imaging technique and OD are discussed in more depth in the section on data collection. The OD is calculated from the images gathered from our data is given by,

$$OD = -\ln\left(\frac{Im1 - Im3}{Im2 - Im3}\right). \quad (3.3)$$

The resulting processed OD image and the original 4 are saved.

The final programs used in the collection and analysis of data are another Visual Basic code and a Fortran code. This second Visual Basic code takes the OD files and breaks them down into a matrix of numbers and saves it as an ascii file which can easily be read by the Fortran code. The output format of these .txt files is position (x,y) and counts (with counts being proportion to the energy deposited on the CCD pixel). The program can use a variety of regions of interest (ROI) and the ROI can be adjusted to meet changing experimental images. The output of this program is fed into the Fortran code, which applies a 2-D Gaussian fit to the images and runs to maximize the fit. It outputs the peak OD, summed number of counts (which were found to be more reliable than the straight OD numbers), dimensions, and location of the cloud. For clouds like those trapped in a FORT which are elongated, the program has included an angle parameter so that it may match fit axes to the axial and radial dimensions. From the output number of atoms trapped, density, etc. can be calculated.

3.3 Data collection

In our system, the data produced by a given experimental sequence comes in the form of an absorption image of the atoms. A probe laser is set to be on resonance with the cycling transition of the atom species we are interested in imaging. The atoms in the cloud will scatter light out of the probe laser beam. This scattering results in a shadow in

the probe beam image, and from this shadow the OD and then the column density of the atoms can be calculated. This mathematics of this method (absorptive imaging) is discussed in more detail below.

The shadow from the atoms is imaged by a charge-coupled device (CCD) camera. These images are recorded by the Winview program previously discussed, and once recorded can be subsequently analyzed. Our first experiments measuring reabsorption were conducted with a MOT. All subsequent experiments were conducted in a Far Off Resonant Trap (FORT). The imaging techniques are similar between the two cases, but not quite the same. For instance, the MOT is physically larger than the FORT, so the collection optics for the two cases were different. The MOT used a collection lens to roughly collimate the light from the probe laser and produce an image of the atom's shadow. Then another lens focused down that image onto the CCD camera. For the MOT images, most of the probe light is collected and imaged. The CCD pixel array was maximally binned (4x4) with a resulting scale of 60 μm /binned pixel.

For the FORT, the extent of the atom cloud is much smaller than it is in the MOT in one of the dimensions of the FORT. Because of this, the imaging system was changed to magnify the image. The two lenses were replaced with a single converging lens, and that image overlapped with the CCD camera. Much of the probe light is neglected, and only that portion containing the FORT was overlapped with the CCD and imaged. An additional distortion which wasn't present with the MOT is that the probe beam came in at an angle to the axial direction of the FORT. Due to the cigar shape of a FORT, coming in non-normal to the axial FORT axis will cause the imaged shape to appear smaller than it really is along the longest axis. We found that the probe beam came in at 50° off the

normal, and this is corrected for in our final analysis. In contrast to the MOT, the FORT images were 5.44 μm / binned pixel, and 2x2 binning was used.

3.3.1 Absorption imaging techniques. The most common imaging technique for ultracold atoms is called absorptive imaging and is the technique employed for all the data presented in this thesis. In absorption imaging, one illuminates a cloud of atoms with on-resonant or near-resonant light. The light will be absorbed by the cloud and the resulting image of the probe beam is recorded. What is imaged is the shadow of the ultracold atom cloud, and by comparing it to an image of the probe laser without the atoms present it is possible to calculate the optical depth of the atoms cloud, and hence the column density of the atoms in the cloud. The equation for this calculation is given in equation 3.2, though it's presented in a form appropriate for our data collection and experimental units. This expression can be presented in terms of laser intensity instead. As the laser light illuminates the cloud, each atom will scatter at a rate given by equation 2.1. The drop in the intensity of the probe laser is related to the number of photon scattering events $N \cdot R$, where N is the number of atoms in the probe laser field in the area of the probe beam. If we take z as the direction of propagation direction of the probe laser, the change in intensity as a function of distance is given by [9]

$$\frac{dI}{dz} = -n\sigma I. \quad (3.4)$$

Where n is the density ($N = \int n \cdot d^3x$) which can be approximated by assuming a Gaussian distribution with rms width σ_x , σ_y , and σ_z ,

$$n = \frac{N}{\sqrt[3]{2\pi\sigma_x\sigma_y\sigma_z}} \exp\left(-\frac{x^2}{2\sigma_x^2} - \frac{y^2}{2\sigma_y^2} - \frac{z^2}{2\sigma_z^2}\right). \quad (3.5)$$

As for the other terms in equation (3.4), I is the intensity, and σ is the effective cross section and given by,

$$\sigma = \frac{h\nu}{2\tau} \frac{1}{I + I_{sat} \left(1 + 4 \left(\frac{\delta}{\gamma} \right)^2 \right)} = \frac{\sigma_o}{\left(1 + 4 \left(\frac{\delta}{\gamma} \right)^2 \right) + I / I_{sat}}. \quad (3.6)$$

Where h is Plank's constant, ν is the frequency of the light. The right side equation is a convenient expression as it puts σ in terms of the resonant cross section $\sigma_o = 3\lambda^2/2\pi$.

Thus in the low intensity limit ($I \ll I_{sat}$) it's clear from equation 3.6 that on resonance ($\delta=0$) $\sigma = \sigma_o$. It is important to note that 3.6 is for a closed transition, with σ_o coming from a two-level atom. In general, the illuminating light can be set to drive other transitions and alterations to I_{sat} must be made. In such a case, the right hand side of 3.6 becomes,

$$\sigma = \frac{\sigma_o}{\alpha^*} \frac{1}{\left(1 + 4 \left(\frac{\delta}{\gamma} \right)^2 \right) + I / \alpha^* I_{sat}}. \quad (3.7)$$

Where α^* is a dimensionless quantity which can account for a wide variety of effects [14]. Essentially, if a closed transition is not considered there are various parameters such as polarization of probe light, atom excited state structure, m_F population distribution, etc which can cause an apparent increase in the saturation intensity. This is because the light field can then drive more than one specific transition and the Clebsch-Gordan coefficients are smaller. We will consider the case of a closed cycle transition, which is appropriate for our conditions. This is because our probe laser light is circularly polarized. The atoms are spin polarized into the proper stretched states to allow us to

consider the imaging of the atoms as a closed transition. Thus from equation 3.6 we can derive an expression for the intensity through the cloud as

$$\int_{I_0}^I \frac{1 + I/I_{sat} + 4(\delta/\gamma)^2}{I} dI = -\sigma_o \int_{-\infty}^{\infty} n(x, y) \frac{1}{\sqrt{2\pi}\sigma_z} \exp\left(\frac{-z^2}{2\sigma_z^2}\right) dz$$

where :

$$\frac{h\nu}{2\tau} = I_{sat}\sigma_o \quad (3.8)$$

$$n(x, y) = \frac{N}{2\pi\sigma_x\sigma_y} \exp\left(\frac{-x^2}{2\sigma_x^2} - \frac{y^2}{2\sigma_y^2}\right)$$

For convenience the solution is expressed in terms of the resonant cross section. The right side of equation 3.8 is the optical depth (when integrated out, it becomes $-\sigma_o * n(x, y)$ = -optical depth) which is essentially the column depth of the atom cloud at (x, y)..

Integrating equation 3.8, we get the entire form of the optical depth

$$-OD = -\sigma_o n(x, y) = \frac{I - I_o}{I_{sat}} + \left(1 + 4\left(\frac{\delta}{\gamma}\right)^2\right) \ln\left(\frac{I}{I_o}\right) \quad (3.9)$$

I_o is the initial intensity of the probe laser while I is the transmitted intensity. This equation reduces to the basic form of equation 3.3 when we take 3.9 in the low intensity limit. Under these conditions solving for the transmitted intensity, equation 3.9 becomes.

$$OD = -\ln\left(\frac{I}{I_o}\right) \quad (3.10)$$

Equation 3.3 allows for background subtraction off of the images, but other than that is the same as 3.10, thus 3.10 is the equation for the measured optical depth. The program handles all the image math and displays the optical density file, which is the image used for any calculations of temperature and atom number. While the program doesn't take into account detuning and saturation intensity, these can be calculated from the measured

optical depth ($OD_m = -\ln(I/I_o)$) and measured probe intensity if necessary (for instance if detuning is necessary to avoid saturation effects). From the measured optical depth, the actual optical depth becomes.

$$OD = \left(1 + 4 \left(\frac{\delta}{\gamma} \right)^2 \right) OD_m - \frac{I - I_o}{I_{sat}} \quad (3.11)$$

Equation 3.9 and the bottom relation of equation 3.8 also give us the means to calculate the number of atoms in the trap, though this number can also be calculated from the OD files themselves without any fits through summing the observed OD of each pixel in the image. From a Gaussian fit we can get a peak OD and the rms widths of the cloud.

Combining this with equation 3.9 we get an equation for the number,

$$N = \frac{2\pi\sigma_x\sigma_y}{\sigma_0} OD_{peak} \cdot \quad (3.12)$$

The OD, σ_x , and σ_y are all obtained from data, so from measurement all necessary parameters can be obtained.

3.3.2 The probe laser imaging system. The basics of the imaging system are shown in figure 3.5. The frequency of the probe laser is typically set directly on resonance with the main cycling transition of the isotope we wish to image. Typically, the probe could be scanned over both the ^{87}Rb F=2 to F'=3 and ^{85}Rb F=3 to F'=4 transitions without much effort. An occasional grating tweak was necessary, however, to keep the transitions in the center of the PZT range so that it was possible to switch from imaging one isotope to the other simply by altering the PZT voltage and the lock point.

The laser beam first encounters a beam splitter. This is designed to take a part of the beam and feed it to a DAVLL setup. The beam is then coupled through an acousto-optic modulators (AOM), where the first deflected beam is taken and used as the probe

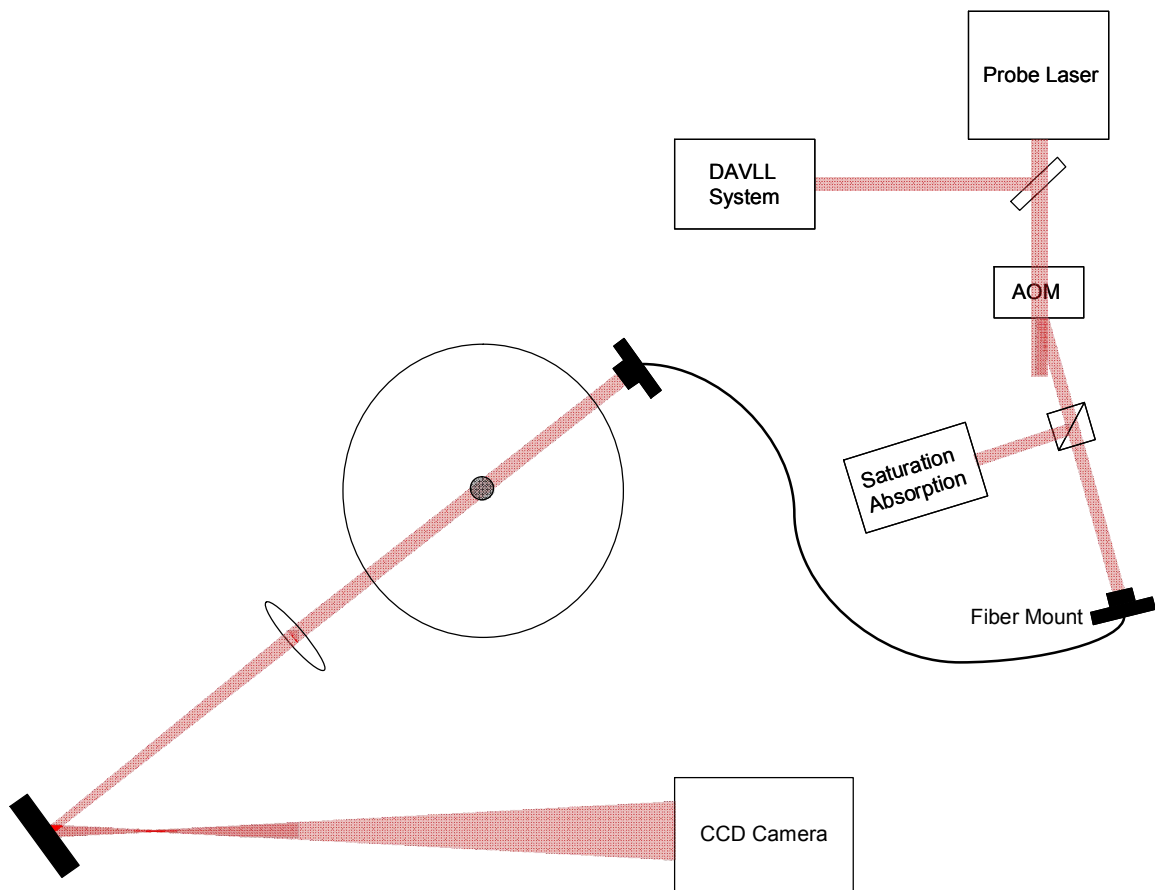


Figure 3.5 Imaging system used for the experiments. Imaging consisted of a probe laser and used absorption imaging techniques to collect data. This cartoon depicts the single lens configuration used for FORT imaging. Early data composed of MOT images had two lenses to collect and collimate the light, and then later another lens to focus the light onto the CCD camera. The probe laser utilized a single mode optical fiber for long term pointing stability.

beam. Part of that probe beam is picked off and sent to a saturation absorption set up. This somewhat complex combination of the DAVLL and saturation absorption was necessary because the deflected AOM beam is shifted in frequency from the undeflected beam. The ideal situation is to have a saturation absorption signal which is directly related to the DAVLL signal. However, the probe uses the deflected beam of the AOM (which had rapid turn on/turn off times of ~few ns, which allowed for the precise control of beam intensity) which is shifted by 80 MHz. The DAVLL could not use the deflected beam as that beam is not always on, and without the beam the electronics which control the DAVLL would have no signal to which it could lock the laser. Thus the DAVLL signal had to be taken from the laser beam before the AOM. The saturation absorption signal could come from the same spot, but since we take the deflected beam as the probe, this would put the saturation absorption signal 80 MHz (the AOM's frequency) below the actual transition. To eliminate daily calibration and for overall ease of use, the saturation beam was taken from the deflected AOM beam so that its signal is unshifted. The DAVLL still covers the enough frequency range and thus even with an 80 MHz shift there is a linear voltage range to which we can lock.

The probe laser is coupled into a single mode fiber to be directed to the atoms. At the input of the fiber, there is a $\lambda/2$ waveplate to match the laser's polarization into the fiber. At the output of the fiber is a polarizer and $\lambda/4$ waveplate which makes the beam circularly polarized. The fiber itself is a polarization maintaining fiber. Initially, the fiber was used because the probe laser was on a separate table and the fiber was used to span the two optical tables. The use of the fiber has an added bonus, however, which is that the fiber preserves of the probe path over time. Since laser alignment changes over

time, the better pointing stability from the fiber allows us to preserve the probe path so that all data is comparable. Instead of altering alignment, changes in probe beam direction result in less efficient fiber transmission. By tweaking the fiber alignment periodically, however, long-term drifts can be compensated for. For our experimental setup, it is much easier to compensate for power variations than alignment variations. This is due to our data taking process in which background, probe alone, and probe with atoms images are taken and processed to develop our OD images. Additionally, the fiber also cleans up the probe laser's TEM structure, which improves our beam quality. At the output of the fiber, the probe is propagated into the ultra high vacuum chamber and overlapped onto the atom cloud. After the light is collected it is then imaged onto the CCD camera where the data is collected and analyzed by a series of programs already discussed.

3.4 The Far Off Resonant Trap.

The basics of a FORT have previously been discussed in Chapter 2.2. Here we will discuss the actual control and characterization of the FORT. Figure 3.6 shows a schematic of the FORT configuration used for the experiments. The laser used for the FORT is a Coherent Gem Select 50 single mode CO₂ gas tube laser. The laser was optimized for single mode TEM₀₀ operation, and thus has no adjustments which can be made by the user. The laser is rated for 50 W output, and measures very near that, though over time degradation of power has been observed to occur in part due to dirt build up on the optics. This can be particularly troublesome with a 50W CO₂ laser as dust and other dirt which gets on the optics can be burned on. If this occurs it could require the optics to be replaced, and a realignment of the FORT as is discussed in

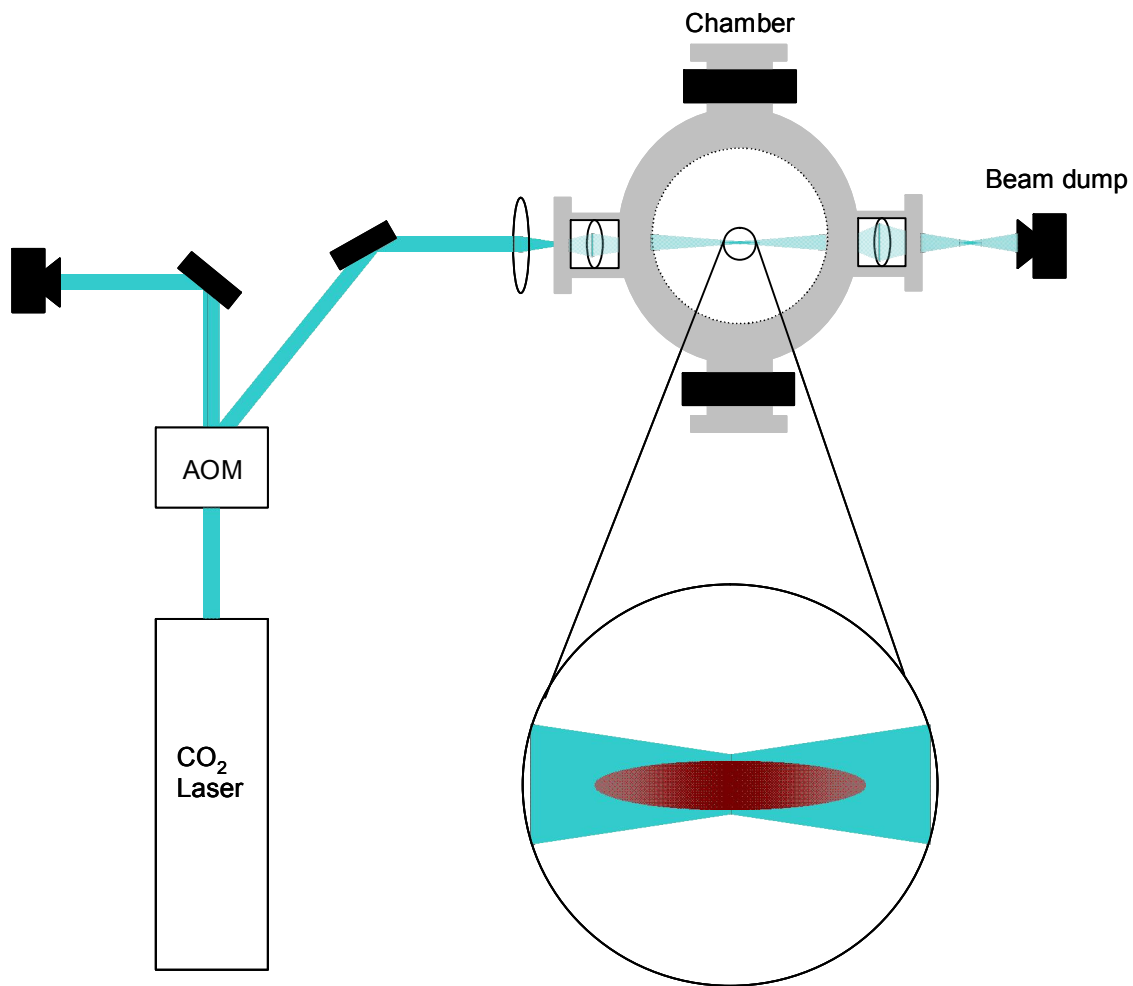


Figure 3.6 Far Off Resonant Trap configuration. The circle is a blow up of the waist of the CO₂ beam where the FORT is created. The oval represents the Rb atoms trapped in the FORT and depicts the aspect ratio which is innate to single laser FORTs (although is is not to scale). The FORT uses the deflected beam from the AOM. The through beam is picked off and sent to a beam dump. Since the FORT is not retroreflected, the beam on the other side of the chamber is also sent into a beam dump. Not all the optics involved in beam shaping before propagation into the chamber are shown.

Chapter 3.4.1. Fortunately if only one optic needs to be replaced it can be done without requiring a full FORT realignment. Our system uses a lens outside the chamber as well as inside the chamber, as depicted in figure 3.6. The focal length of the lens inside the chamber is selected to be half the distance from that lens to the atoms, so it allows for 1:1 imaging of the spot after the final outside lens onto the MOT region. This is different than most other groups in which a collimated beam is sent into a lens inside the chamber which will focus the beam down onto the atoms. Our design was made with the idea that we can eventually use non-cylindrically symmetric FORT beams. The 50 W beam is first magnified and collimated before being directed into the AOM (lenses not shown in figure 3.6). The FORT is composed from the deflected beam out of the AOM. The AOM's driver is controlled by an Agilent arbitrary wave form generator (33520A 80 MHz function/arbitrary waveform generator). While normally set for a square pulse that turns the FORT on at full power, the arbitrary wave form generator allows for time varying pulse AOM output power and thus trap powers. Using this, we can measure the trap frequency via parametric heating as discussed in Chapter 2. The undeflected beam from the AOM is sent directly into a beam dump, and during normal operation all 50 W from the CO₂ laser is deposited there. The deflected beam is reshaped (optics not shown in figure 3.6) and propagated into the chamber through a final outside lens. The lens is mounted to a 3-D translation stage which allows for some amount of beam steering and waist placement for alignment of the FORT onto the MOT. Inside the chamber there are two lenses on either side of where the atoms are trapped. The one closest to the laser images the spot created by the first lens. This image produced inside the chamber is the light that actually composes the FORT. The lens on the other side simply collects all the

remaining CO₂ light so that it can escape the chamber. On the other side of the chamber, the beam is sent into a beam dump.

3.4.1 Alignment of the Far Off Resonant Trap. The initial alignment of the MOT and FORT can be tough to initially set up, as the CO₂ beam is not visible to the naked eye, and does not scatter significantly off the atoms. For the FORT utilized for our experiments, the initial alignment was performed in a grid-like manner in order to attempt find some position in which any atoms were observed to be confined in the FORT. The first two times the FORT was aligned relied on trial and error to obtain a signal. While we eventually found a good indicator for the initial overlap, the FORT and MOT were not aligned often enough for us to have developed a good, consistent method by which we can overlap the two traps.

While there were difficulties in the initial alignment of the MOT and FORT, we did find a good indicator for rough alignment. Once the FORT becomes roughly aligned with the MOT, we see a spatial distortion in absorption images of the MOT. This “tugging” of the MOT atoms indicates that the FORT trapping region is beginning to overlap the MOT. Once the tugging is observed, the amount of tugging can be optimized until standard FORT trap images can be taken and the FORT atoms number optimized directly.. This direct optimization is done first by adjusting the x-y alignment of the last outside lens to maximize the number of atoms trapped in the FORT (here we take z to be along the direction of the FORT beam). Then the z alignment (which adjusts the FORT focus overlap with the MOT) is set by the same method, using the translation stage to move the lens forward and backward until maximum number is loaded into the trap.

The FORT beam does not necessarily go through the center of the lens inside the chamber, and thus slight changes to the waist size can occur when the overlap is changed. For that reason, each time the FORT is optimized on the MOT, a parametric heating test as described in Chapter 2 must be conducted to measure the trap frequency. It is necessary to occasionally realign the FORT due to beam path changes that occur with time. Additionally, beam power through the AOM can slowly drop over time. When this happens the AOM must be recoupled to produce maximum power in the deflected beam.

3.4.2 CO₂ beam characterization. When the FORT was first installed, there seemed to be a discrepancy between the calculated and measured trap depth and frequency. The trap depth of the FORT is proportional to the intensity of the trapping beam. The smaller you can focus down a beam; the stronger you can make the confining potential. The discrepancy in trap confinement suggested that we were not focusing down the laser beam as well as we had calculated. One way in which this discrepancy can develop is if the beam we are using is not TEM₀₀, which is what many of the beam propagation equations typically used assume. A way to check this is to measure the M² value of the laser beam. The M² value is an industry standard for beam quality [15]. It is a ratio of a laser beam's divergence as compared to the divergence of a diffraction limited beam of the same waist size. It can be thought of as measure of how “purely” TEM₀₀ a beam is. A M² value of 1, for example, is a pure TEM₀₀ beam. Anything higher indicates that the beam is not strictly a TEM₀₀ beam (by definition, M² ≥ 1). Because of this mode mixing, a laser will have a waist size which is larger than it would have if it were a pure TEM₀₀ mode,

$$\omega_o = W_o / M . \quad (3.13)$$

Where ω_0 is the waist size of a TEM₀₀ mode and W_0 is the waist size of the laser beam.

M^2 is defined as [16],

$$M^2 = \frac{\Theta}{\theta}$$

where

$$\Theta = \frac{2\lambda M^2}{\pi W_0} \quad (3.14)$$

$$\theta = \frac{2\lambda}{\pi \omega_0}$$

The M^2 value then shows how much “larger” a beam is for a fixed divergence if it is mixed with non-TEM₀₀ modes. Not only will mixing modes cause the minimum waist size to increase, but it will change the beam size ($W(z)$) as the beam propagates, which effects the intensity gradient of the beam. Thus any calculation does for the CO₂ optics system would have to take into account the M^2 value if it were significantly greater than

1. A free space beam expands as,

$$W(z) = W_0 \sqrt{1 + \frac{(z - z_0)^2}{z_R^2}}$$

where

$$z_R = \frac{\pi W_0^2}{M^2 \lambda} \quad (3.15)$$

W_0 is them minimum waist size, z_0 is the location of that waist size. With $M^2=1$, we see the equations are the familiar equations for a TEM₀₀ beam.

It is somewhat difficult to measure M^2 . There have been a few techniques developed that can accurately characterize beam and measure the M^2 factor [16, 17]. To characterize the beam, several measurements of the beam’s spatial profile must be taken. In general there are 3 unknowns to equation 3.15; W_0 , z_0 , and M^2 . In [17], it is suggested that a 4 “cut” method be employed for precise M^2 calculation. However, one of these

cuts is right at the waist of the beam, and for the CO₂ beam that could lead to problems since the beam is so small at its waist that it can deposit a lot of energy in a very small area there. Even the razor blades used to measure the beam diameter can take damage at the waist. Therefore, for our system the 4th cut was impractical. 3 cuts were taken, the minimum necessary to calculate all the unknowns. Burn marks from the CO₂ beam were taken so that the approximate waist position could be found. Then beam measurements were taken on either side of that waist and then once more further down the beam path.

From there, equation 3.15 was used to simultaneously solve for the unknowns. We measured an $M^2 = 1.6$ for our CO₂ laser, a very significant deviation from a pure TEM₀₀ beam. This means that our beam is 26% larger at its minimum waist size than we had previously calculated, and this was consistent with the measurements of the FORT. Given that the laser was quoted to have an $M^2=1$, this measurement was a bit disturbing in that the laser quality could be so far off from design. However, even with this large mode mixing, the strength of the FORT was great enough as to perform to a satisfactory level, and the experiments did not suffer from having such an imperfect beam quality.

3.5 Vacuum chamber, light fields, and magnetic gradient.

Thus far we have discussed the specific traps, diode lasers, calibration of laser light frequency, etc. There are still a few more pieces of equipment necessary for creating a MOT and FORT. One of which is the vacuum chamber itself. Figure 3.7 shows a simplified cartoon of the overall set up presented in a top down view. The laser system shown is simplified and not all the optics are shown, though all the lasers associated with cooling and trapping of the atoms in a MOT are shown. All lasers are overlapped with each other, magnified to the correct diameter, and then directed into their

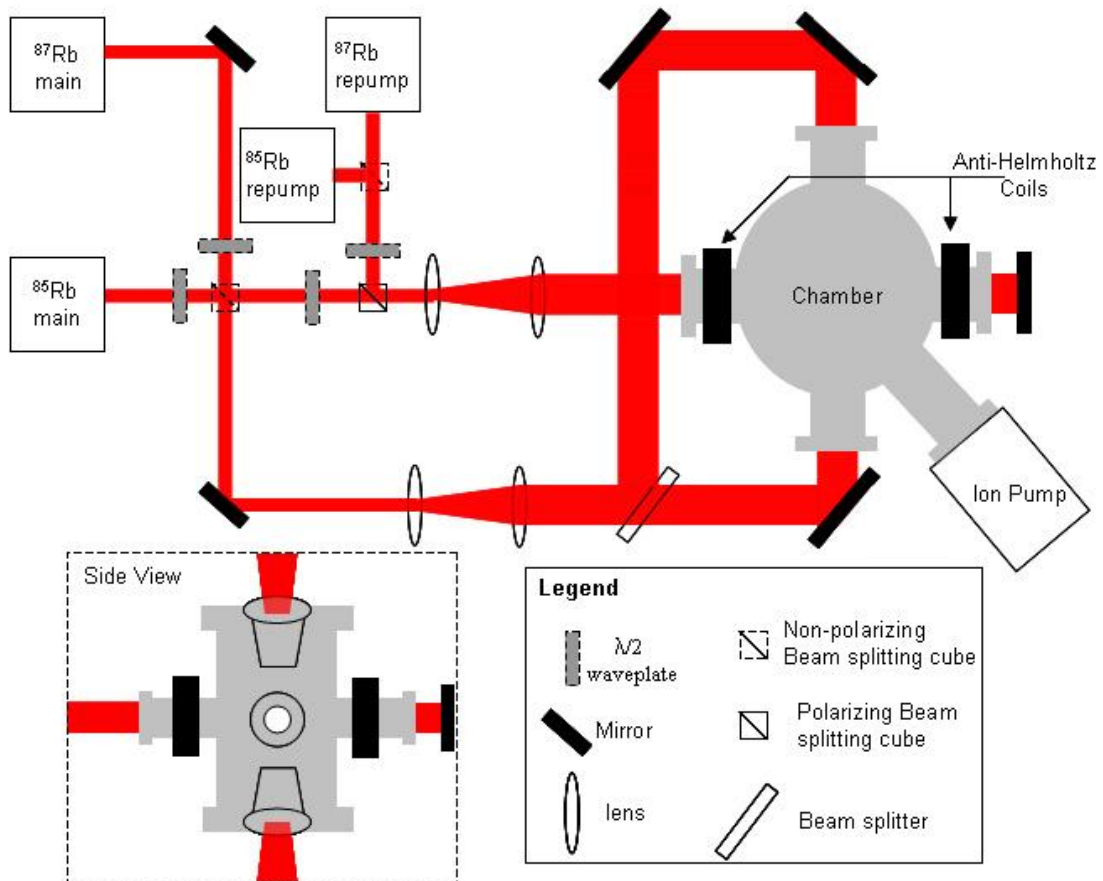


Figure 3.7. Generalized lay out of the vacuum chamber and lasers. The cartoon is simplified and does not show all the optics in the system. The main trapping lasers are coupled together with a non-polarizing beam splitting cube to break the beam path for both into radial and axial components. The repump lasers are coupled into the axial path with a polarizing beam splitting cube. A $\lambda/2$ waveplate couples both the main beams and repump beams into the axial path maximally.

individual ports. The $\lambda/2$ waveplates help to couple the lasers along the appropriate path through polarizing beamsplitting cubes and ensure that all beams have the proper polarization alignment. All laser beams are orthogonal in direction to each other as they propagate through the chamber. The MOT is retroreflected, which means that each of the 3 beam paths have a mirror at the exit port from the chamber. This reflects the beam back through the chamber and provides the counter propagating beam necessary for Doppler cooling and MOT trapping. To simplify the diagram, figure 3.7 shows retroreflection for the axial direction through the chamber, but not for the radial directions.

The chamber itself is a multiport, stainless steel, ultra high vacuum (UHV) chamber. There are eight 2.75 inch diameter conflats designed for the trapping lasers. Six are needed for the MOT, two additional ones for the FORT. The MOT conflats have a 1.5 inch window, and all MOT lasers are designed to be approximately that size before they are directed into the chamber. Because the CO₂ beam is absorbed by glass, the standard commercial window cannot work with that laser. All CO₂ lenses and windows are made out of Zinc Selenide (ZnSe). Due to the properties of ZnSe, the optical access for the CO₂ beam through the 2.75 inch conflat is only one inch. Additionally, the seals are weaker than they are for the normal glass conflats. Baking with ZnSe conflats attached requires a lower temperature. In addition to these eight ports, there are many additional smaller ports which are used for other experimental demands. The imaging system, which is not shown in figure 3.7, uses two of the additional ports. The probe laser is not orthogonal to the trapping lasers, so an asymmetric trap such as a FORT will be viewed at a non-90° angle. Thus a correction must be applied to the images to

calculate the actual widths. There is a large port at the bottom of the chamber which is connected to a 40 L/s ion pump. The ion pump is the sole vacuum pump during normal operation of the apparatus, and provides the ultrahigh vacuum ($\sim 10^{-9}$ Torr) necessary for work with MOTs and FORTs. Also, not shown is a T-section between the chamber and the ion pump. The T contains a Titanium sublimation pump (Ti-sub pump). It was left out of the diagram as it was never used for the data presented in this thesis. It was not until recently in which the Ti-sub pump was fired at all, and for our vacuum conditions it did not have any noticeable, long-term effect.

Two additional ports are used for real time monitoring of MOT fluorescence. One port has a photodiode used to capture the fluorescent light emitted by the MOT. The fluorescence signal is monitored on an oscilloscope. While this signal was occasionally used for auxiliary measurements to characterize the performance of the system, the main use for the MOT fluorescence signal was to measure the number of atoms in the MOT so that experimental cycles could always be started under the same conditions. In addition to the photodiode, there is a small security camera capable of detecting the light scattered by the MOT atoms. This camera monitors the MOT through another small port. This signal is displayed on two small TVs; one directly over the experiment and one by the main experiment computer. This gives an actual real time image of the MOT so changes over time in shape or position can be measured. This camera MOT image was also used to optimize the molasses by making sure the expansion of the cloud was very slow when the anti-Helmholtz field was rapidly shut off.

Near the top of the chamber is a 2.75 inch port connected to a bakeable valve. The only time which this valve is used is when the chamber must be pumped down from

air, such as for a system bake. When needed, a turbo pump is attached to the bakeable valve. The turbo pump and its small roughing pump are built into a pumpout station which allows us to simply move the pumps into place when needed and remove them from the optical table area when not.

On top of the chamber rests a small T. On either side of the T are conflats which have BNC feedthroughs, allowing for electrical feed into the chamber. Each conflat has four BNCs feedthroughs. The bottom BNC on each conflat is attached to either end of a small wire loop, which is to be used in future experiments. The other two on each conflat hold a getter, with the final BNC being utilized as the ground for those getters. Thus in total between the two conflats there are up to four getters. These getters are the source of Rb in our chamber, and provide accurate control over the amount of Rb released.

In previous experiments elsewhere, Rb was sourced from ampoules which were broken under vacuum [9]. Our experiment utilized getters instead, as they provide many advantages over the ampoule. Each getter has only a very small amount of Rb (μg). When current is passed through the getter; it heats up and releases Rb into the vacuum chamber. The amount of Rb released can be controlled by adjusting the time for which the getters are “run” (i.e. how long current flows through them). This time is set through the labview program controlling the experiment, and the load rate seen on the oscilloscope gives an indication of how much Rb has been released. Additionally, there is a visible vapor on the monitoring screens when a lot of Rb is released. All this gives information for precise control of Rb level inside the chamber. Switching between getters can be done merely by changing which BNC connections are employed. A full

set of getters can last close to four years of typical operation. Once all getters are exhausted, the system must be brought up to air and the getters replaced.

The final conflat which is located at the top of the T has a 1.5 inch window. An additional security camera monitors this view; though this view is rarely used. All other ports and windows are used when necessary and/or convenient.

The final necessary piece of equipment for creation of a MOT is the magnetic field gradient. The anti-Helmholtz coils provide this gradient and were mounted to the outside of the chamber, as shown in figure 3.7. The disadvantage to mounting the coils outside is that the further the coils are away from each other, the weaker the field tends to be. Increased current and number of turns of each coil can compensate for this, but the coils and/or power supply then need to be bigger. However, in the end, mounting on the outside of the chamber is a convenient choice as the coils are easy to get to, install, remove, etc. Smaller coils can be used if the coils are mounted inside the chamber, but this in and of itself creates a variety of problems and can lead to vacuum contamination if the coils are not cleaned properly. Additionally, coils inside the chamber would require additional water cooling and electrical feedthroughs into the vacuum chamber, which could have undesirable results.

Our coils were hand wound on a lathe. Coil forms were created out of plastic to hold the coils in place temporarily so that the layers could be wound. Each layer was set with a coating of insulating epoxy to cover any scratches in the insulation in order to protect against electrical shorts and to physically glue the layers in place. If this step is not done, when the tension on the wire is released, the coil will spring apart and you will have to start all over. This is due to the stiffness of the wire used for the main anti-

Helmholtz coils, necessary since the coils must carry decent amperage (our system uses 20 Amps). The wire used for the main anti-Helmholtz coils was NEMA MW36-C, square magnetic wire. The square wire is supposed to help with wrapping of coils, but in practice for hand wrapping the way we did it was not much of an improvement. After the coils were fully made, and the insulating epoxy had cured, the coils were removed from the lathe and the coil forms removed before the coils were mounted to the chamber. The coil forms were removed in order to allow the coils themselves to be pushed as closely to the chamber as possible.

The anti-Helmholtz coils must be designed to produce an adequate magnetic field gradient to allow for the selective scattering which creates the spatial force. These gradients can be calculated directly [18] from the full equations for the system. In general, the B field can be written by first finding the vector potential A and then taking the curl ($\mathbf{B} = \nabla \times \mathbf{A}$). For a single coil with N loops, radius R, at $z = d$, the field can be written as

$$B_z = \frac{\mu NI}{2\pi} \frac{1}{\sqrt{(R + \rho)^2 + (z - d)^2}} \left(K(k^2) + \frac{R^2 - \rho^2 - (z - d)^2}{(R - \rho)^2 + (z - d)^2} E(k^2) \right) \quad (3.16)$$

where

$$k^2 = \frac{4R\rho}{(R + \rho)^2 + (z - d)^2}$$

Where I is the current, and K and E are elliptic integrals. The z axis is selected to run perpendicular to the area of the coil. Equation 3.16 is the exact expression for the z-component of the B field of a single coil. [18] gives an expression for the anti-Helmholtz configuration, which is

$$B_z = \frac{3\mu INdR^2}{(R^2 + d^2)^{5/2}} \left(z + \frac{5(4d^2 - 3R^2)}{6(d^2 + \rho^2)^2} (z^3 - \frac{3}{2}z\rho^2) + \dots \right) \quad (3.17)$$

By setting ρ to be zero, equation 3.17 can be used to find the on-axis gradient. (Though for calculation of an on-axis gradient field, one need not go through the full formal calculations. Using the result for an on-axis B field caused by a wire loop will suffice in yielding an appropriate value for the magnetic field gradient.) For a single loop, the on-axis magnetic field is,

$$B_z = \frac{\mu N I R^2}{2(R^2 + z^2)^{3/2}}. \quad (3.19)$$

Equation 3.19 can be modified for the two coils of the anti-Helmholtz pair simply by multiplying by 2, and the gradient can be calculated directly from that. For our system; $R = 3.81$ cm, $I = 20$ Amp, $N = 36$, $z = 10$ cm. We have a magnetic field gradient which is ~ 4 G/cm. This is a bit lower than in most experiments [19, 20, 21], but it was found advantageous for atom cloud temperature and efficiency of polarization gradient cooling. This is because magnetic fields can destroy the efficiency of polarization gradient cooling. When the Zeeman energy splitting approaches that of the light shifts, the mechanics behind polarization gradient cooling begin to break down. Thus for strong magnetic fields, the temperature of the atom cloud actually rises and the density decreases. The gradient for our system was optimized for temperature and density of the MOT which yielded a gradient of about 4 G/cm.

Besides the main anti-Helmholtz coils, there are several other coils surrounding the chamber. These are the shim coils, which are much smaller in diameter than the main anti-Helmholtz coils. They are hand wound on the lathe much like the anti-Helmholtz coils. The coil forms are permanent, however, and the wires are much thinner; making to much easier to create and hold in place. The shim coils have 100 or more turns (depending on radius of the coils); each shim has an additional small N coil around them

to act as an Earth shim. Because they are meant to shim the overall magnetic field, they themselves do not need to produce large magnetic fields. A large numbers of turns are employed and small current used to provide the small magnetic shims. There are a total of three pairs of shim coils on orthogonal axes, in general the use of all 6 shims can allow one to completely zero out the field and gradient where desired. In practice, a few of the shims are used in order to optimize the molasses. Using the shims is preferable to alignment modification as the settings of the shim currents are very reproducible and easy to adjust. The alternative is to adjust the optics to change beam placement to optimize the molasses, but using mirror mounts as opposed to current through a coil is less reproducible.

3.5.1 Bootstrapping, normal vacuum operation and getter operation.

During the course of normal operation, the vacuum chamber remains closed to air and relies on its ion pump to maintain the vacuum. The ion pump, however, cannot be turned on at atmospheric pressure, and thus a bootstrapping vacuum system is necessary to initially drop the vacuum low enough that the ion pump can take over. The essentials of the vacuum system are its; stainless steel chamber, 40 L/s ion pump, titanium sublimation pump, Rb getters, and bakeable valve which allows the chamber to be attached to a bootstrapping pump (while other pieces of the system are disassembled during the bakeout process, see chapter 3.3.6, these pieces always remain connected). For normal operation, the bootstrapping pump is disconnected from the system, and the bakeable valve closed off to air. While the Titanium sublimation pump can be used to improve the vacuum, it is a one-shot device and thus is not on during normal operation. The getters provide the only influx of material into the chamber, and are also one of the

main markers for how long the chamber can be left in normal operation before a bakeout is necessary.

In general, the chamber is brought down to pressure by attaching a turbo pump to the bakeable valve. The turbo pump and its roughing pump are referred to as a bootstrapping pump. The turbo pump can begin to take the chamber down below atmosphere. The ion pump cannot operate at atmosphere pressures, and can be safely turned on when the chamber pressure falls to $\sim 10^{-3}$ Torr. Once the chamber has been pumped down far enough, the ion pump is turned on. For normal operating conditions of the chamber, the bakeable valve is closed and the system is left with only the ion pump. The current gauge on the ion pump is used to measure the vacuum inside the chamber (this can also be used for leak detection for small leaks).

As mentioned previously in the chapter, Rb is introduced into the chamber through getters inside the vacuum chamber. The getter is heated up by running current across it and sputters Rb into the chamber. The current set up facilitates up to 4 Rb getters, and a getter seems to last about 1 year with normal use. Though if the chamber is thoroughly baked (multiday 300 °C), the chamber needs to be coated with Rb before a decent background of Rb vapor can be reached. One complication with this in terms of the current set up is that the getters are attached to a “T” and are pointed towards each other and not directly down into the chamber. This was done to facilitate other pieces (including a wire loop for future experiments) with the BNC feed throughs used for the getters. Originally, there was one BNC feed through conflat at the top of the chamber so that the Rb getters pointed down directly into the chamber where the trapping lasers overlap. Since that line of sight is now lost, we are dependent upon Rb moving down

into the chamber from the T into the trapping region. We found on our last bakeout of the system, where the system was thoroughly baked for several weeks, that it required a long run and the exhaustion of one of the getters to sufficiently load the chamber with Rb to allow for reasonable load times.

3.5.2 Baking the system. The overall performance of the system is improved when the system has been thoroughly cleaned. Since contamination can so negatively influence trap performance (primarily through the decrease in trap lifetime), the system is designed to be opened to air as little as possible. Additionally, as long as the chamber is not opened, the vacuum should get better with time. This is because contaminants which outgas will slowly be exhausted over time. The main limitation to how long the system can be closed is the getters. Once they all run out of Rb, the system must be opened in order to replace them. Other changes to the experiment may warrant the chamber being brought up to air if additional hardware must be added or subtracted from the inside of the chamber. Besides cleaning the optics on the table and chamber, the vacuum system itself can be cleaned through a process known as baking. The baking process requires that the vacuum chamber be brought up in temperature and left there for several days (depending on the temperature of the bake). Baking the chamber removes further impurities from the inside of the chamber. These impurities (water, oils, etc) stick to the surface of the chamber and outgas over time. The outgassing limits the vacuum pressure by providing a background gas pressure. By baking the system, we increase the outgassing of these contaminants and thus can drive them from the surface of the chamber. Because everything from optics to magnetic coils is mounted to the outside of the chamber, disassembly is relatively simple. We then don't need to worry about

temperature limitations of optics and coils. However, we do need to worry about temperature isolation of the system from the optical table given the temperatures used in baking the system.

To address this problem, the chamber and the ion pump are both mounted on stands which can be elevated off the table to reduce thermal contact. The port at the top of the chamber with the bakeable valve is attached to a turbo pump, and the valve opened. The whole of the chamber, including the ion pump, is wrapped in heater tape (resistive heater). Each section of heater tape is controlled by a variac, which adjusts the current through the strip and allows us control of the temperature. For the first bake, nichrome wire was used as well as heater tape, but the wire turned out to not perform as well as the tape. A total of three heater tapes are used in the bakeout process. The temperature is monitored at several places, and adjustments to the variacs are made to achieve the desired temperature. The whole of the apparatus is then covered in many layers of aluminum foil to create an oven. Ideally, the system is typically brought up to 300 °C for several days to clean the system. This cannot be done when the ZnSe windows are mounted. In that case the chamber can not be brought up above 150 °C. This is because the indium seals used on those conflat will pop if brought to 180 °C. The system went through a total of three bake cycles while I worked with the system.

The first bake was for the initial assembly of the vacuum system in November of 2004. The system was relatively clean at that point. Not only being new but we also had the parts chemically degreased and ultrasonically cleaned. As with all bake out processes, the first step was to ultrasonically clean each piece thoroughly before bake. This was done professionally for most of the parts for the first assembly. Each piece

received several alternating methanol/distilled water rinses and the system was then bolted together. The first bake was the only bake to use nichrome wire since it is easily tailored in length, can be made to wrap the chamber well, and could be brought up to 400 °C. The first bake also utilized heater tape as well. The initial chamber configuration did not have the small “T” on the top. Rather, a conflat with 4 BNC feed throughs was placed directly on top of a zero reduction flange. The Rb getters were mounted to the feedthroughs and directed straight into the chamber towards the trapping region. The chamber was brought up to near 300 °C and held there for several days. In the later stages of the bake out, the current from the ion pump was used to monitor the pressure inside the chamber. The initial bake proceeded smoothly, the chamber was baked, cooled down, and produced suitable vacuum.

The second bake out was really two bake outs due to complications that arose in the first attempt. These bakes were done in June of 2006. The chamber had to be brought up to air in order to replace the getters and make changes to the system to allow for future experiments. The chamber received substantial additions, which brought it to its current form. The small “T” (four way cross) was added to the top of the chamber, which holds the getters and the RF coils. The RF coils were added to the chamber to be used for later experiments. The initial installation of these coils was less than satisfying. The coils were made to hang in free space but the stiffness of the wire prevented it from hanging freely, and instead is hung at an angle. ZnSe lenses were placed in the arms of the chamber for the creation of the FORT (these lenses are shown in figure 3.6), placed approximately 2.3 mm in from the knife edge of the conflat flange. The ZnSe windows were also added for access into the chamber for the CO₂ beam. Microwave antennas

were also placed in the chamber as well. These were metal cylinders which came to a point, the purpose of which was to couple microwaves into the chamber for m_F state mixing. Because the ZnSe windows were added to the chamber, we could no longer bake at 300 °C since the indium seals would pop. Thus, for this bake out, the chamber was raised to 150 °C.

The first bake proved problematic on several fronts, including the monitoring of the chamber temperature. Ultimately, the current on the ion pump shot up and never came down, indicating that the bake was not removing contamination. The chamber was brought back down to room temperature, but during the cool down, the current on the ion pump did not come down either. In the end, the vacuum was poor and unworkable for the experiment. Leak testing found that a newly installed viewport had a leak. This was corrected, and in addition the RF coils were changed out and posts were added to the top conflat so that the RF coils could be mounted securely, preventing them from moving in the chamber and ensuring the coils were level. The chamber was rewrapped in heater tape and once again brought up to 150 °C two weeks after the first attempt at the second bake out. Current came up again on the ion pump and stabilized. Though it wasn't satisfactory, the decision was made to live with it and the chamber was cooled down and unwrapped. The vacuum was sufficient for the current experiments, though not as good as it should be. Problems persisted in what appeared to be leaks, but the problem seemed to have resolved itself. Later measurements of the vacuum and MOT lifetime showed that the current vacuum could not meet the requirements for the next round of experiments.

The third bake out occurred in the spring of 2009 and proved one of the most problematic bake outs to date. With the vacuum needing improving and the getters needing to be replaced, the chamber was brought up to air to replace the needed parts and prepare for bake out. One problem contributing to the poor vacuum from the previous bake out was thought to be the low bake out temperature. 150 °C may not have been enough to sufficiently drive impurities out of the chamber. As such, this bake out was designed for two stages; a 300 and a 150 bake. For the 300, the ZnSe windows are replaced with blanks, the chamber was wrapped and brought up to temperature. It sat at 300 for some time, and the current on the ion gauge was slowly decreasing, everything proceeded smoothly. One morning, we came in to find the 40 L/s Varian Starcell ion pump was dead, there is no indication as to exact cause. It could have been due to leak or Rb overload. The ion gauge which we were using for this bake out indicated a pressure of 10^{-6} torr on the turbo pump side. Considering the conduction through the tube which attaches the turbo pump to the chamber, it was calculated that the chamber should be an order of magnitude higher in pressure (10^{-5} torr), well too high.

The chamber was cooled back down, the ion pump replaced with a 45 L/s diode ion pump. It was also found that one of the small viewport windows had developed a leak, and this view port was replaced by a blank. The chamber was rewrapped and brought up to temperature. As the chamber heated up, one of the heater tapes shorted out and blew a small hole through the aluminum oven. This required the arm to be rewrapped. During the course of this bake out, there were many problems. We baked at 300 °C for a week, replaced the ZnSe conflat, baked it for several more days at 150 °C, cooled down, and attempted to regain our MOT. One problem we encountered was the

placement of the Rb getters. The long 300 bake appeared to have cleaned the chamber well, and we were no longer able to keep Rb in the main chamber for long. We theorized that since the chamber was so hot for so long, the Rb was driven from the walls. Running the getters deposited Rb into the chamber, and the Rb quickly adhered to the side. Complicating the issue was that the getters were mounted to the “T” facing each other, and not looking directly into the chamber. In the end, we ran completely through one Rb getter to try to get enough Rb into the chamber to coat the walls. But when evaluating the system overall, it appeared as if we had problems with the ZnSe optics.

The chamber was once again brought to air. We found much of the ZnSe windows and lenses had what appeared to be a thin coating of contaminant. New lenses and windows were ordered, but we later found out that this often happens to ZnSe optics and that it does not appear to inhibit performance. The used up getter was replaced, the system baked a final 150 °C. Ultimately, the system was remarkably clean and we can achieve sufficient vacuum for our intended experiments.

3.6 Conclusion

While the amount of equipment and control for the system can appear to be overwhelming, a MOT system can be made relatively cheaply, less than \$3,000 [1]. Constructing a MOT is relatively straight forward, and relatively simple to maintain. The vast majority of the equipment used in these experiments, described in this chapter, are built in-house and can be replicated easily. Diode lasers are cheap and relatively abundant which makes their use convenient. Additionally the technology used to control the diodes, from the grating feedback to the spectroscopy used for calibration are well understood. The anti-Helmholtz coils necessary for spatial trapping are easily wound,

and the fields needed are easily accessible with a standard power supply. While the FORT is slightly more expensive due to the equipment necessary, it too is a relatively straight forward optical trap. The difficulties with the FORT mostly come in the form of initial alignment of the FORT with the MOT in order to properly load the FORT.

The most expensive piece of equipment, and one which needs a lot of planning, is the vacuum chamber itself. A lot of planning is necessary since the optical access to the chamber is important and enough ports must be added in order to meet the experimental demands. While we used a stainless steel chamber, other groups have used glass chambers. While much more expensive, glass chambers can typically realize lower vacuum pressures and have better optical access. Regardless of type, baking the system after opening to air can greatly improve the vacuum of the chamber. Since outgassing is a problem, and the outgassing rate goes as the double exponential of the temperature, heating the system can significantly reduce contamination inside the chamber. The overall improvement to the vacuum will cut down on background gas collisions with trapped atoms; allowing for an increase in the trap lifetime.

The convenience of our system is that it can be controlled entirely by a Labview program with a convenient front page display. Much of the program had evolved along with the system, and specifically what is necessary for front page control will depend on the particulars of the experiment. Though the Labview program was made to be easily upgraded to keep up with changing experimental demands. The use of TTLs to control the vast majority of the equipment facilitates the Labview program and is extremely reproducible as well as convenient. Most of the equipment (if not all) can be made to trigger from a TTL, and so timing and control of equipment reduces a single Labview

program which can oversee the whole of the experiment. Thus the system on the whole encompasses a relatively cheap, reliable, and convenient system for probing the dynamics of ultracold atoms.

References for Chapter 3

- ¹ Carl Wieman, Gwen Flowers, and Sarah Gilbert, *Am. J. Phys.* **63**, 317 (1995)
- ² C. J. Hawthorn, K. P. Weber, and R. E. Scholten, *Rev. Sci. Instrum.* **72**, 4477 (2001)
- ³ A. Q. Liu, X. M. Zgang, D. Y. Tang, and C. Lu, *Appl. Phys. Lett.* **85**, 3684 (2004)
- ⁴ L. D. Turner, K. P. Weber, C. T. Hawthorn, and R. E. Scholten, *Opt. Commun.* **201**, 391 (2002)
- ⁵ A. S. Arnold, J. S. Wilson, and M. G. Boshier, *Rev. Sci. Instrum.* **69**, 1236 (1998)
- ⁶ L. Ricci *et. al.*, *Opt. Commun.* **117**, 541 (1995)
- ⁷ T. Hof, D. Fick, and H. J. Jansch, *Opt. Commun.* **124**, 283 (1996)
- ⁸ B. Mroziewicz, *Opto-Electron. Rev.* **16**, 347 (2008)
- ⁹ Jacob L. Roberts PhD thesis, University of Colorado (2001)
- ¹⁰ Kristan L. Corwin *et. at.*, *Appl. Opt.* **37**, 3295 (1998)
- ¹¹ <http://laser.physics.sunysb.edu/~bazmoun/RbSpectroscopy/#The%20D2%20Transition>
- ¹² Demtröder, W. *Laser Spectroscopy: Basic Concepts And Instrumentation*, Berlin: Springer-Verlag, 1981.
- ¹³ Jessica M. Reeves, Ofir Garcia, and Charles A. Sackett, *Appl. Opt.* **45**, 372 (2006)
- ¹⁴ G. Reinaudi, T. Lahaye, Z. Wang, and D. Guery-Odelin, *Opt. Lett.* **32**, 3143 (2007)
- ¹⁵ Baida Lu, Bin Zhang, and Shirong Luo, *Appl. Opt.* **38**, 4581 (1999)
- ¹⁶ A. E. Siegman, G. Nemes, and J. Serna, *OSA TOPS* **17**, 184 (1998)
- ¹⁷ Thomas F. Johnston Jr. *Appl. Opt.* **37**, 4840 (1998)
- ¹⁸ T. Bergeman, Gidon Erez, and Harold J. Metcalf, *Phys. Rev A* **35**, 1535 (1987)
- ¹⁹ D. E. Prichard, E. L. Raab, V. Bagnato, C. E. Wieman, and R. N. Watts, *Phys. Rev. Lett.* **57**, 310 (1986)
- ²⁰ E. L. Raab, M.G. Prentiss, A. E. Cable, S. Chu, and D. E. Prichard, *Phys. Rev. Lett.* **59**, 2631 (1987)
- ²¹ D. W. Sesko, T. G. Walker, and C. E. Wieman, *J. Opt. Soc. Am. B* **8**, 946 (1991)

Chapter 4

Suppression of Reabsorption in Ultracold Gases via Modulation of Light

4.1 Reabsorption in optically thick clouds

Reabsorption is a process inherent to light scattering in optically thick gases. It consists of the multiple scattering of spontaneously emitted photons in these gases before these photons exit the gas. By way of contrast, in optically thin samples, reabsorption is far less significant. This is due to the fact that in optically thin samples a spontaneously emitted photon is likely to exit the cloud without being reabsorbed by another atom.

Reabsorption is one of the major limitations to efficient optical pumping and laser cooling. The multiple scattering of the spontaneously emitted photons in these gases results in undesirable heating and depolarization of the optically pumped atoms.

Reabsorption has often plagued laser cooling and trapping schemes by critically limiting the efficiency of optical pumping, ultimately reducing achievable cooling rates. These limitations due to reabsorption have been observed experimentally in studies showing a decrease in laser cooling efficiency with increasing optical depth [1,2,3,4,5]. In fact, the disruption to the cooling efficiency caused by reabsorption is believed to be the primary reason as to why Bose-Einstein condensates (BECs) cannot be created using non-evaporative techniques. Thus being able to understand the dynamics of reabsorption could lead to methods by which its effects could be mitigated, allowing for improvements to optical pumping and laser cooling in ultracold gases. For our conditions, the ultracold gas has a typical temperature of 10's μK , a density of $\sim 10^{10} \text{ cm}^{-3}$, an on-resonant optical

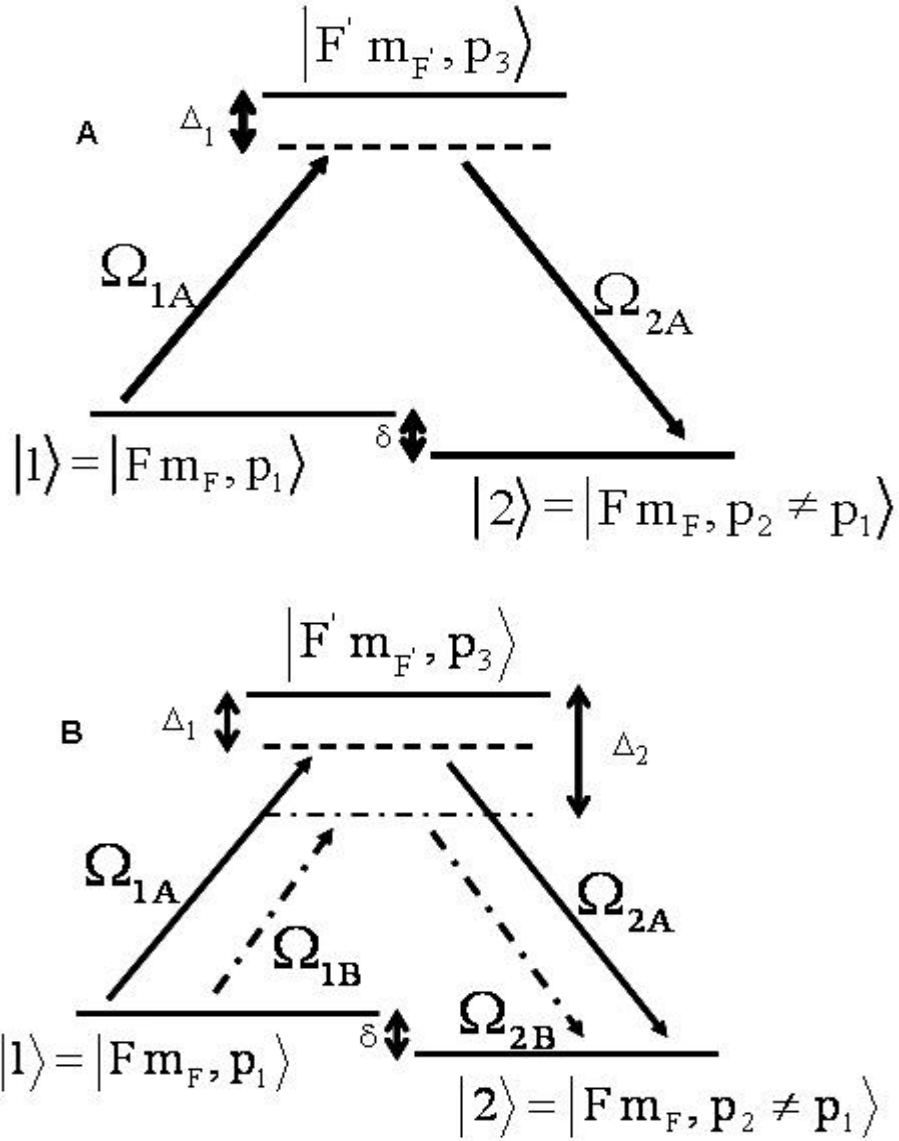


Figure 4.1 One-photon (A) and two-photon (B) reabsorption diagram. The quantum states (solid horizontal lines) and light (diagonal lines) involved in the two reabsorption processes are illustrated. The atom is driven from one momentum state (p_1) to another (p_2) in the same hyperfine magnetic sublevel. For two-photon reabsorption, this is done via a combination of pump light (Ω_{1A} , Ω_{1B}) and spontaneous emission in the ultracold cloud (Ω_{2A} , Ω_{2B}). δ is a frequency detuning that is a function of the kinetic energy difference between states $|1\rangle$ and $|2\rangle$, the magnitude of the photon recoil, the relative direction of the spontaneous emission and pump light, the relative velocities of the atom transiting between states $|1\rangle$ and $|2\rangle$, and the atoms emitting the spontaneous emission light. (A) shows reabsorption with a single frequency illuminating the cloud, (B) shows the case in which two lasers with two different detunings (Δ_1 and Δ_2) are used. For (A) with intensity I , the scattering rate is proportional to I , while heating is proportional to I^2 . Whereas for (B) with both lasers at intensity $I/2$ (maintaining the total intensity), the scattering rate is proportional to I , while heating is proportional to $I^2/2$.

depth (OD) of ~ 10 OD, and the atoms are randomly distributed in space. To date, most of the experimental and theoretical work has focused on the use of trap geometry and tightly confining potentials to decrease reabsorption [6,7,8,9,10]. For instance, by using elongated traps the average density of the gas can be maintained while reducing the optical depth in two directions out of the cloud. This decreases reabsorption effects in those directions, making it easier for photons to escape in those directions before they can be reabsorbed [6, 9]. In other work, optical lattices have been used to mitigate reabsorption since their naturally strong confinement potentials allow for operation in the *festina lente* regime [2, 8]. In this regime $\Gamma_s \ll \omega_0$ where Γ_s is the spontaneous scattering rate and ω_0 is the trap frequency. The spontaneous scattering rate is dependent on detuning and intensity, which are tunable parameters in an experiment. In the *festina lente* regime, reabsorption is mitigated through the decrease in the scattering rate [7]. The control of the scattering rate allows one to extinguish the inelastic reabsorption processes which result in additional heat to the cloud. Since the two-photon reabsorption process is a Raman process, it requires coherence between the pump light and scattered light. The lower scattering rate compared to trap potential in the *festina lente* regime allows for more motion of the atoms in the potential in between scattering events. There is a phase difference between atoms involved in the reabsorption process given by the optical path length difference between the atoms. Essentially, this phase will be dependant upon the motion of the atom in the potential. Since the atoms are moving in the potential, averaging over the phases of the reabsorption process during the atoms' motion results in a disruption of the secondary absorption; thus mitigating the effects of reabsorptive heating of the cloud. Though not all forms of reabsorption are eliminated,

there are still allowed elastic processes. However, the elastic processes are energy conserving and thus do not contribute to the overall problem reabsorption has on dense ultracold atom clouds.

While there have been methods created to mitigate reabsorption, these rely on specific trap geometries or strengths. There has not yet been a generalized method by which reabsorption could be reduced without relying on geometry or trap strength. Ideally, reabsorption mitigation could be accomplished with alterations to the laser cooling light itself. Such a process would remove the limitation of preparing atoms in a specific type of trap, instead allowing for a mitigation technique that could be utilized by most any system. Thus, we searched for an optical method by which reabsorption could be mitigated through modification of the laser light illuminating the ultracold atom cloud. We found such a method, and obtained experimental evidence of this mitigation. The method relies on the simultaneous alteration of the frequency spectrum of and creating a spatial interference pattern in the applied laser field. This technique is broad reaching and should be able to be applied to many systems to reduce the amount of reabsorption regardless of trap geometry or confinement strength. Beyond the experimental evidence, a semiclassical model which explains our experimental results was developed. Previous theoretical descriptions used simple two-atom treatment to develop their theory [6, 7]. In principle, this is not a bad starting point as the process of reabsorption relies on the absorption by an atom of another atom's spontaneously emitted photon. It is easy to consider this process with only two atoms and a laser field present. However, the main problematic reabsorption process is a coherent two-photon Raman scattering process whose rate is dependent on the phase coherence of the scattered light in the cloud. While

it is easier to consider a two-atom system, there is a loss of information concerning the phase coherence and stability of this scattered light in a many-atom cloud. In order to explain our experimental observations, we had to go beyond the simple two-atom treatment to develop a more complete description of the nature of spontaneous emission and inter-particle correlations in a many-atom ultracold gas.

4.1.1 The Reabsorption Processes. There are two reabsorption processes which can take place in an optically thick cloud. Both of them rely on the presence of pump and scattered photons. Here we refer to pump photons as the photons incident on the cloud, coming directly from the lasers. Scattered photons refer to the photons spontaneously emitted by atoms after they absorb a pump photon. The first process [11] is the simplest. This first type of reabsorption depends on an atom spontaneously emitting photon and that newly created scattered photon then being absorbed by a second atom in the cloud. In an ultracold cloud, once the density becomes large enough a scattered photon it becomes extremely unlikely that a photon can travel through the cloud without rescattering. As such, a photon can “rattle” around in the atom cloud, rescattering one or more times before it eventually escapes the cloud. This multiple scattering introduces undesirable heating and depolarization of the atoms. The spontaneously emitted photon is emitted with random direction and polarization. Reabsorption of this photon can cause photon recoil in random a random direction, which can cause heating. Also since the polarization of the spontaneous photon is not related to the cooling laser field, it can induce depolarization of the atom with respect to the cooling laser field. However, in this first type of scattering the rate is essentially given by equation 2.1, with the intensity in that equation being set equal to the intensity of the scattered light. Thus, this first process

is detuning dependent, and so this reabsorption can be mitigated through larger detuning of the laser light.

The second process is a two-photon Raman scattering phenomenon in which a scattered photon and a pump photon of the same frequency simultaneously drive a transition between two ground states of differing momenta. Figure 4.1 shows a typical one of these two-photon transitions with just a few sample states shown. The three states of a single atom in the cloud shown in Figure 4.1 are coupled together by the pump laser light and spontaneous light from one particular direction. There are, in general, more than the three states shown in Figure 4.1 that are involved in the reabsorption transitions. This is because there are a large number of momentum states for each atom that are coupled together by the two-photon reabsorption process since spontaneous emission light will be striking a given atom in the cloud from many directions. Despite this complexity, the three states shown are sufficient to describe the basic physics associated with the changes in the observed reabsorption effects.

Because the scattered light does not in general travel in the same direction as the pump light, this two-photon reabsorption drives atoms between different momentum states and the net effect of several of these reabsorption events is momentum diffusion. This in turn results in the heating of the cloud. However, unlike the one-photon process, the two-photon process is independent of the detuning of the pump light from the excited state ($\Delta_{1,2}$ in figure 4.1(B)) for a fixed scattering rate since the scattered photons have the same frequency as the pump photons which create them [6]. Thus for the coldest, densest ultracold gases (e.g. cooled atoms in an optical trap) the two-photon process is ultimately the main contributor to reabsorption at significant detunings. Since the experiments

described here investigated the nature of the two-photon reabsorption process by operating at significant detunings, whenever the word reabsorption is used henceforth it will be in reference to the two-photon rather than the one-photon process.

Figure 4.1(B) shows two different detunings (Δ_1, Δ_2) with different Rabi frequencies associated with them which can couple the two ground states together. This situation corresponds to an ultracold cloud being illuminated not by a pump beam with a single frequency, but pump light that consisted of two separate frequencies. Since reabsorption relies on the pump and scattered light being the same frequency, our original idea to mitigate the effects of it were to use two laser beams with different detunings. By using two different frequencies, it guarantees that not all the pump photons and scattered photons will be at the same frequency. In our original line of thinking, this mismatch would reduce the number of reabsorption events due to the inability of scattered photons associated with frequency #1 to couple to pump photons of frequency #2 (and vice versa) to drive reabsorption transitions. This reduction would in turn reduce the undesirable effects of reabsorption. Our first course of experiments searched for such a reduction by illuminating an ultracold cloud of atoms with pump light containing either one or two distinct frequency components and then measuring the resulting heating. Since the heat imparted is related to the amount of reabsorption, measuring the imparted heat allowed for the determination of alterations to reabsorption effects caused by alterations in the pump light. It was found that multiple-frequency pump light *was* able to measurably reduce the amount of reabsorption in the atom cloud.

However, additional experiments showed that the frequency modulation in and of itself was not sufficient to reduce reabsorption. Rather, the beams associated with the

different frequency components must create an interference pattern in space with a characteristic length scale smaller than the mean free path of the photons in the cloud. While this was contrary to our initial expectations, subsequent calculations (described below) confirmed that the reabsorption mitigation we used should exhibit this dependence. This dependence on a spatial interference pattern was observed by comparing two different data sets, one with an interference pattern and one without, in which an ultracold cloud of ^{85}Rb atoms was heated by laser light with two distinct frequency components.

In the following section of the chapter, the analytical calculations of the reabsorption rate are presented. These calculations show that both a spatial interference pattern and multiple distinct frequencies are necessary to suppress reabsorption. After these calculations have been described, our experimental data showing the suppression of reabsorption in a dense, ultracold atom cloud is presented. Our results match the behavior predicted by our calculations.

4.2 Reabsorption rate calculation.

A detailed calculation of the rate equation for the reabsorption process demonstrates how multiple frequencies incident upon a cloud can mitigate reabsorption and also explains why a spatial interference pattern having a characteristic length scale smaller than the mean free path of the photons in the cloud is also required to obtain reabsorption mitigation. The model of the two-photon reabsorption process we developed is one in which the pump light and the spontaneous emission light are treated semiclassically for a typical atom in the cloud. In the past, the theoretical treatment [6, 7, 8] of reabsorption occurred in a two-atom model where the probability of a spontaneous

photon emitted by one atom being absorbed by another formed the basis of the calculation. In our model we take into account the fact that the scattered light field as seen by an atom in the cloud consists of light originating from many different directions. This atom we call the “atom of interest”, and we calculated the reabsorption rate for this typical atom in the cloud. Hence, our model is inherently a multi- (rather than two-) atom model. This is important because interference effects in the scattered light explain our observed reabsorption reduction. Thus, an atom in the cloud is illuminated by the pump light from the lasers plus the collective spontaneous light emitted by all the other atoms in the cloud which are within about one mean free path of spontaneously emitted photons.

To describe the reabsorption, a calculation involving a “two-level” atom with only a ground and excited electron state is used. The pump and spontaneous emission light, for the case where the pump light consists of two frequencies (A and B, as shown in Figure 4.1(B)), are described by Rabi frequencies $\Omega_{1A(B)}$ and $\Omega_{2A(B)}$, respectively. The Rabi frequencies are defined as

$$\Omega_{1\alpha} = \frac{\mathbf{d} \cdot \mathbf{E}_{1\alpha}}{2\hbar} \quad (4.1)$$

$$\Omega_{2\alpha i} = \frac{\mathbf{d} \cdot \mathbf{E}_{2\alpha i}}{2\hbar} \quad (4.2)$$

where $\alpha=A,B$, \mathbf{d} is the atomic dipole moment and $\mathbf{E}_{1\alpha}$ is the electric field amplitude of the pump light associated with the α frequency component. $\mathbf{E}_{2\alpha i}$ is the electric field amplitude of the component of the spontaneous emission light emitted by the i^{th} atom that contributes to the total spontaneous emission light. To calculate the total light field from the spontaneous emission, a sum over all the atoms contributing to the transition will be

made, and in this way the total rate can be calculated. While equation 4.2 shows the spontaneous emission light from one atom, the full field ($\Omega_{2A(B)}$) is composed of the dipole radiation fields of many atoms in the cloud, as seen in the analysis in this section.

Figure 4.1 shows the dominant process of reabsorption that is the two photon Raman scattering which couples one ground electronic state ($|1\rangle$) to another ground electronic state ($|2\rangle$) with a different momentum state. The majority of the atoms that produce the scattered light that couples any two momentum states are located within about one photon mean-free path away from the atom receiving the radiation. An atom that is further away will not on average contribute to reabsorption since its scattered photon will be absorbed and reradiated before reaching the atom of interest, limiting the radius at which atoms in the cloud can contribute to the change in momentum of any given atom in the cloud. At the same time, however, the number of atoms in the cone-shaped volume of space from which spontaneous emission contributes to a particular change in momentum states increases with distance from the atom of interest. Essentially, while there is a maximum radius by which atoms in the cloud will stop significantly contributing to reabsorption effects for a particular atom, the number of atoms that provide spontaneously emitted light which couples to a particular change in momentum increases till this radius is reached. The interplay between these two factors results in most of the spontaneous emission light which drives any particular two-photon transition originating from atoms about one photon mean-free path away. While atoms within that path length contribute, due to the smaller number of atoms that volume they won't produce the majority of the spontaneous light as seen by the atom of interest.

The analysis in this calculation that follows shows that reabsorption reduction relies on not only multiple detunings of laser beams, but also on the presence of a spatial interference pattern. While the necessity of the spatial interference pattern is not obvious, we developed a general physical picture which demonstrates how the amount of reabsorption can be reduced with multiple pump light frequency components as long as these multiple components create a spatial interference pattern when combined. First, note that two-photon reabsorption involves a coherent transition between ground states; a pump photon and a scattered photon at the same frequency coherently couple two ground states with differing momentum. For a sufficiently large detuning between the two frequency components of the pump light (i.e., sufficiently large $\Delta_1 - \Delta_2$), the two-photon reabsorption transition would not appear likely to be driven by a combination of an $\Omega_{1A(B)}$ photon and an $\Omega_{2B(A)}$ photon since such a process would be off-resonant. Ensuring that not all the pump and scattered photons are of the same frequency would appear to deny the coherent scattering for some combinations of photons. Thus at first glance it might seem that using multiple frequency components, as opposed to a single component, could alone reduce the reabsorption rate for a fixed total intensity of light.

This initial supposition is not correct, however, because it does not take into account the response time of the atom's atomic dipoles, which for detunings larger than the natural linewidth is $\sim 1/\Delta$, or a few nanoseconds for the detunings used in our work. Because of this relatively rapid time scale, the atoms do not see separate frequency components, but rather see an instantaneous frequency that is an average of the multiple frequency components. Because of this, the reabsorption rates with a single or several

frequency components will be the same if the only alteration is simply increasing the number of frequency components in the pump light.

In order to reduce the reabsorption rate with multiple frequency components a spatial interference pattern between multiple frequency components can be used to disrupt the phase coherence of the two-photon reabsorption transition. Figure 4.2 illustrates the effect spatial interference patterns have on the reabsorption process. In the absence of a spatial interference pattern (Figure 4.2(A)), the overall amplitude of the light illuminating the cloud can vary with time. However, due to the rapid response of the atom's dipoles, the pump and spontaneous emission light will vary their amplitude in tandem, and the relative phase between the pump and spontaneous emission light at the location of any particular atom will remain constant in time. Thus the pump and spontaneous emission light are always at the same frequency and relative phase and thus drive coherent transitions to ground states with different momentum; this condition contains the full effects of reabsorption. Figures 4.2(B) and 4.2(C) illustrate how this changes when a spatial interference pattern is created through the overlap of the different frequency beams. With multiple frequency components, the bright and dark regions of the spatial interference will oscillate between maximum and minimum intensity at the beat frequencies between the frequency components. This causes the identity of the particular atoms that are responsible for producing spontaneous emission light to vary in time as well. Because the position of the atoms in the gas are random and the atoms are on average separated by more than one optical wavelength, the different optical path lengths between the atoms means that changing the particular atoms that contribute to spontaneous emission light also changes the phase of that light. This variation in the

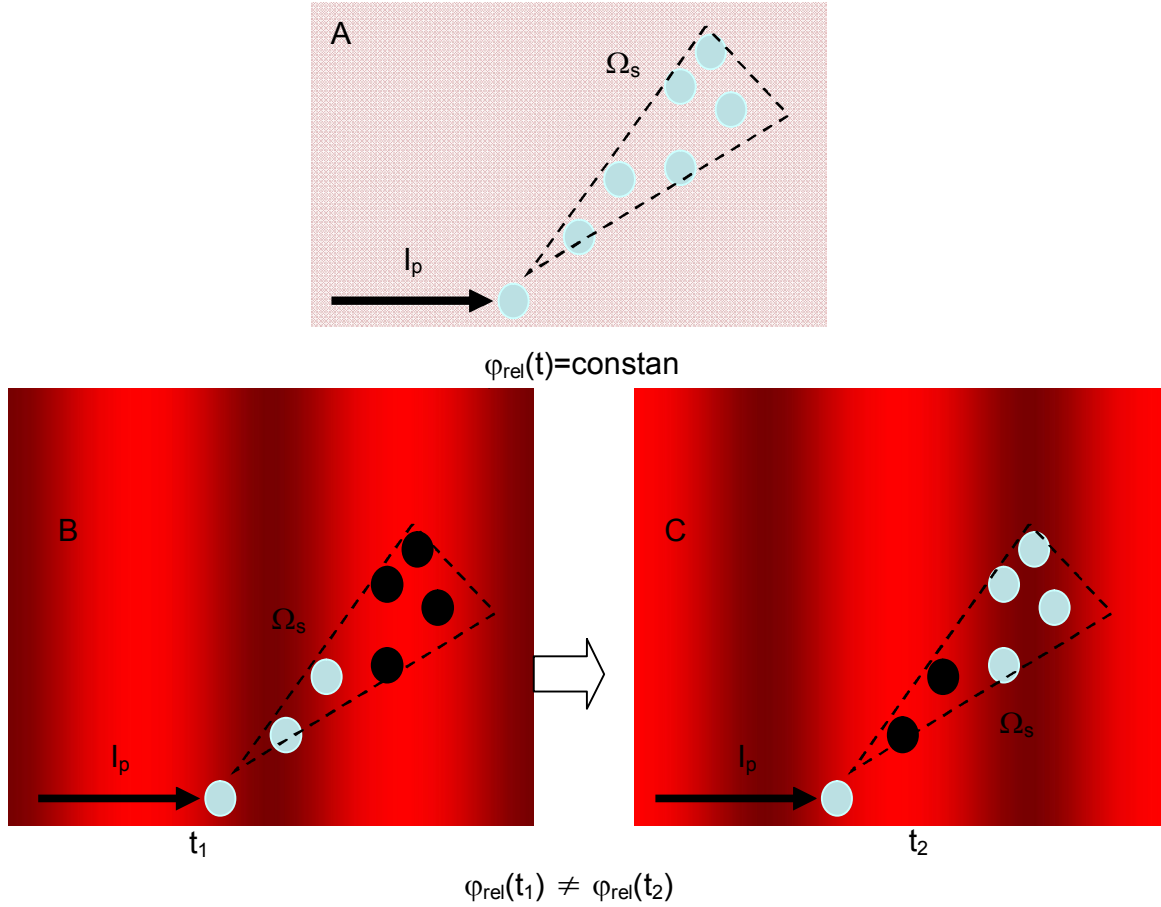


Figure 4.2: An atom's view of the spontaneous emission light in a cloud that contributes to a particular momentum state. I_p is the pump light and Ω_s indicates the sum of all of the spontaneous emission light that couples into the same set of momentum states like those shown in Figure 1. The meaning of the patterns shown in the different parts of the figure (A, B, and C) and the meaning of φ_{rel} are explained in text. In parts B and C the atoms which radiate are lightly shaded and the atoms which do not are darkly shaded.

phase can then cause disruption to the coherent Raman process which is responsible for reabsorption since the spatial interference pattern leads to a time variation in the phase of the spontaneous emission light. The time scale of this variation is given by the beat frequencies between the multiple frequency components of the pump light, and if these beat frequencies are greater than the effective transition rate between states (i.e. from $|1\rangle$ to $|2\rangle$ in Figure 1) of the reabsorption process, the spatial interference pattern induced phase variation disrupts the two-photon reabsorption process and thus reduces its rate.

In order to investigate this disruption in more detail, we calculate the two-photon reabsorption rate analytically. To perform the calculation we first write the time evolved wave function for the reabsorption process.

$$|\Psi(t)\rangle = C_1(t)|1, p_1\rangle + C_2(t)|2, p_2\rangle + C_3(t)|3, p_3\rangle \quad (4.3)$$

Where p_1, p_2 , and p_3 denote the different momenta for the three states. Then, starting with the Hamiltonian for the interaction of atomic states with multifrequency classical light fields, the rate equation for the reabsorption heating process can be calculated. The Hamiltonian for the system described in Figure 1 is

$$H = \begin{pmatrix} \frac{p_1^2}{2M} & 0 & 2\hbar\Omega_{1A} \cos(\omega_{1A}t) + 2\hbar\Omega_{1B} \cos[(\omega_{1B} + \beta_i)t + \Theta] \\ 0 & \frac{p_2^2}{2M} + \hbar\omega_{21} & 2\hbar\Omega_{2A} \cos(\omega_{1A}t + \Phi_i) + 2\hbar\Omega_{2B} \cos[(\omega_{1B} + \beta_i)t + \Phi_i + \Theta_i] \\ 2\hbar\Omega_{1A}^* \cos(\omega_{1A}t) + 2\hbar\Omega_{1B}^* \cos[(\omega_{1B} + \beta_i)t + \Theta] & 2\hbar\Omega_{2A}^* \cos(\omega_{1A}t + \Phi_i) + 2\hbar\Omega_{2B}^* \cos[(\omega_{1B} + \beta_i)t + \Phi_i + \Theta_i] & \frac{p_3^2}{2M} + \hbar\omega_{31} \end{pmatrix} \quad (4.4)$$

Θ is the phase difference between the Ω_{IA} and Ω_{IB} beams at the atom of interest. Φ_i accounts for the optical path length difference between the atom of interest and the i th scattering atom contributing to a specific momentum state. Θ_i' accounts for the phase difference between the Ω_A and Ω_B beams at the scattering atom. For instance, if we take two beams which co-propagate in the z direction, the propagation for both is $\exp[ikz]$, and the phase difference is nearly zero. Whereas counter-propagating beams would have one beam propagating with $\exp[ikz]$, and the other with $\exp[-ikz]$. Thus for this situation, the phase difference between the two would vary over the wavelength of the light. β_i is determined by a Doppler shift due to the velocity of the i th atom. Because Φ_i , Θ_i' , and β_i involve specific scattering atoms, these terms must be summed over the N atoms which contribute to the population transfer to a specific momentum state.

Since an atom will experience transitions to many momentum states other than the $|1\rangle$ state once it is in the $|2\rangle$ state, population does not build up in $|2\rangle$, and the evolution from $|1\rangle$ to $|2\rangle$ is governed by a rate equation. To calculate the rate equation a method similar to that presented in Moler *et al.*[12] was used to develop equations for $|1\rangle$ to $|2\rangle$ while adiabatically eliminating the excited state. The following change in variables was made in order to facilitate these calculations:

$$B_1(t) = C_1(t) \exp\left[i \frac{p_1^2}{2M\hbar} t\right] \quad (4.5)$$

$$B_2(t) = C_2(t) \exp\left[i \left(\frac{p_2^2}{2M\hbar} + \omega_{21} \right) t\right] \quad (4.6)$$

$$B_3(t) = C_3(t) \exp\left[i \left(\frac{p_3^2}{2M\hbar} + \omega_{31} \right) t\right] \quad (4.7)$$

The detuning of the A beam (Δ_A), the B beam (Δ_B), and the frequency shift between the two ground states (δ_i) are defined as

$$\Delta_A = \frac{p_3^2}{2M\hbar} + \omega_{31} - \frac{p_1^2}{2M\hbar} - \omega_{1A} \quad (4.8)$$

$$\Delta_B = \frac{p_3^2}{2M\hbar} + \omega_{31} - \frac{p_1^2}{2M\hbar} - \omega_{1B} \quad (4.9)$$

$$\delta_i = \frac{p_2^2}{2M\hbar} + \omega_{21} - \frac{p_1^2}{2M\hbar} - \beta_i \quad (4.10)$$

The β_i has been omitted from equations 4.8 and 4.9 since it is much smaller than the sum of the other terms in equations 4.8 and 4.9. Through the use of the time dependent Schrödinger's equation, the Hamiltonian found in equation 4.4, and the wave function, the time evolution of the B 's can be calculated. These time dependent B equations are

$$\dot{B}_1 = -2i\{\Omega_{1A} \cos(\omega_{1A}t) + \Omega_{1B} \cos[(\omega_{1B} + \beta_i)t + \Theta]\} \times B_3 \exp[-i(\Delta_A + \omega_{1A})t] \quad (4.11)$$

$$\begin{aligned} \dot{B}_2 = & -2i\{\Omega_{2A} \cos(\omega_{1A}t + \Phi_i) + \Omega_{2B} \cos[(\omega_{1B} + \beta_i)t + \Phi_i + \Theta'_i]\} \\ & \times B_3 \exp[-i(\Delta_B + \beta_i + \omega_{1B} - \delta_i)t] \end{aligned} \quad (4.12)$$

$$\begin{aligned} \dot{B}_3 = & -2i\{\Omega_{1A}^* \cos(\omega_{1A}t) + \Omega_{1B}^* \cos[(\omega_{1B} + \beta_i)t + \Theta]\} \times B_1 \exp[i(\Delta_A - \omega_{1A})t] \\ & - 2i\{\Omega_{2A}^* \cos(\omega_{1A}t + \Phi_i) + \Omega_{2B}^* \cos[(\omega_{1B} + \beta_i)t + \Phi_i + \Theta'_i]\} \\ & \times B_2 \exp[i(\Delta_B + \beta_i + \omega_{1B} - \delta_i)t] \end{aligned} \quad (4.13)$$

With the development of the \dot{B} equations, appropriate approximations can be utilized to solve for the B equations. The first approximation which is used was the rotating wave approximation. The cos terms found in equations 4.11-4.13 were expanded into their exponential forms. Any resulting exponential varying at optical frequencies (i.e. $\omega_{31} + \omega_{1A(B)}$) are eliminated. Next, an adiabatic elimination of the excited state is used to directly integrate \dot{B}_3 . In performing the adiabatic excited state elimination, it is assumed

the population in B_1 and B_2 vary slowly with time compared to the detunings Δ_A and Δ_B .

This allows us to treat B_1 and B_2 in equation for \dot{B}_3 as constants; allowing for the direct integration of equation 4.13. Solving for B_3 and substituting that into equations 4.11 and 4.12 yields an approximate set of equations for \dot{B}_1 and \dot{B}_2 .

$$\begin{aligned} \dot{B}_1 = & iB_1 \left(\frac{|\Omega_{1A}|^2}{\Delta_A} + \frac{|\Omega_{1B}|^2}{\Delta_B} \right) \\ & + iB_2 \left(\frac{\Omega_{1A}\Omega_{2A}^*}{\Delta_A - \delta_i} \exp[-i(\delta_i t + \Phi_i)] + \frac{\Omega_{1B}\Omega_{2B}^*}{\Delta_B - \delta_i} \exp[-i(\delta_i t - \Theta + \Phi_i + \Theta')] \right) \end{aligned} \quad (4.14)$$

$$\begin{aligned} \dot{B}_2 = & iB_1 \left(\frac{\Omega_{2A}\Omega_{1A}^*}{\Delta_A} \exp[i(\delta_i t + \Phi_i)] + \frac{\Omega_{2B}\Omega_{1B}^*}{\Delta_B} \exp[i(\delta_i t + \Phi_i + \Theta' - \Theta)] \right) \\ & + iB_2 \left(\frac{|\Omega_{2A}|^2}{\Delta_A - \delta_i} + \frac{|\Omega_{2B}|^2}{\Delta_B - \delta_i} \right) \end{aligned} \quad (4.15)$$

Terms which had included the beat frequency ($\Delta_A - \Delta_B$) in the exponentials were eliminated as these terms oscillate rapidly compared to the Rabi-flopping frequency and thus tend to average to zero in comparison. This is predicated on the beat frequency being significantly larger than the transition rate, as was the case in our experiments.

At this point in the development of the \dot{B} equations, the rate equation for the population in $|1\rangle$ and $|2\rangle$ needed to be developed. As noted above, the use of a rate equation is justified by the fact that there are several other states besides $|1\rangle - |3\rangle$ involved and so the Rabi-flopping from $|1\rangle$ back to $|2\rangle$ will be suppressed. And while the evaluation of the reabsorption process could be done through the use of optical Bloch equations from the beginning, the use of the B coefficients makes the application of the rotating wave approximation and adiabatic ground state elimination more transparent for

the development of a rate equation. A rate equation allows us to include these other states through a phenomenological decay rate. Additionally, the use of a rate equation facilitates the summation of the spontaneous emission light over multiple sources. As such, the following the treatment in [13] for the derivation of the rate equation for the population of state $|1\rangle$, ρ_{11} :

$$\dot{\rho}_{11} = \lambda_1 - \gamma_1 \rho_{11} - R[\rho_{11} - \rho_{22}] \quad (4.16)$$

A similar equation with the same rate term R applies for the population in $|2\rangle$, ρ_{22} . In this equation, R is the desired rate which needs to be calculated, the ρ 's are elements of the density matrix, and the γ is a phenomenological decay rate. λ_1 is the rate at which population is transferred into state $|1\rangle$ from one-photon and two-photon processes. In order to calculate these rate equations, the conversion to the density matrix elements is performed in the standard way, with the following transforms

$$\rho_{ab} = B_a^* B_b \Rightarrow \dot{\rho}_{ab} = \dot{B}_a^* B_b + B_a^* \dot{B}_b, \quad (4.17)$$

where $a, b=1, 2$. Note that unlike most standard treatments, here $|1\rangle$ and $|2\rangle$ are both electronic ground states of the atom with different momenta. From these definitions, we can construct the four time evolved density matrix elements (where a summation over the i atoms contributing to the spontaneous emission light is understood).

$$\begin{aligned} \dot{\rho}_{11} = & i\rho_{12} \left(\frac{\Omega_{1A}\Omega_{2A}^*}{\Delta_A} \exp[-i(\delta_i t + \Phi_i)] + \frac{\Omega_{1B}\Omega_{2B}^*}{\Delta_B} \exp[-i(\delta_i t + \Phi_i + \Theta'_i - \Theta)] \right) \\ & - i\rho_{21} \left(\frac{\Omega_{1A}^*\Omega_{2A}}{\Delta_A} \exp[i(\delta_i t + \Phi_i)] + \frac{\Omega_{1B}^*\Omega_{2B}}{\Delta_B} \exp[i(\delta_i t + \Phi_i + \Theta'_i - \Theta)] \right) \end{aligned} \quad (4.18)$$

$$\begin{aligned} \dot{\rho}_{12} = & i \left(\frac{|\Omega_{2A}|^2}{\Delta_A} + \frac{|\Omega_{2B}|^2}{\Delta_B} - \frac{|\Omega_{1A}|^2}{\Delta_A} - \frac{|\Omega_{1B}|^2}{\Delta_B} \right) \rho_{12} \\ & + i \left(\frac{\Omega_{1A}^* \Omega_{2A}}{\Delta_A} \exp[i(\delta_i t + \Phi_i)] + \frac{\Omega_{1B}^* \Omega_{2B}}{\Delta_B} \exp[i(\delta_i t + \Phi_i + \Theta'_i - \Theta)] \right) (\rho_{11} - \rho_{22}) \end{aligned} \quad (4.19)$$

$$\begin{aligned} \dot{\rho}_{21} = & i \left(\frac{|\Omega_{1A}|^2}{\Delta_A} + \frac{|\Omega_{1B}|^2}{\Delta_B} - \frac{|\Omega_{2A}|^2}{\Delta_A} - \frac{|\Omega_{2B}|^2}{\Delta_B} \right) \rho_{21} \\ & + i \left(\frac{\Omega_{1A} \Omega_{2A}^*}{\Delta_A} \exp[-i(\delta_i t + \Phi_i)] + \frac{\Omega_{1B} \Omega_{2B}^*}{\Delta_B} \exp[-i(\delta_i t + \Phi_i + \Theta'_i - \Theta)] \right) (\rho_{22} - \rho_{11}) \end{aligned} \quad (4.20)$$

$$\begin{aligned} \dot{\rho}_{22} = & i \rho_{21} \left(\frac{\Omega_{2A} \Omega_{1A}^*}{\Delta_A} \exp[i(\delta_i t + \Phi_i)] + \frac{\Omega_{2B} \Omega_{1B}^*}{\Delta_B} \exp[i(\delta_i t + \Phi_i + \Theta'_i - \Theta)] \right) \\ & - i \rho_{12} \left(\frac{\Omega_{1A} \Omega_{2A}^*}{\Delta_A} \exp[-i(\delta_i t + \Phi_i)] + \frac{\Omega_{1B} \Omega_{2B}^*}{\Delta_B} \exp[-i(\delta_i t + \Phi_i + \Theta'_i - \Theta)] \right) \end{aligned} \quad (4.21)$$

Equations 4.18-4.21 are calculated directly from the definition of the time evolved density matrix elements given in equation 4.17. To find the desired rate equation, these equations need to be put into the form given by equation 4.16. Only one of the time evolved density matrix elements needs to be solved in this manner as the rate, R , will be the same regardless. To solve for $\dot{\rho}_{11}$ the off-diagonal density matrix elements were integrated in a steady-state approximation which yields a solution,

$$\dot{\rho}_{11} = -2 \left[\begin{aligned} & \frac{\Omega_{1A}^2 \Omega_{2A}^2}{\Delta_A^2} \left(\gamma \cos(\Phi_i - \Phi_j + (\delta_i - \delta_j)t) + \delta_i \sin(\Phi_i - \Phi_j + (\delta_i - \delta_j)t) \right) \\ & + \frac{\Omega_{1B}^2 \Omega_{2B}^2}{\Delta_B^2} \left(\gamma \cos(\Phi_i - \Phi_j + \Theta'_i - \Theta'_j + (\delta_i - \delta_j)t) \right. \\ & \quad \left. + \delta_i \sin(\Phi_i - \Phi_j + \Theta'_i - \Theta'_j + (\delta_i - \delta_j)t) \right) \\ & + \frac{\Omega_{1A} \Omega_{2A} \Omega_{1B} \Omega_{2B}}{\Delta_A \Delta_B} \left(\begin{aligned} & \gamma \cos(\Phi_i - \Phi_j + \Theta'_i - \Theta' + (\delta_i - \delta_j)t) \\ & + \gamma \cos(\Phi_i - \Phi_j - \Theta'_i + \Theta' + (\delta_i - \delta_j)t) \\ & + \delta_i \sin(\Phi_i - \Phi_j + \Theta'_i - \Theta' + (\delta_i - \delta_j)t) \\ & + \delta_i \sin(\Phi_i - \Phi_j - \Theta'_i + \Theta' + (\delta_i - \delta_j)t) \end{aligned} \right) \end{aligned} \right] \times \frac{\rho_{11} - \rho_{22}}{\gamma^2 + \delta_i^2} \quad (4.22)$$

The i, j indices which appear in equation 4.22 are each summed from 1 to N and account for multiple atoms contributing to a reabsorption transition. In the derivation the effectively small AC Stark shift was ignored and the phenomenological decay constant γ was added. Also note that in the derivation of 4.22, the Ω 's were defined as real numbers. In doing so, the time evolution in the population of $|1\rangle$ can be determined. The full form of $\dot{\rho}_{11}$ derived in equation 4.22 has the same form as equation 4.16, allowing for the extraction of a rate constant, R . It is necessary to sum over all i, j for the N atoms whose spontaneous emission in the proper direction contributes to the $|1\rangle$ to $|2\rangle$ transition. However, since the position of the atoms in the cloud is random, the phase (Φ_i) due to the optical path length difference varies randomly as well and most of the i, j terms will average to zero. The only contribution that will contribute after the averaging is when $i = j$. Keeping only the $i = j$ terms, the rate equation determined from equation 4.22 for the reabsorption process is given by

$$R = \sum_i^N \frac{2\gamma}{\gamma^2 + \delta_i^2} \left(\frac{\Omega_{1A}^2 \Omega_{2A}^2}{\Delta_A^2} + \frac{\Omega_{1B}^2 \Omega_{2B}^2}{\Delta_B^2} + \frac{2\Omega_{1A} \Omega_{2A} \Omega_{1B} \Omega_{2B}}{\Delta_A \Delta_B} \cos(\Theta'_i - \Theta) \right) \quad (4.23)$$

The $(\Omega_{1A}^2 \Omega_{2A}^2) / \Delta_A^2$ term in the sum is proportional to I_A^2 , where I_A is the intensity of the pump light at frequency A. Looking at just the first term, when the sum over the N atoms is performed, this term results in a rate that is proportional to I_A^2 multiplied by a factor related to the thermal distribution of velocities in the ultracold gas that comes from the sum over $\gamma / (\gamma^2 + \delta_i^2)$ coefficient. Likewise the second term in the parenthesis is a rate proportional to I_B^2 , where like before I_B is the intensity of the pump light at frequency B. The final cosine term has a magnitude proportional to $I_A I_B$. The dependence of the reabsorption rate on the presence of a spatial interference pattern is contained in the last term of equation 4.23. In the absence of any interference pattern, Θ'_i is equal to Θ for all i and the last term will contribute maximally to the reabsorption rate. With the presence of a rapidly varying interference pattern, $\Theta'_i - \Theta$ will vary rapidly and the last term will average to zero over all of the atoms in the cloud and not contribute to the overall reabsorption rate.

This predicted rate equation suggests that as long as a spatial interference pattern exists whose length scale is smaller than the photon mean-free path length in the cloud, the reabsorption rate is reduced due to a phase disruption of the reabsorption process. By measuring the heat imparted by reabsorption with single frequency component pump light with no spatial interference pattern, and multiple frequency component pump light with a spatial interference pattern, it is possible to test the predicted reduction in reabsorption rate in equation 4.23. To characterize these changes, a quantity called the “heat per unit of intensity flux” is defined which has units of $\mu\text{K}/(\text{J}/\text{m}^2)$. This allows for

the direct comparison of the amount of heat imparted under a variety of different conditions into the cloud for different experimental configurations.

4.3 Measurement of the reabsorption reduction.

To look at the two-photon reabsorption process, we examined the effects of introducing light into the cloud in different ways. The basic premise of most of the investigations was to examine two different ways that one can double the intensity of light on the cloud: one may either double the intensity of a single beam or add a second beam with the same intensity as the first. The data presented in this chapter is of a comparative nature, looking at the heat imparted into a cloud by a single frequency component whose intensity has been doubled versus adding two equal intensity beams with different frequencies and either inducing a spatial interference pattern between them or not. Equation 4.23 predicts that under the condition of multiple frequency components with sufficiently large beat frequencies and the presence of a spatial interference pattern between these components, the effects of reabsorption should be mitigated and the heat imparted into the cloud should be proportional to $I_A^2 + I_B^2$. However, under the full effects of reabsorption, equation 4.23 predicts that the heat imparted into the cloud will be proportional to $(I_A + I_B)^2$ (I_A and I_B are the intensities of the first and second beam illuminating the cloud). Methods which reduce the amount of reabsorption will show a marked decrease in heat imparted into the cloud, thus the comparative method of looking at our data makes it clear as to when we have observed mitigation of the reabsorption process. This comparative method of analyzing the data has the benefits of not needing any specific model of the radiation trapping in the cloud as the comparisons of data sets

occur under nearly identical cloud density, optical depth, number, and temperature conditions.

4.3.1 The experimental set up. To test the effect of multiple frequency component pump light on reabsorption, ^{85}Rb atoms were first prepared in a Magneto-Optical-Trap (MOT) as described in chapter 2 using standard techniques [14]. The reabsorption experiments utilized only one species of Rb (^{85}Rb) in a MOT (all other experiments reported in this thesis utilize an optical dipole trap). For this experiment, a typical experimental cycle first involved the MOT being loaded with atoms. The typical load detuning for the MOT was ~ 10 MHz to the red of the ^{85}Rb cycling transition (trapping laser in figure 2.1; $5S_{1/2} F=3 \Rightarrow 5P_{3/2} F=4$). After the atoms are loaded into the MOT, there was a 15 ms Compressed MOT (CMOT) stage [15]. The CMOT is a MOT in which the detuning of the cooling lasers is increased to decrease radiative pressure caused by multiple photon scatterings in optically dense ultracold gas clouds. This drop in repulsive radiative pressure leads to a compression of the MOT size. The detuning for the CMOT stage was 15 MHz to the red of the ^{85}Rb cycling transition. After the CMOT stage was complete, the atom cloud underwent a 3 ms optical molasses. In an optical molasses, the magnetic field gradient of the MOT is turned off and the atoms are allowed to expand and cool. The detuning was also further increased from the CMOT stage, to ~ 40 MHz to the red of the ^{85}Rb cycling transition. The lack of magnetic field and large detuning allow the atoms to cool even further than they would in the MOT itself. At this point, the atom cloud had temperatures between 15 μK to 30 μK with a peak on-resonant optical depth (OD) (see equation 3.8) of approximately 10 and atom numbers of about 100 million. The atom cloud had a density of $9(4)\times 10^9 \text{ cm}^{-3}$. The cooling light was then

shut off and 1 ms later the cloud was heated by one or more laser beam pulses. An acoustic optical modulator (AOM) controlled the heating pulses, with typical pulse lengths of 40-1600 μs . Most of the time, the heat pulses were set to be in the range of 40-60 MHz blue detuned of the ^{85}Rb cycling transition, though a wide variety of detunings were investigated, including red detuning.

After the heating pulse, the atoms underwent an 18 ms free expansion before finally being imaged via absorption imaging. The expansion of the cloud is related to temperature of the cloud, the hotter the cloud the faster the expansion. The measured widths are related to the temperature of the cloud by

$$\sigma_i^2(t) = \sigma_i^2(t=0)(1 + v_{rms}^2 t^2), \quad (4.24)$$

$$v_{rms} = \sqrt{\frac{k_b T}{m}}. \quad (4.25)$$

Where $i=x, y$, since only 2 directions can be imaged (for instance, if the probe beam is propagated along the z-axis, the z-dimension of the cloud is not imaged), m is the mass of the atom, v_{rms} is the rms velocity of the atoms in the cloud, and can be calculated from the temperature of the atoms (see equation 4.25) or by taking measurements at different expansion times. A measurement of the cloud size with two different expansion times allows us to fully constrain the variables in equation 4.24, and thus $\sigma_i^2(t=0)$ and v_{rms} can be determined from these measurements.

As data was taken in a comparative manner, images with heating pulses are compared to images without heating pulses. The difference in the size of the cloud after expansion can be attributed to the heat induced into the cloud by the heating pulses. Thus for various heating pulse configurations, the amount of heat introduced into the cloud by

them can be calculated and compared to each other. Methods which mitigate reabsorption effects will show smaller expansion sizes. Thus, from the size of the cloud after expansion, the kinetic energy increase of the atoms due to the heating pulses was determined. We imaged the cloud along the same axis that the heating beams were applied. This was done to ensure insensitivity to any changes in the center-of-mass motion. Even when multiple beams were used to heat the cloud, care was taken to make sure that the beam alignment did not result in significant center-of-mass motion of the cloud in any direction orthogonal to the imaging axis. Our beams were overlapped to be in the same direction to better than 20 mrad. This is sufficient to avoid any apparent heating due to misalignment since to first order a center-of-mass motion does not effect the temperature measurement. Changes in the amount of reabsorption manifested themselves as a change in the amount of heat (kinetic energy) imparted by the heating pulses. The beat frequency between the two separate frequency components in multiple frequency heat pulses was always selected to be fast enough that any mechanical effects of the light on the atoms' motion was negligible.

As mentioned above, for most of the data taken for this experiment, heating pulses with blue detunings were used. This was done as a precaution since red detuned laser beams at the 40-60 MHz detunings (convenient for these measurements) result in a significant number of off-resonant non-cycling transitions, driving atoms to the lower hyperfine state. To ensure that population would not accumulate in the lower hyperfine state for any significant amount of time, a strong hyperfine repump laser (Hyperfine Repump in Figure 2.1; $5S_{1/2} F=2 \Rightarrow 5P_{1/2} F=3$) was kept on at all times during the course of the measurements. With this repump present, simple estimates indicated that there

should be little effect of any hyperfine pumping on our results. Additionally, we never observed significant differences between the reabsorption reduction of red and blue detuned light, and the reabsorption reduction did not seem to be sensitive to changes in the hyperfine repump light. Still, since the blue detunings reduced the required hyperfine pumping rate by typically an order of magnitude, blue detunings were the ones primarily used.

The reabsorption data presented in this thesis is presented in terms of “heat per unit of intensity flux”. As stated in the previous section, this unit allows for the direct comparison of the amount of heat imparted under different experimental conditions. Heat imparted to the cloud in the absence of saturation goes as

$$C_1 I \Delta t + C_2 I^2 \Delta t . \quad (4.26)$$

Where C_1 is a coefficient of one-photon scattering, C_2 is a coefficient of two-photon scattering, I is the total intensity of the beam, and Δt is the pulse length. Heat per unit of intensity flux (H/IF) is defined as

$$H / IF = C_1 + C_2 I . \quad (4.27)$$

This quantity is merely the heat (i.e. temperature increase) imparted into the cloud divided by $I \Delta t$. Through the course of these experiments, either one laser or two lasers were used to provide the heating pulses for the clouds. The exact set up of the lasers is discussed in more detail in section 4.4, the results of the experiment. For single laser experiments, an AOM with multiple RF signals (multiplexing) was used to produce the two beams of different frequency. Whereas the experiments with two lasers only used AOMs to control pulse length time and not for multiplexing.

4.4 Experimental Results

In the first set of experiments, a single laser was used to create two separate heating pulses. This was accomplished by sending two radio frequencies to an AOM which produced two deflected, non-overlapped beams separated in frequency by 10 MHz. These two beams were separated and then subsequently overlapped in a non-polarizing beam splitting cube and then directed into the chamber to illuminate the atoms. Figure 4.3 shows a simple schematic for the layout of this experiment along with the detunings of each beam used for this experiment. 40 μ s pulses were used to heat the cloud under four different conditions. For reference, the two beams coming out of the AOM are referred to as laser beam A and laser beam B, and are labeled as such in the figure 4.3. The conditions which establish the upper bounds of the reabsorption-induced heating are two of the conditions; laser beam A at I_A , and laser beam B at I_B . These are the two data points on the right side in figure 4.3. These two data points show the heat per unit of intensity flux for the full effects of reabsorption for each individual laser. The test condition, to see if the effects of reabsorption were affected, was laser beam A at $I_A/2$ and laser beam B at $I_B/2$ applied to the cloud simultaneously (labeled simultaneous in figure 4.3). Since $I_B \sim I_A$ where I_A and I_B refer to the two AOM deflected beams, all three of these conditions had roughly the same intensity. Any reduction in reabsorption would be expected to result in the simultaneous data imparting less heat to the cloud than the full intensity conditions. While the intensities of the two beams were roughly the same, figure 4.3 does show a difference in the heat per unit of intensity flux between the data points for full I_A and I_B . The slight difference between beams A and B at full intensity was due to the fact that drifts in the atom number over the course of several hours could

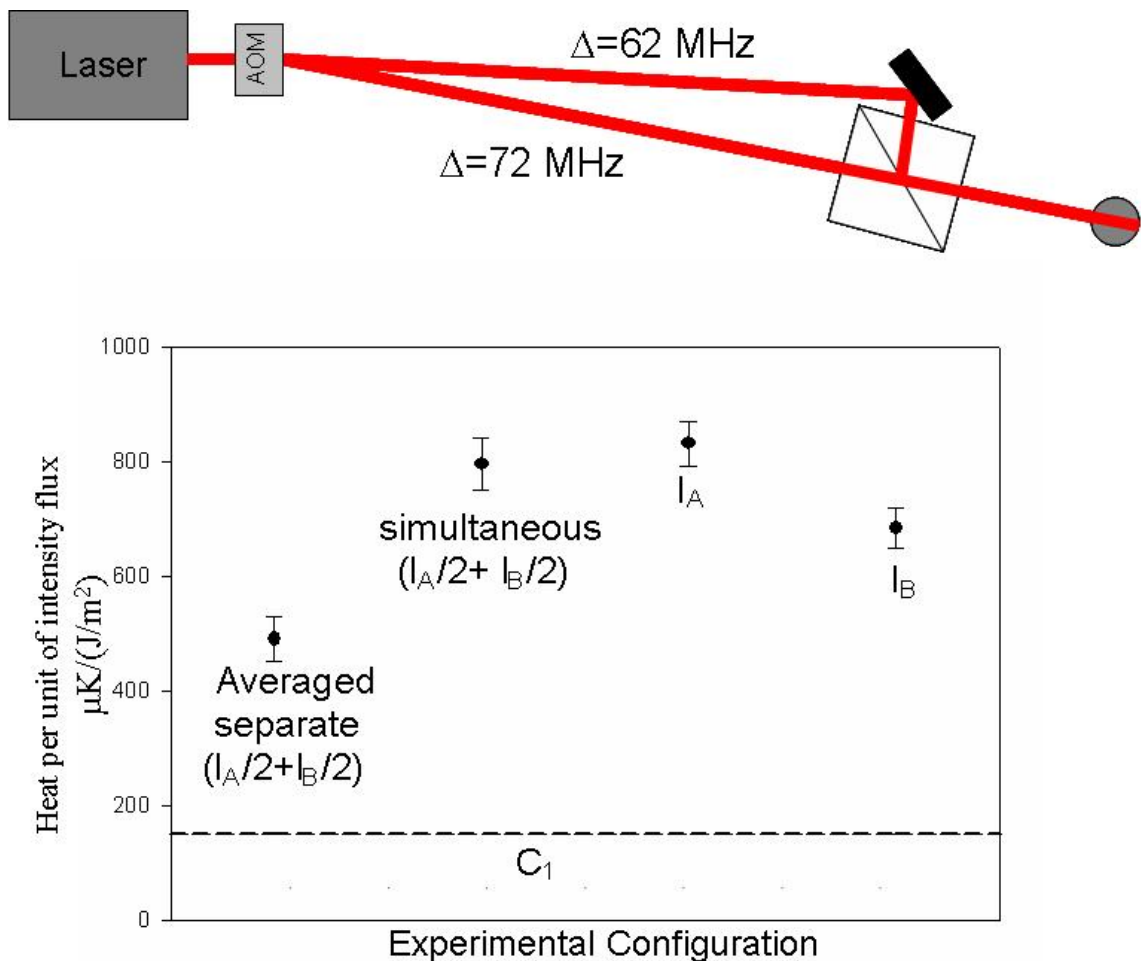


Figure 4.3 Heat per unit of intensity flux vs. experimental configuration for a single laser/multiplexed AOM experiment. No spatial phase pattern is present in this experimental setup. The two beams were detuned 62 MHz and 72 MHz to the blue of the ^{85}Rb cycling transition. Initial temperature of the cloud was 27 μK . At full intensity, $I/I_{\text{sat}} = 8$. The dotted line in this and subsequent figures shows the heat per unit intensity flux for single-photon reabsorption (i.e., the heat per unit intensity flux in the limit of zero intensity). Conditions are labeled and show no difference between two $I/2$ beams illuminating the cloud simultaneously and one beam at I .

chance the optical depth of the cloud. This in turn changed that amount of heat imparted from reabsorption, but does not impact our conclusions. The fourth condition was an average of laser beam A alone at $I_A/2$ and laser beam B alone at $I_B/2$, called the averaged separate data. Since these data were taken at lower intensity, there is expected to be less reabsorption and hence less heat per unit of intensity flux. The averaged separate data represents a lower limit to the amount of reduction in reabsorption which could be realized. Data were taken with a variety of intensities, detunings, atom number, and pulse lengths. The results shown in figure 4.3 are those of a typical experiment. The error bars displayed in this and other data figures in this chapter represent the statistical uncertainty associated with each data point. Since for this measurement the beams originated from the same laser and were co-propagated, there is not a spatial interference pattern present which fulfills the conditions of equation 4.23. Looking at figure 4.3, the heat per unit intensity flux for the simultaneous data is consistent with that imparted in both the full intensity cases. Thus with this configuration, even with two different frequencies of light illuminating the cloud, the atom cloud experiences the full effects of reabsorption.

The second set of experiments used two different lasers (still called laser A and laser B) to illuminate the atoms. As in the first set of experiments, the beams were co-propagated and used to simultaneously apply heat to the cloud. This experiment had the same four experimental conditions as the first experiment. Since separate lasers were used to make the two different laser beams this time, the separate beams had different phase and amplitude spatial profiles, and so overlapping the beams produced a spatial interference pattern. The heating pulses had a 1.5 mm spot size and had an intensity of

I/I_{sat} of about 40 at full intensity. Figure 4.4 show a simple schematic for the laser layout used in the second experiment along with a sample set of data. While figure 4.4 has only a sample set of data, the same general trends were observed in all data sets. In all cases, simultaneous data showed a statistically significant reduction in the heat per unit intensity flux as compared to single-component data taken at the same total intensity. Similar data like those presented in figure 4.4 were taken over a wide range of intensities and detunings with similar results being observed. Additionally, the relatively high I/I_{sat} of 40 for our system allowed us to make measurements with a high degree of signal-to-noise ratio, but is high enough that there are likely some saturation effects in the data presented in figure 4.4. It was found, however, that the degree of saturation was dependent on the initial conditions in the cloud (e.g., initial temperature) and that for the case of the data presented in figure 4.4 the saturations effects were not significant on the scale of the statistical uncertainties shown in the figure. In any case, tests at lower intensities indicated the same general trends. That is, the presence of the spatial interference pattern with beams of different detunings can reduce the effects of reabsorption as predicted by equation 4.23.

While this two-separate-laser data demonstrated that the amount of reabsorption could be reduced for a fixed total intensity by using multiple frequency components with a spatial interference pattern, the intensity pattern that was created relied on the poor spatial beam quality of the two diode lasers used. To further confirm the predictions in a more controlled way, the two-frequency AOM experiments were revisited. However, unlike the previous experiments which co-propagating beams, this time the heating pulses were made to be counter-propagating, resulting in an interference pattern. This

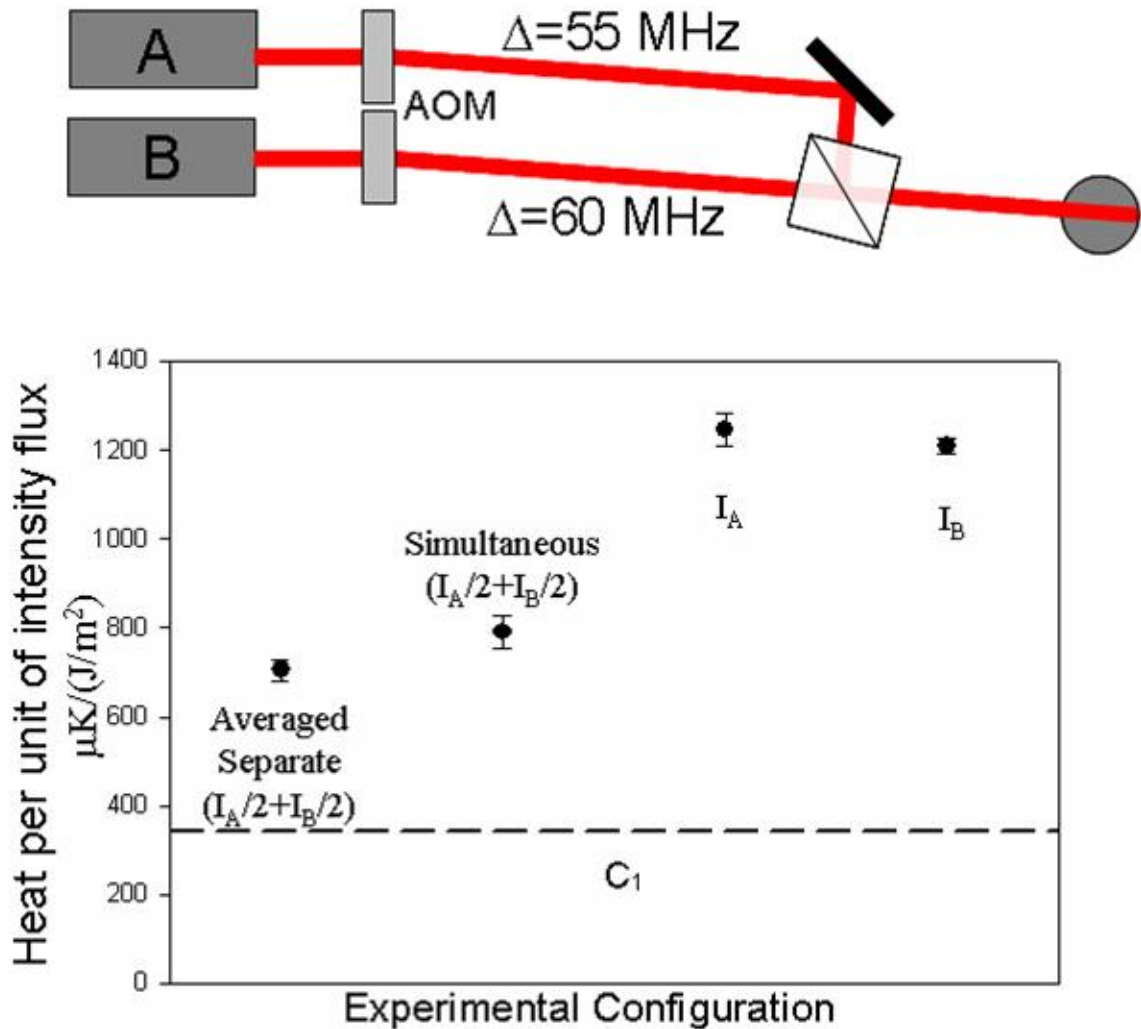


Figure 4.4 Heat per unit of intensity flux versus experimental configuration for a two laser experiment. A spatial interference pattern is present in this experimental setup. For this set of data, the two lasers were detuned 55 and 60 MHz to the blue of the ^{85}Rb cycling transition. The initial temperature of the cloud was 22 μK . Conditions are labeled and clearly show a difference between the two $I/2$ beams illuminating the cloud simultaneously and one beam at full intensity, I . This indicates that with the difference in frequency and spatial interference pattern, effects of reabsorption can be mitigated.

interference pattern meets all the necessary conditions for reabsorption mitigation contained in the model developed in this chapter. Figure 4.5 has a simple schematic showing the laser layout for this experiment and also shows the results for one of these experiments, which unlike previous figures, plots heat per unit of intensity flux vs. I/I_{sat} . The circles are the data for the heat per unit intensity flux for each of the full intensity beams averaged together; thus this marks the full effects of reabsorption. The squares are the data for the simultaneous, counter-propagating half-intensity beams. Again, the data are presented in a comparative manner in which the averaged, full reabsorption data can be directly compared to that of the counter-propagating half-intensity beams at twice the I/I_{sat} . The black arrows present in figure 4.5 were added to explicitly show the comparisons being made. The mitigation of reabsorption is demonstrated in the heat per unit intensity flux being the same within the uncertainty for the full intensity beams (circles) as it is for the counter-propagating beams (squares) at twice the intensity. That is to say, for example, the heat per unit of intensity flux for the counter-propagating beams at an I/I_{sat} of 10 is the same as it is for the single, full intensity beam at an I/I_{sat} of 5. Thus this experiment shows that implementing heating beams with a rapidly varying spatial interference pattern allows one to nearly double the intensity of the heating beams without increasing the heat per unit intensity flux. These results are consistent with predictions made in equation 4.23.

At the intensities of $I/I_{sat} = 40$ and higher for the data in figure 5, there was noticeable saturation effects which became apparent. The observed saturation in the heat per unit flux was present in both single- and multiple-beam configurations. However, such saturation is expected to occur in these systems. At high intensities, a significant

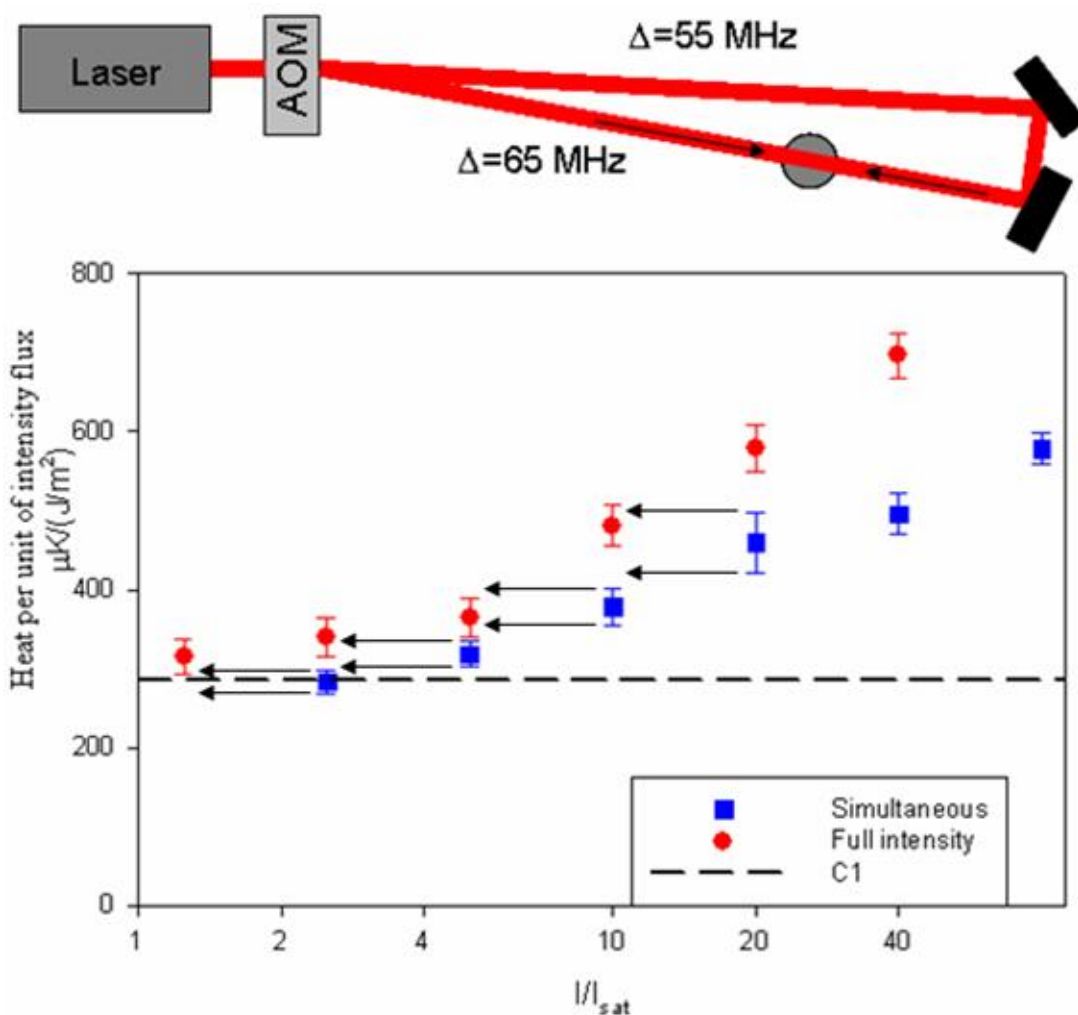


Figure 4.5 Heat per unity of intensity flux verses intensity for the single laser, counter-propagating experiment; detuned 55 MHz and 65 MHz to the blue of the ^{85}Rb cycling transition. The initial temperature of the cloud was 25 μK . Circles are for the single beam at full intensity while the squares are the two simultaneously counter-propagating beams each at half intensity. Saturation effects prevent data above $I/I_{sat} = 40$ from being compared. Black arrows are for comparison purposes, showing that for the same amount of heat per unit intensity flux, the overall intensity of the simultaneous beams needed to be twice that of the full intensity, marking a decrease of about half in the effects of reabsorption.

fraction of the atom population is in the excited state. This reduces the optical depth of the cloud for both one- and two-photon processes. Furthermore, a large intensity also corresponds to a large value of γ (phenomenological decay constant) in equation 4.23. For a sufficiently large value of γ , R is no longer proportional to I^2 , but becomes proportional to just I , and thus the heat per unit of intensity flux saturates to a constant [6]. It was found that the onset of saturation was dependent upon the initial density and temperature of the atom cloud.

4.4.1 Experimental conclusions. A possible explanation for the data not related to the suppression of reabsorption effects in ultracold gases could have come through the Mollow triplet, and thus the effects the Mollow triplet could have in the mitigation of reabsorption was investigated [16]. However, upon investigation of the Mollow triplet for our experimental configurations, we found that the total incoherent portion of the spectrum is relatively small. Even at the relatively high $I/I_{sat} = 40$ used in these experiments, the incoherent spectrum has only a few percent of the light on resonance. As such, the contribution to reabsorption from radiation trapping of the on-resonant fluorescent component is expected to be small. Furthermore, if the Mollow triplet played a major role in reabsorption, there should be relatively little difference between the co-propagating and counter-propagating tests. However, during the course of the experiments it was found that the effects of reabsorption relied heavily on the difference between the two cases, and in fact the theory developed in this chapter predicts that there should be a difference between the two cases. This suggests that the on-resonant component of the fluorescence is not a major factor in the reabsorption process. There have been investigations in which the reabsorption of the incoherent Mollow triplet

radiation was believed to have played a larger role [8,9]. However, in those cases the optical depth of the atom clouds were significantly higher than in the work presented in this thesis. It is possible for the Mollow triplet to contribute to the difference in saturation between single and multiple frequency light present in our data at high I/I_{sat} , since having multiple frequencies will reduce the amount of on-resonant light due to the incoherent part of the scattering being spread out over a greater number of frequencies. However, for the conditions for these experiments, it is concluded that the Mollow triplet does not heavily contribute to the reabsorption process.

The semiclassical model of reabsorption predicts that the reduction in two-photon reabsorption scales linearly with the number of beams that have sufficient spatial and frequency variation from one another. Therefore it should be possible to reduce the reabsorption beyond the factor of 2 demonstrated in this work by creating additional frequency components with an AOM, separating the components, and then either deliberately altering the phase of their beam profiles relative to one another or sending them into the atom cloud at sufficiently different propagation directions. The system used to measure the reduction of a factor of two had limitations which prevented such a test from being conducted in a practical manner, since the use of a free space MOT requires the heat beam path and imaging path to be the same in order to avoid problematic center-of-mass motion. This limits the propagation directions and prevents the insertion of optics into the heat beam path.

Some work was conducted with diffusers which can be used to scramble phase of the incident laser beam wavefront. These diffusers amount to a piece of poor quality glass whose thickness varies by several optical wavelengths across the surface. While it

would be theoretically possible to use diffusers to ensure that the wavefront phase between the two AOM beams was uncorrelated, it was found to be too impractical. Once diffused, the heating laser could not be collimated so as to be propagated into the chamber. If one wished to use diffusers, they would have to be mounted somewhere close to the atom cloud itself since collimation is not possible afterwards.

The measurements described in this chapter could potentially be improved through the use of a different trap, such as a far off resonant optical trap (FORT) instead of a free space MOT. With a trap such as a FORT, the restrictions which come with the free space MOT requiring the heating beams to be directed along the path of the imaging beam are removed allowing heat beams from multiple directions to be used. In particular, more than two heating beams could be used to see if the reabsorption could be mitigated by more than a factor of 2.

The experiments presented in this chapter have successfully demonstrated the mitigation of reabsorption using beam modulation techniques. The results are explained by a semiclassical model which indicates that the physics of multiple light scatterers in a random gas medium must be considered in order to understand the mechanics and effects of the reabsorption process. Understanding the reabsorption process will allow current optical pumping techniques to be modified, which should increase the efficiency of optical pumping schemes and promises to improve the lowest temperatures that can be achieved in optically thick gases using laser cooling techniques.

References for Chapter 4

¹ D. J. Han, M. T. DePue, and D. S. Weiss, Phys Rev. A **63**, 023405 (2001).

² V. Vuletic, C. Chin, A. J. Kerman, and S. Chu, Phys. Rev. Lett. **81**, 5768 (1998).

³ H. Perrin *et al.*, Europhys. Lett. **46**, 141 (1999).

⁴ A. J. Kerman, V. Vuletic, C. Chin, and S. Chu, Phys. Rev. Lett. **84**, 439 (2000).

-
- ⁵ D. Boiron, A. Michaud, A. Lemonde, Y. Castin, C. Salomon, S. Weyers, K. Szymaniec, L. Cognet, and A. Clairon, *Phys. Rev. A* **53**, R3734 (1996).
- ⁶ Y. Castin, J. I. Cirac, and M. Lewenstein, *Phys. Rev. Lett.* **80**, 5305 (1998)
- ⁷ J.I Cirac, M. Lewenstein, and P. Zollar, *Europhys. Lett.* **35**, 647 (1996)
- ⁸ S. Wolf, S. J. Oliver, and D. S. Weiss, *Phys. Rev. Lett.* **85**, 4249 (2000)
- ⁹ M. Vengalattore, W. Rooijakkers, R. Conroy, and M. Prentiss, *Phys. Rev. A* **67**, 063412 (2003)
- ¹⁰ L. Santos, F. Floegel, T. Afair, and M. Lewenstein, *Phys. Rev. A* **63**, 063408 (2001)
- ¹¹ A. Fioretti *et al.*, *Opt. Commun.* **149**, 415 (1997)
- ¹² K. Moler, D. S. Weiss, M. Kasevich, and S. Chu, *Phys. Rev. A* **45**, 342 (1992)
- ¹³ P. Meystre and M. Sargent III, *Elements of Quantum Optics*, 2nd ed. (Springer-Verlag, New York, 1991).
- ¹⁴ E.L Raab, M. Prentiss, A. Cable, S. Chu, and D. . Pritchard, *Phys. Rev. Lett.* **59**, 2631 (1987)
- ¹⁵ W. Petrich *et al.*, *J. Opt. Soc. Am. B* **11**, 1332 (1994)
- ¹⁶ B. R. Mollow *et al.*, *Phys. Rev.* **188**, 1969 (1969)

Chapter 5

Homonuclear Loading Measurements and Optimizations of the Loading of a Far Off Resonant Optical Trap.

In chapter 2.2, the basic physics of a Far Off Resonant Trap (FORT) was discussed. Equation 2.16 describes the evolution of the number of atoms trapped in the FORT when loading the FORT from a MOT with only one type of atom present. Equation 2.17 describes the number of atoms trapped when more than one type of atom (e.g. ^{85}Rb and ^{87}Rb) is being loaded into the FORT simultaneously. Atoms load into the FORT with some rate ($R(t)$) and are lost from the trap through collisions (primarily light-assisted collision) given by the two-body loss coefficient (β). The goal of most FORT load procedures is to create a load sequence which is fast, robust, and can lead to large numbers of atoms trapped in the FORT. In this chapter, we describe our optimization of the number of atoms of a single isotope trapped in the FORT. During the course of this optimization, we discovered that using an optical molasses dramatically improved the number of atoms that could be loaded into the FORT as compared to loading the FORT directly from the MOT. This chapter presents the data we collected investigating this fact and our conclusions about why the optical molasses loading is more effective.

The load rate is dependent upon many factors such as atom temperature, trap volume, laser detuning and power, etc. Additionally, since the FORT in our experiments was loaded from an optical molasses, overlap with the Magneto Optical Trap (MOT) becomes very important. Chapter 2 described the general alignment procedures as to

how this overlap is first constructed. The factors which influence the FORT load needed to be investigated in order to maximize the load rate and number into the FORT. The full procedure listed in this chapter for homonuclear FORT loading optimization is described in [1].

While many experiments in this thesis focus on various collisions, elastic or inelastic; it is necessary to understand the load dynamics of the FORT in both the homonuclear and heteronuclear (chapter 8) load cases so that load procedures can be tailored to the needs of the experiment. Future experiments will take advantage of a high density, optically thick species in collisions with a low density, optically thin species. The density (number) of one of the Rb species in the FORT can be controlled through that species's optical molasses loading of the FORT, giving us control over how much of an isotope we load into the trap.

5.1 Parameters of the FORT load.

In initial FORT experiments only a very low number of atoms were loaded into the trap; the methods used also took advantage of the optical molasses but were only able to trap around 500 – 1300 atoms [2,3]. While the early experiments trapped relatively few atoms, there was great potential to increase both the number and density of atoms trapped in an optical trap. Thus considerable effort was invested into understanding the dynamics behind optical trap loading. The FORTs emerged as one of the more common forms of optical traps used as their large detuning significantly reduced scattering of optical trap light by the atoms [3].

The difficulty of FORT loading from a MOT is born in the inherent nature of the FORT itself. A FORT is essentially a conservative potential, since the FORT itself is

unable exert a damping force on atoms which pass through its trap volume. Thus atoms passing through the FORT region require additional cooling to be successfully captured by the FORT. This capture is more difficult if the trap depth of the FORT is shallow, as is the case for our system. Because of the shallow nature of our FORT, the atoms are more susceptible to heating effects such as collisions with background atoms, and this can cause loss from the trap [4]. However, at higher numbers typical of our experimental parameters the heating induced from collisions with background atoms does not significantly contribute to the loss of atoms from the FORT during loading. Instead, collisional processes between the trapped atoms themselves were the dominant loss mechanism[5]. These can include; light assisted collisions, collision induced decoherence (which can prove significant for heteronuclear loading of a FORT), ground state hyperfine changing collisions, etc. However, while the FORT is loaded, the majority of the loss in our system comes in the form of light-assisted collisions

With these facts in mind, several parameters by which one could affect FORT loading were studied. The interaction of these parameters means that the loading dynamics of a FORT can be rather complex, but interesting as well. First of all, the FORT load will be dependent upon the specific conditions of the MOT. The optical molasses is used to load the FORT, and we rely on atoms transiting the FORT volume to undergo enough cooling to be captured into the FORT. As a result, the density, atom number, and temperature of the MOT will be very important in optimization of the FORT load [6]. The number and density were important for the obvious reason of providing the atoms necessary for the load. The MOT temperature was important since it will influence how much additional cooling atoms will need before being captured by the

FORT given its trap depth. The spatial overlap also was important as it determines how many atoms will transit the FORT volume. Additionally, through our studies we found that it was beneficial to have the minimum waist size of FORT beam slightly off the center of the MOT. This allows for a larger FORT trapping region to be spatially overlapped with the MOT, allowing for more time to be cooled and captured into the FORT. This is particularly important for shallow FORTs where the trap depth is much less than that of the MOT. The larger the trap volume, the more atoms will transit the volume. Thus in shallow traps, off-setting the FORT allows for a larger volume overlap without ultimately reducing further the trap depth.

The parameters of the FORT itself were important to the load as well. Trap power has been investigated, as the potential depth of the FORT scales linearly with the beam power. The number trapped in a FORT as a function of power does not have a simple relationship. As will be discussed later on in this chapter, this is due to the dependency of light fields and other factors which can vary from system to system. A $P^{3/2}$, where P is the power of the FORT laser, dependency has been observed [7], as well as a linear dependency [8]. There is a saturation effect with the power of the FORT trapping laser where there is a turn over in the number of atoms which can be trapped and eventually even with increased power in the FORT laser, the number of atoms trapped in the FORT remains constant [9]. We, however, are operating under conditions far from this saturation point.

Trap geometry was also a factor in FORT loading [9], our studies showed a dependency on trap number with the waist size of the FORT laser. In this work, the number of atoms trapped in the FORT was observed to increase with increasing waist

size of the FORT laser. While the number trapped in the FORT should scale with w^2 (where w is the waist size) this dependency was not observed though it was claimed that saturation effects (which scale linearly with w). However, this result is consistent with our own experimental observation that offsetting the minimum waist size of our FORT beam from the MOT improves the loading rate and ultimately the number of atoms trapped in the FORT. This is presumably because offsetting the minimum waist location allows the FORT laser to expand as it begins overlapping the MOT, thus allowing for a larger volume for the atoms to traverse as the atoms pass through the FORT trapping region. This corresponded to an observed increase in the total number of atoms captured.

Other research groups have investigated many other properties of FORTs that have an impact on the number of atoms that can be loaded into the FORT. Studies of the impact of FORT detuning and ellipticity [8], continuous wave or pulsed FORT beam [10], and trap depth [11] have been conducted. Though for our FORT the most applicable are those with changes in the MOT laser field (such as hyperfine repump power reduction), FORT volume (controlled through the overlap of the minimum waist size and the MOT), and FORT power (controlled through the CO₂ AOM).

The total number of atoms which can be loaded into the FORT is a competition between load rates and loss rates. The loss rates are dominated by collisions in the ultracold gas [6]. While some collisions, say hyperfine ground state changing collisions can be discouraged (though not eliminated during our FORT load procedure) through setting atoms in particular hyperfine states. Tricks of this nature do not work on collisions such light assisted collisions (the dominate loss in our system) since these collisions affect atoms in differing hyperfine states. While the losses are dominated

primarily by collisions, the load rate is affected by many parameters, some of which have been previously discussed. Factors such as FORT power, volume, MOT atom temperature and number, sub-Doppler cooling efficiency, cooling and repump power and detuning, and MOT/FORT overlap can affect the load rate into the FORT. Thus these parameters which control load rate are in contrast with the parameters which control loss out of the FORT, and optimizing the FORT load requires finding the parameter space in which the load rate to loss ratio can be maximized for our system.

We observed a strong dependence of the ultimate number of atoms trapped in the FORT on the hyperfine pump power during the CMOT and molasses stages [6, 12]. It was found that a strong reduction in the hyperfine repump power several milliseconds before the molasses stage led to a significant increase in the number of atoms which were trapped in the FORT. This reduction is thought to be caused by a reduction in density limiting processes [13].

In our system we loaded the FORT directly from an optical molasses, as mentioned in Chapter 2.2.1. While other groups have taken advantage of the optical molasses in loading a FORT [1, 7, 14, 15, 16, 17, 18], the dynamics of FORT loading from an optical molasses (especially as opposed to being loaded from a MOT) have not fully been characterized before the work presented here in this chapter. There has been work in general with loading dynamics of a FORT from a MOT which take into account the overall loading and loss mechanisms into the FORT. In particular, in [6] the loading process is examined and it was found that the ultimate number of atoms trapped in the FORT is a balance between the load rate of atoms into the FORT and loss rate out of it where the loss rate is dominated by light-assisted collisional processes. Working to

minimize this loss rate can produce more efficient FORT loads leading to a larger number of atoms trapped in the FORT. Additionally, the processes and loss mechanisms inherent to FORT loading are rich in physics and interesting dynamics.

5.1.1 Experimental measurement of load rate and loss rate. In our system, the FORT we used was a relatively shallow (~ 120 μK deep) FORT. The shallow FORT provided a larger trapping volume than a deep FORT, and as found in [9] a larger trap volume is beneficial in trapping a larger number of atoms. This is true for our system as well, which we found experimentally. In determining the optimization for maximum number loaded into the FORT we examined both a load into the FORT from an optical molasses (referred to as molasses loading for the rest of this chapter) and directly from the MOT itself (referred to as MOT loading for the rest of this chapter). Both methods of loading the FORT were optimized by finding the proper light field (laser power, detuning, etc.) which produced the largest load. Then, both molasses loading and MOT loading can then be directly compared to each other. During the course of setting up and loading our FORT, we had found that the molasses was critical to obtaining a good FORT load. The reason behind this dependency was puzzling as the only difference between the molasses stage and was the use of the anti-Helmholtz coils. Thus we wished to investigate the molasses dependence of our FORT load as compared to the MOT load.

The sequences for MOT and molasses loading are very similar and follow the procedures outlined in section 5.4. The only difference between the molasses and MOT loading is that in the latter the anti-Helmholtz coils are not shut off. The presence of the anti-Helmholtz field has a prominent effect on the loading of the FORT, and can have

significant effects on the load rate between the MOT load and molasses load conditions [1]. This has an effect on the total number of atoms which can be loaded into the FORT

The number of atoms in the FORT (N) can be characterized through a loading equation [6]

$$\frac{dN}{dt} = R(t) - \beta\bar{n}N - \Gamma N . \quad (5.1)$$

While written slightly differently from equation 2.16, many of the terms are the same. \bar{n} is the average density of the atoms trapped in the FORT. $R(t)$ is the load rate of the atoms into the FORT. β is the two body loss rate out of the FORT, and Γ is the single body loss rate out of the FORT. The single body loss does not contribute heavily in the time taken to load the FORT and thus Γ can be approximated as zero for our conditions. Furthermore, the two body loss rate does not vary significantly over the course of the FORT load and thus can be treated as a constant. With the use of equation 5.1, we can model the load of our FORT and find the parameters under which we can maximize $R(t)$ while minimizing β .

The goal of this set of experiments, as it was with other experiments, was to find the conditions under which we can produce the maximum number of atoms trapped in the FORT. Figure 5.1 shows a typical loading measurement for ^{85}Rb . Figure 5.1 shows a MOT load, but a molasses load has a very similar shape. The interesting feature of these loading curves is that the number loaded into the FORT initially quickly rises nearly linearly. After some time, however, the load rate reduces, and becomes comparable to the loss rates. As this happens, the rate at which atoms were loaded into the FORT dropped. Eventually, as the load rate drops, the loss terms will dominate the system and cause a decrease in the number of atoms trapped in the FORT.

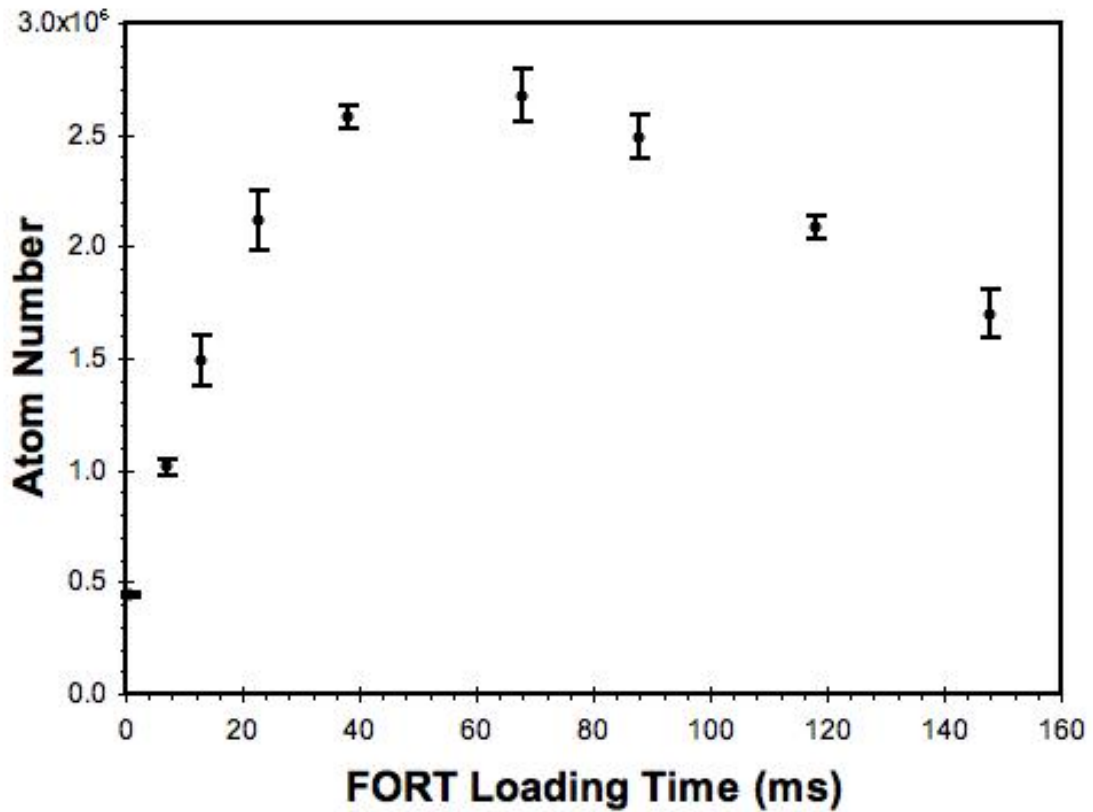


Figure 5.1. Typical atom number evolution as a function of FORT loading time for MOT loading of the FORT for ^{85}Rb . For this curve, the second CMOT stage was detuned 33 MHz to the red of the cycling transition of ^{85}Rb with the hyperfine repump power attenuated to $5 \mu\text{W}/\text{cm}^2$. In the study of the loading dynamics of the FORT, the goal is to increase the maximum number of atoms which can be loaded into the MOT. For these conditions for this graph, the maximum number is ~ 2.6 million atoms at ~ 59 ms of CMOT load time.

Since we are looking for the maximum number of atoms which can be loaded into the FORT, we are particularly interested in the time span during the FORT loading where the number of atoms was at its peak. At this point, the loss rates have become large enough to balance out the load rate into the FORT and any additional time will cause atom number loss. By definition, at the turn over point $\frac{dN}{dt} = 0$, and so from equation 5.1 we can find an expression for the loss rate coefficient (β). In terms of this peak load rate and atom number β is given by,

$$\beta = \frac{R_{peak}}{\bar{n}_{peak} N_{peak}} = \frac{R_{peak} V}{N_{peak}^2}. \quad (5.2)$$

The peak values listed here (R_{peak} , N_{peak} , \bar{n}_{peak}) were the values when the number of atoms loaded is at its maximum. Other than that, the variables retain their definitions from equation 5.1. The rightmost expression is derived by noting that $\bar{n} = \frac{N}{V}$, where V is the FORT trap volume. R_{peak} is the loading rate necessary to evaluate the maximum number of atoms loaded into the FORT. By using the peak values for load rate and number, it becomes easier to compare different experimental conditions to one another as R_{peak} is a constant value while in general the load rate $R(t)$ has a time variation dependent on the experimental parameters. Comparisons between measurements can be quickly made as a function of experimental conditions to examine the conditions for which N_{peak} can be maximized. Thus we collected data consisting of measurements of R_{peak} and β from both MOT loading and optical molasses loading of the FORT over a range of detunings for both the MOT and molasses stages and hyperfine power to evaluate the

optimum parameters for FORT loading and to examine the difference in performance between these two loading schemes.

5.2 Experimental setup and conditions.

As is the case for all of our FORT experiments, the first stage in the sequence was the loading of a MOT (section 2.1.4 in chapter 2). The details of the sequence for FORT experiments was described in section 2.21, and so the only thing that will be touched on here are the relevant experimental parameters for the experimental results presented in this chapter. The FORT (section 3.4) was formed from with a 30 W beam resulting in FORT trap depth of 120 μK . The MOT was allowed to fill till approximately 200 million atoms have been captured in the MOT before initiating the experimental sequence. This ensured consistency with starting number in our FORT loading measurements so that we can confidently compare values measured under different experimental conditions. Each of the 6 beams for the MOT had an average peak intensity of 2.5 mW/cm^2 for ^{85}Rb and 8 mW/cm^2 for ^{87}Rb . ^{87}Rb requires a higher intensity for its trapping laser due to the difference in natural number between ^{85}Rb and ^{87}Rb . ^{85}Rb is about 2.6 times more numerous than ^{87}Rb , thus to trap the same amount of ^{87}Rb as ^{85}Rb in roughly the same time [19], a stronger light field is required to capture more of the ^{87}Rb present in the thermal vapor. While we examined various timings and detunings for the second CMOT and molasses stages, the load detuning for the MOT and first CMOT stage of both ^{85}Rb and ^{87}Rb was consistently 12 MHz and 20 MHz respectively to the red of their respective transitions. However, during the first CMOT stage, the hyperfine repump laser was attenuated. This attenuation was an experimental variable; we examined the effect on the loading dynamics of the FORT for hyperfine repump powers between 1.2 to 20 $\mu\text{W}/\text{cm}^2$

for ^{85}Rb . The effect of changing the ^{87}Rb hyperfine repump power at the same stage in the experimental cycle was over a similar power range.

This first CMOT stage lasts about 13 ms and there seemed to be little dependence of the load on the length of and the cooling laser detuning during this CMOT stage. However, the overall performance of the FORT load was better with this first CMOT stage than it was without. The second CMOT stage was one of interest as for MOT loading this was the stage active while loading the FORT. The second CMOT stage keeps the same hyperfine attenuation as the first CMOT, but the detuning was varied as an experimental parameter.

In a MOT load of the FORT, there was no molasses stage. Instead, the FORT is loaded during the time in which the FORT is overlapped with the second CMOT stage. Measurements of the loading behavior during this time were taken by varying the turn on time and the loading duration for a selected cooling laser detuning and hyperfine repump power. The turn on time refers to when during the second CMOT stage the FORT is turned on, and duration time is the length of time for which the FORT is left on. The hold time of the atoms in the FORT and the imaging sequence are the same as described in section 5.4. Prior to holding the atoms in the FORT, the hyperfine repump was turned off slightly before the main trapping laser to allow the atoms to be optically pumped to the lower hyperfine ground state ($F=2$ for ^{85}Rb and $F=1$ for ^{87}Rb). Also, the anti-Helmholtz coils are turned off at that time.

5.2.1 MOT loading. In the MOT loading sequence then, the parameters of the experiment for the maximization of the load include the hyperfine repump power, the second stage CMOT detuning, and the timings associated with the FORT turn on and off

times. The first parameters tested were the hyperfine power and the second stage CMOT detuning to probe the effect they had on the peak load rate and loss coefficient. The R_{peak} and β values were extracted and mapped as a function of the selected hyperfine repump power and detuning and were then compared to find which settings produced the largest peak number of atoms trapped in the FORT. The first step in this process is to find where the peak number in the evolution of the load (such as that shown in figure 5.1) occurred; i.e. the point in time where $\frac{dN}{dt} = 0$. Figure 5.1 shows such a measurement. To obtain these curves, the FORT and the second CMOT stage were turned on together and coexist together for a variable amount of time (hence both the second CMOT and the FORT turn on and off together) called the FORT loading time. The number of atoms which are trapped in the FORT were plotted as a function of this time and a curve such as figure 5.1 was obtained. From this curve we can find the maximum number of atoms which can be loaded into the FORT and the loading time at which it occurs. For example, in figure 5.1, the peak load time was 59 ms and the maximum number of atoms was about 2.7 million atoms. This load time at which the peak occurs will be referred to as t_{max} .

Once the time at which the maximum number of atoms was loaded was known, the next goal was to measure $R(t)$ at that time in order to extract R_{peak} . This is done by delaying the turn on time of the FORT until t_{max} . By turning the FORT on at t_{max} and taking two short load time measurements, the value of $R(t)$ can be extracted. The FORT was typically allowed to load from the MOT for two or more times of length 2-6 ms before imaging. The difference in atoms loaded between these two times was used to extract the R_{peak} .

A potential concern with taking data in this fashion was that the presence or absence of the FORT light would have an impact on how the MOT changes in time. If this were the case, then the load rate measured after delaying the turn-on of the FORT would not be the same as the load rate once the FORT has been on for some time. Measurements we made, however, indicated that the FORT light has a negligible effect on the load rate. These measurements are consistent with estimates that we made about the effect of the FORT light on the evolution of the MOT in time. The measurements for this test consisted of a series of low number $R(t)$ measurements for a molasses load. The load rate was measured when the FORT was turned on at the beginning of the molasses stage and when it was turned on earlier in the second CMOT stage. There was no noticeable change in the measured $R(t)$. This suggests that the FORT light itself does not impact the MOT evolution (and thus loading dynamics).

The FORT load rate was thus dominated by the MOT light fields and MOT/FORT overlap. The evolution of the atoms in the CMOT stage (which is dominated by radiation pressures, collisions, sub-Dopper cooling caused by the light MOT light field) and the MOT/FORT overlap which noticeably affect $R(t)$. Furthermore, in early experiments $R(t)$ itself was measured and mapped out over the FORT loading time using the method described above (Figure 5.2). If delaying the FORT turn on time merely shifted the zero of the loading start, then no matter what we should have always measured the same $R(t)$, but we found that the load rate into the FORT was indeed time dependent and were able to accurately map out the time dependency of R .

Because we are delaying the turn on of the FORT till t_{max} , the number during the measurement of R_{peak} was low and two-body losses were there relatively less significant.

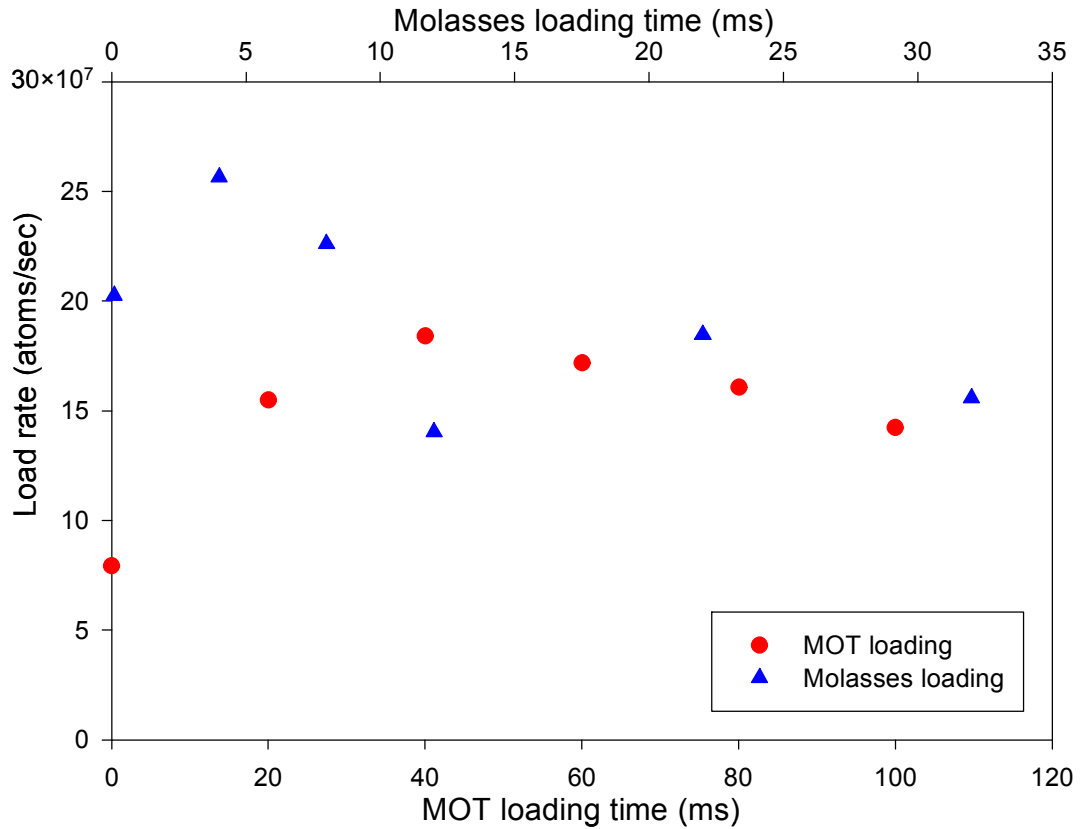


Figure 5.2 Loading rate ($R(t)$) measurements for both MOT loading (red circle) and molasses loading (blue triangle) of ^{85}Rb into a FORT. The molasses loading times are displayed on the top axis while the MOT loading times are displayed on the bottom axis. The detuning used for the MOT loading was 32 MHz to the red of the ^{85}Rb cycling transition. The detuning used for the molasses loading was 80 MHz to the red of the ^{85}Rb cycling transition. These detunings represented the optimal detuning settings for each particular loading scheme.

Thus equation 5.1 is dominated by the $R(t)$ term and not the β term for these measurements.. However, because there were always some number of atoms in the FORT, the two body loss was not zero. To correct for this, data on the load rate and loss rates were taken and to calculate R_{peak} and β , equations 8.1 and 8.2 are solved simultaneously. This process was repeated for each set of experimental conditions. For the MOT loading experiment, that includes the hyperfine pump attenuation and the second CMOT stage detuning.

Since β is a constant (while R is not necessarily constant, we performed a sample set to look at β as a function of FORT turn on which indicated that for our system, β appeared to be constant), we only need to find it at one spot. Once β is known, we can make measurements of $R(t)$ for the entire loading cycle, not just limited to the time around t_{max} where $\frac{dN}{dt} = 0$. Figure 5.2 has a standard load rate measurement for both the MOT loading (red circles) and molasses loading (blue triangles). The data is taken for the optimal detuning for each loading procedure. $R(t)$ is not constant over the load time of the FORT. Both forms of FORT loading show an increase in load rate, a maximum, and then a subsequent decrease over. As stated above, the load rate is dependent upon the MOT (or molasses) laser field and the overlap of the atoms with the FORT trapping volume. As it turns out, the MOT moved in space during the FORT loading as the hyperfine pump power and laser detunings were adjusted. The exact cause of the movement has not been definitely determined. It could be that imperfections in beam balance and slight misalignments in the MOT and molasses lasers could lead to this movement. The movement was dependent upon many factors including the detuning of cooling laser, the power of the hyperfine repump laser, and the applied magnetic shim

fields. Interesting though for our system was that the movement seemed most dependent on hyperfine repump power. This seems to indicate that the movement was due to more than just simple optical or magnetic force balance. Had this been true, both the detuning and power would have similar effects. Regardless, since one of the parameters governing the load rate is the overlap of the atoms with the FORT, the moving MOT and molasses clouds can account for the initial increase seen in the loading rates for both load procedures. Figure 5.3 shows a sample of the movement of the MOT as a function of time through the FORT trapping region; the black line indicates the position of the FORT. The MOT clearly moves down into the FORT trapping volume so that at later times the areas of densest atoms overlap with the FORT volume to its new equilibrium point. As the cloud fell, the load rate increased as more atoms traverse the FORT volume. At some point in the load, the load rate will begin to decrease. For MOT load this decrease is due to the atom number in the MOT having decayed due to the MOT not loading any further. For molasses load it is due to the fact that the cloud is actually expanding, which dropped the density of atoms in the FORT trap volume. As detuning was a factor in how fast the MOT or molasses moved, this can also explain the difference in time scale for the two plots shown in figure 5.2. The much larger detuning of the molasses loading compared to the MOT loading resulted in the maximum load rate being reached much earlier in the molasses load as compared to the MOT load condition. (Though this can be attributed to the fact that the MOT density does not drop as quickly as the molasses density).

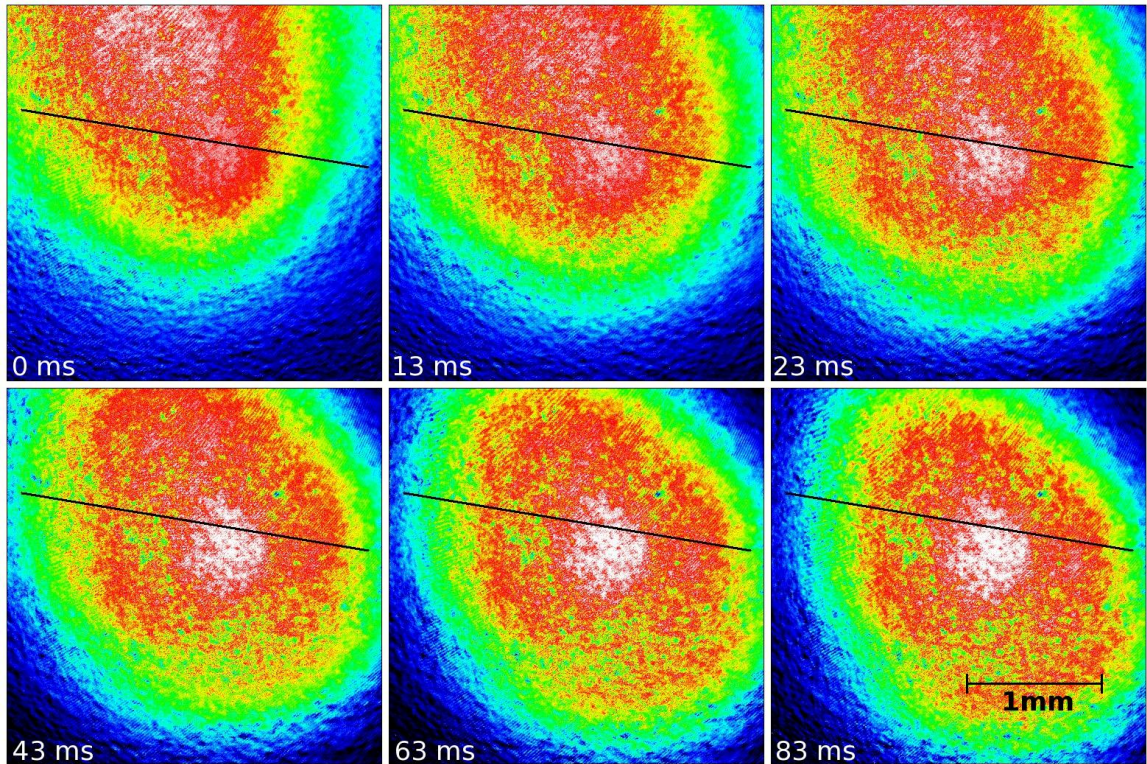


Figure 5.3 False color representations of pictures of the MOT temporal position evolution. The degree of movement of the MOT or molasses is dependent upon the power and detuning of the laser field. This figure is of a sample CMOT stage to observe the movement in the MOT during the second CMOT stage. The black line corresponds to the position of the FORT. The false color scheme is such that the white center of the MOT represents the densest region and black represents the least dense regions. As the MOT moves in time, the overlap with the FORT changes as well. This explains the behavior illustrated in figure 5.2 where there is an initial increase in load rate.

5.2.2 Molasses loading. The molasses load was examined in a similar method as the MOT load described above. As was the case of MOT loading, for the molasses load the detuning of the light field and power of the hyperfine repump laser were parameters of interest. Unlike the MOT loading, after the end of the second CMOT stage, the anti-Helmholtz coils are shut off and the detuning of the trapping laser changed once again. This is the molasses stage and loading of the FORT occurs during this stage, instead of during the second CMOT stage as it does for MOT loading. Thus the FORT laser is not turned on until the beginning of the molasses stage. One of the parameters of this set of measurements was the length of the molasses stage where the FORT and molasses were both operating simultaneously. A second CMOT stage was still present, however, and thus the length of the second CMOT stage was additional parameter in this set of measurements that does not have a parallel to the MOT loading measurements. The second CMOT stage was set at 33 MHz to the red of the cycling transition of ^{85}Rb . Both CMOT stages are still used as the detuning and duration of the CMOT stage prepare the atoms for loading during the molasses stage. Since the anti-Helmholtz coils are turned off for the molasses, there is no longer a spatially dependent force to keep the atoms in one place. The cloud is free to expand, and thus the starting density of the CMOT is important as it will help determine how many atoms will enter the FORT trapping region. Additionally the power of the trapping and repump beams had an effect on the position of the MOT as discussed above, and this position was also a factor in the overlap of the atoms and the FORT trapping region.

The overlap of the CMOT and FORT trapping region was still an important variable. As discussed already, the position of the CMOT was dependent upon laser

detuning and the hyperfine repump (HFP) laser's attenuation. Another factor impacted by these two parameters was the number of atoms in the CMOT as a function of time. The increase in detuning of the laser and the attenuation of the HFP will also cause an atom number decay in the CMOT with time (and is the source of the decrease in $R(t)$ during the load of the FORT). The CMOT movement and number loss impacts the efficiency of the molasses load. As such, when optimizing the molasses load, the second CMOT stage must be optimized as well. This optimization took place in parallel with optimizing the molasses as the optimum set of CMOT parameters depended on the molasses parameters used. The second CMOT stage was 33 MHz detuned to the red. Then for any chosen molasses detuning and HFP attenuation, an evolution curve similar to those measured for MOT loading was taken. The difference in these evolution curves was that the parameter is the second stage CMOT time. The final molasses stage timing, detuning, and HFP attenuation was kept constant as the CMOT time was varied. This measurement determines the optimal time for the CMOT stage to maximize atom number in the FORT from the molasses load. An example of these evolution curves is shown in figure 5.4. These evolution curves are not quite as extensive as that shown in figure 5.1. This is because we are most interested in the CMOT time which maximizes the load, and thus are only interested in finding the peak.

For the measurements for the optimization of the second CMOT stage, the FORT was turned on at the start of the second CMOT stage. It remains on for 100 ms after the conclusion of the molasses stage. The optimal CMOT time was investigated for a variety of molasses detunings and times as well as HFP attenuation. For example, figure 5.4 is the evolution curve with a 15 ms molasses stage detuned 90 MHz to the red of the ^{85}Rb

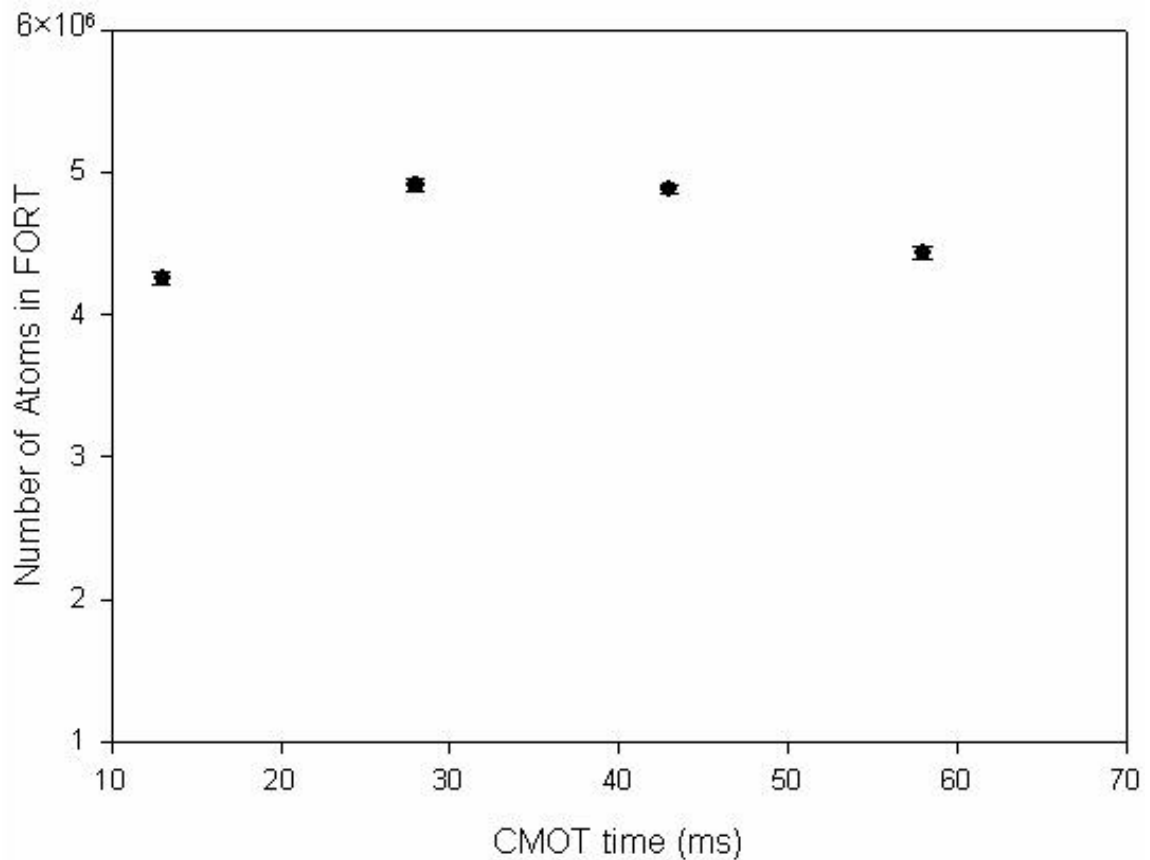


Figure 5.4 This is the evolution curve for the FORT as a function of the second stage CMOT stage. The conditions for this evolution curve are: 33 MHz red detuned from the ^{85}Rb cycling transition CMOT, 15 ms molasses detuned 90 MHz to the red of the ^{85}Rb cycling transition, and a hyperfine repump power attenuation of 30 dB. This evolution curve shows a maximum number load with ~ 30 ms of CMOT time.

cycling transition, and a HFP attenuation of 30 dB. These experiments were repeated for different combinations of molasses time, detuning, and HFP attenuation. In this way the optimal CMOT time can be set for molasses loading, allowing for the optimization of the molasses load itself.

The optimization of the molasses stage proceeds in the same manner by which the MOT loading was investigated and optimized. The FORT is turned on at the start of the molasses stage, and an evolution curve similar to that presented in figure 5.1 is measured. At this point, measuring R_{peak} and β for the molasses load follows exactly the procedure for that of the MOT load experiments (see chapter 5.3.1).

5.3 Data and Results

5.3.1 MOT load. Figure 5.5 shows an example data set for a MOT loading experiment which shows the effect of laser detuning and hyperfine attenuation. The measurements for the experiment examined a large range of HFP attenuations and laser detunings to optimize the FORT load. For example, in figure 5.5 the detuning range investigated was about 30 MHz. The HFP power range was investigated from near full attenuation ($\sim 1 \mu\text{W}/\text{cm}^2$) to $\sim 20 \mu\text{W}/\text{cm}^2$. The fact that there were two significant variables in the load process resulted in a wide parameter space in which to map out the FORT loading numbers, load rates, and losses in order to optimize the FORT load. For each set of parameters in this typical data set, R_{peak} is shown figure 5.5 (a, c). Values for β are depicted in figure 5.5 (b, d). R_{peak} and β are shown as a function of both MOT detuning data (figure 5.5 (a, b)) and HFP power data (figure 5.5 (c, d)).

For MOT loading, figure 5.5 (a) shows a steady decrease in R_{peak} with increasing detuning. This can be understood by noting that as the detuning increases, the scattering

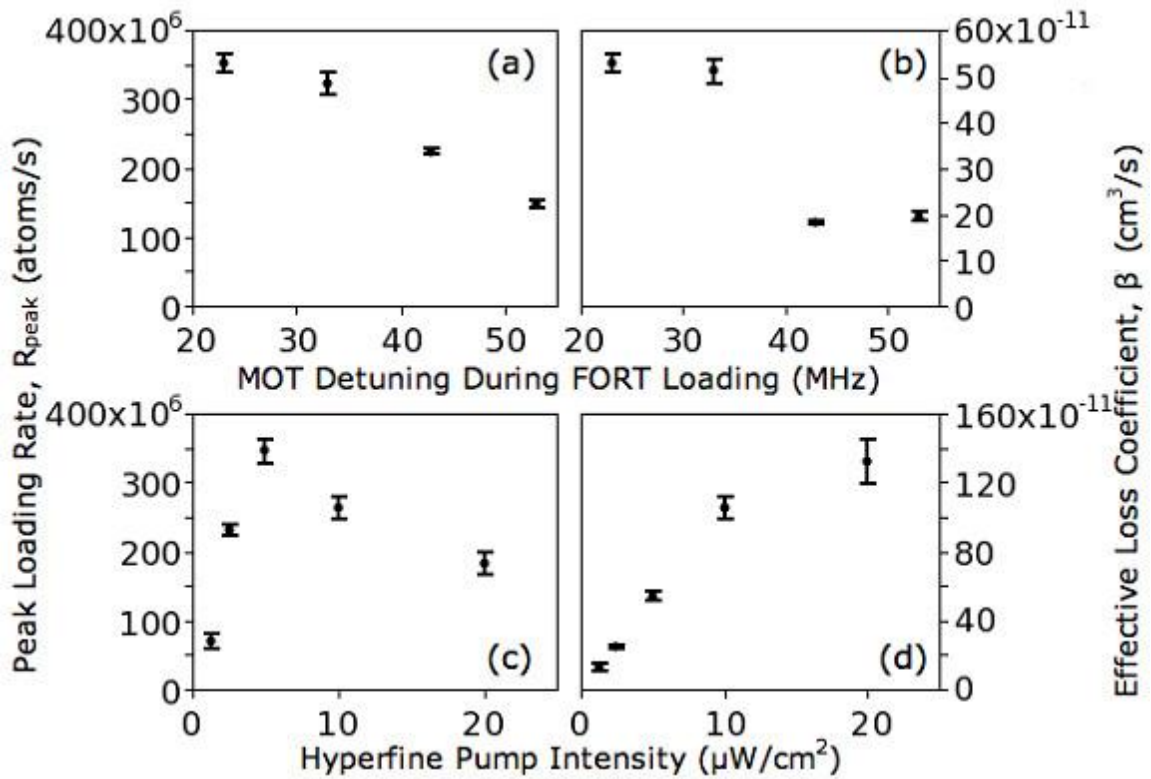


Figure 5.5 A sample set of data for the MOT loading experiments. The values of R_{peak} vs. MOT detuning is given in (a), values of β vs. MOT detuning is given in (b). For both cases, the MOT detuning is to the red of the ^{85}Rb cycling transition. The hyperfine repump power is set to $5 \mu\text{W}/\text{cm}^2$ for both (a) and (b). The values of R_{peak} vs. hyperfine repump power is given in (c), values of β vs. hyperfine repump power is given in (d). For both (c) and (d) the MOT detuning was 33 MHz to the red. The large drop in β shown in (b) is consistent with other data sets which also show the decrease.

rate decreases. The scattering necessary for sub-Doppler cooling therefore decreases as well. As sub-Doppler cooling is necessary to cool atoms into the conservative FORT, affecting the efficiency of sub-Doppler cooling mechanisms will cause the load rate into the FORT to decrease. With increasing detuning, there was also a drop in the value of β as seen in figure 5.5 (b) as atoms will spend more time in their lower hyperfine ground state. This caused the light-assisted collisions rate caused by the trapping light to decrease, leading to a decrease in the loss rate. Additionally, the light assisted collision cross section was affected by the detuning, which could also decrease the rate at which these collisions occur.

Likewise, the effects of the HFP power can also be explained through changes in scattering rate. Figure 5.5 (c) shows the response of R_{peak} with hyperfine repump power. There is initially a steep rise followed by a gradual decrease with increasing hyperfine power. Too little hyperfine pump power, and there are a larger number of atoms in the lower hyperfine state. This prevents them from being cooled by the trapping lasers, and thus takes them out of the sub-Doppler cooling mechanisms necessary to load the atoms into the FORT. Too much hyperfine power and the cooling efficiency was also negatively affected. One reason for this is that with greater HFP power, the dense cloud will experience more rescattering of photons in the cloud, which can add to heating and other disruptive processes. Also, as noted earlier in the chapter, the MOT position is dependent upon HFP power to some degree. So with large HFP power, there are larger average forces on the MOT, and this can disrupt the overlap of the FORT and MOT which is necessary for effective loading. We also saw a general rise in β as the HFP power is increased. The higher HFP power means a larger population in the upper

hyperfine ground state. The increase of this population lead to more light assisted collisions, thus increasing the rate of these collisions resulting is an increase in β .

5.3.2 Molasses load. Molasses loading was handled in much the same way. As mentioned chapter 5.2.2., for these measurements, we first optimized the second CMOT stage. After that, the experiment proceeds in the same manner as the MOT loading experiments. Figure 5.6 shows a standard data set for the molasses load presented in the same manner as for MOT loading. The main difference for the molasses loading is that in figure 5.6 (a, b) there are two sets of data presented. These represent two different hyperfine pump powers, one at $6.3 \mu\text{W}/\text{cm}^2$ (red) and one at $3.3 \mu\text{W}/\text{cm}^2$ (blue). The molasses load data shows the same general trends as the MOT loading, and in general can be explained by the same mechanisms. The real difference between the two types of loading is the detuning scale over which each is optimized. Where as the MOT load number is optimized around 20-30 MHz to the red; the molasses loading is optimized around 60-80 MHz to the red. Both types of loading can yield similar peak load rates at their optimal detuning. However, the molasses loading had significantly lower loss terms. Additionally, R_{peak} vs. hyperfine power for the molasses load (figure 5.6 (c)) did not peak and then slowly decay as it did with the MOT loading. Rather it increased with power and then bent over as if saturating.

5.3.3 Data variation. Care had to be taken to account for drifts in our system over time. Diode lasers are relatively sensitive to changes in their environment. If, for example, the lab temperature varied too widely during the day, the performance of the diode lasers will have changed as well. Along with the daily variations caused by the lab temperature drifts, there are long term drifts on the order of weeks or months. These very

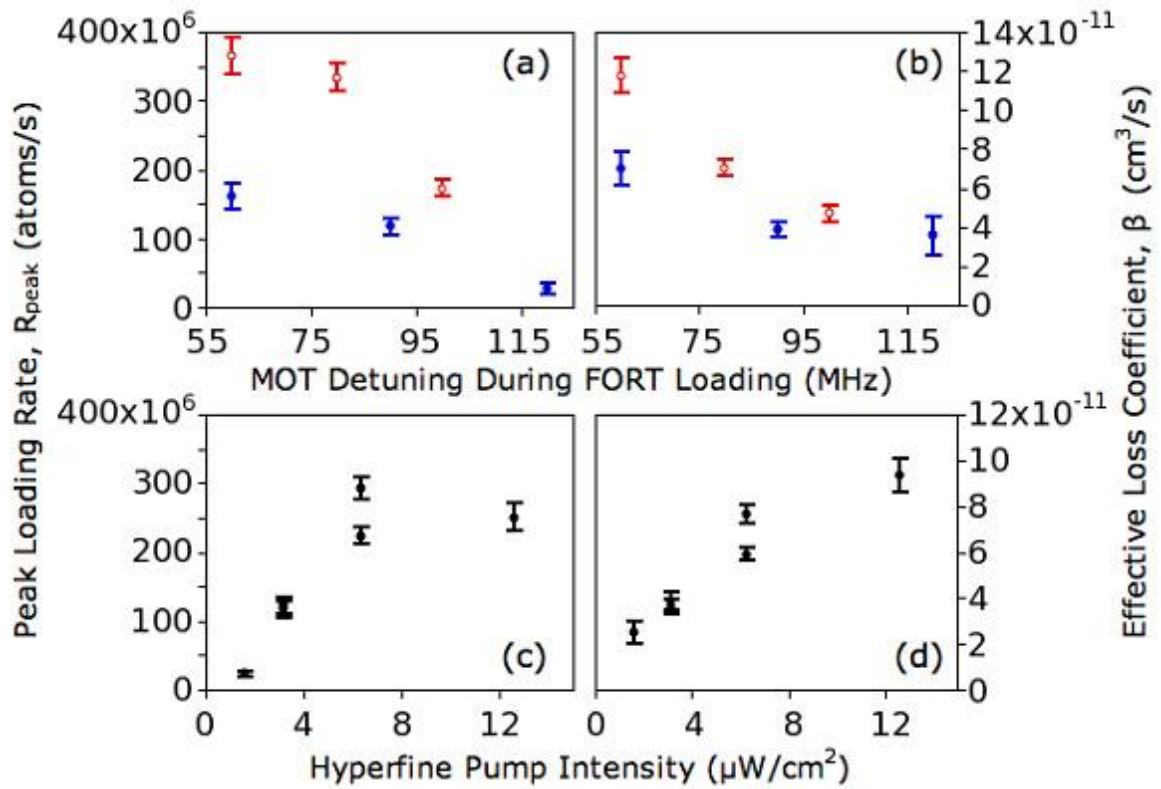


Figure 5.6 A sample set of data for the molasses loading experiments. The values of R_{peak} vs. molasses detuning is given in (a), values of β vs. molasses detuning is given in (b). For both cases, the molasses was detuned to the red of the ^{85}Rb cycling transition. The hyperfine repump power is set to $6.3 \mu\text{W}/\text{cm}^2$ for the open red circles and $3.3 \mu\text{W}/\text{cm}^2$ for the closed blue circles for both (a) and (b). The values of R_{peak} vs. hyperfine repump power is given in (c), values of β vs. hyperfine repump power is given in (d). For both (c) and (d) the MOT detuning was 90 MHz to the red.

long term drifts were due to slow changes in the experimental system. Over time, alignment, etc. will slowly degrade. We believe that the slight changes to alignment which occur over time can cause significant changes in the magnetic sublevel distribution of the atom cloud due to changes in the polarization field created by the overlap of the six MOT/molasses beams. The changes in m_F population lead to changes in the effective optical pumping rates. FORT loading can be especially sensitive to this, as it can cause changes in the sub-Doppler cooling efficiencies as well as collisional losses. The drifts then caused variations in the measured values of R_{peak} and β over time. The comparative data such as that shown in figure 5.5 and figure 5.6, therefore, were taken in relatively short time spans to reduce the effects of drifts. Furthermore, this alignment effect on the R and β was checked by purposefully misaligning the axial retro-reflection mirror by a small amount and was consistent with our experimental observations.

Interestingly, the observed drifts ultimately did not impact the measured values for the maximum number loaded as much as the values of R and β themselves. While drifts can cause changes in both R_{peak} and β , they tended to fluctuate in the same manner, and thus the ultimate number of atoms loaded remains roughly the same. Additionally, while R_{peak} and β fluctuate, the optimal values for laser detuning and HFP power remain relatively constant. This again isolates the maximum number loaded into the FORT from fluctuations in R_{peak} and β . However, a significantly large change to the MOT and FORT alignment can cause major changes in all the loading parameters and thus can ultimately lead to a drop in the number of atoms loaded.

5.3.4 Data analysis. The most significant difference between the MOT and molasses loading conditions came in the range of detunings where R_{peak} was maximized.

In figure 5.5 (a) and 5.6 (a) we see the same general trends with R_{peak} with detuning. The maximum load rate for each is similar, ~ 350 atoms/sec. However, R_{peak} occurs at very different detunings between the two systems, 33 MHz to the red for the MOT load and 90 MHz to the red for the molasses load. These optimal detuning values were used in figure 5.5 (c) and 5.6 (c), where again we see rather similar trends and R_{peak} values for both loading procedures. Thus it appears that the molasses becomes much more efficient at FORT loading at large detunings compared to MOT loading.

Figures 5.5 and 5.6 show that the peak load rate for both the molasses load and MOT load were nearly the same, but the detunings at which those peaks occur are different. The peak load rate for the molasses load occurred at a significantly larger detuning than that of the MOT load. Operating at this larger detuning is beneficial to the overall load of the FORT, allowing for a higher number of atoms to ultimately have been trapped in the FORT. This is manifested in the loss rate (β) between the two cases. The molasses load has a much lower β than that for the MOT load. However, if one were to plot β from both the MOT and molasses load conditions (with the same HFP power) as a function of detuning, the plot would be a continuous function. This indicates that β is not so much dependent on the presence of the anti-Helmholtz field, but rather is more dependent upon the detuning. As the detuning is increase, β will decrease in value. This is not the case with the load rate, if R_{peak} for the molasses and MOT load conditions are plotted on the same graph as a function of detuning; there is an abrupt change in the value of R_{peak} at the transition between the two conditions. Since the molasses operates without an anti-Helmholtz field, its peak load rate occurs at a much larger detuning. While that peak load rate is very similar to the peak load rate of the MOT load, the increased

detuning allowed us to operate in a regime where β is significantly decreased. This allows for the better performance in loading the FORT of the molasses load as compared to the MOT load condition.

In order to maximize the number of atoms loaded into the FORT, we need to find the detuning and HFP power where R_{peak} was large while β was small. As seen in figures 5.5 and 5.6 R_{peak} and β have similar trends as one another with HFP power and detuning. Thus a large peak load rate would correspond to large loss rate. In order to find the conditions that produce the maximum number of atoms loaded, then, the ratio of R_{peak}/β must be examined. The maximum number of atoms loaded into the FORT will occur at the largest ratio of R_{peak}/β . Since both variables were dependent in similar ways upon the laser detuning and HFP power, the optimal load parameters depended on quantities such as the relative slope of R_{peak} and β as a function of detuning and HFP power. This ratio is maximized for the MOT load at 43 MHz to the red, where as for the molasses the maximum is at 80 MHz to the red. When the system parameters were set at their optimal load values, the MOT load yielded $\sim 2.5 \times 10^6$ atoms where as the molasses load yielded $\sim 5 \times 10^6$ atoms. Thus the molasses load technique was adopted as the method of loading the FORT as it can ultimately yield more atoms trapped in the FORT.

While the optical molasses provides the best load into the FORT, the only difference between the molasses and the MOT is the presence of the magnetic field gradient. Thus a question arises as to the effect magnetic fields have on the load rate and loss of the FORT. To test this, we used the shim coils to provide a uniform magnetic field (as opposed to a magnetic gradient) while we loaded the FORT using the molasses. The addition of the uniform magnetic field did not greatly affect the MOT position. Thus

the MOT/FORT overlap did not change significantly enough to change the load rate. Figure 5.7 shows the result of this investigation. We took load rate data with a uniform magnetic field ranging from 0 to 136 mG. From figure 5.7 we see that both the total number atoms trapped (closed black circles) and the peak load rate (open green circles) decrease with increasing magnetic field. By 100 mG, the peak load rate is nearly half that with no magnetic field present.

The addition of the magnetic field changes the equilibrium conditions for the atoms in the light field. In [20] the effects of magnetic fields on the average velocity of the atom is discussed. From approximations of the equations given there, it is possible to estimate the equilibrium average velocity of the atoms. For a uniform field of 100 mG, we calculated that the atoms' velocity will damp to ~ 8 cm/s (absent statistical heating from multiple photon scatters). This is compared to the absence of a magnetic field where atoms would theoretically be damped to 0 cm/s. The actual average thermal velocity of the atoms in our standard optical molasses is ~ 5 cm/s. So the addition of the magnetic field significantly changes the velocity to which the atoms will damp. At 100 mG of field, the atoms damp to a velocity similar to the average thermal velocity of atoms in our optical molasses.

The change in the velocity of the atoms can change the cooling of those atoms into the FORT and thus the load rate. Since additional cooling is required to trap atoms into the FORT, any disruption to the sub-Doppler cooling techniques can have a measurable affect on the FORT load. Figure 5.7 suggests that the magnetic fields present during MOT loading are enough to have an affect on the load efficiency of the FORT. Since we load the FORT away from its center, where the trapping volume is larger, atoms

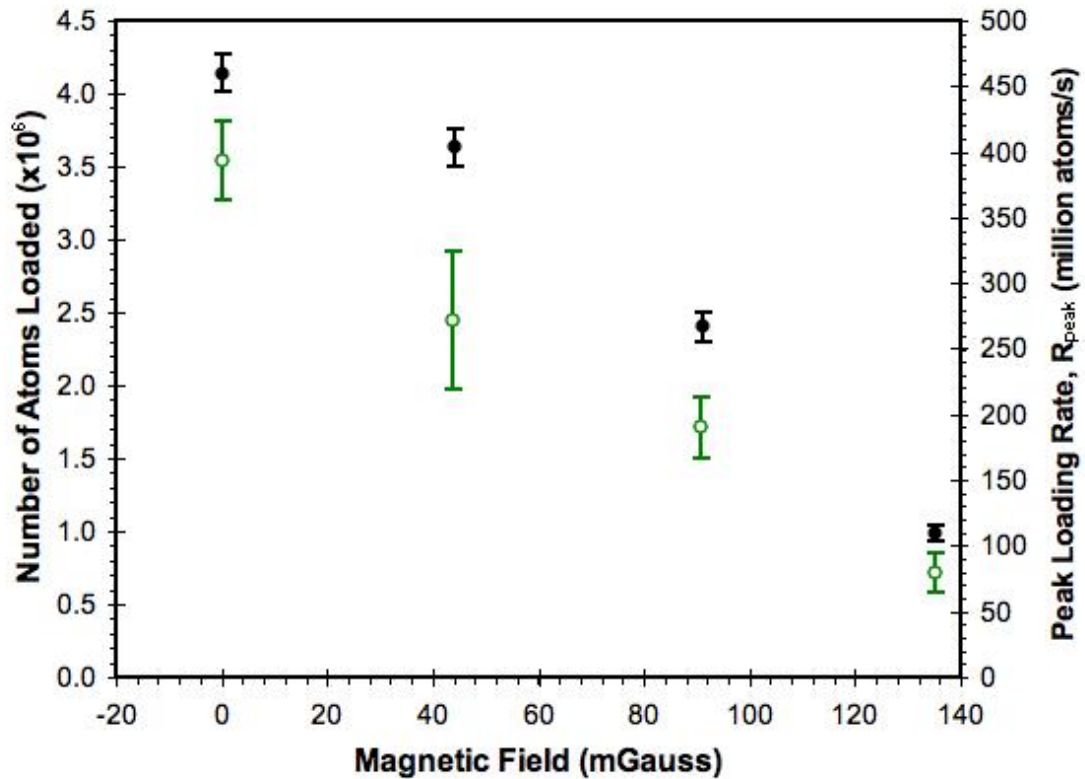


Figure 5.7 The number of atoms and peak load rate more a molasses load of the FORT as a function of applied magnetic field. The black closed circles (associated with the left axis) depicts the number of atoms trapped in the FORT. The open green circles (associated with the right axis) depicts the peak load rate (R_{peak}) for the molasses load. Since the addition of a magnetic field causes the atoms to damp to a non-zero velocity, the cooling efficiency of the atoms as they are trapped into the FORT is decreased. The result of the reduction of cooling efficiency is manifested in a drop in both the number of atoms trapped and the loading rate.

are being loaded at a location where the magnetic field is non-zero. For our system, we have a typical magnetic gradient of ~ 3 G/cm for our MOT in the direction aligned with the axis of the FORT. In that gradient a 100 mG magnetic field (where the load rate has dropped by almost half in figure 5.7) would be located at a distance .33 mm away from the magnetic zero. Thus we would expect that the cooling on the edges of the cloud in this case to be less efficient than it is if there was no magnetic field present. The change in cooling efficiency would manifest itself as a drop in the load rate and number into the FORT. Examination of the temperature of the atoms in the two conditions revealed that with the anti-Helmholtz magnetic field present the temperature of the atoms is approximately $30 \mu\text{K}$, as opposed to $20 \mu\text{K}$ in the absence of the anti-Helmholtz magnetic field. The fact that the magnetic field causes the atoms to damp to a non-zero velocity is enough to account for the measured decrease in the load rate with a magnetic field present.

5.4 FORT loading sequence

Thus with all the measurements of the load of the FORT made, we established a standard sequence for loading the FORT which was used in all subsequent measurements involving the FORT. In chapter 3 we discussed the Labview program used to control the system, including the timing structure, TTL signals, and the set points on the laser diode controls. The amount of control on our experimental system allows us μs precision in the TTLs being sent to the various devices. A typical sequence will cover everything from the initial MOT loading, to the FORT loading and imaging. The load efficiency of the FORT depends on laser power, detuning, timing, etc. Section 5.2 talks in detail on how

these parameters were measured and set to optimal levels. Every sequence has roughly the same layout in FORT loading.

The FORT loading and analysis consists of several stages where atoms are collected and cooled to ultracold temperatures, MOT parameters are adjusted to compress and cool the atoms further, the FORT is turned on and atoms load into the FORT, and eventually the FORT atoms are imaged to determine their number and temperature. The sequence of stages starts with MOT loading. For both isotopes the MOT was loaded from the background Rb vapor in the cell using the cooling and repump lasers described in chapter 2. For both ^{85}Rb and ^{87}Rb the cooling laser detuning was 12 MHz to the red of their respective cycling transition during this part of the sequence. The MOT load is monitored by a photodiode which displays the fluorescence of the MOT cloud on an oscilloscope. This allows for a consistent number of atoms to be loaded into the MOT before the next stage of the sequence is started. The timings reported here are for the optimal ^{85}Rb FORT load sequence, the sequence is the same for ^{87}Rb , but the timings can be slightly different. Once the next part of the sequence is started, the MOT is allowed to load further for approximately 1 s. Afterwards, the hyperfine repump laser is attenuated and the main trapping laser detuning is changed. The trapping laser detuning was 20 MHz to the red of the cycling transition. This change in detuning is often called a Compressed MOT (CMOT) stage as the increase in detuning and reduced hyperfine repump power reduces scattering rates, and thus radiation pressure and as a result the cloud of atoms compresses, increasing the density of atoms.

After this first CMOT stage, a second CMOT stage is used. The second CMOT stage comes 13 ms after the first, and is accompanied by another increase in the cooling

laser detuning; 33 MHz to the red of the cycling transition for both isotopes. This further compresses the atoms to be loaded into the FORT. While many details of the first CMOT stage (duration, detuning) did not produce noticeable difference on the FORT loading efficiency, the system worked better with it than it did without. 1 ms into the second CMOT stage, the AOM which controls the CO₂ FORT trapping laser is turned on. The FORT trapping volume overlaps that of the MOT. The FORT and CMOT are allowed to exist simultaneously for about 18 ms, at which point the molasses stage is started.

The molasses is the stage at which the majority of the FORT loading occurs. The previous MOT and CMOT stages were primarily to optimize the number and density of ultracold atoms near the FORT trapping volume. In the molasses stage, the anti-Helmholtz coils are turned off, which allows the atoms to freely expand in space. The trapping and repump lasers are left on, which allows for Doppler and sub-Doppler cooling mechanisms to continue. Also during the molasses stage, the final cooling laser detuning jump is performed. The FORT load is sensitive to this detuning. For ⁸⁵Rb the detuning is increased to 80 MHz to the red of its cycling transition, ⁸⁷Rb the detuning is increased to 120 MHz to the red of the cycling transition. These detuning settings are found experimentally and explained in the following section. The large detuning allows for the sub-Doppler cooling necessary for atoms crossing the FORT volume to be trapped while limiting destructive events such as rescattering of spontaneously emitted photons and light-assisted collision which could prevent atoms from loading into the FORT. The atoms are allowed to expand in this light field for about 49 ms, after which the repump laser is turned off.

Turning the repump laser off first allows the atoms to be pumped into the lower hyperfine ground state which is helpful in avoiding hyperfine changing collisions. Such collisions were observed to produce loss of atoms from the trap when the atoms were held for 100's of ms. 1 ms after the hyperfine repump is shut off, the trapping laser is shut off as well. This allows the atoms to remain in the FORT absent any light field which can promote heating or unwanted collisions such as light assisted collisions. The atoms are allowed to remain in the FORT for about 100 ms with no other light around, after which the hyperfine repump is again turned on at full power. This is to prep the atoms for imaging. The lower hyperfine ground state for the isotopes is a "dark" state; so called because "dark" atoms will not scatter light that is tuned to the cycling transition. The hyperfine laser on alone will move the atoms to the upper ground hyperfine state. Once the atoms are promoted to the proper hyperfine state, the atoms are imaged and the images recorded. The final step in the sequence is to reset the system to the original conditions so that cycle can be performed.

5.5 Conclusion

In the course of the optimization of the FORT load, it was discovered that several parameters have significant contributions to the load efficiency of the FORT. The FORT load is dependent upon; the cooling laser detuning, hyperfine repump power, the exact sequence of stages (e.g. CMOT stages, molasses load) and the length of these stages during the load. For our FORT conditions, we had found that the best FORT load utilized two CMOT stages and was loaded from the molasses. In fact, not including the molasses (i.e. MOT load) could cause the number of atoms trapped in the FORT to drop by a factor of 2 under optimal conditions. Additionally, when investigating the length of

the stages necessary to optimize load we found that if a molasses load is used, turning on the FORT several ms before (during the second CMOT stage) or right at the beginning of the molasses stage did not have any significant impact on the FORT load itself. This insensitivity to FORT turn on time should come as no surprise as the atom number quickly comes into equilibrium during the molasses stage. Starting the load of the FORT slightly later is compensated by the relatively large load rate of the molasses under optimal conditions.

When examining early turn on of the FORT for a molasses load, when the HFP power and cooling laser detuning were set to optimal values there was little difference between the number of atoms trapped when the FORT was turned on right at the start of the molasses or several milliseconds before during the second CMOT stage. This was true even though in the latter case there are atoms already trapped in the FORT at the start of the molasses. When the HFP power and cooling laser detuning were purposefully set to be non-optimal, the behavior was different and turning the FORT on during the final CMOT stage did contribute to a higher value of N_{max} . The reason for this comes in the behavior of $R(t)$ for the molasses load. $R(t)$ is relatively constant during molasses loading during the time it takes for the loss rate and load rate to come into equilibrium, decreasing only slightly in that time. Since that means that $R(t)$ will remain somewhat close to its peak value over the course of a molasses load, waiting to load out of the molasses or starting with a non-zero number of atoms in the FORT will have little effect on N_{max} for optimal setting.

Thus the optimal settings of the molasses load provided the most efficient FORT load in terms of the maximum number of atoms trapped. We had investigated the peak

load rates and two-body loss rates for loading the shallow FORT under the MOT and molasses load conditions. While during the course of the investigation it became obvious that several factors influenced the efficiency of the MOT load, we were able to develop an effective sequence of MOT, CMOT and molasses stages for FORT loading. We found that the load and loss rates were strongly dependent upon hyperfine repump power and cooling laser detuning. This dependency allowed us to optimize the system to produce the largest number of atoms loaded into the FORT. Further investigation showed us that while the load rate is influenced by the presence of the anti-Helmholtz field, the loss rate was not. The influence on the load rate caused the molasses R_{peak} to occur at a larger detuning, and because of the detuning dependence of β resulted in a similar load rate with reduced loss under the molasses load. The overall dynamic meant that we could significantly improve our load using a molasses load, nearly doubling the number of atoms in the trap for optimal conditions. The loading sequence and parameters from this inquiry were used in subsequent FORT loading experiments.

While all the measurements presented in this chapter were made for homonuclear loading, the load procedure was also examined for heteronuclear loading. That is briefly discussed in Chapter 8.

References for Chapter 5

- ¹ Mathew S. Hamilton, Anthony R. Gorges, and Jacob L. Roberts, Phys Rev A **79**, 013418 (2009)
- ² Steven Chu, J. E. Bjorkholm, A. Ashkin, and A. Cable, Phys. Rev. Lett. **57**, 314 (1986)
- ³ J. D. Miller, R. A. Cline, and D. J. Heinzen, Phys. Rev. A **47**, R4567 (1993)
- ⁴ S. Bali *et al.*, Phys. Rev. A **60**, R29 (1999)
- ⁵ T. Walker and P. Feng, Adv. At. Mol. Opt. Phys. **34**, 125 (1997)
- ⁶ S. J. M. Kuppens *et al.*, Phys. Rev. A **62**, 013406 (2000)
- ⁷ J. Wu *et al.*, J. Appl. Phys. **100**, 054903 (2006)
- ⁸ E. J. Prime, J. A. Behr, and M. R. Pearsom, Can. J. Phys. **85**, 1 (2007)
- ⁹ P. Ahmadi, B. O. Timmons, and G. S. Sunny, Phys. Rev. A **72**, 023411 (2005)
- ¹⁰ M. Shiddiq, E. M. Ahmed, M. D. Havey, and C. I. Sukenik, Phys. Rev. A **77**, 045401 (2008)
- ¹¹ K. M. O'Hara, S. R. Granade, M. E. Gehm, and J. E. Thomas, Phys. Rev. A **63**, 043403 (2001)
- ¹² C. Y. Yang *et al.*, Phys. Rev. A **76**, 033418 (2007)
- ¹³ C. S. Adams *et al.*, Phys. Rev. Lett. **74**, 3577 (1995)

-
- ¹⁴ R. Dumle *et al.*, *New J. Phys.* **8**, 64 (2006)
- ¹⁵ H. J. Lexec, O. Alloschery, R. Mathevet, and J. Weiner, *Opt. Express* **14**, 26 (2006)
- ¹⁶ T. Muller *et al.*, *Phys. Rev. A* **76**, 063611 (2007)
- ¹⁷ P. F. Griffin *et al.*, *New J. Phys* **8**, 11 (2006)
- ¹⁸ R. Newell, J. Sebby, and T. G. Walker, *Opt. Lett* **28**, 1266 (2003)
- ¹⁹ While not necessary in this specific experiment since the homonuclear loading dynamics for the two isotopes is examined separately, other experiments relied on simultaneous loading of ⁸⁷Rb and ⁸⁵Rb into the FORT. For these experiments, it was important to start the loading of the FORT with similar numbers of ⁸⁷Rb and ⁸⁵Rb atoms in their respective MOTs. Therefore, the system used for all experiments was constructed with stronger ⁸⁷Rb trapping lasers to allow for the two MOTs to load for the same time and trap similar numbers.
- ²⁰ P. van der Straten, S. Q. Shang, B. Sheehy, H. Metcalf, and G. Nienhuis, *Phys. Rev. A* **47**, 4160 (1993)

Chapter 6

Light Assisted Collisional Loss in a ^{85/87}Rb Ultracold Optical Trap

Two-body collisions for both homonuclear and heteronuclear collisions in an ultracold gas are one of the main loss mechanisms in laser cooling and trapping. In particular, these collisions in the presence of near-resonant have been of great interest since the beginning of laser cooling [1-12]. Of these two-body collision processes, this chapter will focus on light-assisted collisions. The light-assisted collisions described in this chapter consist of an atom pair coupled in the ground-state (S+S) absorbing a photon and being promoted to an excited-state potential (S+P). In particular, but studying light-assisted collisions under Far Off Resonant Trap (FORT) loading, it becomes possible to identify characteristics of light-assisted collisions. For example, the experiments involved with light-assisted collisions described in this chapter have found the structure of the excited-state potentials appear to have significant effect on the collision rates. Excited-state potentials which exhibit stronger repulsive features tend to have markedly lower loss rates than those with stronger attractive features. By studying light-assisted collisions under both heteronuclear and homonuclear conditions, details about they dynamics of light-assisted collisions can be understood better. This includes differences in load rates, loss rates, and excited-state potential structure. To study the dynamics of light-assisted collisions, we investigated these collisions using a FORT.

FORT loading from a Magneto-Optical Trap (MOT) is discussed in several chapters in this thesis. The FORT and MOT used in these experiments are described in

Chapter 3. In Chapter 5 the dynamics and procedure for homonuclear FORT loading were discussed in detail. The procedure for heteronuclear loading is detailed in Chapter 8. In both heteronuclear and homonuclear loading, light-assisted collisions are the predominant source of loss during the loading. These losses were mentioned in Chapter 5 and were associated with the β coefficient in Equation (5.1). When loading multiple species into the FORT, not only homonuclear light-assisted collisions but heteronuclear light-assisted collisions occur and lead to loss. Heteronuclear loading of the FORT was briefly mentioned in Chapter 2, and the load rate equations are similar to those discussed in Chapter 5. For heteronuclear loading, the load rate equations are

$$\begin{aligned}\frac{d}{dt}N_A &= R_A(t) - \frac{\beta'N_A N_B}{V} - \frac{\beta_A N_A^2}{V} \\ \frac{d}{dt}N_B &= R_B(t) - \frac{\beta'N_A N_B}{V} - \frac{\beta_B N_B^2}{V}.\end{aligned}\tag{6.1}$$

In equation 6.1, $N_{A(B)}$ is the number of atoms for species A(B), V is the trap volume. $R_A(t)$ and $R_B(t)$, and β_A and β_B are the load rates and loss rates for species A and B, and have been discussed in detail in Chapter 5. As with earlier discussions of FORT loading, the one-body loss terms have been ignored. These equations will be treated in much greater detail in Chapter 8. The appearance of a heteronuclear (β') loss term in addition to homonuclear ($\beta_{A,B}$) loss terms in the loading equations is a new feature not discussed in Chapter 5. The β' term is a cross species loss term which accounts for the loss rate during the FORT load due to heteronuclear dynamics producing a two-body loss.

The focus of this chapter will center on the β' and β terms of equation 6.1. Instead of focusing on the full of optimization of heteronuclear FORT load (Chapter 8), this chapter details our study of the hetero- and homonuclear excited-state-ground-state

collisions occurring in a FORT simultaneously loaded with both ^{85}Rb and ^{87}Rb . Many of the loss mechanisms, such as light-assisted collisions discussed in this chapter, are highly hyperfine-state dependent. That is, the collision rates are heavily influenced by the hyperfine-state of the colliding pair and the rates vary greatly depending on the hyperfine-states of the colliding atom pair. Because of the relatively weak confinement of the FORT, the hyperfine structure of the different isotopes plays a crucial role in the loss from the FORT. This dependence on hyperfine structure combined with the possibility of observing either heteronuclear or homonuclear light-assisted collisions allows us to measure collisions associated with long-range interatomic potentials with very different characteristics, such as long and short ranged; or such as purely attractive, purely repulsive, or mixed attractive and repulsive. Such a comparison of the light-assisted collision rate on these general characteristics of the excited-state potential had not been done in an optical trap where there is the greatest sensitivity to the long-range part of the excited state-ground state interatomic potentials. We observed significantly different loss rates for different types of excited-state potentials. Additionally, we observed that some collisional channels' loss rates are saturated at our operating intensities (15 mW/cm^2). These LAC losses are the primary limitation to the number of atoms one can load into the FORT.

6.1 Effect of Collisions in Ultracold Atom Dynamics

Atomic collisions in an ultracold gas in the presence of near-resonant laser light have been studied both experimentally and theoretically since the advent of laser cooling, with both heteronuclear and homonuclear collisions having been studied [1-12]. These light assisted collisions are responsible for limiting the density of atoms in MOTs [13-15] and

play an important role in limiting the number of atoms that can be loaded into FORTs [16-19]. Because our FORT is comparatively shallow (and can be considered a conservative potential), changes in its loading parameters, including changes to $R(t)$, β' and β , are readily observable. While light assisted collisions have a small effect on $R(t)$, its major effect on the loading of a FORT comes through two-body losses. To fully understand heteronuclear loading of a FORT, then, we need to investigate light-assisted collisions. By measuring the associated loss rates, we can probe the collisions associated with heteronuclear and with homonuclear long-range potentials [20].

These light-assisted collisions are strongly dependent upon the excited state potential and thus hyperfine states of the colliding pair. Since the ^{85}Rb and ^{87}Rb isotopes are so similar in mass, have nearly the same photon recoil energy, equilibrate to nearly the same temperature in the FORT, and experience nearly identical FORT potentials, the observed loss rates are directly related to the nature of the excited-state potentials. This allows us to probe the dependence of the light-assisted collision rate as a function of interatomic potential between atoms by comparing loss rates as a function of the isotopes and hyperfine states of the colliding pair. While many of these interatomic potentials are complex, some are simple with either purely attractive or purely repulsive characteristics. These “pure” potentials provide for an easier interpretation of the observed collision physics. In turn, by comparing the observations of loss involving these “pure” potentials to potential curves with a more complicated structure we could get an insight into what characteristics of the more complicated potentials influenced the observed loss rates.

Light-assisted collisions occur when an atom pair, typically in a ground-state, is excited to an excited-state interatomic potential. Figure 6.1 shows a cartoon of the light-

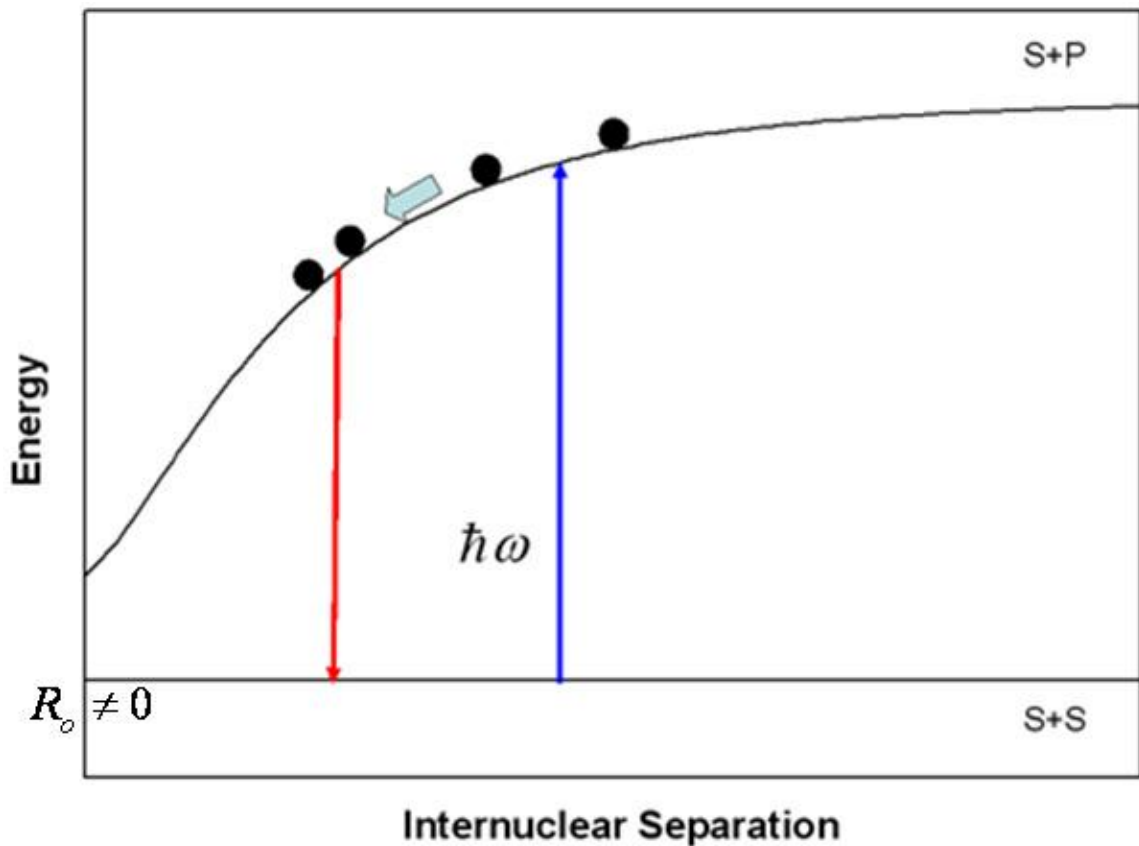


Figure 6.1 A cartoon showing an example of the light-assisted collision process. This cartoon shows an atom pair on the ground-state potential. The atom pair absorbs a photon which promotes the atom pair to an excited-state potential. Once on the excited state potential, the atoms feel a force towards each other and thus “slide” down the potential. After some time (the excited-state lifetime), the atom pair emits a spontaneous photon and returns to the ground-state. The emitted photon is less energetic than the one absorbed, and the difference in the energy is given to the atom pair in the form of kinetic energy. If enough kinetic energy is gained by the atom pair, the pair will be lost from the trap

assisted collision processes. After being excited, the atom pair is accelerated along the potential curve. After the atom pair has existed on the excited state curve for the lifetime of the excited state, it can undergo spontaneous emission and fall back down to the ground-state. The emitted photon is in general less energetic than the one absorbed, and the difference is between the two is converted into kinetic energy of the atom pair. Note that this absorption/emission sequence results in something that is an inverse of the result of Doppler cooling where the spontaneously emitted photon is of greater energy and thus the emission removes energy from the system. In a light-assisted-collision, if the atom pair receives enough kinetic energy, the pair will be ejected from the trap. This is observed as a loss rate from the system. Much of the work on light-assisted-collisions has been performed on ultracold atoms confined to a MOT [1]. However, because of the trap depth of the MOT (~ 1 K), the effects of light-assisted-collisions can be harder to discern. Because the trap depth of the MOT is so much greater, excited-state atom pairs do not spend enough time in the excited-state to gain enough kinetic energy to be lost from the MOT. By contrast, our shallow FORT exacerbates the loss due to light-assisted-collisions since it requires much less energy to eject an atom pair from a FORT than it does from a MOT. Our FORT has a trap depth of ~ 100 μ K whereas a MOT has a typical trap depth of ~ 1 K. Because of the shallower depth, loss inducing collisions are much more likely to occur at longer internuclear separations. Because the difference in hyperfine energies between the two isotopes is much greater than the energy shift due to the interatomic potential at the internuclear radii relevant for loss in the optical trap, the ^{85}Rb and ^{87}Rb mixture behaves as a heteronuclear mixture.

To understand the collision rates due to light-assisted collisions as a function of potential, the long-range interaction potentials for different combinations of colliding pair excited and ground states were calculated [21]. Some of these potentials are shown in Figures 6.2 and 6.3. To calculate these potentials, it was assumed that the interatomic distance between the two atoms is large enough so that exchange interactions could be ignored. Including the hyperfine structure, the dipole-dipole interactions were calculated. The large number of hyperfine and magnetic sublevel combinations gives rise to numerous individual interatomic potentials. To calculate the potential curves, such as those depicted in Figure 6.2 and 6.3, is to define the Hamiltonian of the system,

$$H = H_O + V . \quad (6.2)$$

Here H_O is the Hamiltonian describing the states of the two colliding atoms, including the hyperfine states of the atoms and V is the potential for the dipole-dipole force. These are the only interactions we consider when calculating the potential curves. The hyperfine interaction leads to energy splittings as described in [22], and we can write down the energy difference between F states in a single isotope due to the hyperfine interaction (W_F),

$$W_F = -\frac{1}{h}AK + hB \left[\frac{\frac{3}{2}K(K+1) - 2I(I+1)J(J+1)}{2I(2I-1)2J(2J-1)} \right]. \quad (6.3)$$

W_F is the hyperfine energy. I is the nuclear angular momentum, J is the total electron angular momentum ($J=L+S$, where L is the orbital angular momentum and S is the spin angular momentum). The energy is given in the $|J, I, F, m_F\rangle$ basis (F is the total angular momentum, $F=J+I$). The other variables listed in equation 6.3 are;

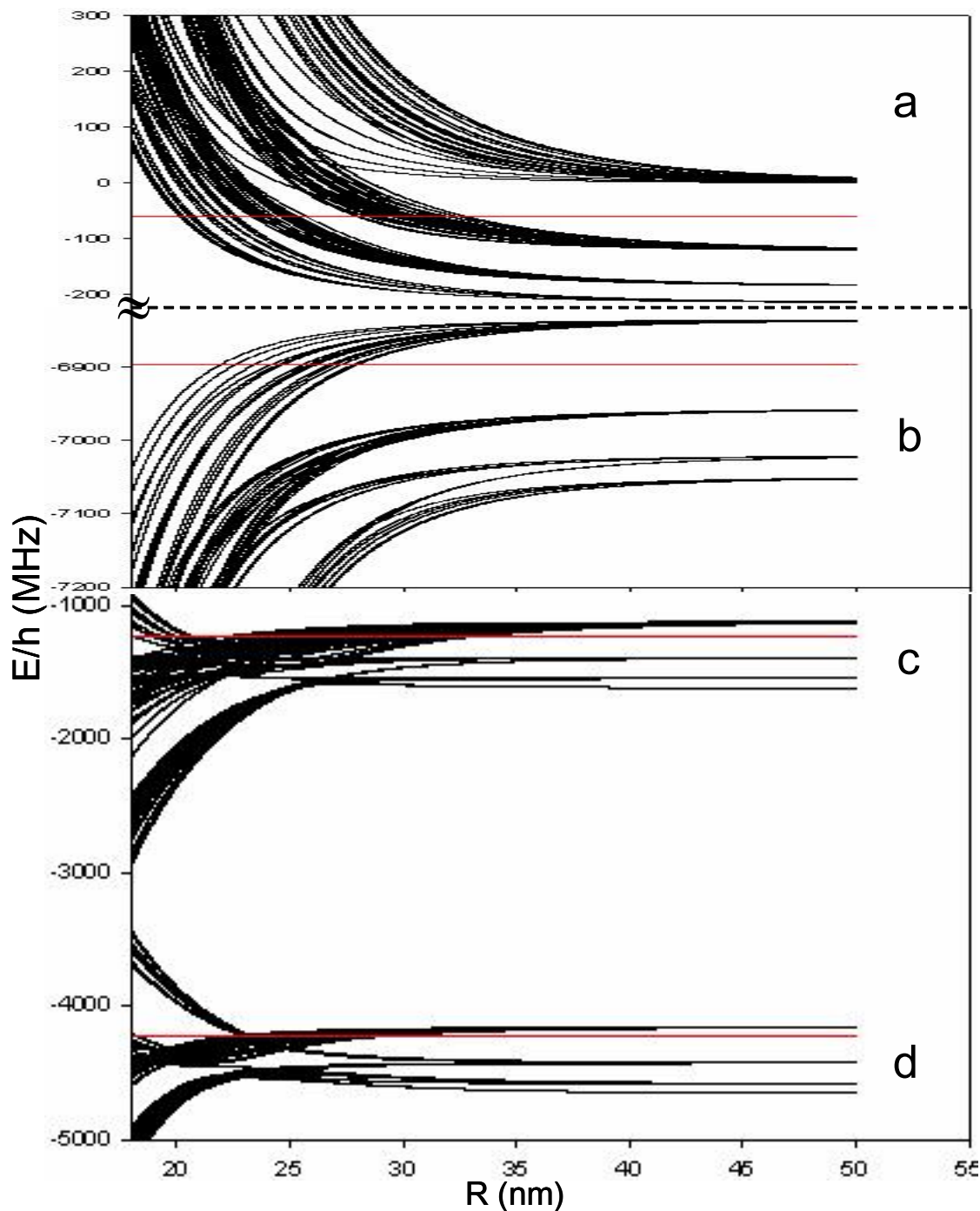


Figure 6.2 Excited state potentials relevant for heteronuclear light-assisted loss. R is the internuclear separation, E/h is the energy of the state divided by Planck's constant expressed in MHz. At infinite R , these potentials correspond to an atom pair in the $5S_{1/2}+5P_{3/2}$ states. The zero of the energy scale is arbitrary. Transitions are accessed from initial ground hyperfine states of (a) $^{85}\text{Rb}(F=3)$, $^{87}\text{Rb}(F=2)$; (b) $^{85}\text{Rb}(F=3)$, $^{87}\text{Rb}(F=1)$; (c) $^{85}\text{Rb}(F=3)$, $^{87}\text{Rb}(F=2)$; (d) $^{85}\text{Rb}(F=2)$, $^{87}\text{Rb}(F=2)$. Both (a) and (b) are accessed with a pulse light which is detuned by 60 MHz to the red of the ^{85}Rb cycling transition, whereas (c) and (d) are accessed with a pulse light which is detuned by 72 MHz to the red of the ^{87}Rb cycling transition. The horizontal red lines depict laser frequency used to access each transition.

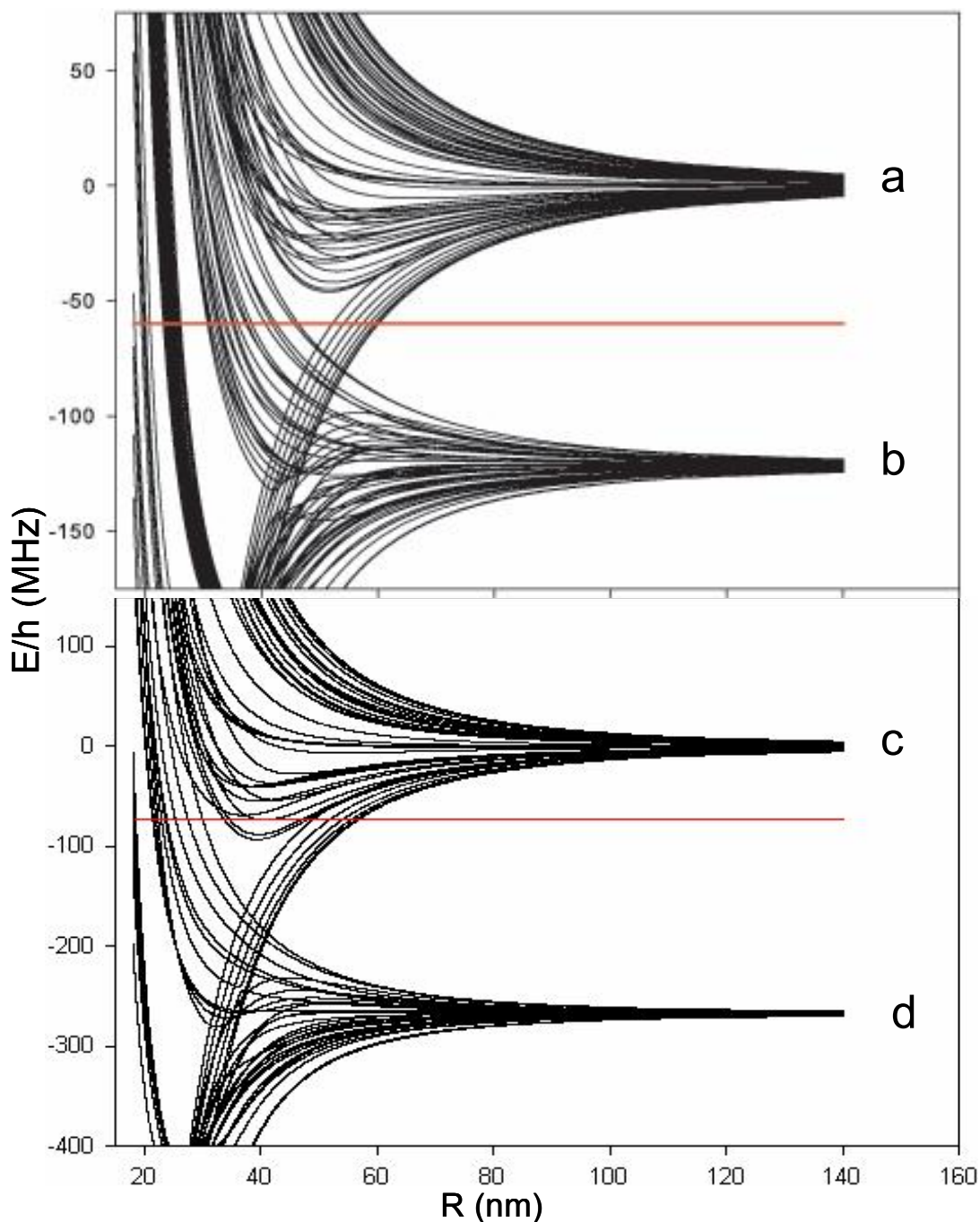


Figure 6.3 Excited-state potentials relevant for homonuclear light-assisted loss. R is the internuclear separation, E/h is the energy of the state divided by Plank's constant expressed in MHz. At infinite R , these potentials correspond to an atom pair in the $5S_{1/2}+5P_{3/2}$ states. The zero of the energy scale is arbitrary. Transitions are accessed from initial ground hyperfine states of (a) and (b) ^{85}Rb ($F=3$); (c) and (d) ^{87}Rb ($F=2$). Both (a) and (b) are accessed with a pulse of light which is detuned by 60 MHz to the red of the ^{85}Rb cycling transition. Whereas for (c) and (d) are accessed with a pulse light which is detuned 72 MHz to the red of the ^{87}Rb cycling transition. In contrast to Figure 6.1, the lettering scheme in this plot refers to specific hyperfine states rather than hyperfine manifolds. The red horizontal red lines depict laser frequency used to access each transition.

$$\begin{aligned}
K &= F(F+1) - I(I+1) - J(J+1), \\
A &= -\frac{1}{h} \frac{\mu_o}{4\pi} \mu_B^2 \frac{2l(l+1)}{J(J+1)} g_I \langle r^{-3} \rangle_{nl} \quad (l > 0) \\
A &= -\frac{4}{3h} \mu_o \mu_B^2 g_I |\Psi_s(0)|^2 \quad (l = 0) \\
B &= \frac{1}{h} \frac{e^2}{2\pi\epsilon_o} \frac{2J-1}{2J+2} \langle r^{-3} \rangle_{nl} Q
\end{aligned} \tag{6.4}$$

A has two values depending on the value of l . l is the orbital angular momentum quantum number. For an atom in the ground state (s), $l=0$; for any excited state (p or higher), $l>0$.

$\langle r^{-3} \rangle_{nl}$ is the average over the wave function of the electronic state nl (n is the principle quantum number). $\Psi_s(0)$ is the value of the Schrödinger wave function at the position of the nucleus. Q is just a scalar quantity, it is usually taken as a measure of the nuclear quadrupole moment. g_I is the g factor associated with the nuclear magnetic moment. While this treatment will produce the proper hyperfine splittings, for the calculated excited-state potentials shown in this thesis other effects were taken into consideration. Effects such as the isotope shift (which depends on the difference in mass between the two isotopes) are included. Since the eigenstates of H_0 are hyperfine state eigenstates, we can use measured values from spectroscopic measurements for the eigenenergies [23].

The second part of the Hamiltonian given in equation 6.2 is the potential associated with the dipole-dipole interaction between the atom pair. This interaction leads to the van der Waals force in the ground-state. A treatment for the Van der Waals' interaction applicable for our system can be found in [24]. In our system we are concerned with long range dipole-dipole interaction, and for systems where $r \gg a_o$ (Bohr radius), the dipole-dipole interaction is written as,

$$V = \frac{e^2}{4\pi\epsilon_0 r^3} (x_1 x_2 + y_1 y_2 - 2z_1 z_2). \quad (6.5)$$

In equation 6.5, all higher order terms in the atom-atom interaction have been ignored. What is kept represents an interaction of two electric dipoles $e\mathbf{r}_1$ and $e\mathbf{r}_2$ separated by \mathbf{r} [24] along the z axis. Equation 6.5 can be represented by spherical harmonics with $l=1$. It is convenient for our applications to do just this, and thus we can make the following substitutions,

$$\begin{aligned} x_{1(2)} &= \sqrt{\frac{2\pi}{3}} r_{1(2)} [Y_1^{-1}(\theta_{1(2)}, \varphi_{1(2)}) - Y_1^1(\theta_{1(2)}, \varphi_{1(2)})] \\ y_{1(2)} &= i\sqrt{\frac{2\pi}{3}} r_{1(2)} [Y_1^{-1}(\theta_{1(2)}, \varphi_{1(2)}) + Y_1^1(\theta_{1(2)}, \varphi_{1(2)})]. \\ z_{1(2)} &= 2\sqrt{\frac{\pi}{3}} r_{1(2)} Y_1^0(\theta_{1(2)}, \varphi_{1(2)}) \end{aligned} \quad (6.6)$$

Where the Y 's are the spherical harmonics. Substituting equation 6.6 into equation 6.5 yields,

$$V = -\frac{e^2}{3\epsilon_0 r^3} r_1 r_2 \left[\begin{aligned} &(Y_1^{-1}(\theta_1, \varphi_1) Y_1^1(\theta_2, \varphi_2) + Y_1^1(\theta_1, \varphi_1) Y_1^{-1}(\theta_2, \varphi_2)) \\ &+ 2Y_1^0(\theta_1, \varphi_1) Y_1^0(\theta_2, \varphi_2) \end{aligned} \right]. \quad (6.7)$$

As mentioned previously, the H_0 energies are in the $|J, I, F, m_F\rangle$ basis, which is appropriate for the system. However, V is best calculated in the $|m_I, m_s, m_L\rangle$ basis, as V is only dependent upon L . While it is easier to calculate the matrix elements of V in the $|m_I, m_s, m_L\rangle$ basis, it must be converted back to the $|J, I, F, m_F\rangle$ basis for calculation of the total H . Thus the Clebsch-Gordan (CG) coefficients to convert V in the $|m_I, m_s, m_L\rangle$ basis to the $|J, I, F, m_F\rangle$ need to be used. For convenience of the following derivation, J and I are left out as indexes of the F, m_F basis set. J does not need to be listed since we

are only considering $J=3/2$, and I is fixed by the identity of the isotope being considered.

To convert between the two basis sets, we can start with the basis set we want ($|F, m_F\rangle$)

and insert a complete basis set such as,

$$|F, m_F\rangle = \sum_{m_I, m_J} |I, m_I; J, m_J\rangle \langle I, m_I; J, m_J | F, m_F\rangle. \quad (6.8)$$

The sum shown in equation 6.8 is zero for all cases unless $m_I + m_J = m_F$. So we can make

the substitution of $m_J = m_F - m_I$. Thus, we can write equation 6.9 as,

$$|F, m_F\rangle = \sum_{m_I, m_J} |I, m_I; J, m_F - m_I\rangle \langle I, m_I; J, m_F - m_I | F, m_F\rangle. \quad (6.9)$$

And $\langle I, m_I; J, m_F - m_I | F, m_F\rangle$ is one of the CG coefficients needed in the conversion.

However, the goal is to find the conversion from the $|m_I, m_s, m_L\rangle$ basis, so we can add

another complete set into equation 6.9.

$$|F, m_F\rangle = \sum_{m_I, m_J} |I, m_I; L, m_F - m_I - m_s; S, m_s\rangle \langle I, m_I; L, m_F - m_I - m_s; S, m_s | I, m_I; J, m_F - m_I\rangle \langle I, m_I; J, m_F - m_I | F, m_F\rangle. \quad (6.10)$$

In equation 6.10, we also used the relation $m_L = m_F - m_I - m_s$. Thus we find the conversion

between basis sets we seek. The CG coefficients from this conversion are

$\langle I, m_I; J, m_F - m_I | F, m_F\rangle$ and $\langle I, m_I; L, m_F - m_I - m_s; S, m_s | I, m_I; J, m_F - m_I\rangle$. To find

the necessary coefficients to convert the matrix elements of V , we first consider the one

atom case in which we seek $\langle F', m'_F | V_{1-atom} | F, m_F\rangle$. Once this is found for the one atom

case, it can be extended easily to the two atom case. We find for the one atom case,

$$\begin{aligned}
\langle F', m'_F | V_{1-atom} | F, m_F \rangle &= \sum_{m_I m_S} \langle I, m_I; J', m'_F - m_I | F', m'_F \rangle \langle I, m_I; J, m_F - m_I | F, m_F \rangle \\
&\langle I, m_I; L', m'_F - m_I - m_S; S, m_S | I, m_I; J', m'_F - m_I \rangle \langle I, m_I; L, m_F - m_I - m_S; S, m_S | \\
&| I, m_I; J, m_F - m_I \rangle \langle I, m_I; L', m'_F - m_I - m_S; S, m_S | V_{1-atom} | I, m_I; L, m_F - m_I - m_S; S, m_S \rangle
\end{aligned} \quad (6.11)$$

In the derivation of equation 6.11, the fact that V only acts on L was used to simplify the expression. As such, the prime indices only include J , F , and L (quantum numbers which depend on L). Since m_I , m_S , I , and S will be unchanged by V , the primes have been dropped on those values. Equation 6.11 shows that for the 1-atom case, there are a total of 4 CG coefficients necessary to convert basis states. This can then be extended into the 2-atom case where we are looking for $\langle F'_1 F'_2 m'_{F1} m'_{F2} | V_{12} | F_1 F_2 m_{F1} m_{F2} \rangle$. This will tell us the proper CG coefficients necessary for converting the matrix elements of V to the desired basis state.

$$\begin{aligned}
\langle F'_1 F'_2 m'_{F1} m'_{F2} | V_{12} | F_1 F_2 m_{F1} m_{F2} \rangle &= \sum_{m_{I1} m_{S1}} \sum_{m_{I2} m_{S2}} \langle I_1, m_{I1}; J'_1, m'_{F1} - m_{I1} | F'_1, m'_{F1} \rangle \\
&\langle I_2, m_{I2}; J'_2, m'_{F2} - m_{I2} | F'_2, m'_{F2} \rangle \langle I_1, m_{I1}; L'_1, m'_{F1} - m_{I1} - m_{S1}; S_1, m_{S1} | I_1, m_{I1}; J'_1, m'_{F1} - m_{I1} \rangle \\
&\langle I_2, m_{I2}; L'_2, m'_{F2} - m_{I2} - m_{S2}; S_2, m_{S2} | I_2, m_{I2}; J'_2, m'_{F2} - m_{I2} \rangle \langle I_1, m_{I1}; J_1, m_{F1} - m_{I1} | F_1, m_{F1} \rangle \\
&\langle I_2, m_{I2}; J_2, m_{F2} - m_{I2} | F_2, m_{F2} \rangle \langle I_1, m_{I1}; L_1, m_{F1} - m_{I1} - m_{S1}; S_1, m_{S1} | I_1, m_{I1}; J_1, m_{F1} - m_{I1} \rangle \\
&\langle I_2, m_{I2}; L_2, m_{F2} - m_{I2} - m_{S2}; S_2, m_{S2} | I_2, m_{I2}; J_2, m_{F2} - m_{I2} \rangle \\
&\langle I_1, I_2, m_{I1}, m_{I2}; L'_1, m'_{F1} - m_{I1} - m_{S1}, L'_2, m'_{F2} - m_{I2} - m_{S2}; S_1, S_2, m_{S1}, m_{S2} | \\
&V_{12} | I_1, I_2, m_{I1}, m_{I2}; L_1, m_{F1} - m_{I1} - m_{S1}, L_2, m_{F2} - m_{I2} - m_{S2}; S_1, S_2, m_{S1}, m_{S2} \rangle
\end{aligned} \quad (6.12)$$

Equation 6.12 is then the final equation for using the necessary CG coefficients for the desired conversion.

The individual matrix elements of V_{12} are calculated via a Fortran program in the $|J, I, F, m_F\rangle$ basis. In that basis, H_0 is diagonal, and the elements of H_0 were included as determined from experimental values from spectroscopic measurements [23]. A particular value of internuclear separation r is selected and the eigenvalues of the $H_0 + V$

matrix are calculated. These eigenvalues correspond to the energies of the interatomic potential states. Figures 6.2 and 6.3 show some of the calculated potential curves from this program.

Figure 6.2 shows that there are many different types of potentials for heteronuclear collisions: purely repulsive (figure 6.2 (a)), purely attractive (figure 6.2 (b)), or a complex mixture of the two (figure 6.2 (c, d)). For transitions with mixed potentials, there are numerous avoided crossings and so some initially attractive potentials become repulsive, and vice-versa. Figure 6.3 shows the homonuclear potentials. Unlike heteronuclear collisions, there are no purely attractive or repulsive excited-state potentials involved in these collisions. The isotopic difference in hyperfine structure produces different homonuclear excited-state potentials for ^{85}Rb and ^{87}Rb . However, for the highest set of energy levels the structure of the potentials are qualitatively the same. In addition, homonuclear potentials are longer ranged than heteronuclear potentials. We could choose which individual potential was excited in our experiments, and could thus systematically study loss rates associated with each set of potentials shown in figures 6.2 and 6.3.

6.2 Experimental conditions and equipment

To measure the light-assisted collisions, we loaded a FORT with either one or simultaneously both isotopes of Rb. Simultaneous loading was accomplished by first capturing and cooling ultracold gases of ^{85}Rb and ^{87}Rb into their MOTs [25]. The MOT's cooling and hyperfine repump lasers [26] for the two isotopes were aligned so that the two MOTs overlap in space. The FORT is the same as that described in Chapter 5, and the alignment and loading follow similar procedures. For these experiments, the

FORT had a trap depth of 120 μK with trapping frequencies of 450 Hz radial by 35 Hz axial. Typical gas cloud temperature for atoms trapped in our FORT was $\sim 15 \mu\text{K}$. Standard detunings during the last stage of loading the optical trap for the MOT cooling lasers were 72 MHz and 60 MHz to the red for ^{87}Rb and ^{85}Rb respectively. As described in previous chapters, the FORT light is turned on and off using an acousto-optical modulator (AOM). After atoms were loaded into the FORT, all other light (MOT and repump lasers) was shut off and the atoms were held for 100 ms in the FORT to allow for equilibration. Imaging was accomplished through standard absorptive imaging techniques described in Chapter 3.3.1. With our parameters, 3.5 million ^{87}Rb atoms or 4.5 million ^{85}Rb atoms could be loaded separately. However, when simultaneously loaded the number dropped to around 2 million for each isotope. This reduction is due in part to light assisted collisions causing loss from the optical trap. Other mechanics are also involved in the reduction of number of atoms that can be trapped, including long range dipole-dipole decohering collisions which are described in Chapter 7.

Once the atoms were prepared in the FORT, we illuminated the atoms with a pulse of laser light to induce light-assisted collision loss. To drive these light-assisted collision losses, one of the MOT cooling lasers at its standard detuning was used to couple atom pairs from the ground state to a selected excited-state potential. The pulse intensities used to make this coupling were 15 mW/cm^2 for ^{85}Rb and 25 mW/cm^2 for ^{87}Rb . We used a typical pulse length of 4 ms for most of our data. However, in the course of our investigation, we collected data extending over a range of pulse times from 0.5 ms to 20 ms. The main trapping and repump MOT lasers provided the pulse light, thus creating an optical molasses. While the complicated polarization structure of an optical molasses is

undesirable for these measurements, using a single beam of comparable intensity would produce too much recoil heating to make effective measurements. We found that there was an elevated initial loss associated with the first few hundred μs of the pulse while the atoms were being hyperfine pumped. In order to avoid these complications, we used a 0.5 ms pulse to establish a baseline and then used longer pulses to measure loss from that point.

An additional complication from illuminating the atom cloud with an optical molasses pulse came in the form of mechanical heating of the cloud. Once the pulse was applied, the atoms in the trap would largely be in the upper hyperfine ground state. The large density of atoms in this state can lead to significant heating of the atoms in the trap due to rescattering effects [27, 28]. This form of mechanical heating is dependent upon the detuning, however, so one would expect that larger detunings could mitigate the heating affects to some extent. But the mechanical heating can have adverse affects on our light-assisted collision loss measurements. First, mechanical heating could lead to density-dependent losses due to subsequent evaporative cooling from the optical trap if the atoms are held there long enough. This would give an appearance of light-assisted collision loss, making it hard to differentiate the actual loss rate. One way this potential systematic uncertainty was mitigated was through our choice of pulse laser detuning. We also adopted a method of data taking which used two image subtraction to measure atom loss.

The subtraction was performed using measurements of the atom loss that involved holding the atoms in the optical trap for only a short ($\sim 5\text{ms}$) time compared to the elastic scattering time. In this technique, images were taken either while the FORT was held on

(in-trap) or after a 5 ms free expansion time (out-of-trap). The idea is to be able to hold atoms for a short enough period of time that many of the effects of mechanical heating will not impact the loss rate measurements. However, for such a short hold time, there isn't enough time for atoms which are not trapped in the FORT to leave the image region. Instead, there is a cloud ("halo") of atoms around the FORT which are not trapped, but are not energetic enough to leave the volume before imaging. To account for this, an in-trap image is taken. In-trap images were taken under the same experimental configurations as the out-of-trap. The only difference was that the FORT was held on longer so that the image included the FORT itself. Without allowing the atoms to be released from the trap, we can image the atoms which form the "halo" around the trap. That is, the atoms which aren't actually trapped in the FORT, but are still able to be imaged. The in-trap image is taken and the image of the FORT is removed. All that is left then are the atoms in the "halo". The "halo" image is subtracted off of the out-of-trap image. This properly accounted for the atoms that had remained in the FORT after the pulse, without having to wait until the atoms lost from the FORT had completely fallen away from the imaging region. The corrected images allowed us to compare then images of the FORT with and without the presence of a "flash" pulse (laser light used to induce light assisted collision loss). The change in number of atoms trapped in the fort between these two corrected images can then be attributed to loss induced by light assisted collisions.

6.3 Data and analysis

In order to confirm that we were observing density-dependent losses, we took data with a single isotope (^{85}Rb) that examined the number remaining in the trap as a function

of pulse time. This data is shown in figure 6.4 as $\log(N)$ vs. pulse time. In figure 6.4, there are also 2 fit curves. The solid line is a straight line fit to the last three data points, where the dashed line is a fit to the data itself. A one-body loss process would fit to the solid straight line fit in figure 6.4, whereas density dependent losses will scale non-linearly with the logarithmic number of atoms in the trap. Since our data did not follow a straight line, we confirmed that we were measuring density-dependent losses. The number remaining as a function of pulse time combined with the measured density of the atoms in the FORT allow for the two-body loss rate (K_2) to be extracted. Equation 6.13 defines the equations for both Rb isotopes for our measured light-assisted collisional loss rates for both isotopes,

$$\begin{aligned} \int d^3x \frac{dn_{85}^F}{dt} &= -K_{2(85-85)}^{Fi} \int d^3x (n_{85}^F)^2 - K_{2(85-87)}^{FF'i} \int d^3x n_{85}^F n_{87}^{F'} \\ \int d^3x \frac{dn_{87}^{F'}}{dt} &= -K_{2(87-87)}^{F'i} \int d^3x (n_{87}^{F'})^2 - K_{2(85-87)}^{FF'i} \int d^3x n_{85}^F n_{87}^{F'} \end{aligned} \quad (6.13)$$

In equation 6.13 $K_{2(85-85)}^{Fi}$, $K_{2(87-87)}^{F'i}$, and $K_{2(85-87)}^{FF'i}$ are the light-assisted collisional loss rates for homonuclear $^{85}\text{Rb}/^{85}\text{Rb}$, $^{87}\text{Rb}/^{87}\text{Rb}$, and the interspecies $^{85}\text{Rb}/^{87}\text{Rb}$ respectively. The label i is for the pulse light frequency used. n_{85} and n_{87} are the ^{85}Rb and ^{87}Rb densities. F and F' are the ground hyperfine states involved in the collision for ^{85}Rb and ^{87}Rb respectively.

We examined all the transitions which could be resonantly excited under our experimental conditions, except for the mixed homonuclear ground-state distributions. For homonuclear conditions, it was relatively easy to set the atoms in either the upper hyperfine ground state or the lower one. However, at the time we did not believe we could reliably measure the fractional hyperfine state distribution of the atoms. As a

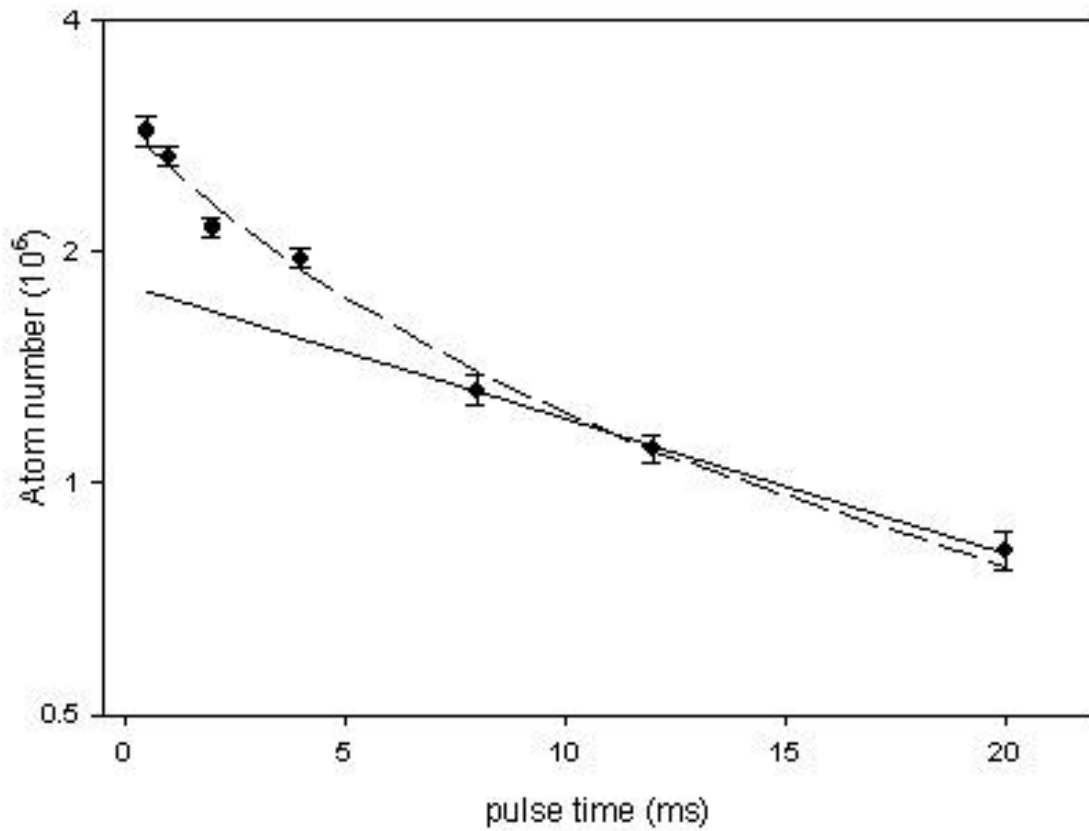


Figure 6.4 Logarithm of ^{85}Rb atom number vs. pulse time. The dashed line is a fit to the curve assuming two-body loss while the straight line is a fit to the last three points. There is clear deviation of the number evolution from a straight line fit to the last data points. This deviation indicates that the measured loss in the system is in fact two-body loss.

result, we did not attempt to take that data. For this reason, we did not investigate the mixed homonuclear ground-state losses. All the measured K_2 values are reported in Table 6.1. In addition to the statistical uncertainties shown in the table, there is an additional overall uncertainty of about 40% in the absolute values of the rates due to uncertainty in our density calibration. This uncertainty is an estimate of our systematic uncertainty; rooted in our uncertainties in the atom number determination, temperature determination, and density calculation. The measured loss rates are much higher than those measured in MOT light-assisted collisions for comparable laser intensities. This can be understood since the trap depth of the MOT is so much greater than that of our FORT. Thus to produce loss in a MOT, significantly more energy must be delivered to the atom pair than what is needed in the FORT.

Loss Table ($\times 10^{-10}$ cm ³ /s)	⁸⁷Rb (F=2) 72 MHz red of the ⁸⁷Rb cycling transition	⁸⁵Rb (F=3) 60 MHz red of the ⁸⁵Rb cycling transition
⁸⁷ Rb (F=2)	6.92(0.52): 6.3(c)	0.48(0.35): 6.2(a)
⁸⁷ Rb (F=1)	---	2.36(0.68): 6.2(b)
⁸⁵ Rb (F=3)	2.22(0.57): 6.2(c)	4.75(0.40): 6.3(a)
⁸⁵ Rb (F=2)	0.61(0.99): 6.2(d)	---

Table 6.1 The measured K_2 values. The isotope and initial hyperfine ground state of each atom in the collision is specified. Also, the pulse light used to induce the loss is specified. The labels for each measured loss rate refer to the specific excited-state potentials shown in figures 6.2 and 6.3. The numbers in parentheses indicate the statistical uncertainties for each measurement.

As is evident in table 6.1, there are statistically significant differences between the measured rates. For example, heteronuclear collisions with ^{87}Rb in the F=2 hyperfine ground-state have significant difference in loss rate depending on which hyperfine ground-state the ^{85}Rb is in. With ^{85}Rb in the F=3 hyperfine ground-state, the rate is $2.22 \times 10^{-10} \text{ cm}^3/\text{s}$; whereas ^{85}Rb in the F=3 ground-state has a rate which is consistent with zero. If we look at figures 6.2 and 6.3, we see that the interatomic separation of the atom pair for a resonant excitation is similar between pairs of potentials with different measured loss rate, meaning that there would be similar number of atom pairs available for a resonant transition. The example listed above corresponded to figure 6.2 (c, d), with both these potentials the resonant excitation occurs at an internuclear separation of about 32-34 nm. Given the shallow nature of the FORT, it seemed reasonable to assume that almost any atom pair which was resonantly excited was likely to be lost. Thus we initially expected the loss rate for these two transitions to be similar. The measured difference between the loss rate of these two transitions indicates otherwise -- that the differences between the interatomic excited-state-ground-state potentials can lead to significant differences in the light-assisted collisional loss rates. By examining the trends in the measured loss rates as a function of the interatomic potential characteristics (e.g., attractive vs repulsive) we can attempt to look for general trends for how these characteristics impact the ultimate collision rate.

To compare the loss rates as they relate to the specific potential characteristics, we started with the simplest of the potentials. The most straightforward collision rates to compare are those which were associated with the potentials shown in figure 6.2 (a, b). These potentials have the simplest structure of all the heteronuclear excited-state

potentials. Unlike the other cases, the long-ranged excited-state potentials are either purely repulsive (figure 6.2 (a)), or purely attractive (figure 6.2 (b)). In previous experiments with photoassociation and light-assisted collisions, repulsive potentials were sometimes associated with “optical shielding” that was used to reduce collision rates [29-34]. Optical shielding works via an atom pair being coupled to a repulsive excited-state. On that excited-state potential, as the atoms approach each other they eventually are “turned around” and move away from each other. Thus the maximum energy which could be acquired by the atom pair was less than the trap depth of the FORT, preventing the loss of the atom pair from the trap. At best they can decay on the upward slope of the repulsive potential in which case kinetic energy from the atom pair is removed and radiated away in the spontaneous photon. Because the atom pairs are prevented from approaching closer to each other from the “turn around”, atom pairs which could have been lost are prevented from being lost. However, those experiments relied on a resonant excitation with the shielding light where the pair could only gain a maximum kinetic energy which was less than the trap depth, and thus not lost from the trap. For our parameters, a resonant excitation can impart ~ 10 times the trap depth in kinetic energy; in previous experiments these conditions led to additional loss [35, 36]. Therefore, if the collision rate is controlled by resonant excitations, the loss rate for purely repulsive and attractive potentials should not be markedly different for our parameters. Our observations, however, show the loss rates for the purely repulsive potentials were significantly lower than for the purely attractive potentials. In order to try to better understand the origin of the difference, we examined both the semiclassical and Landau-Zener model of these losses.

6.4 Models

When looking at different models to explain the results of our experiment, we started with one of the most commonly employed models, the Gallagher-Pritchard (GP) model [37]. In the GP model, they consider a stationary atom pair with interatomic separation R_o which is promoted to an excited-state potential with some rate \mathcal{R} . For the treatment in [37], the excited state potentials are just the long range electrostatic dipole-dipole interaction; represented by $\pm CR^{-3}$ (for repulsive and attractive potentials respectively). The rate \mathcal{R} is given by,

$$\mathcal{R} = \left[\frac{(\Gamma_M / 2)^2}{[\omega_L - \omega(R_o)]^2 + (\Gamma_M / 2)^2} \right] \frac{I}{\hbar \omega_L} \frac{\lambda^2}{2\pi}. \quad (6.14)$$

Where Γ_M is the spontaneous decay rate ($\Gamma_M = 2\Gamma_A$, Γ_A is the natural linewidth of the atomic transition). I and ω_L are the laser's intensity and frequency respectively. ω_o is the atomic resonant frequency, $\omega(R_o)$ is simply ω_o - the potential as a function of R_o (in frequency terms). For our calculations, we simply use a curve from figure 6.2 as those were calculated in MHz. However, the degree of suppression of the measured loss rates for the purely repulsive potentials was not expected in a semiclassical (GP) model of the collision that takes only the excitation rate to the excited-state potentials into account.

Once promoted to these potentials, there is a time ($t(R_o)$) associated with how long it would take the atom pair to move from R_o to R where loss from the trap can occur. The predominate loss mechanism for this process is radiative escape.

Given the excited state lifetime, it is then possible to assign a probability of loss (usually the inverse is quoted, the survival probability) for an atom pair initially excited at R_o . By

convolving the survival probability and the excitation rate \mathcal{R} while assuming a random distribution of atom separations, it is possible to calculate a loss rate in this model.

Since this model treats the internuclear separation of the atom pair as a single number, this is a semiclassical model for calculating the loss. For our conditions, the de Broglie wavelength was on order of both the range over which loss-inducing excitations were significant and the interatomic separation where these excitations occurred. Thus, a semiclassical treatment can only be expected to be approximately correct. Nevertheless, we used this model to calculate our loss; the reason being that the GP model is widely used as calculations for radiative escape trap loss, even for other systems which also do not meet the requisite assumptions of the GP model [12]. Thus our calculation provides a reference on the accuracy of the model compared to actual measurements, and to compare our results to other groups whom have made similar calculations. In making this calculation, we included only radiative escape losses and determined the survival probability for the excitation at a given internuclear radius on this basis. This was performed by explicitly integrating the motion of atom pairs on a representative excited-state potential to find the time the pair would require to accelerate to the trap escape velocity.

These GP model calculations did not reproduce our observed loss rates. In fact, for the detunings used in our experiment the GP model gives a loss rate for the purely repulsive potentials which was an order of magnitude greater than what we actually measured. Furthermore, the model predicted that the purely repulsive potentials would yield a comparable loss to the attractive potentials. Thus the GP model misses both the magnitude and the ratio (repulsive vs. attractive) of the measured light-assisted collision

loss of our system, although it matches our initial intuitions about the nature of the expected loss.

Since the semi-classical picture couldn't explain the observed differences, we sought out a different model to explain the experimental results. A better description of the collision dynamics for these potential was obtained by using a dressed-state picture and examining Landau-Zener (LZ) crossing probabilities. While the GP model considers the atom pair in an undressed state, the LZ model employed considers the atom pair in a dressed state. As the atoms approach one another during a collision, they encounter avoided crossings. These avoided crossings are produced at the value of internuclear separation R_C (Condon radius) where the light resonantly couples the ground and the excited state. At these avoided crossings, the atoms can either remain in the ground-state or adiabatically transfer to the excited-state. Depending on the properties of the excited-state potentials, these adiabatic transfers can either result in “shielding” or loss. By examining the avoided crossings, we can calculate probabilities for making loss inducing transition. This LZ approach has been shown to accurately reproduce more sophisticated theoretical treatments (e.g. Monte-Carl Wavepacket Dynamics) for both attractive [38] and repulsive [39] potentials.

According to the LZ theory [40, 41], the probability for making a diabatic crossing is given by,

$$P = \exp\left[-\frac{\hbar\Omega^2}{2\pi\alpha v}\right]. \quad (6.15)$$

In equation 6.16 $\Omega = \Gamma\sqrt{(I/I_{sat})/2}$ (Γ is the natural linewidth), α is the slope of the potential curve at the Condon radius, and v is the velocity of the atom pair. Figure 6.5

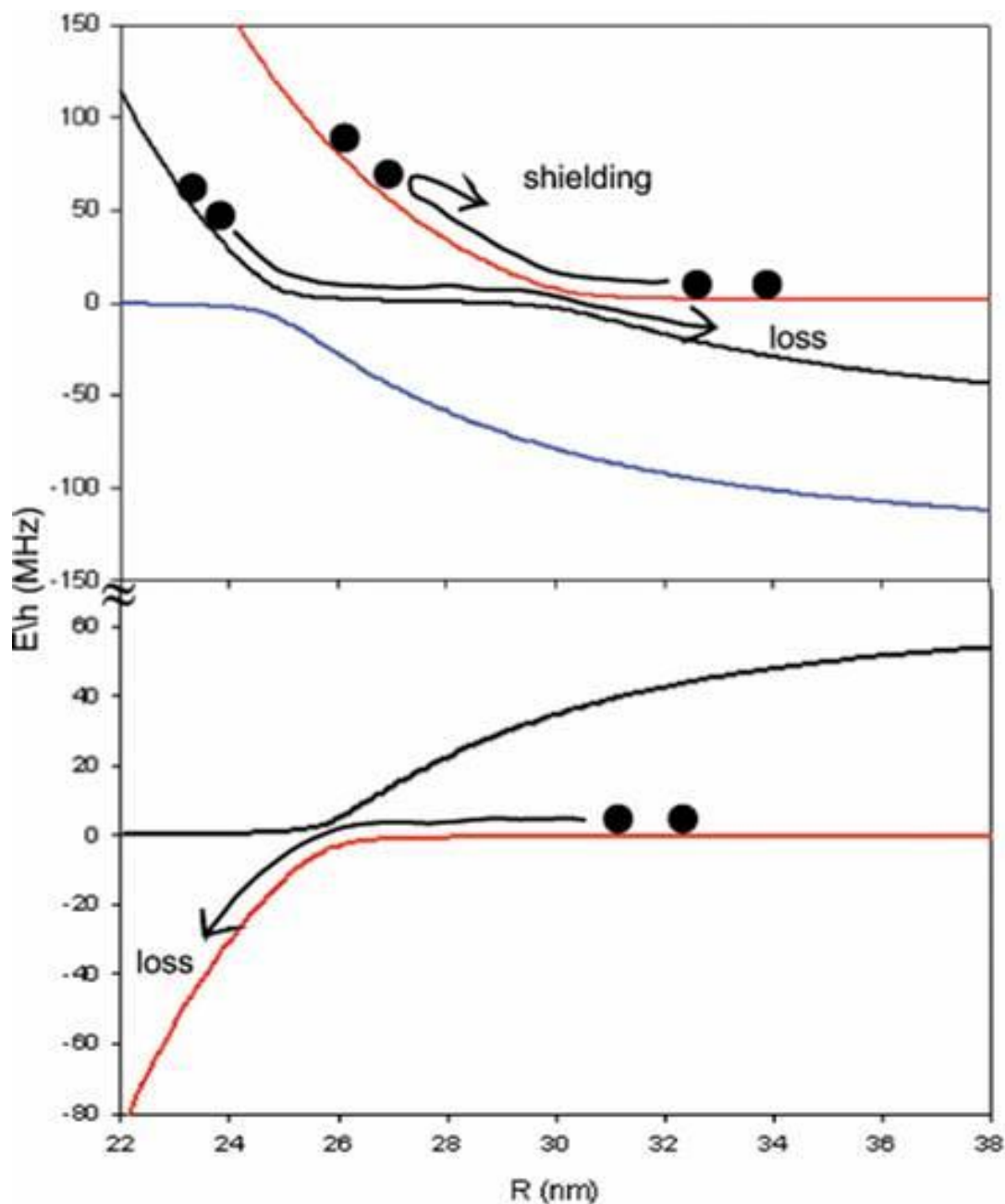


Figure 6.5 Representative dressed state potentials used in the LZ calculation of relative loss probabilities. The zero of the energy scale is selected to correspond to the bare ground-state energy at $R=\infty$. The top figure corresponds to the purely repulsive potential case [corresponding to figure 6.2(a)] and the bottom figure corresponds to the purely attractive case [corresponding to figure 6.2(b)]. In the top figure, a sample shielding and loss sequence of crossings are indicated. In the bottom figure, a sample loss sequence is shown.

shows examples of the LZ crossing for the repulsive (figure 6.5(a)) and attractive (figure 6.5(b)) potential curves. By comparing the sequence of adiabatic and diabatic crossing that result in the loss in the attractive and repulsive cases, we can formulate an LZ prediction for the ratio of those loss rates and compare them to our measurement.

If we consider the most simplistic way in which the probabilities of transitions can be considered, the atoms undergo a transition between dressed states at each avoided crossing or not. For a series of avoided crossings, then, the probability is determined by the product of the individual transitions in this simple picture.

To estimate the ratio between the attractive and repulsive case, we model the numerous atom potentials with just a few representative potentials. In actuality, the potential curves associated with the excited-state potentials in our system are extremely complex. The model, however, will give information as to magnitude and ratio of loss between the attractive and repulsive cases. In our calculation of Ω we average over all possible light polarization and include a Clebsch-Gordon coefficient based on the asymptotic hyperfine state character of the excited-state potential. For our parameters, the value of P at the mean velocity is 0.70 and 0.94 for the outermost and innermost avoided crossings in figure 6.5(a) and 0.59 for the avoided crossing shown in figure 6.5(b). By tallying all the possible crossings, determining which crossing sequences produce loss, performing a thermal average over all the collision energies in the cloud, and using equation 6.15; we can estimate the diabatic crossing probability at each avoided crossing. The ratio of the loss probability in the attractive case to the loss probability in the repulsive case can then be calculated.

For the experimental parameters for our system, that calculated ratio is 1.6. This ratio was obtained by ignoring spontaneous emission at R_C and hyperfine changing collisions near $R=0$. Ignoring these collisions does not dramatically change the ratio of attractive to repulsive loss; going to 1.3 when estimates of the magnitude the hyperfine changing spontaneous emissions are included. While the change in ratio from 1.6 to 1.3 may seem significant, it is made in comparison to the experimental ratio which is 4.9. What this demonstrates is that spontaneous emission and hyperfine changing collisions cannot account observed experimental difference. The reason for this insensitivity is that approaching the attractive potential case avoided crossing from $R=0$ is very similar to approaching the outermost repulsive potential avoided crossing from $R=\infty$. This means that increasing the loss at these avoided crossing increases the loss probability for both the attractive and repulsive potential case.

While this ratio of probabilities suggests that the attractive potential should produce a larger loss rate than the repulsive, the factor of 1.6 is not consistent with our measured rates at the 95% confidence level. I note, though, that to determine whether the difference between the predicted and observed values was statistically significant involved non-standard error propagation. For example, given the size of the uncertainty compared to the measured rate for the ^{85}Rb , $F=3$ + ^{87}Rb , $F=2$ collision channel ($0.48 \pm 0.35 \times 10^{-10}$ cm³/s), we could not use the usual error propagation techniques that implicitly assume that the uncertainty is small compared to the measured value. Instead, we used Gaussian distributions of the appropriate width centered at the measured central values and then explicitly calculated the probability of various ranges of loss ratio, and this treatment indicated that the results appear to be statistically different than predicted.

There are several factors that could explain this disagreement. First, the LZ model calculates a probability of loss, but in order to produce a loss rate an incoming flux needs to be specified as well. Since R_C is similar for both the repulsive and attractive curve cases, from purely geometric considerations then the influx between the two states should be similar, and in any case the repulsive potentials would be favored since R_c is slightly greater. One would, ideally, expect the same number of atom pairs available for these collisions in both the purely attractive and purely repulsive case. However, this reasoning is semiclassical in nature and this is a quantum system. In reality, different partial waves will experience different angular momentum barriers at the relevant radii. The interatomic potential will tend to enhance these barriers in the repulsive case and suppress them in the attractive case and so determining the appropriate incoming flux at R_c is more complicated than as would be determined from purely geometric considerations.

Not only the incoming flux should be treated quantum mechanically. A quantum consideration of the collisions allows for the opportunity for destructive and constructive interferences to arise. For instance, during some collisions in the attractive potential case, atoms pairs will make multiple transits between $R=0$ and $R=R_C$ as they are reflected at $R=0$ and at the avoided crossings. The ultimate outward flux of these oscillating atoms pairs depends on acquired phases that are not included in our simple model. Also, for our parameters the approximation of reducing the numerous potential curves to a single potential curve is not severe if only average LZ crossing probabilities are considered. However, this reduction will remove interference effects arising from multiple crossings [42, 43, 44]. For our system, though, thermal averaging over incoming velocities and the

fact that the incoming collisions occur with a range of magnetic sublevels would likely wipe out some of these interference effects.

Beyond these interference considerations, problems with the simple LZ picture can also arise because of the assumption of average polarization. In reality, the atom's magnetic sublevel distributions and the light polarization are not uncoupled. Optical pumping will correlate the atom states and the light polarization. This can produce different effective values for Ω for the repulsive and attractive cases. However, estimates of the impact due to this optical pumping should not change the ratio by more than 20%. Additionally, central to the LZ assumption is that v is a constant during the crossing and that the actual potentials can be modeled by replacing them with the appropriate tangent lines near R_C . Given that the potentials for our parameters near R_C are not as sharp in an absolute sense as in other experiments [29, 31, 35, 36]; these assumptions may be more questionable in our work. Our main conclusion is that even for the potentials with the simplest of structure, neither the GP model nor the LZ model reproduce the observed ratio of loss rates between the attractive and repulsive cases. Thus, the dynamics of the collision are not well described by these simple models and appear to depend sensitively on the details of the potentials. This seems to suggest that a more rigorous quantum mechanical treatment is necessary even for purely attractive and repulsive potentials.

6.5 Mixed potentials

The majority of this chapter so far has focused on the relatively simple potentials of figure 6.2(a, b) due to the simplicity of the excited-state potentials. The structures of the other potentials contained in figure 6.2 are more complicated, making even qualitative comparison of their loss rates more difficult. In particular, when mixing both attractive

and repulsive potentials, many avoided crossings are generated in the potentials themselves. This complex nature of the potentials is depicted in figure 6.6. Thus some potentials which are initially attractive during the collision can become repulsive at short range and vice-versa; this lead to complex dressed-state potential curves. While detailed calculation in this system would be difficult, it is reasonable to expect that the presence of repulsive potential curves could mitigate the loss rate. The repulsive curves can turn colliding atom pairs away from short internuclear radii and slow initially accelerated atom pairs, thus reducing the loss rate from what it would be otherwise.

Comparing the loss rates associated with the potentials in figure 6.2(c, d) is suggestive of this. The loss rate for the potential associated with figure 6.2(d) is less ($0.66 \pm 0.99 \times 10^{-10} \text{ cm}^3/\text{s}$) than that for the potentials represented in figure 6.2(c) ($2.22 \pm 0.57 \times 10^{-10} \text{ cm}^3/\text{s}$). One of the differences between the two potentials was that the one in figure 6.2(d) is shorter ranged, leading to an expectation of less loss based on the number of atom pairs that collide with sufficiently low impact parameters. In addition, the avoided crossing structure of figure 6.2(d) is much sharper, leading to steeper repulsive potential curves, from which a mitigation of the loss rate would be expected.

In contrast to the potentials shown in figure 6.2, those in 6.3 depict a few of the homonuclear excite-state potentials. Figure 6.3(a, b) for ^{85}Rb alone while figure 6.3(c, d) are for ^{87}Rb alone. Similar to some of the heteronuclear potentials of figure 6.2, these potentials too have a mixture of attractive and repulsive potentials. However, the homonuclear potentials are longer ranged than the heteronuclear ones. This is due to the difference in the asymptotic nature between the two cases. The asymptotic nature of the heteronuclear potentials is $1/R^6$ whereas for homonuclear potentials it is $1/R^3$. This can

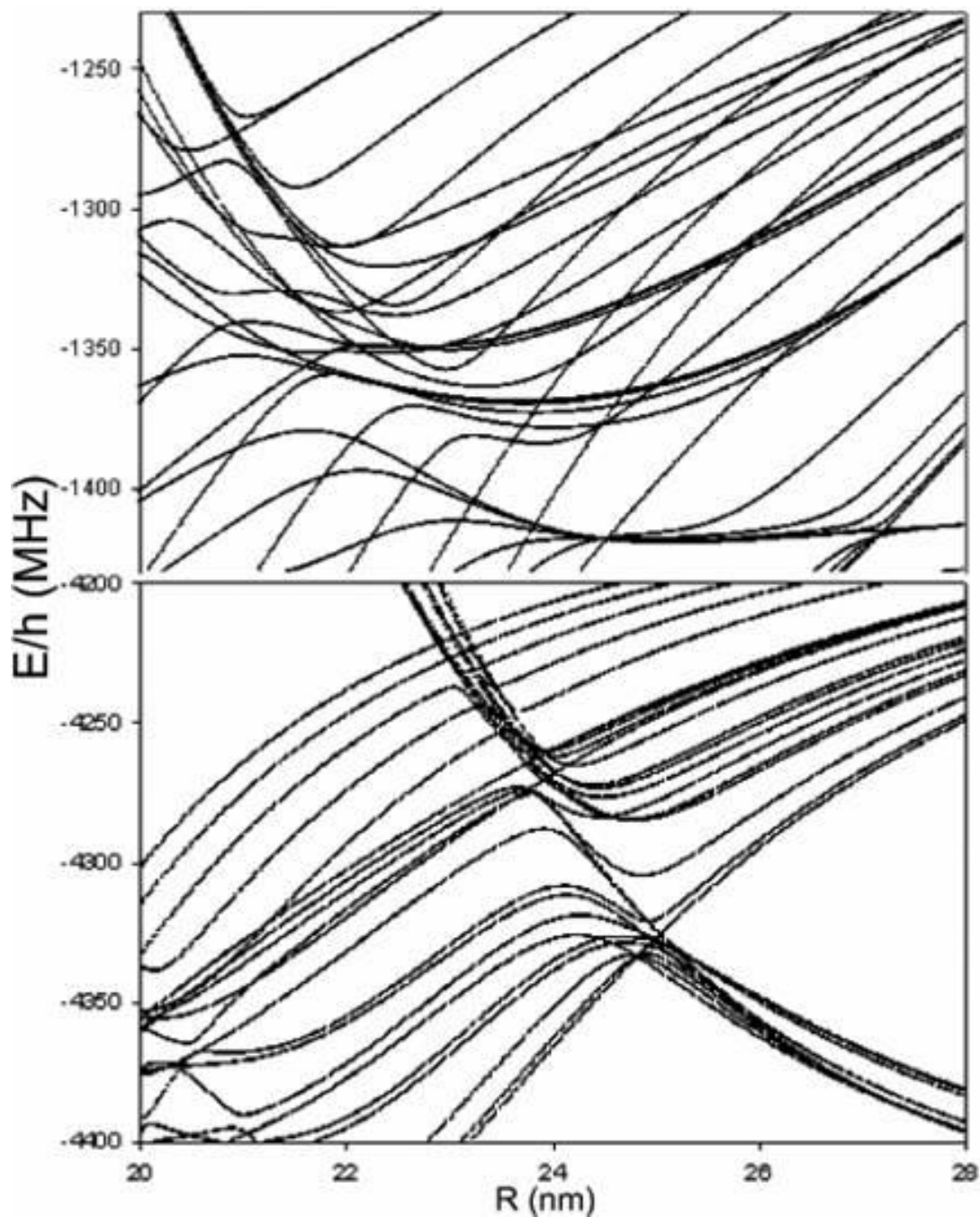


Figure 6.6 Excited bare state potential avoided crossings. The top plot is the potential show in figure 6.2(c) with its x and y axes rescaled. The bottom plot is the same for the potential indicated in figure 6.2(d). This plot shows two regions of the excited-state heteronuclear potentials in more detail to indicate the complicated avoided crossing structure of these potentials.

be seen in figures 6.2 and 6.3, where for heteronuclear potentials by $R=45$ nm the potentials have become relatively flat, wherein homonuclear potentials do not become relatively flat till about $R=95$ nm. This longer range would suggest, all other things being equal, a larger light-assisted collision cross section. In fact, the measured loss rates (see table 6.1) indicate that the loss rates are larger for the homonuclear case. However, since the homonuclear potentials of ^{85}Rb and ^{87}Rb are so qualitatively similar, one would expect the homonuclear loss rates of the two isotopes to be similar as well. Despite the similarities, the measured homonuclear loss rates for the two isotopes is different, with ^{85}Rb loss being slightly less than ^{87}Rb . The difference in measured loss rate could be produced from a combination of the difference in the relevant Clebsch-Gordan coefficients for the transitions and the presence of the repulsive potentials in ^{85}Rb which are longer ranged. This could allow for higher “self-shielding” effects as were discussed earlier. Once again, the lower loss rate is associated with the potential with the more repulsive character.

6.5.1 Saturation effects. An interesting effect observed in the homonuclear data was that the loss rate was saturated at our intensities [45-49]. To measure the saturation of our losses, we decreased the intensity of our lasers by half during the pulse which induced light-assisted collisions. The ratio of the half intensity loss rate to the full intensity loss was then computed. Due to limitations in our experimental apparatus, not all conditions could be tested for half intensity loss. This was due to insufficient signal-to-noise for the lower values of K_2 . Additionally, in order to consistently achieve the number of atoms loaded into the FORT between the full and half intensity cases, we needed all the laser power available in the trapping laser. Thus, we could not use the

deflected beam from the AOM for the main trapping lasers. This meant that the intensity of those beams (which also composed the pulse used to induce light-assisted collisions) could not be continuously reduced to zero without significant decline in the number of atoms trapped in the FORT in the first place. We were able to test the half intensity case for light-assisted collisions induced by the hyperfine repump laser, though. Without saturation effects, the loss should scale linearly with the light intensity. With ^{85}Rb and ^{87}Rb homonuclear loss, the ratio of the measured K_2 at half-intensity to the rate measured at full intensity is 0.98 ± 0.12 and 1.08 ± 0.12 respectively. The fact that no significant change was observed indicates that the losses are severely saturated at our trap intensities.

Given the reported results for photoassociation saturation, we first examined whether or not the unitarity limit could be responsible for the observed saturation [47, 48, 49]. The thermally averaged s-wave loss rate at our temperatures was 2×10^{-10} cm^3/s . Our measured loss rates are greater than this, but we expect contributions from higher order partial waves. A classical estimation of the most probable collision energy in the cloud indicates that contributions up to at least d-wave produces a unitarity limit of 18×10^{-10} cm^3/s ; higher than the loss rates measured. This indicates that unitarity is not the cause of the observed saturation. Furthermore, in the unitarity limited regime the scattering rate should not distinguish between ^{85}Rb and ^{87}Rb , yet the homonuclear loss rate saturates at different collision rates. This seemingly suggests the details of the potential must play a role in determining the loss rate. Additionally, the heteronuclear loss rate does not appear to saturate and a decrease in the flash intensity by half seems consistent with a decrease in the loss rate by half. The measured ratio of the heteronuclear loss of half-intensity to full-intensity was measured to be 0.60 ± 0.20 .

Thus it seems from our data that unitarity is not the cause of the homonuclear loss rate saturation, our data is more consistent with what is known as ground-state depletion. Ground-state depletion refers to the finite pair formation rate of the atoms in the cloud [50]. A classical hard-sphere estimate for our experimental conditions shows that for a required close approach, internuclear separation of $R=72$ nm, the maximum pair formation rate is 7×10^{-10} cm³/s; consistent with the observed loss rate. While this is just an estimate, it along with the observed saturation indicates that ground-state depletion likely plays a role in these collisions. However since the observed saturation rates are different, the homonuclear potentials must induce some dynamics which alter the collision rates. All this is consistent with a model where not every atom pair that collides at the critical radius suggested by ground-state depletion is lost.

In conclusion, the measurements of the light-assisted collision loss rates for both homonuclear and heteronuclear conditions varied significantly depending on the isotopes involved in the collision and their hyperfine state. We observed that a purely repulsive potential reduced the loss rate, in spite of the fact that a direct excitation to the excited state would be expected to produce a large enough gain in kinetic energy to the atom pair to eject them from the FORT. A saturation of the homonuclear collisions at intensities lower than in many other light-assisted collisions and photoassociation experiments seemingly points towards ground-state depletion contributions to the saturation loss rates. Despite the fact that ⁸⁵Rb and ⁸⁷Rb homonuclear loss rates were saturated, they saturate at different rates, indicating that the details of the potentials involved in the collision play a significant role in the dynamics. For all measured losses, there was a general trend that the more repulsive the character of the potential (both through purely repulsive states and

states which had become repulsive via avoided crossings), the lower the loss rate. Future experiments will involve dual loading of our FORT in which we will wish to be able to “tune” independently the number of atoms of each isotope we trap in the FORT.

Ultimately, understanding the nature of the light-assisted collisions will be useful in predicting number load as well as understanding how these collisions may vary over the load time of the FORT. Additionally, understanding which hyperfine states induce the least amount of light-assisted collisions can aid in the reduction of and account for loss out of our FORT as we perform optimization experiments.

References for Chapter 6

- ¹ John Weiner *et al.*, Rev. Mod. Phys. **71**, 1 (1999)
- ² M. Prentiss *et al.*, Opt. Lett. **13**, 452 (1988)
- ³ L. Marcassa *et al.*, Phys. Rev. A **47**, R4563 (1993)
- ⁴ D. Sesko, T. Walker, C. Monroe, A. Gallagher, and C. Wieman, Phys. Rev. Lett. **63**, 961 (1989)
- ⁵ M. G. Peters, D. Hoffmann, J. D. Tobiason, and T. Walker, Phys. Rev. A **50**, R906 (1994)
- ⁶ R. S. Williamson III and T. Walker, J. Opt. Soc. Am. B **12**, 1393 (1995)
- ⁷ J. Kawanaka, K. Shimizu, H. Takuma, and F. Shimizu, Phys. Rev. A **48**, R883 (1993)
- ⁸ N. W. M. Ritchie *et al.*, Phys. Rev. A **51**, R890 (1995)
- ⁹ G. D. Telles *et al.*, Phys. Rev. A **63**, 033406 (2001)
- ¹⁰ M. E. Holmes, M. Tschernack, P. A. Quinto-Su, and N. P. Bigelow, Phys. Rev. A **69**, 063408 (2004)
- ¹¹ He Wang and C. Stwalley, J. Chem. Phys. **108**, 5767 (1998)
- ¹² M. W. Mancini *et al.*, Eur. Phys. J. D **30**, 105 (2004)
- ¹³ C. D. Wallace, T. P. Dinneen, Kit-Yan N. Tan, T. T. Grove, and P. L. Gould, Phys. Rev. Lett. **69**, 897 (1992)
- ¹⁴ Paul Feng, Dominikus Hoffmann, and Thad Walker, Phys. Rev. A **47**, R3495 (1993)
- ¹⁵ P. D. Lett *et al.*, Phys. Rev. Lett. **71**, 2200 (1993)
- ¹⁶ S. J. M. Kuppens, K. L. Corwin, K. W. Miller, T. E. Chupp, and C. E. Wieman, Phys. Rev. A **62**, 013406 (2000)
- ¹⁷ K. M. O’Hara, S. R. Granade, M. E. Gehm, and J. E. Thomas, Phys. Rev. A **63**, 043403 (2001)
- ¹⁸ Jinwei Wu *et al.*, J. Appl. Phys. **100**, 054903 (2006)
- ¹⁹ J. D. Miller, R. A. Cline, and D. J. Heinzen, Phys. Rev. A **47**, R4567 (1993)
- ²⁰ M. Marunescu and H. R. Sadeghpour, Phys. Rev. A **59**, 390 (1999)
- ²¹ M. Marunescu and A. Dalgarno, Phys. Rev. A **52**, 311 (1995)
- ²² E. Arimondo, M. Ingascio, and P. Violino, Rev. Mod. Phys. **49**, 31 (1977)
- ²³ G. P. Barwood, P. Gill, and W. R. C. Rowley, Appl. Phys. B **53**, 142 (1991)
- ²⁴ J. J. Sakurai, *Modern Quantum Mechanics*, edited by San Fu Tuan (Benjamin/Cummings, Menlo Park, CA, 1985)
- ²⁵ W. Suptitz *et al.*, Opt. Lett. **19**, 1571 (1994)
- ²⁶ The $5S_{1/2} F=1 \rightarrow 5P_{1/2} F=2$ and $5S_{1/2} F=2 \rightarrow 5P_{1/2} F=3$ transitions were used for pinging ^{87}Rb and ^{85}Rb respectively.
- ²⁷ C. G. Townsend *et al.*, Phys. Rev. A **52**, 1423 (1995)
- ²⁸ Thad Walker, David Sesko, and Carl Wieman, Phys. Rev. Lett. **64**, 408 (1990)
- ²⁹ V. Sanchez-Villicana *et al.*, Phys. Rev. Lett. **74**, 4619 (1995)
- ³⁰ D. Hoffmann, S. Bali, and T. Walker, Phys. Rev. A **54**, R1030 (1996)

-
- ³¹ S. R. Muniz *et. al.*, Phys. Rev. A **55**, 4407 (1997)
- ³² M. Walhout, U. Sterr, C. Orzel, M. Hoogerland, and S. L. Rolston, Phys. Rev. Lett. **74**, 506 (1995)
- ³³ Reginaldo Napolitano, John Weiner, and Paul S. Julienne, Phys. Rev. A **55**, 1191 (1997)
- ³⁴ James P. Shaffer, Witek Chalupczak, and N. P. Bigelow, Phys. Rev. A **61**, 011404(R) (1999)
- ³⁵ S. Bali, D. Hoffmann, and T. Walker, Europhys. Lett. **27**, 273 (1994)
- ³⁶ D. Hoffmann, P. Feng, and T. Walker, J. Opt. Soc. Am. B **11**, 712 (1994)
- ³⁷ Alan Gallagher and David E. Pritchard, Phys. Rev. Lett. **63**, 957 (1989)
- ³⁸ K. A. Suominen, Y. B. Band, I. Tuvi, K. Burnett, and P. S. Julienne, Phys. Rev. A **57**, 3724 (1998)
- ³⁹ K. A. Suominen, M. J. Holland, K. Burnett, and P. Julienne, Phys. Rev. A **51**, 1446 (1995)
- ⁴⁰ C. Zener, Proc. R. Soc. London, Ser. A **137**, 696 (1932)
- ⁴¹ L. Landau, Phys. Z. **2**, 46 (1932)
- ⁴² W. Harsgawardhan and G. S. Agarwal, Phys. Rev. A **55**, 2165 (1997)
- ⁴³ A. A. Rangelov, J. Piilo, and N. V. Vitanov, Phys. Rev. A **72**, 053404 (2005)
- ⁴⁴ S. S. Ivanov and N. V. Vitanov, Phys. Rev. A **77**, 023406 (2008)
- ⁴⁵ C. I. Sukenik, D. Hoffmann, S. Bali, and T. Walker, Phys. Rev. Lett. **81**, 782 (1998)
- ⁴⁶ C. Haimberger *et. al.*, J. Phys. B **39**, S957 (2006)
- ⁴⁷ S. D. Kraft *et. al.*, Phys. Rev. A **71**, 013417 (2005)
- ⁴⁸ U. Schloder, C. Silber, T. Deuschle, and C. Zimmermann, Phys. Rev. A **66**, 061403(R) (2002)
- ⁴⁹ I. D. Prodan, M. Picler, M. Junker, R. G. Hulet, and J. L. Bohn, Phys. Rev. Lett. **91**, 080402 (2003)
- ⁵⁰ Alan Gallagher, Phys. Rev. A **44**, 4249 (1991)

Chapter 7

Collisional Disruption During Shallow Optical Trap Loading in an Ultracold

Mixture of $^{85}\text{Rb}/^{87}\text{Rb}$.

Previous chapters have discussed the simultaneous loading of ^{85}Rb and ^{87}Rb into the Far Off Resonant Trap (FORT). In particular, chapter 6 discussed in some detail light-assisted collisions (LAC) which caused heteronuclear loss from the FORT during a simultaneous load. The heteronuclear loss rates can be examined and measured to predict the maximum number of atoms which can be loaded into the trap during a simultaneous load. Yet while examining the loading of the FORT from a Magneto-Optical Trap (MOT), we found a discrepancy between the measured and calculated maximum trap number. For example, when loaded alone (homonuclear) under a certain set of conditions, we obtained a maximum number for ^{85}Rb of ~ 4 million and for ^{87}Rb of ~ 3.5 million atoms. Ideally there would be no interaction between ^{85}Rb and ^{87}Rb , in which case for a heteronuclear load we could expect a total of 7.5 million atoms. However, there are known heteronuclear loss rates such as LAC and if we account for those loss mechanisms we find that we should expect a total of about 6.2 million atoms in the FORT. Yet the actual measurement is closer to about 4.8 million atoms trapped in the FORT. Thus there appears to be something besides the heteronuclear LAC losses at work in limiting the number of atoms loaded into the FORT during heteronuclear loading.

This chapter will focus on our observations concerning the loading of ^{87}Rb into the FORT in the presence of an ultracold cloud of ^{85}Rb . The presence of the ^{85}Rb resulted in a marked decrease of the ^{87}Rb load rate. Ultimately, we believe that this decrease was due to a decrease in the laser cooling efficiency needed for effective loading. While many dynamics which disrupt loading efficiency have been observed to arise in other systems when cooling in a dense cloud of atoms (such as radiation pressure, reabsorption, adverse optical pumping mechanisms, etc.); the large detuning between the transitions of ^{85}Rb and ^{87}Rb should isolate the isotopes from these effects. Yet the observed load rate decrease indicates that there was significant interaction between ^{85}Rb and ^{87}Rb while ^{87}Rb was loaded into the FORT. Collisions between the isotopes in the absence of the laser light did not have a sufficiently large rate to account for these losses. Additionally, the measured loss rates of LAC in our system could not account for the observed decrease in trapped atom number. In the absence of other collision mechanisms, we surmise that the presence of the laser light alters the collision rates and affects the overall cooling efficiency of the atoms while being loaded into the FORT.

As part of our experimental investigation to understand this cross-isotope loading disruption, we investigated the effect ^{85}Rb possibly had on the optical pumping (hyperfine-state distribution) of ^{87}Rb while loading the FORT. We examined the change in the steady state hyperfine distribution fraction in the ^{87}Rb F=2 hyperfine state between a simultaneous FORT load and an ^{87}Rb alone FORT load. The change in the fraction was then investigated as a function of ^{85}Rb number. This change in fraction allowed us to see if the presence of ^{85}Rb could influence the optical pumping (and hence steady-state hyperfine distribution) of ^{87}Rb during the load. A disruption to the optical pumping

could produce decoherence in the ground state or reduce the efficiency of sub-Doppler cooling. These effects could negatively impact the number of atoms we could load into the FORT as well as reducing the load rate at which atoms can be loaded into the FORT.

7.1 Effective laser cooling and coherence

Effective laser cooling in dense clouds of ultracold atoms is necessary for efficient loading of the atoms into a shallow FORT (such as the FORT in our system [1]) from an optical molasses [2-9]. As mentioned in previous chapters, our FORT is essentially a conservative potential. Because of this, laser cooling mechanisms such as sub-Doppler cooling are needed to achieve optimum load rate and numbers. In general, it is known that the performance of the sub-Doppler cooling mechanisms decreases as the density of the atoms in the cloud being cooled increases; this has been observed both theoretically [10,11,12] and experimentally [13, 14, 15]. This decrease is mainly a result of scattered near-resonant laser light by the atoms, however. Given this fact, the introduction of another isotope (^{85}Rb) with resonances which are well detuned from the initial isotope (^{87}Rb) should not significantly impact cooling performance. This is because the cross scattering of light should be minimal due to the large detuning (e.g. the scattering of ^{85}Rb -resonant light by ^{87}Rb atoms was negligible). As such, there is little reason to suspect that during a simultaneous FORT load of both ^{85}Rb and ^{87}Rb should have a large effect on each others' laser cooling performance. However, in the course of our simultaneous FORT loading, we found a significant decrease in the number of the ^{87}Rb atoms in the FORT when ^{85}Rb is simply present in a MOT during the load, indicating the presence of some cross-isotope effect. In addition, we found that the presence of ^{85}Rb was able to affect the ^{87}Rb steady-state hyperfine distribution. This

cross-isotope dynamic affected the sub-Doppler cooling mechanisms necessary for FORT loading, which produced the observed decrease in the load rate and number.

Additionally, coherence had a significant effect on the optical pumping which occurs as an atom traversed the laser light's polarization field. This was manifested in the change in the steady state hyperfine state distribution. An excited-state m_F level can be coupled to a variety of lower-state m_F levels through various polarizations. However, coherence added interference to this coupling. The coherence caused an enhancement or reduction in the coupling between lower-state m_F levels and produces a specific spin state distribution. It will be shown later that the effect of coherence is essential to our sub-Doppler cooling and FORT loading for our experimental parameters.

There are other mechanisms such as reabsorption which can lead to heating in optically thick clouds as well [16-19]. However, the large detuning between isotopes also negates cross-species effects due to these other mechanisms. In the light field of our optical molasses used to cool ^{87}Rb , any ^{85}Rb atoms in the same light field would scatter photons at a rate which was ~ 400 times slower than that of ^{87}Rb itself (for ^{85}Rb atoms in the $F=2$ ground state). Furthermore, the light scattered from these non-resonant atoms is also extremely coherent, with only a tiny incoherent contribution to the scattered spectrum. Thus it should have been the case that ^{85}Rb would have acted essentially as a non-interacting species with respect to the ^{87}Rb FORT load. Thus, cross-species light scattering is an insufficient explanation of our observations.

7.1.1 Known collisions. In the absence of scattered light being able to explain any cross species reduction in cooling efficiency, it seems reasonable to ask if there was some type of collision that could be responsible. A chief difficulty with a collision-based

explanation, though, is that the low density of ^{85}Rb would require a large collision cross section to explain our observations. Common forms of collisions which can occur with ultracold atoms are: spin exchange (including hyperfine exchange), elastic, and light-assisted collisions. To determine if these collisions could account for the observed decrease in FORT atom number, we first estimate the cross-section necessary to produce the observed load rate reduction. During the simultaneous load of the FORT, we observed that about $\frac{1}{4}$ of the ^{87}Rb atoms were disrupted in some way as to prevent their loading into the FORT. For loading the FORT, the waist of the FORT was slightly offset from the MOT so that there was a larger FORT trap volume to capture more atoms. At the edges of the trap, it took an atom approximately 5 ms to cross the trap volume. Thus we took 5 ms to be the time in which the disruption to the load rate can occur.

Using the requirement of a loss of $\frac{1}{4}$ of our atoms in 5 ms gives a collision time of 20 ms, which yields a collision rate of $\tau=50 \text{ s}^{-1}$. With this rough estimate for the collision rate, we can estimate the collision cross-section required to produce the loss from,

$$\langle n \rangle \sigma \langle v \rangle = \tau . \quad (7.1)$$

In equation 7.1, $\langle n \rangle$ is the average density for ^{85}Rb which for our experimental conditions is approximately $4 \times 10^{10} \text{ cm}^{-3}$. $\langle v \rangle$ is the rms relative velocity of the colliding atoms in the cloud, which is $\sim 10 \text{ cm/s}$ for the atoms being loaded into the FORT. Finally, σ is the collision cross-section. From equation 7.1 and our estimates of our collision rate, we estimate a collision cross-section of roughly $1.25 \times 10^{-10} \text{ cm}^2$. This yields a collision radius of around 44 nm. These estimates were made under the assumption that a colliding atom will not be loaded into the trap. The cross-section of the various collision types can be calculated for our system, and compared to the estimate we derived for the

load rate reduction measured during our simultaneous loading of the FORT. That comparison is shown in table 7.1 where we have shown the ratio of the calculated cross-section for our loss to that of the cross-section for the collision ($\sigma_{\text{dis}}/\sigma$).

Collision type	Collision cross-section ratio ($\sigma_{\text{dis}}/\sigma$)
Spin Exchange	40
Hyperfine Exchange	160
Elastic	7
Light-Assisted Collision	5

Table 7.1 A list of the ratio of the estimated necessary collision cross-section for the observed load rate disruption (σ_{dis}) to the known collision cross-section of common collisions in an ultracold gas (σ). This table shows that the cross-section needed to produce our observed loss is larger than the other known loss producing collisions.

As seen from table 7.1, our estimated collision cross-section is still 5 times greater than that for light-assisted collisions, which have the largest cross-section of the collisions listed in table 7.1. Furthermore, light-assisted collisions are measured and accounted for in our measurements. This suggests that these common types of collisions are too small to explain observed loss. Not only are these rates too small to explain the load rate reduction, but estimates show that the hyperfine-changing collision rate is ~ 1000 times too small to explain the observed steady-state hyperfine state population changes as well. Thus the presence of the light must alter the collision rates, increasing collisions. Presumably, these collisions disrupt the laser cooling and the optical pumping of the atoms, preventing the atoms from becoming trapped in the FORT.

In order to investigate the possible mechanisms for the loss, we investigated the FORT load and hyperfine distribution as atoms were loaded into the FORT. In the following section our experimental procedures and observations are described.

7.2 Experimental conditions and setup

During the course of the investigation into the collision dynamics, we measured the load rate disruption caused by the presence of ^{85}Rb on ^{87}Rb FORT loading. Additionally, we investigated the effect that ^{85}Rb had on the optical pumping of the ^{87}Rb by investigating the hyperfine distribution of ^{87}Rb as a function of ^{85}Rb number. A description of these two measurements will be given in turn. To characterize the load rate reduction, we measured the load rate of ^{87}Rb into the FORT both with and without the presence of ^{85}Rb atoms. As was standard with the FORT loading procedure detailed in this thesis, the FORT was directly loaded from the MOT. The standard cycling and hyperfine repump transitions were used for trapping ^{87}Rb and ^{85}Rb in the MOT (see Chapter 2.1). The load rate was determined by measuring the number of ^{87}Rb atoms trapped in the FORT as a function of time after the FORT was turned on. This measurement is very similar to the load rate measurements presented in Chapter 5.

In addition to the load rate measurements, we investigated the hyperfine state distribution of ^{87}Rb as a function of the number of ^{85}Rb trapped in the FORT. This was conducted in order to determine if the presence of one isotope could have an effect on the optical pumping of the other. Since sub-Doppler cooling and optical pumping are closely related, a disruption to the optical pumping indicates an effect likely to result in less efficient sub-Doppler cooling and ultimately lower number of atoms trapped in the FORT. For these measurements, ^{87}Rb was loaded under its standard load conditions.

^{85}Rb is loaded in variable amounts to examine the system as a function of ^{85}Rb number. The atoms are then imaged, and the fractional hyperfine state distribution was measured.

In this chapter the load rate reduction measurements are discussed in detail first. After the data for the load rate reduction is presented, the measurements on the optical pumping disruption will then be presented.

7.2.1 Load rate reduction experimental setup. To quantify the load rate reduction, we first measured the ^{87}Rb FORT load rate without any ^{85}Rb present. The procedure for measuring the ^{87}Rb load rate without ^{85}Rb (“alone”) was very similar to that used to measure the ^{87}Rb load rate with the ^{85}Rb atoms present (“dual”). For the alone loading, ^{87}Rb was first collected into its MOT. To prepare for a FORT load, the hyperfine repump power was decreased and the cooling (cycling) laser detuning was detuned to 120 MHz to the red of the cycling transition. The FORT was then turned on through the use of an acousto-optic modulator (AOM) as described in Chapter 3.4. Once the FORT was turned on, the atoms began to load and the trap was allowed to load for a selected time (called the evolution time). After the desired evolution time was reached, the ^{87}Rb trapping light was shut off and the trapped atoms were held in the FORT for 100 ms to allow any untrapped atoms time to fall away before imaging. This 100 ms hold time is standard for trapping and imaging in the FORT for our experimental setup. At the end of this hold time, the atoms were released from the FORT and were then imaged using standard absorption imaging techniques as described in Chapter 3.3.1.

The dual loading sequence was mostly the same as it was for the alone. Here, however, ^{85}Rb was collected in a MOT which spatially overlapped the ^{87}Rb MOT. Before the FORT was turned on, however, one of the ^{85}Rb lasers was turned off.

Typically the hyperfine repump laser was shut off. However, we also collected data in which the ^{85}Rb cooling light was shut off instead (and found no observable difference between the two sets). By turning off one of the ^{85}Rb 's trapping lasers, ^{85}Rb was prevented from significantly loading into the FORT. The evolution time, additional hold, and imaging was exactly the same as it was for the alone data. The results of these measurements are shown in figure 7.1.

7.2.2 Data analysis for the load rate reduction data. Once the load rate reduction data had been collected, some additional analysis was required to extract the load rate. The collection and analysis of the data for the load rate measurements were very similar to those presented in Chapter 5. The ^{87}Rb atom number was measured as a function of evolution time, we then extracted the loading rates from the evolution data. The number of ^{87}Rb atoms trapped as a function of time is given by,

$$\frac{dN_{87}}{dt} = R_{87}(t) - \beta N_{87}^2 - \beta' N_{87} N_{85}. \quad (7.2)$$

Equation 7.2 is very similar to equation 5.1, though the single-body loss rate (I) has been neglected as it doesn't significantly contribute to the overall loading compared to the other loss terms. Also, the heteronuclear loss rate due to ^{85}Rb has been added. As is standard with the number evolution equation, R is the load rate, β is the homonuclear two-body loss rate, and β' is the heteronuclear two-body loss rate. N_{87} and N_{85} are the ^{87}Rb and ^{85}Rb numbers respectively.

β is measured through the study of homonuclear FORT loads following the methodology in [2]. β' was measured in a series of additional experiments and includes known loss terms such as light-assisted collision loss (see Chapter 8). Both ^{85}Rb and ^{87}Rb are loaded

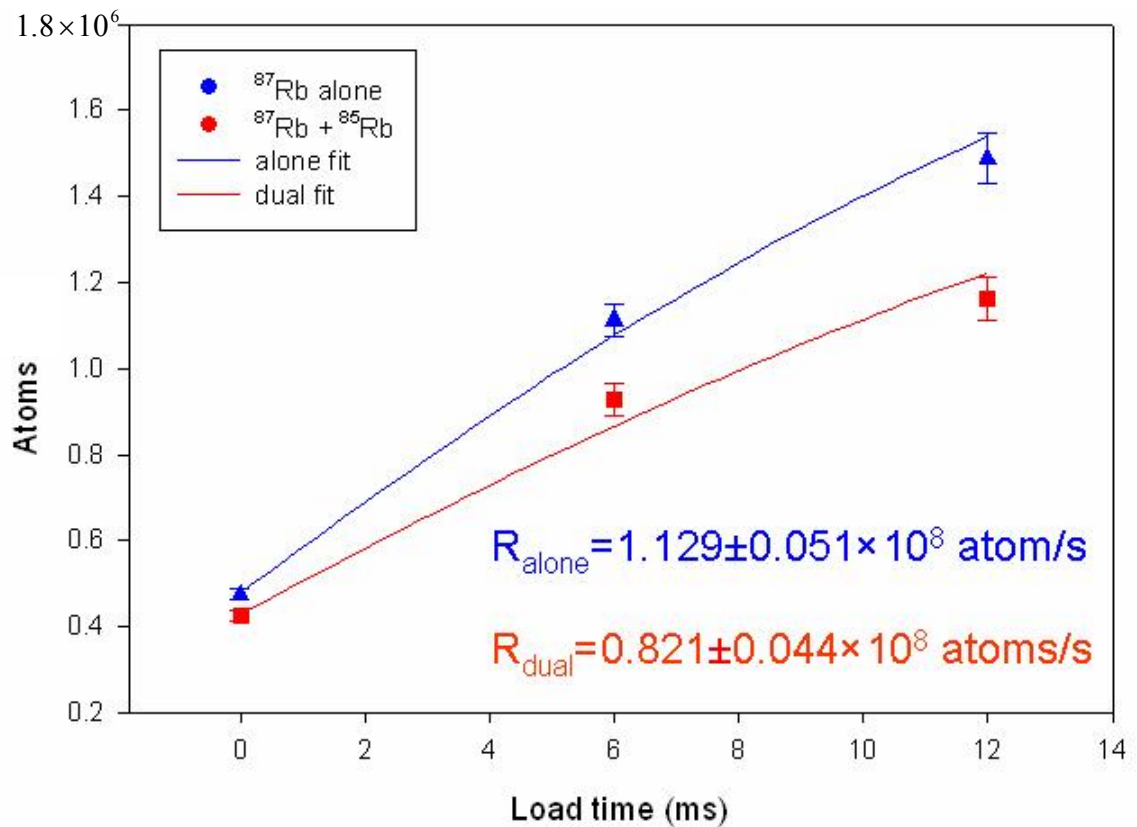


Figure 7.1 FORT loading data for the ^{87}Rb alone (blue triangle) and ^{87}Rb in the presence of an ^{85}Rb MOT (red square). The plot shows the number of ^{87}Rb in the FORT vs. evolution time. For the data in this plot, ^{85}Rb is loaded only minimally into the FORT so as to avoid light-assisted collisions. The data here show a measurable decrease in the load rate (R) of ^{87}Rb in the presence of ^{85}Rb . It should be noted that all load times have a 1.9 ms molasses load time built in (i.e. the 0 ms data points were a 1.9 ms molasses load, the 6 ms data points were a 7.9 ms load, etc.).

into the trap. Once both isotopes have been loaded, one of the ^{85}Rb trapping lasers is turned off. This will prevent ^{85}Rb from further loading into the FORT. Then the number of both isotopes was measured as a function of evolution time. With the load cut off, the number of ^{85}Rb atoms decreased due to heteronuclear and off-resonant homonuclear light-assisted collisions. The value of β' can be determined from this loss data.

Once β and β' were known, all data were then fit to equation 7.2 to determine $R(t)$. The load rate reduction caused by the presence of the non-resonant isotope is apparent in figure 7.1. The $R(t)$'s measured for the two conditions were $R_{\text{alone}}=1.129\pm 0.051\times 10^8$ atoms/s and $R_{\text{dual}}=0.821\pm 0.044\times 10^8$ atoms/s. The presence of the ^{85}Rb thus caused a $27\pm 5\%$ decrease in the overall loading rate. This difference was not sensitive to the precise value of β and β' . Variations of the loss coefficients of 50% or more produced no noticeable effect on the ratio of the $R_{\text{alone}}/R_{\text{dual}}$. While the ^{85}Rb was not actively loaded into the FORT, there was always some amount loaded simply by turning on the FORT [5]. This is due to the fact that when the FORT laser is turned on, there was some finite number of ^{85}Rb atoms in the trapping volume. In addition to these trapped atoms, there were also ^{85}Rb atoms which passed through the FORT volume that were not trapped yet contributed to the ^{85}Rb density in the trap region. The total number of ^{85}Rb atoms was relatively low ($\sim 0.4\times 10^6$ atoms or less) compared to the number of ^{87}Rb atoms ultimately loaded into the FORT for these measurements.

To ensure that what was being observed was an actual load rate disruption to the FORT, several checks were performed. First, the number of atoms in the ^{87}Rb MOT before the CMOT stage was measured with and without the presence of ^{85}Rb . Less than a 10% reduction in number was measured. Images of the ^{87}Rb MOT after the CMOT and

molasses stage indicated an even smaller limit to the reduction in ^{87}Rb MOT number due to ^{85}Rb , less than 5%. Such a small reduction is not expected to significantly impact our loading as the FORT loading rate is expected to scale as $N^{1/3}$, where N is the number of atoms in the MOT. This is due to the parameters of our trap. The MOT peak density is roughly constant; thus a decrease in number corresponds to a decrease in MOT/FORT overlap only along the long axis of the FORT. Second, we checked to see if the load rate reduction was due to the presence of ^{85}Rb trap light alone. To test this, we loaded ^{87}Rb atoms alone with and without one or both of the ^{85}Rb lasers on. For the case where both lasers were on, they were turned on just before the FORT was turned on. This prevented ^{85}Rb from being trapped in a MOT prior to FORT loading. In all these cases, the measured load rate showed no significant reduction due to the ^{85}Rb trap light. This is consistent with the fact that the scattering rate of ^{85}Rb light by ^{87}Rb is hundreds of times slower than ^{87}Rb scattering ^{87}Rb light. Thus little interaction between the ^{85}Rb light fields and the ^{87}Rb atoms was expected. In fact, the ^{87}Rb alone data displayed in figure 7.1 was collected in the full ^{85}Rb trap light field, but with the light detuned during MOT loading far enough so as to have prevented ^{85}Rb from loading into a MOT.

As discussed earlier, a reasonable explanation for the observed decrease in the load efficiency of the FORT would be some form of collision. Light scattering itself cannot be the cause as the cross isotope scattering rate for the laser light is too low. Dark collisions (collisions in the absence of light) also cannot explain fully the observed loss. As shown in table 7.1, the dark collisions for the parameters of our experiment do not have the necessary cross-section estimated to produce the observed load rate disruption. In principle, light-assisted inelastic collisions could be responsible for the observed

reduction in trapped atom number during the loading. However, the loss rate due to this has previously been measured and accounted for explicitly in our analysis. Furthermore, a characteristic of light-assisted collisions is that the collision loss rates are strongly state-dependent [20]. We investigated the load rate reduction with different ^{85}Rb hyperfine-state populations; the load rate reduction was measured when the ^{85}Rb were all in the lower hyperfine state ($F=2$) and when they were all in the upper hyperfine state ($F=3$) to see if there could be an observed difference in the load rate disruption. However, we found no observable dependence on the ^{87}Rb load rate reduction which was dependent upon the ^{85}Rb hyperfine state.

Another explanation for our observations could be that evaporative cooling out of the FORT is resulting in loss that is mimicking a reduction in the load rate. If the presence of ^{85}Rb could cause an increase in the evaporative cooling rate of ^{87}Rb in the FORT during the 100 ms hold time, this would manifest itself as a perceived reduction in the load rate. To test this, the evolution of the atom number in the FORT was observed with and without any cooling or repump laser light present with FORT hold times up to 900 ms. Though the dual data did show more evaporation than the alone, the increase was not large enough to explain the effect on the load rate. This observation was in accordance with simple estimates. Thus dark collisions, light-assisted collisions, and evaporation are ruled out as possible mechanism which could produce the observed decrease in load rate.

7.2.3 Optical pumping rate change experimental setup. In addition to investigating the impact of ^{85}Rb on the ^{87}Rb load rate, the effect of ^{85}Rb on the optical pumping of the ^{87}Rb atoms in the FORT was investigated. Disruptions to the optical

pumping rates manifested itself as a change in the hyperfine state distribution of the atoms in the FORT. In the optical molasses (used for loading the FORT), the hyperfine repump was heavily attenuated and the detuning of the cooling laser field was large. The steady-state hyperfine state distributions are then set through a balance between the “up-pump” rate from the attenuated repump and the “down-pump” rate from off-resonant transitions from the main cooling laser. In a series of experiments, both ^{87}Rb and ^{85}Rb were loaded into the FORT with the number of ^{85}Rb loaded as the variable. The changes in the relative hyperfine state distribution between the two ^{87}Rb hyperfine ground states due to ^{85}Rb atoms loaded into the FORT was then measured. This was analyzed in terms of a change in the fraction of the ^{87}Rb in the F=2 hyperfine ground-state. In order to extract the change in this fraction, the ^{87}Rb F=2 population fraction for each of the conditions was first measured. The hyperfine state distribution fraction was found by measuring the total number of ^{87}Rb in the FORT and the number of ^{87}Rb in the F=2 state. To measure the number of ^{87}Rb atoms in the F=2 ground-state, the ^{87}Rb cooling and hyperfine repump light was rapidly shut off during the loading of the FORT. This “froze” the atoms in their respective hyperfine state. The probe laser was set to the cycling transition of ^{87}Rb , and thus only imaged atoms in the ^{87}Rb F=2 hyperfine state.

To measure the total number of atoms, the same experimental sequence was followed except that before imaging the hyperfine repump for ^{87}Rb is turned back on. This ensures all the atoms are in the F=2 ground state and so the probe laser is resonant with all of the atoms in the gas. This is the standard procedure we used to measure atom number. With the total number of atoms and the number of F=2 atoms measured, the fraction (Ω) was calculated. The ^{87}Rb fraction was determined under both alone and dual

load conditions for varying load times (and therefore number) of ^{85}Rb . The alone and dual measurements allowed us to measure the fractional hyperfine distribution of ^{87}Rb ($\Omega_{\text{without } 85\text{Rb}}$) and the fractional hyperfine distribution in the presence of ^{85}Rb ($\Omega_{\text{with } 85\text{Rb}}$). The change in steady state hyperfine distribution fraction is simply the ratio of the percentage of ^{87}Rb atoms in the F=2 ground-state with ^{85}Rb present to that without ^{85}Rb present ($\Omega_{\text{with } 85\text{Rb}}/\Omega_{\text{without } 85\text{Rb}}$).

While it is possible to tune the probe laser to image the ^{87}Rb atoms in the F=1 hyperfine ground-state, it was easier for the experiment to simply measure the total number of atoms and the F=2 ground-state number of atoms in the FORT instead of recalibrating the probe laser to image the F=1 ground-state ^{87}Rb atoms. Additional complications can arise when imaging atoms in the F=1 state in that the transition used to image would not be closed. This would cause some atoms to be in a “dark-state” which would result in some atoms not being imaged. Thus for our experiment, it was easiest to measure the atoms in the F=2 hyperfine ground-state. With this procedure the percentage of ^{87}Rb atoms in the F=2 ground-state with and without the presence of ^{85}Rb can be measured. Multiple data points were taken for varying numbers of ^{85}Rb trapped in the FORT.

Figure 7.2 shows the data obtained from these optical pumping experiments. At low numbers of ^{85}Rb in the trap, there was relatively little change in the ^{87}Rb ground state distribution. However, as the number of ^{85}Rb atoms in the FORT increases, there is a measurable difference in the ground-state distribution of ^{87}Rb . Estimates of the off-resonant scattering of the ^{87}Rb cooling and hyperfine repump light are insufficient to explain any optical pumping effect. Heteronuclear hyperfine changing and light-assisted

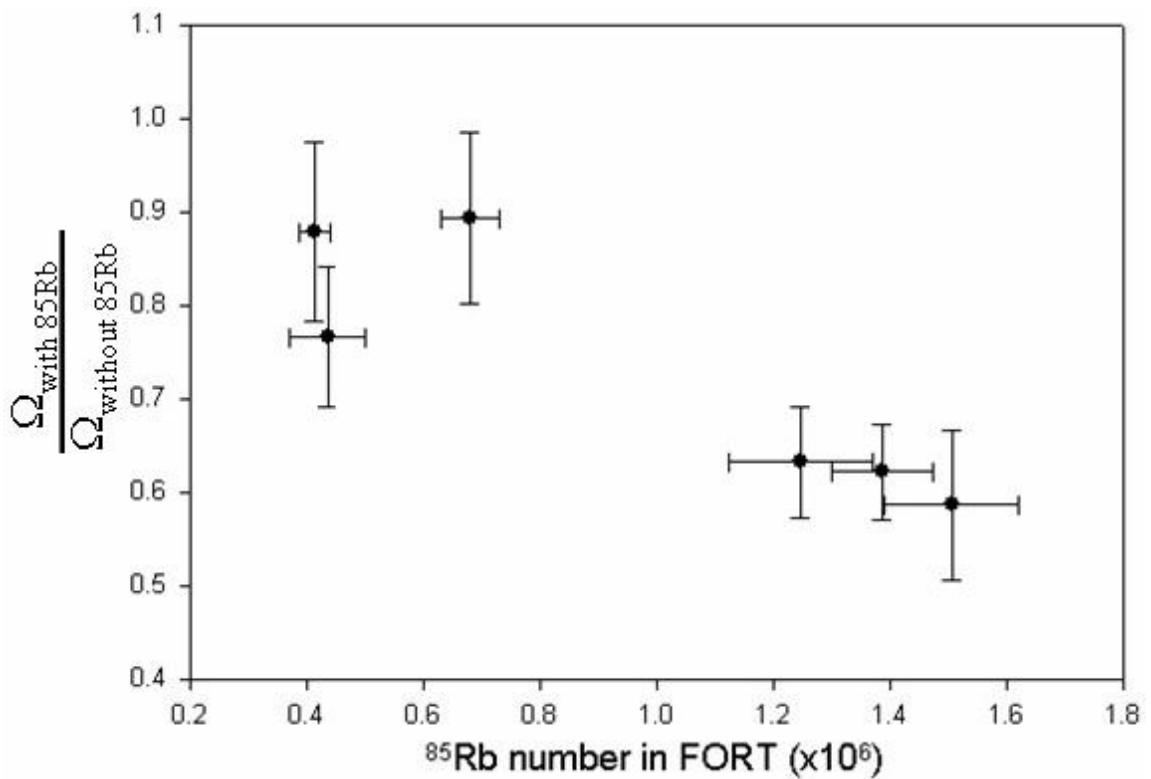


Figure 7.2 The change in the fractional amount of ^{87}Rb in the $F=2$ ground-state as a function of the number of ^{85}Rb loaded into the FORT. At small numbers of ^{85}Rb in the trap, there is relatively small change to the hyperfine ground-state distribution for ^{87}Rb . However, as the number of ^{85}Rb increases in the FORT, there was significant change in the ground-state distribution of the ^{87}Rb . This demonstrates that ^{85}Rb present in the trap can affect the optical pumping of ^{87}Rb in the trap.

collision rates were measured explicitly and accounted for in the data presented in figure 7.2, and in any case the magnitude of these collisions terms was too small to explain the observed changes (see section 7.1.1).

7.2.4 Hyperfine state distribution measurements. The load rate measurements indicated that the presence of ^{85}Rb disrupted the loading of ^{87}Rb into the FORT. Thus we sought to investigate ^{85}Rb density-dependent effects on ^{87}Rb light scattering. If there are collisions that could disrupt laser cooling, it is likely that these collisions would impact the optical pumping as well. Such disruptions to the optical pumping would then manifest itself as a decrease in the atom load rate. To see if the presence of ^{85}Rb could affect the optical pumping of ^{87}Rb , the change in fraction of ^{87}Rb in the F=2 ground-state ($\Omega_{\text{with } 85\text{Rb}}/\Omega_{\text{without } 85\text{Rb}}$) was investigated as a function of ^{85}Rb atom number in the FORT (Figure 7.2). The comparative nature of this analysis isolated us from systematic effects such as drift in laser power or detuning. This allowed us to easily and directly compare data sets which were taken over several days.

As part of this measurement, it was important to image the atoms under conditions where they had the same hyperfine state distribution as they did in the FORT. To do so, the ^{87}Rb trapping light and hyperfine repump light had to be rapidly turned off at the same time to prevent a distortion of the hyperfine populations that would occur if one laser were left on longer than the other. This was accomplished through the use of LabView controlled shutters. The timing was determined by measuring the turn off time of the laser light and making adjustments to the delay times in the main LabView program.

As shown in figure 7.2, the presence of ^{85}Rb in the FORT did have an effect on the overall ^{87}Rb hyperfine state distribution. At low numbers of ^{85}Rb , the relative change in hyperfine state distribution is low. However, as the number of ^{85}Rb atoms trapped in the FORT was increased, we measured significant changes to the ^{87}Rb hyperfine state distribution. At about 1.4×10^6 ^{85}Rb atoms trapped in the FORT, there was a measured reduction in the ^{87}Rb F=2 population of about 40%. This indicates that the presence of ^{85}Rb in the FORT can in fact influence the optical pumping rates of ^{87}Rb . This interference of the optical pumping rates could be responsible, at least in part, for the observed decrease in $R(t)$ of ^{87}Rb in the presence of ^{85}Rb .

To ensure that we had measured a change in the optical pumping rate, we investigated the loss of atoms due to hyperfine changing collisions during the 100 ms hold time. The measured losses during the hold time were then accounted for in the data presented in Figure 7.2. First, we did an experiment where all of the ^{87}Rb atoms were pumped into the F=2 state in the presence of ^{85}Rb and then we measured the loss rate as a function of hold time to determine the hyperfine changing loss. That indicated that the rate was a small perturbation to our data (which we included in the analysis). Next, we did an additional experiment where we compared the number of ^{87}Rb atoms measured after the 100ms hold time (i.e. normally) in the presence of over 10^6 ^{85}Rb atoms for the ^{87}Rb in the F=2 and F=1 states. There was a mild loss (<10%) for ^{87}Rb in the F=2 state. However, this reduction in the F=2 state was much less than the 40% reduction reported above. This means that collisions during the hold time could not account of the observed change in measured hyperfine state population

7.3 FORT load disruption.

In general, the cross scattering of light cannot account for the observed disruptions. However, it is possible for light fields to change an ultracold collision rate. In [21, 22], the effect of light on hyperfine-changing collisions in an ^{87}Rb MOT was investigated. It was found for low intensities of laser light, that the spin-exchange collisions were intensity dependent; indicating that light fields can enhance this type of loss. (Note that the detunings used for these other investigations were significantly different than our own. Our detuning was nearly an order of magnitude greater than that used in the experiment, thus their light scattering rates were significantly higher than our own.). The presence of light can, then, enhance collision rates and lead to additional loss from a system in general. However, the reduction in our load rate and the influence of ^{85}Rb on the optical pumping of ^{87}Rb cannot be attributed to hyperfine-changing collisions since that would produce an observable loss rate and be accounted for in our measurements of light-assisted collisions. Thus, another mechanism is responsible for our observations.

7.3.1 Collision induced decoherence. Since the FORT is a conservative potential, the optical pumping and hyperfine state distribution of an atom cloud was important to an efficient FORT load. The mechanisms of sub-Doppler cooling require a particular relationship with the atom spin polarization and the polarization field of the light (see Chapter 2.1.2). In principle, this relationship can be maintained through incoherent scattering, but that requires that the scattering time be short enough that the atom does not travel a significant distance in the polarization field before scattering a photon. In our system, this requirement is not met. Our detuning of the molasses stage

used to load the FORT (see Chapter 5) is 120 MHz detuned to the red of the ^{87}Rb cycling transition. With such a large detuning, an atom scattered a photon on average once every 8 μs for our light intensities. The atoms in the cloud had an average velocity of about $\sim 5\text{--}8$ cm/s, which means that typically an atom will move 800 nm in the light field before scattering a photon. However, our polarization field changed every 200 nm. This means that in between scattering events, the atom will have moved significantly in the polarization field. Thus, incoherent scattering is insufficient in maintaining efficient sub-Doppler cooling such as polarization gradient cooling. Since incoherent scattering is insufficient to maintain an atom spin state-light field polarization relationship, coherent processes are necessary to maintain efficient sub-Doppler cooling. A diagram showing how different m_F states are coherently coupled is given in Figure 7.3(a). The coherent scattering is able to maintain the atom dipole/laser polarization relationship necessary for efficient sub-Doppler cooling. As stated sub-Doppler cooling relies on the atom maintaining its spin orientation relative to the laser polarization field. As an atom traverses the laser polarization field, it scatters photons in order to maintain this relationship, which sets the m_F distribution of the atoms to that which best facilitates sub-Doppler cooling [23,24]. Since the incoherent scattering is not fast enough to maintain this proper distribution, multi-photon coherent scattering becomes the dominant scattering process through which sub-Doppler cooling was realized.

The forces from coherent and incoherent scattering can be calculated [24]. It turns out that for the number of states that are present in ^{87}Rb and ^{85}Rb , this particular method in [24] of calculation would involve about 100 separate equations. In order to

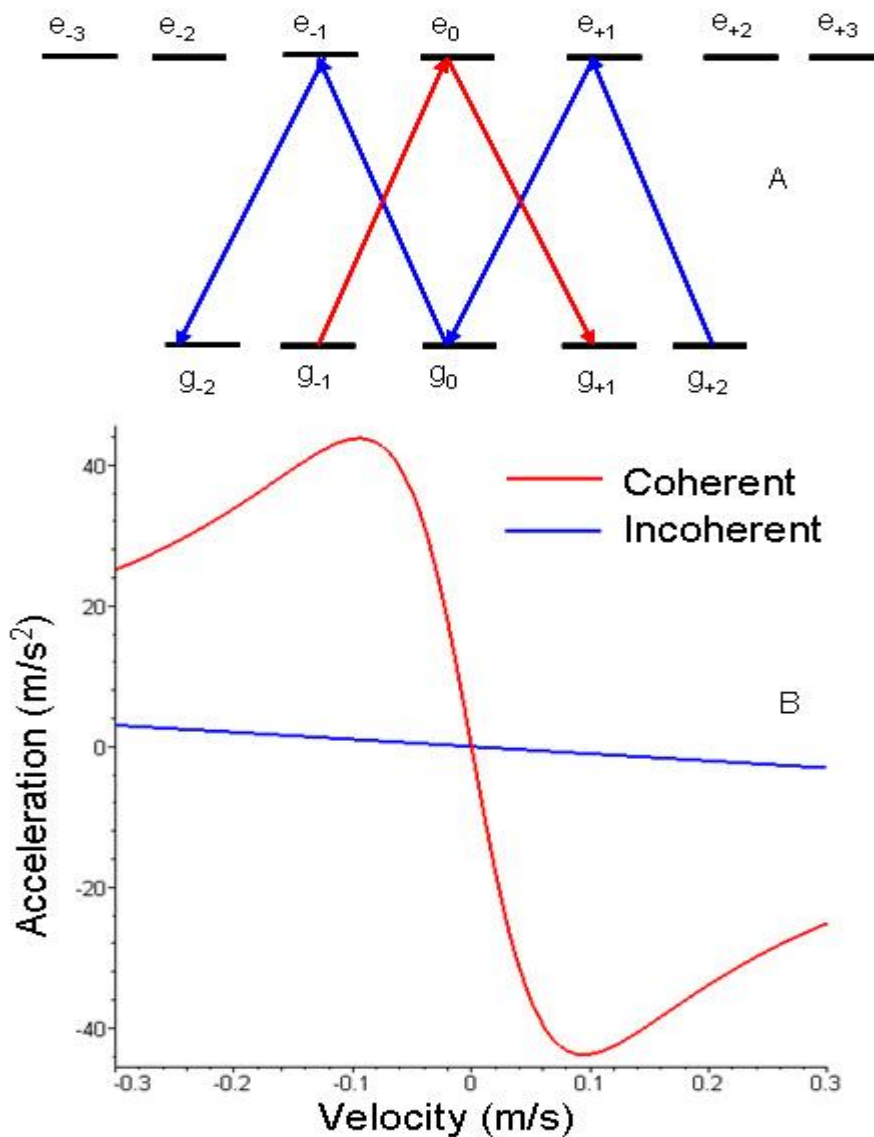


Figure 7.3 The top figure (A) is an example of coherent transitions between ground states. The red and blue arrows denote two different sets of coherent transitions which could be made in this system. The bottom figure (B) shows the acceleration that is ultimately responsible for lasing cooling due to coherent scattering (red) and incoherent scattering (blue) at a detuning (120 MHz) corresponding to that used in our experiments.

illustrate the role of coherence, a simpler system will be described here, that of an F=1 ground state and an F=2 excited state with no other hyperfine structure. While such a system will not agree quantitatively with our system, it will allow for a simpler treatment of the relevant qualitative physics. The force for the polarization gradient cooling for this simple system is given by [24],

$$F = \frac{25}{11} \hbar k \gamma \frac{G}{(1 + \delta^2 / \gamma^2)^2} \frac{k^2 v^2 + (88/85) \tilde{\mu}^2}{k^2 v^2 + \tilde{\mu}^2} \frac{\delta k v}{\gamma^2} + \frac{5}{44} \hbar k \gamma \frac{G^2}{(1 + \delta^2 / \gamma^2)^2} \frac{\delta k v}{k^2 v^2 + \tilde{\mu}^2}. \quad (7.3)$$

Here, G is a saturation parameter, δ is the detuning of our molasses ($2\pi \times 120$ MHz), γ is the natural linewidth ($2\pi \times 5.8$ MHz for Rb), and v is the velocity of the atoms. $\tilde{\mu}$ is given by

$$\tilde{\mu} = \sqrt{\frac{17}{33} \frac{G \gamma \sqrt{5 + \delta^2 / \gamma^2}}{4(1 + \delta^2 / \gamma^2)}}. \quad (7.4)$$

In equation 7.3, the first part of the equation represents the incoherent force, while the second part represents the coherent force (note that it scales as G^2). In figure 7.3(b) we used the equation for the forces to calculate the coherent and incoherent scattering accelerations on an atom whose mass is equal to that of ^{87}Rb . For values of average velocity and molasses detuning typical in our actual system, the coherent scattering process produced a much larger acceleration (force) on the atom than incoherent. In fact, the coherent force was an order of magnitude greater than the incoherent. Thus for cooling atoms into the FORT at our detuning, we are essentially completely reliant on coherent scattering processes. Disruptions to the coherence of our system would thus manifest itself as a reduction in the load rate. Collisions which produce decoherence in

the ^{87}Rb are a good candidate to explain both the interference with the optical pumping and the reduction in the load rate.

Decohering collisions have been reported in other systems, although the dynamics for these collisions vary from system to system. For example, the T_2 time of the atomic dipole is shortened due to collisions [25]. Decohering collisions were also reported in a 1-D optical lattice for Sr [26] and from background gas atoms in matter wave interferometry [27].

As previously stated, our sensitivity to decoherence is due to the relatively large detuning. This detuning was used in our experiments as it optimized the number of atoms which could be loaded into our shallow FORT [2]. At this large detuning, the sub-Doppler cooling (polarization gradient cooling) is especially dependent upon the induced coherences in the ground-state m_F sublevels which facilitate coherent multi-photon processes that produce ground-state m_F population transfer and velocity-dependent scattering [23, 24]. While it can be understood that coherence is essential to trapping atoms at our detuning, and shown that ^{85}Rb can effect the optical pumping of ^{87}Rb , the source of the collisions need to be understood.

7.3.2 Dipole-dipole interaction and wave-packet splitting. Estimates show collisions facilitated through a long-range dipole-dipole interaction would be sufficient to explain both of our observations (i.e. load rate reduction and optical pumping disruption). However, the evidence for these collisions as an explanation for our observations at this time is indirect. From our measured reduction of the loading rate and our measured density of ^{85}Rb atoms, any collisions which would cause the reduction would have to be long-ranged, as well as being induced by the laser light fields. The presence of the laser

cooling light induces dipoles in both ^{85}Rb and ^{87}Rb . The atoms can then interact through these induced dipoles (not entirely dissimilar to how the FORT creates a trapping potential). To consider the impact of these dipole-dipole interactions on atom collisions for ^{85}Rb and ^{87}Rb pairs in the ground state, we calculated dressed ground-state potentials including these induced dipole-dipole interactions for our experimental conditions. In figure 7.4, the potentials between ^{87}Rb in its asymptotic $F=2$ ground-state and ^{85}Rb in its asymptotic $F=2$ ground-state are shown for light linearly polarized along the collision axis. The resulting forces can be large; at an internuclear separation of 50 nm, an atom pair experiences an acceleration of $\sim 20,000 \text{ m/s}^2$ for the steepest potential shown, and at 40 nm the force is $\sim 120,000 \text{ m/s}^2$. In section 7.1.1 we had made estimates for the scattering cross section and the effective collision radius necessary to explain the observed load rate reduction. We had estimated an effective collision radius of about 44 nm would be sufficient to explain our observations. Thus, examining the potentials in figure 7.4 at an internuclear separation of 50 nm is appropriate for our experiment.

The forces applied to the atoms due to this interaction are state-dependent, as is evident from the differing steepness of the potentials shown in figure 7.4. As in a Stern-Gerlach type experiment, these long-ranged induced dipole-dipole interactions will thus in general cause a wave-packet splitting. Note that the collision axis is not aligned with the light-field polarization, and so in any given collision the m_F states natural to the laser field will be projected onto the basis appropriate for the collision, and in general this projection will be over many different m_F state combinations. Any state-dependent wave-packet splitting will tend to disrupt the existing ground-state coherences in several different ways. First, since the forces on the various parts of the wave-packet differ

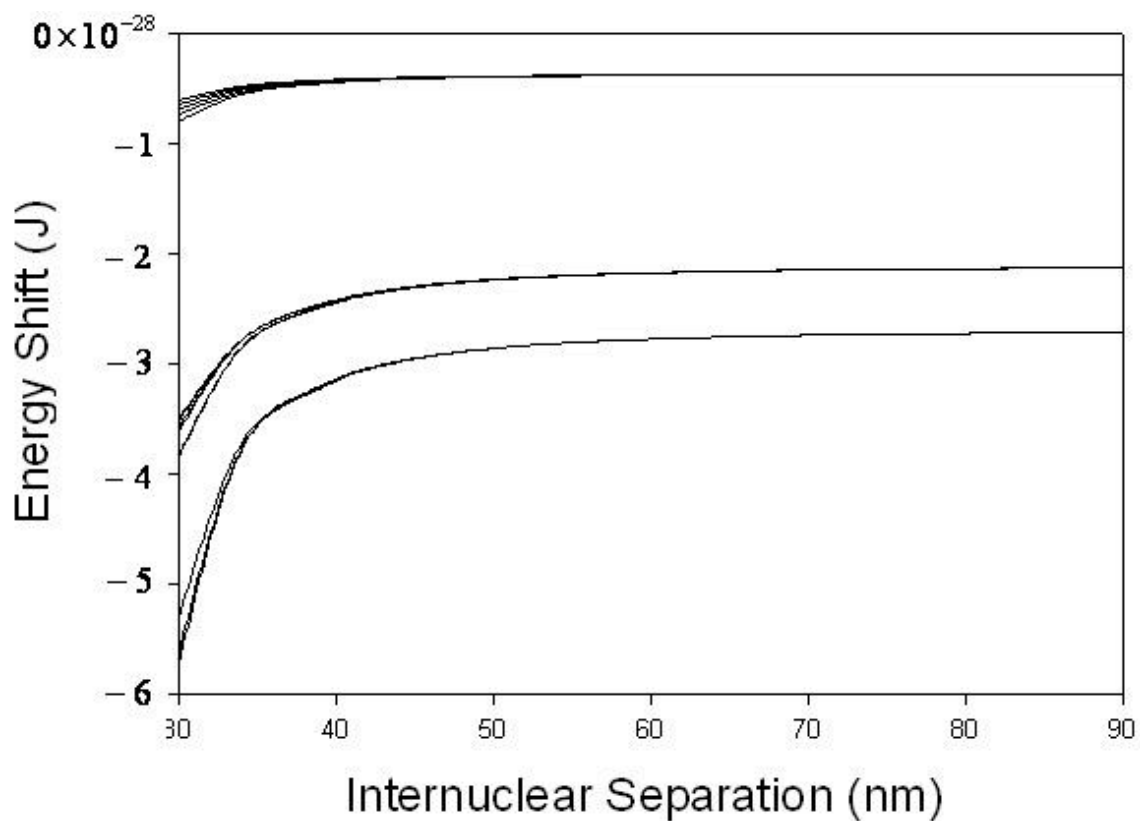


Figure 7.4 The dressed ground-state potentials including the induced dipole-dipole interaction between ^{87}Rb in the $F=2$ ground-state and ^{85}Rb in the $F=2$ ground-state. The potentials have significant curvature even at relatively large internuclear separation (~ 50 nm) and are state-dependent as well.

depending on the m_F state, the split wave-packets follow different paths through the laser light polarization field (see figure 7.5) resulting in different forces, diffusion coefficients, and equilibrium m_F state distributions. After such a collision, the equilibrium states for the individual wave-packets are no longer the same. Second, as viewed from the lab- frame, these collisions can induce significant changes to the wave-packet average kinetic energy. This too leads to a sudden change of the equilibrium state for the different wave-packets. Third, the optical molasses closely couples momentum states separated by $2\hbar k$. A wave-packet splitting collision will suddenly shift those relationships. The split wave-packets develop different phases as they propagate at different speeds and directions. We estimated a typical collision-induced phase shift by considering wave-packet propagation in free space after a state-dependent collision using the dressed state potentials such as those shown in figure 7.4. For the effective collision radius necessary for the disruption, the phase shifts caused by the wave-packet splitting were significant.

Despite the relative weakness in the ^{87}Rb hyperfine repump laser as compared to the cooling laser, similar accelerations in ground-state collisions were produced since the repump laser was much closer to resonance (~ 8 MHz blue detuned). Thus, $F=1$ ^{87}Rb wave-packets can be split as well with similar effects on the disruption of the existing ground-state coherences there.

7.4 Discussion of results and conclusion.

To estimate the effect of these collisions more quantitatively we created a model that used a combination of dressed state potentials and classical atom trajectories to calculate the amount of state-dependent deflection that occurred in a collision. A

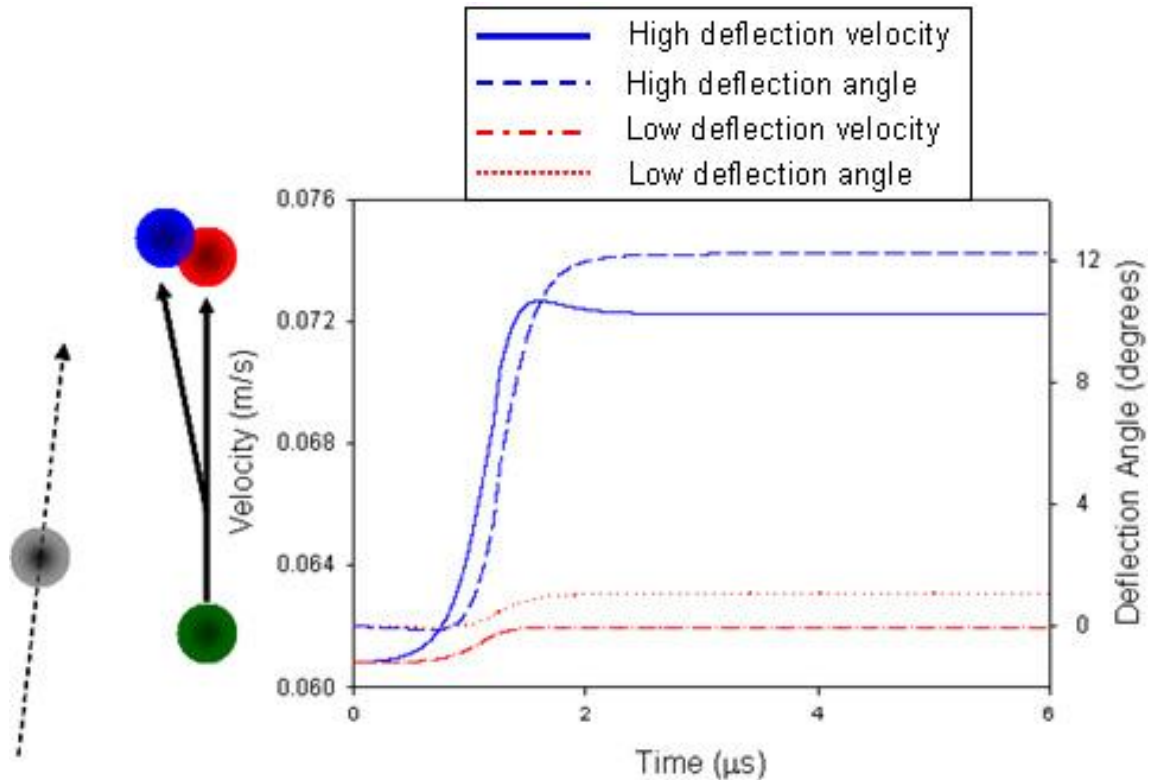


Figure 7.5 A semi-classical view of the wave-packet splitting. As an ^{87}Rb wave-packet (green) experiences the long range dipole-dipole interaction with an ^{85}Rb wave-packet (gray), it is split into two by the state dependent forces (red and blue). A typical collision in the gas is considered here, using velocities near the atoms' average values. The graph shows the different velocities and deflection angles experienced by the split wave-packets. High deflection is depicted by the solid line (velocity) and dashed line (angle). Low deflection is depicted by the dash-dot line (velocity) and the dotted line (angle). A full calculation for these splitting, however, would require something like a 3-D quantum Monte-Carlo simulation of two colliding wave-packets in the laser light field. This would likely prove to be computationally intensive and may need to include cooperative effects since the atom separation would be less than a wavelength. Note that the high-deflection atom's kinetic energy has increased by more than 30% in the lab frame.

collision was labeled “disruptive” if the maximum deflection difference between different states was greater than $\hbar k$ in the lab frame, where k is the wave number associated with the cooling laser. This threshold was chosen because it indicated a significant amount of state-dependent deflection (~ 0.1 rad) and average lab-frame kinetic energy change ($\sim 20\%$), and led to significant phase shifts (much greater than 2π) for the different wave-packets (modeling their propagation as being in free space). In any case, the results are not strongly dependent on the choice of this threshold due to the steepness of the potentials. Doubling the threshold produced a predicted collision rate reduction of 20% and increases beyond that change the rate even less. By performing a thermal average over collision energies and impact parameters our model indicated that a 25% load rate reduction was reasonable if one disruptive collision during a transit of the optical trap region prevented an ^{87}Rb atom from being loaded when it otherwise would have been. 1-D quantum Monte Carlo (QMC) calculations showed that disruptions to coherence significantly lowered the capture probability as an atom transited the optical trap. Since only 10% of the atoms that transit the FORT were trapped, even small disruption from collision-induced optical pumping would likely be enough to disrupt the loading.

With respect to the change in the hyperfine state distribution, the measured optical pumping rate for ^{87}Rb atoms from the $F=2$ ground-state to the $F=1$ ground-state ($1/250$ μs) is much longer than the optical pumping rate calculated for fully decohered atoms ($1/80$ μs). Additionally, the rate of pumping from the $F=1$ ground state is dependent on the coherences among the m_F levels in that state, too. Thus, loss of coherence can lead to less time in the $F=2$ state where the cooling light is resonant. Since only 10% of the atoms that enter the optical trap volume are ultimately trapped, only a small amount of

lost cooling time and additional kinetic energy can prevent the trapping of an atom that otherwise would have been trapped in the absence of the collision.

Recently, we have begun to run quantum Monte Carlo [28] calculations to investigate the role coherence had on the FORT load and optical pumping. While the QMC calculation currently being investigated is for the 1-D case, it has confirmed some of our observations on decohering collisions. Notably, the QMC calculations have shown that we should observe changes in the steady state hyperfine distribution as a function of induced decoherence. This prediction matched our measurement summarized in Figure 7.2. Furthermore, the QMC calculations have shown that we should observe changes in the capture probability (load rate) into the FORT as a function of induced decoherence. This too was observed, and seems to suggest that decohering collisions can explain the observed phenomenon.

While it is true that to fully quantify the dynamic of decohering collisions a full quantum approach is necessary, the semi-classical approach can yield useful information about possible dynamics. One such method is to look at the collisional energy barriers to see if light can in fact influence the loss channels. This is shown in Figure 7.6 which has two sets of potentials. The first (figure 7.6(a)) shows the barrier including only the Van der Waals interaction and the angular momentum barrier $\left(\frac{l(l+1)\hbar^2}{2\mu r^2} \right)$. (l is the orbital angular momentum, μ is the reduced mass, and r is the interatomic separation.) In this consideration even the p-wave collision channel has a barrier of $\sim 90 \mu\text{K}$. The second set (figure 7.6(b)) shows the same, but also takes into consideration the dressed state potentials for the colliding pair in the laser field (taken from figure 7.4). We see that the

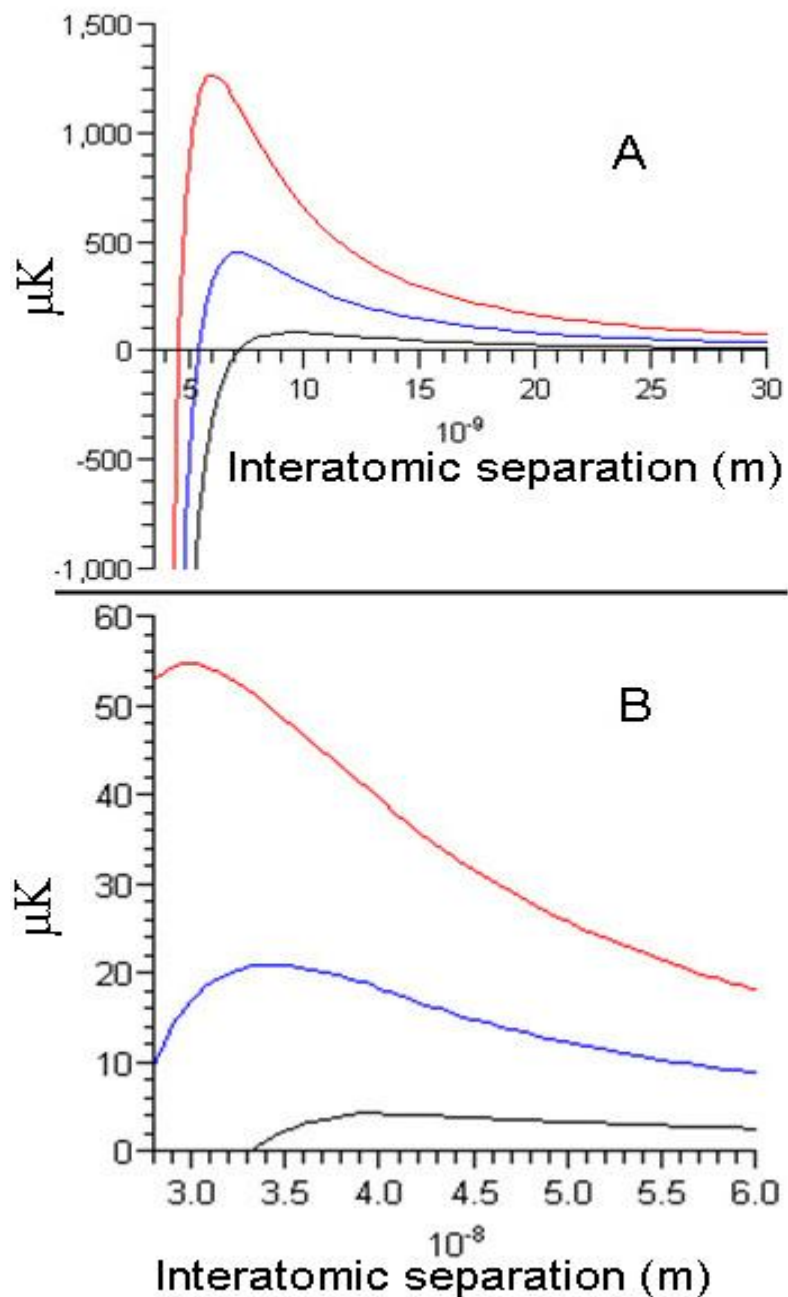


Figure 7.6 The p-wave (black), d-wave (blue), and f-wave (red) collision barriers (in μK) as a function of interatomic separation. 7.6(a) shows the standard barrier heights while 7.6(b) takes into account the dressed state potentials of the colliding $^{87}\text{Rb}/^{85}\text{Rb}$ pair in the laser light field. The presence of the laser light dramatically lowers the potential barrier and for our temperature ($\sim 30 \mu\text{K}$) opens up more collision channels (such as p-wave and d-wave).

presence of light has a dramatic effect on the barrier height. The p-wave channel is reduced to 4.5 μK . Even the f-wave which was reduced from 1.3 mK to 55 μK . Given the temperature of the molasses which is $\sim 30 \mu\text{K}$, this seems to suggest that the presence of the light can open up many more collision channels and should have a dramatic effect on collision rates and FORT capture.

7.4.1 Summary. While the FORT is sensitive to the coherence and sub-Doppler cooling of the atoms being trapped, the fact that ^{85}Rb had an effect on ^{87}Rb 's load rate was surprising. We found that low density clouds of ^{85}Rb led to a load rate reduction for ^{87}Rb . This is despite the fact that the resonance frequencies of the two isotopes are detuned from each other by 100's of linewidths. Estimates of the collision cross-section needed to produce the observed loss are relatively large, especially compared to the more commonly considered collision mechanisms in ultracold gases. And indeed, it was larger than the known collision cross-sections for dark (collisions in the absence of light) and light-assisted collisions.

We had also observed that the presence of ^{85}Rb led to a change in the hyperfine state distribution of ^{87}Rb , which was also predicted by the 1-D QMC simulation. Because of the large detuning between ^{85}Rb and ^{87}Rb , the observed load rate reduction and optical pumping disruption cannot be explained by the light scattering rate of ^{85}Rb . While known collisions between isotopes in the FORT are not sufficient to explain the observed disruptions, a collision between isotopes is likely the cause of the disruptions.

Estimates indicate that long-ranged induced dipole-dipole decohering collisions are a reasonable source of the observed decrease in load rate. Furthermore, this mechanism would also suggest that ^{85}Rb could also interfere with the optical pumping of

^{87}Rb , an effect seen in our data. The long-range induced dipole-dipole collisions have a Stern-Gerlach type of effect where state-dependent forces produce a splitting of the atomic wave-packet. This splitting can cause decoherence of the atoms' ground-state in the optical molasses which negatively impacts the ground-state optical pumping rates as well. Additionally, the calculations of the lower of the energy barriers (shown in Figure 7.6) shows that there is most certainly a significant impact on the collisions facilitated through the induced dipoles. These collisions will most likely induce spin-dependent phases (regardless of wave-packet splitting). Finally, our 1-D QMC code shows that decoherence leads to changes in hyperfine state distribution and capture probability. In general, these effects would be exacerbated in 3-D. The result of this interaction is that a significant fraction of the atoms being loaded into the FORT are lost to the FORT load. This seems to explain our observations at a semi-quantitative level.

References for Chapter 7

- ¹ J. D. Miller, R. A. Cline, and D. J. Heinzen, *Phys. Rev. A* **47**, R4567 (1993)
- ² Mathew S. Hamilton, Anthony R. Gorges, and Jacob L. Roberts, *Phys. Rev. A* **79**, 013418 (2009)
- ³ R. Dumle *et al.*, *New J. Phys.* **8**, 64 (2006)
- ⁴ S. J. M. Kuppens *et al.*, *Phys. Rev. Lett.* **62**, 013406 (2000)
- ⁵ J. Wu *et al.*, *J. Appl. Phys.* **100**, 054903 (2006)
- ⁶ H. J. Lezec, O. Alloschery, R. Mathevet, and J. Weiner, *Opt. Express* **14**, 26 (2006)
- ⁷ T. Muller *et al.*, *Phys. Rev. A* **76**, 063611 (2007)
- ⁸ P. F. Griffin *et al.*, *New J. Phys.* **8**, 11 (2006)
- ⁹ R. Newell, J. Sebby, and T. G. Walker, *Opt. Lett.* **28**, 1266 (2003)
- ¹⁰ G. Hillenbrand, C. J. Foot, and K. Burnett, *Phys. Rev. A* **50**, 1479 (1994)
- ¹¹ G. Hillenbrand, CK. Burnett, and C. J. Foot, *Phys. Rev. A* **52**, 4763 (1995)
- ¹² K. Ellinger and J. Cooper, *Phys. Rev. A* **55**, 4351 (1997)
- ¹³ S. Grego *et al.*, *Optics Comm.* **132**, 219 (1996)
- ¹⁴ M. Drewsen *et al.*, *Appl. Phys. B* **59**, 283 (1994)
- ¹⁵ Andrejs Vorozcovs *et al.*, *J. Opt. Soc. Am. B* **22**, 943 (2005)
- ¹⁶ J. I. Cirac, M. Lewenstein, and P. Zoller, *Europhys. Lett.* **35**, 647 (1996)
- ¹⁷ Y. Castin, J. I. Cirac, and M. Lewenstein, *Phys. Rev. Lett.* **80**, 5305 (1998)
- ¹⁸ S. Wolf, S. J. Oliver, and D. S. Weiss, *Phys. Rev. Lett.* **85**, 4249 (2000)
- ¹⁹ Anthony R. Gorges, Ansel J. Foxley, David M. French, Christopher M. Ryan, and Jacob L. Roberts, *Phys. Rev. A* **75**, 053403 (2007)
- ²⁰ Anthony R. Gorges, Nicholas S. Bingham, Michael K. DeAngelo, Mathew S. Hamilton, and Jacob L. Roberts, *Phys. Rev. A* **78**, 033420 (2008)
- ²¹ Renee C. Nesnidal and Thad G. Walker, *Phys. Rev. A* **62**, 030701(R) (2000)
- ²² S. D. Gensemer, D. L. Gould, P. J. Leo, E. Tiesinga, and C. J. Williams, *Phys. Rev. A* **62**, 030702(R) (2000)

-
- ²³ J. Dalibard and C. Cohen-Tannoudji, *J. Opt. Soc. Am. B* **6**, 2023 (1989)
- ²⁴ S. Chang, and V. Minogin, *Phys. Reports* **365**, 65 (2002)
- ²⁵ Claude Cohen-Tannoudji, Jacques Dupont-Roc, and Gilbert Grynberg, *Atom-Photon Interactions*. Wiley Interscience, New York, 1992
- ²⁶ Ch Lisdat *et al.*, arXiv physics/arXiv:0904.2515v2, (2009)
- ²⁷ Klaus Hornberger *et al.*, *Phys. Rev. Lett.* **90**, 160401 (2001)
- ²⁸ Klaus Molmer, Yven Castin, and Jean Dalibard, *J. Opt. Soc. Am. B* **10**, 524 (1993)

Chapter 8

Determination of $^{85}\text{Rb}/^{87}\text{Rb}$ simultaneous Far Off Resonant Trap load rates and loss coefficients.

Many of the previous chapters have dealt with aspects of loading ^{85}Rb and ^{87}Rb into a shallow Far Off Resonant Trap (FORT). Chapter 5 detailed the characterization of the single isotope loading of the FORT. Chapter 6 described our characterization of homo- and heteronuclear light-assisted collisions that lead to losses from the optical trap. Chapter 7 addressed the surprising result that the load rate, R , of one isotope was dependent upon the presence of the other isotope, despite the resonance frequencies of the two isotopes being far detuned from one another. This chapter attempts to put everything together, and to characterize the overall load rate and loss coefficients for the dual loading of our FORT. Understanding the loading dynamics and loss rates is important to future experiments which will investigate a sympathetic cooling scheme to further cool the atoms that have been trapped in the FORT. This cooling process is discussed in Chapter 9. In general, if one can fully characterize the loading, it should be possible to consistently and deliberately tune the number of atoms of each isotope that are loaded into the trap. Such a deliberate tuning would be particularly advantageous for implementing collision assisted Zeeman cooling for which we would like one isotope to be optically thin and the other to be optically thick.

8.1 Modeling the FORT load.

The load rate equations were discussed in Chapter 5, 6 and 7 for homonuclear and heteronuclear loading conditions. The equation for *homonuclear* loading of the FORT is given by [1],

$$\frac{dN}{dt} = R(t) - \Gamma N - \beta \frac{N^2}{V}. \quad (8.1)$$

This is the standard equation used when describing the load rate, and has been discussed in detail in Chapter 5. N is the number of atoms trapped in the FORT, V is the trap volume. The single body loss term Γ can be and is neglected for our system as our loss is dominated by the two body loss β . Since FORTs are far detuned from the atom's resonance, any effect which could be caused by atom's scattering FORT light can be ignored.

For our system, then, the number of atoms which can be loaded into the FORT is a balance between the load rate and the loss rate. The load rate can be influenced by a variety of factors, including atom temperature in the MOT, MOT/FORT overlap, the number of atoms which transit the FORTs trapping volume per unit time, and the efficiency of sub-Doppler cooling. These factors have been discussed in detail in previous chapters. The loss rate is dominated by two-body loss mechanisms; namely light-assisted collisions. However, there can be other loss channels in addition to light-assisted collisions.

For the same model, the equations for the dual loading are similar to that of equation 8.1:

$$\begin{aligned}
\frac{dN_{85}}{dt} &= R_{85}(t) - \Gamma_{85} N_{85} - \beta_{85} \frac{N_{85}^2}{V} - \beta'_{85-87} \frac{N_{85} N_{87}}{V} \\
\frac{dN_{87}}{dt} &= R_{87}(t) - \Gamma_{87} N_{87} - \beta_{87} \frac{N_{87}^2}{V} - \beta'_{85-87} \frac{N_{85} N_{87}}{V}
\end{aligned} \tag{8.2}$$

The single body loss rate term for each isotope has been left in the equations in equation 8.2, but again they are ignored in our system. Here β denotes the homonuclear two-body loss rate and β' denotes the heteronuclear two-body loss rate. The subscripts in equation 8.2 denote the isotope of interest.

There are a few standard assumptions [1] typically made with respect to the equations in equation 8.1 and 8.2. The assumptions deal with the variability of the loading and loss terms. While $R(t)$ is considered to change with time, it is assumed to be constant with respect to atom number (N). The loss rates themselves are also assumed to be constants. While not explicitly indicated in equations 8.1 and 8.2, the values of β are actually dependent on the relative population of atoms in the upper and lower hyperfine states. The ground-state hyperfine populations fractions are assumed independent of number, being determined solely through optical pumping rates. Within these assumptions, it should be rather straightforward to measure the load and loss coefficients and predict the loading behavior of our FORT for both heteronuclear and homonuclear load conditions.

However, we have learned through our investigation of loading dynamics that not all of these assumptions for FORT loading are upheld. For example, as shown in Chapter 7, the load rate changed due to the presence of an off resonant species MOT. However, the assumptions provided an appropriate starting point.

8.2 Load and loss rate measurements

The experimental sequence for measuring the effective loss rates did not differ greatly from previous experiments. As with previous experiments utilized simultaneous loading of both ^{85}Rb and ^{87}Rb , two MOTs were overlapped using standard techniques [2]. For ^{85}Rb , the single beam average peak intensity for the trapping laser was 2.5 mW/cm^2 , while for ^{87}Rb it was 4.8 mW/cm^2 . The shutter control of the MOT lasers (both main cooling and hyperfine lasers) gave us control over the trapping conditions (i.e. which isotopes are loaded, which lasers illuminate the cloud, timings, etc.). The Rb isotopes could be loaded alone or simultaneously. We could also set the ground-state hyperfine level through the use of shutter control. To ensure consistency, the MOTs were loaded to a constant number as best we could, which was $\sim 2 \times 10^8$ atoms. This allowed us to start each sequence with similar MOT numbers as to remove that variable from the FORT load data. As explained in Chapter 3, a CO_2 laser was used to create the FORT and is controlled through an acousto-optical modulator (AOM). The FORT is shallow, $\sim 120 \mu\text{K}$ deep and the focus of it is slightly offset from the MOT.

The loading of the FORT was accomplished using the same techniques and sequences already described in previous chapters. The load sequence used the standard sequence and detunings for the MOT loading, compressed MOT (CMOT) stages, and molasses stages as discussed in Chapter 5. The FORT was loaded from the molasses stage, which used 80 MHz red detuned light for ^{85}Rb and 120 MHz red detuned light for ^{87}Rb (from their respective cycling transitions), which was the standard loading procedure. The load time was varied in order to plot the number of atoms loaded as a function of time; thus obtaining an evolution curve much like in Chapter 5. Loss

measurements were taken by loading both isotopes to near their maximum number. One of the lasers is then shut off (with the shutter) and the number of both isotopes was measured as a function of the hold time in the FORT. As in previous experiments, there was a 100 ms equilibration time for the atoms held in the FORT before imaging, along with a 5 ms expansion time before the atoms are imaged on a charged-coupled device camera using standard absorption imaging techniques. From these images both number and cloud size were then found.

8.2.1 FORT loading analyzed under simple assumptions. Figure 8.1 shows the load evolution curves for ^{85}Rb (a) and ^{87}Rb (b) under the alone (open circles) and simultaneous (filled circles) conditions. Both ^{87}Rb and ^{85}Rb showed a decrease in the number of atoms loaded under the simultaneous load condition. In fact, ^{85}Rb decreases by almost a factor of 2 from its alone load condition. The loading dynamics of one isotope was significantly affected by the presence of the second isotope. In general, the observed decrease in number can be a result of either a load rate reduction or a two-body cross species loss. In order to figure out the cause of the number reduction, we first had to measure the effective β and β' values for the operating conditions of our experiment. Once the effective β and β' values are measured, we can use equation 8.2 to model the load number evolution and compare that to the measured number evolution. In our initial analysis of the data, we employed the typical assumptions such that the model here would assume that the load rate, β , and β' are independent of number and the fractional hyperfine population is also assumed constant. While we now know that these assumptions are not correct, one reason for using them is to see how closely the assumed and actual load curves agreed. In the absence of a detailed model of the load rate

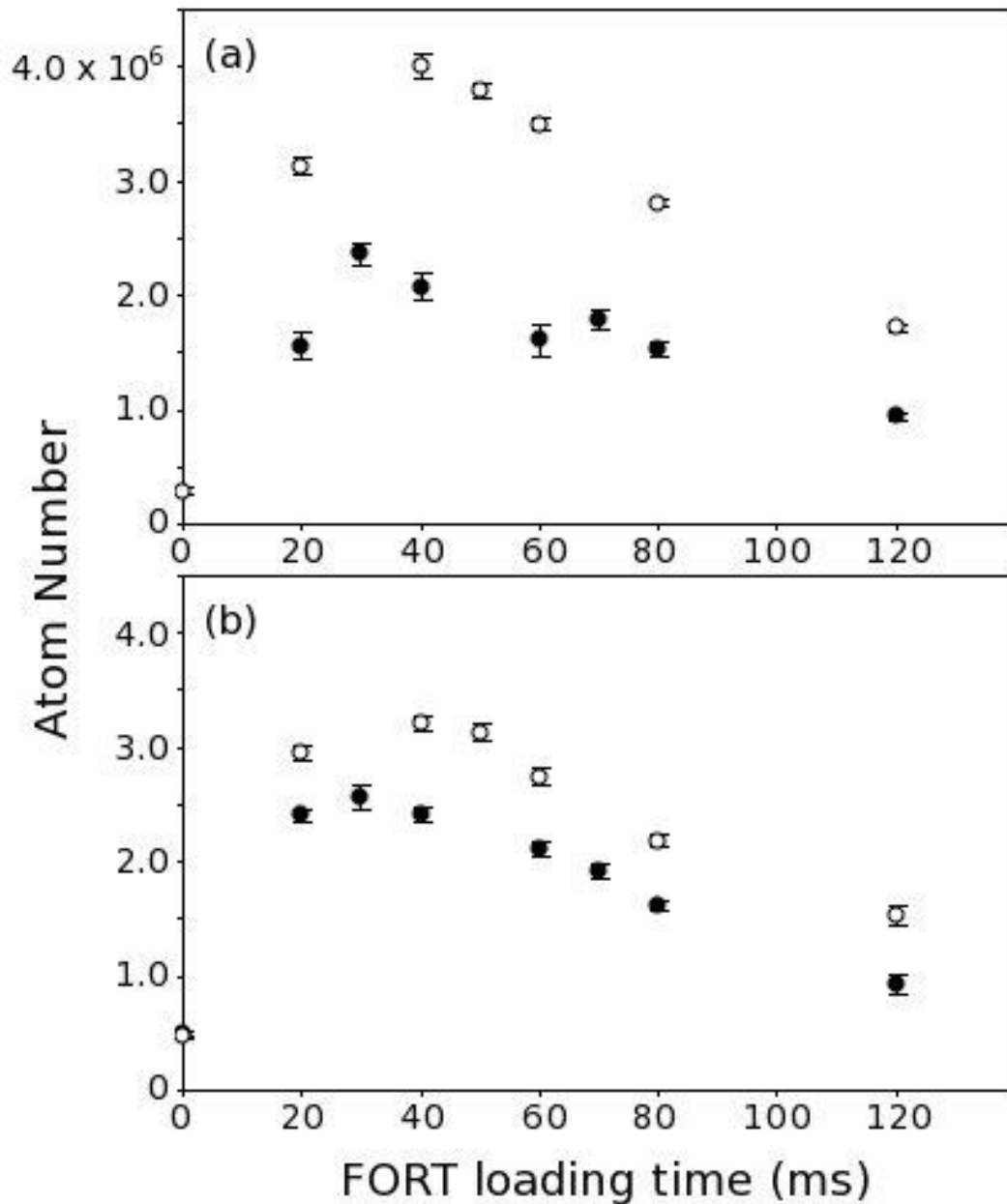


Figure 8.1 A sample of the typical atom number evolution as a function of FORT loading time. Shown is both the ^{85}Rb number evolution (a) and the ^{87}Rb number evolution (b) for both the alone (open circle) FORT load and the simultaneous (filled circle) FORT load. The error bars denote statistical uncertainty. Both isotopes demonstrate a measurable decrease in the number when both isotopes are loaded into the FORT.

reduction and the changes in hyperfine state distribution discussed in Chapter 7, we could not predict the impact on the FORT loading performance *a priori* for these effects. And so, to gauge their relative impact on FORT loading we conducted measurements and then compared the results obtained to the models in 8.1 and 8.2 under the standard assumptions.

To determine a value for $R(t)$ for the model under these assumptions, the first step was to measure the load rate in the same manner as the homonuclear load rates at the peak number of atoms loaded in the FORT were measured in Chapter 5 [3]. Number evolution curves were taken. At the point where the number of atoms trapped in the FORT peaks and turns over we know $\frac{dN}{dt} = 0$. Then by delaying the load of the FORT and taking data with only small number of atoms in the FORT, the value of $R(t)$ at the loading time associated with the peak number was found.

Loss rates for the heteronuclear FORT load were measured by loading the FORT and holding the atoms in the trap allowing the number to evolve with time (the homonuclear loss rates were measured as described in Chapter 5). By measuring the number of atoms which were lost during that time, the effective loss rate was calculated. Since it was assumed that loss rate was a constant, that value of β was then combined with the number evolution curve to find the $R(t)$ function. This is done by fitting the number load evolution to $R(t)$ using a polynomial fit to the evolution curves like those shown in Figure 8.1.

Once the load and loss rates were known from the homonuclear data, we performed a similar experiment with heteronuclear loading. Under the simple assumptions, the measured values of $R(t)$ and β from the homonuclear experiments were

used in Equation 8.2. The heteronuclear loss coefficients are then calculated using the standard procedure for calculating the loss coefficients. The calculated and measured evolution can be compared directly with each other.

We measured a value of β for ^{85}Rb to be $6.3\pm 0.7\times 10^{-11}$ cm³/s and for ^{87}Rb to be $9.2\pm 1.2\times 10^{-11}$ cm³/s. This is purely the homonuclear loss rate for our system. It was calculated using data from the evolution time corresponding to max number for the homonuclear load and without the presence of the other isotope's laser light field.

To determine the appropriate values for β_{85} and β_{87} for use in modeling the heteronuclear loading case, one correction needed to be made to the values measured from the experiments described above. Since light fields can affect certain collisions [4, 5], we had to account for off-resonant loss effects (as simultaneous loading will in general take place in the presence of both isotope's light fields). These off resonant effects are caused by light-assisted collisions like those discussed in Chapter 6. In those homonuclear loading curves, the effect of non-resonant laser light induced loss was not present. The application of the other isotope's laser light results in a measurable decrease in the maximum number of atoms that can be loaded into the FORT during a homonuclear load. From the size of the observed decrease, the additional two-body loss rate can be determined and included in β . For example, when ^{85}Rb was loaded in the presence of ^{87}Rb light; the peak number decreased by about 10%. This decrease implies a 20% increase in the homonuclear two-body loss coefficient. The increase in β for ^{87}Rb was similar. Thus a 20% correction is applied to the measured β 's to account for off-resonant loss. Had the previous work with homonuclear load been performed in the presence of the off-resonant light; this data would not have been required.

Not only was it necessary to measure the individual loss rates associated with the various ground-state hyperfine levels; but the hyperfine population distribution needed to be known as well. The latter can be measured much like it was for ^{87}Rb in Chapter 7. For the simultaneous load for our standard conditions, at max number in the FORT we found that for ^{85}Rb 10% of the atoms were in the $F=3$ ground-state hyperfine state, for ^{87}Rb 20% of the atoms were in the $F=2$ ground-state hyperfine state. Again, the simple assumption was that this hyperfine distribution was not a function of the number of atoms in the trap. As such, we initially took this population distribution as a constant. The hyperfine state distribution is used to weight the proper heteronuclear loss rates.

After quantifying the homonuclear load, the next goal was then to quantify the heteronuclear load. Thus we examined the heteronuclear load in order to extract the two-body cross species loss. In order to accomplish this, the FORT had to first be loaded with both isotopes. Once both isotopes are loaded into the FORT, one of the lasers for an isotope is shut off. This prevented that isotope from further loading into the trap. After that, the atom number for that isotope was measured as a function of FORT hold time. From this data, the heteronuclear loss coefficient was then extracted. Because most of the laser light was left on, the loss coefficient was close to what it would be under a normal load sequence. However, one laser does need to be shut off to prevent the load of an isotope. Therefore, there was a necessity to find the cross species loss as a function of off-resonant loss in order to fully derive the cross species loss coefficient. In order to extract the two-body cross species loss coefficients for off-resonance loss, the homonuclear loss coefficients for off-resonance loss needed to be known as well. Thus data was taken with homonuclear FORT load examining loss with all laser light

illuminating the FORT. This was not the full effective two-body loss rate however. The measurement was specifically off-resonant loss based on hyperfine specific loss channels.

To measure the off-resonant losses, the FORT was prepared with either ^{87}Rb or ^{85}Rb . The Rb was then pumped into a specific hyperfine level and held in the trap in the presence of the other isotope's laser field. From the number decay, the off-resonant β was determined. The results of the off-resonant β for homonuclear loads are listed in the second column of Table 8.1. The systematic uncertainties in number and trap volume make it so that there is $\sim 50\%$ systematic uncertainty to the values for the effective loss rates given in Table 8.1. However, since it's a systematic uncertainty the comparison between the values listed in Table 8.1 are well described by the statistical uncertainty listed in the table itself.

Hyperfine State Dependent losses ($10^{-11} \text{ cm}^3/\text{s}$)	Effective Off-Resonant Single Species	Effective Cross species
^{85}Rb F=3	6.54 ± 0.37	16.81 ± 0.63
^{85}Rb F=2	3.14 ± 0.20	4.33 ± 0.47
^{87}Rb F=2	11.71 ± 0.83	8.07 ± 0.40
^{87}Rb F=1	1.58 ± 0.22	0.08 ± 0.39

Table 8.1 Measured effective hyperfine state dependent losses for homonuclear (second column) and heteronuclear (third column) FORT load. While some of the off-resonant numbers could be used to account for some of the hyperfine dependence for the homonuclear two-body loss term, its primary purpose was the extraction of the cross-species two-body loss terms given in the next column.

It should be noted though that the values presented in Table 8.1 were measured for the purpose of calculating the heteronuclear two-body loss rate. The homonuclear loss rates were corrected as described earlier in this section. We need the specific

homonuclear, hyperfine dependent losses to extract the heteronuclear two-body loss from the off-resonant loss evolution curves.

With the effective hyperfine off-resonant homonuclear loss rates measured, it was then possible to extract the effective heteronuclear loss rates. The data were taken in the same way as the homonuclear tests, and the data fit to the heteronuclear loss to extract an effective β' . As with the homonuclear loss data, the heteronuclear showed that the upper-state hyperfine levels produced higher loss than the lower state. The heteronuclear data was taken under standard operational parameters so that the effective β' measured is directly applicable to our system under maximum load conditions. We then used the previously measured fractional hyperfine state distribution to properly weigh the hyperfine dependent heteronuclear loss rates to extract a total value for β' . With these values, we determined the homonuclear loss rate to be $\beta'=7.50\times 10^{-11}$ cm³/s. The combination of the measurement of the load rate for each isotope and the values of all the possible β and β' terms should have fully determined the number evolution curves for both isotopes, if all the assumptions that were described above are correct. The results of the model predictions are shown in Figure 8.2 as the dotted line. Figure 8.2(a) is the ⁸⁵Rb load, while Figure 8.2(b) is the ⁸⁷Rb. The shaded region and solid line are fits using various parameters which will be discussed later in this chapter.

At first glance, it seems at least that the ⁸⁷Rb is modeled reasonably well using the simple assumptions. Even so, there is significant deviation around the peak of the load curve from the data and the model given the measured load rate and loss terms. The amount of data taken for these experiments was a large enough and the precision with which the terms were determined were good enough that had all the assumptions held up,

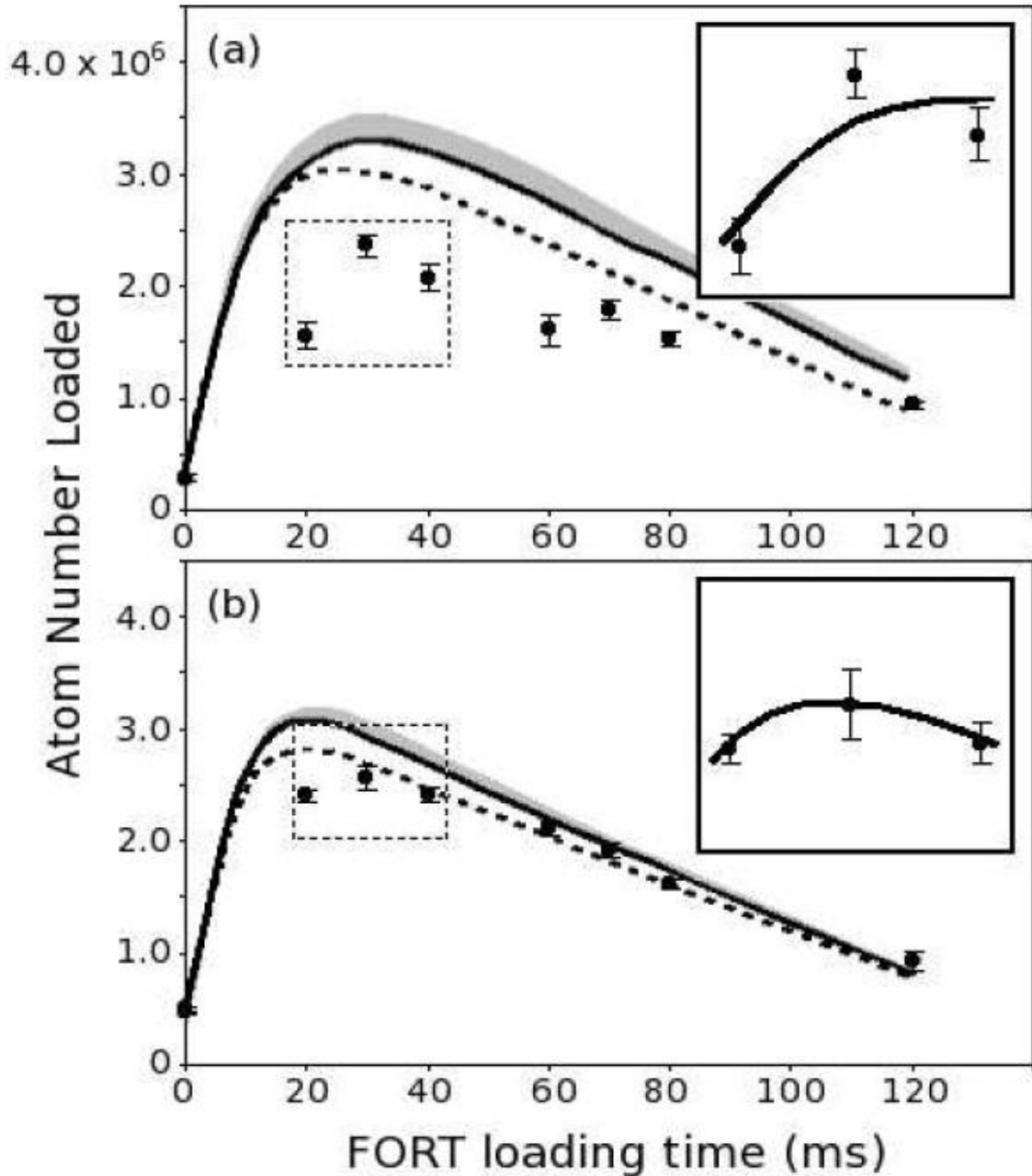


Figure 8.2 The solid circles are the data for the number of ^{85}Rb (a) and ^{87}Rb (b) trapped in the FORT as a function of FORT loading time. The dotted line is the predicted number evolution using standard assumptions. The solid line is the number evolution having corrected for the two-body loss hyperfine state distribution dependencies. The grey shaded area represents uncertainty in the hyperfine-state dependent collision channels. The insert shows a fit of the data given the dependencies and using $R(t)$ as a free parameter to fit the data by scaling the measured $R(t)$ by a constant.

that there should be no such deviation observed. ^{85}Rb shows a much larger deviation between the measured and the predicted FORT number evolution curves. The predicted curve shows a maximum number of almost 3.5 million atoms, wherein the actual measured number was 2.5 million. This indicates that the assumptions normally made when quantifying the load of a FORT may be breaking down..

A simple adjustment of one parameter cannot account for the observed discrepancies. For instance, if one wants to “fix” the ^{85}Rb curve by treating either the homonuclear or heteronuclear loss rates as a free parameter and adjusting it to increase agreement, the ^{87}Rb curve loses agreement with the measured curve except through a carefully chosen adjustment of the two loss rates in tandem. In any case, the resulting values of β or β' required to make such an adjustment would not be consistent with the other sources of measurement that we have for them.

One of the main goals of this investigation is to characterize our load in such a way as to allow us to independently tune the number of ^{85}Rb and ^{87}Rb in the FORT. However, the assumptions normally for Equation 8.2 fail in this regard, and this must be discarded. In light of our observations, we investigated the variability in both the load rate and loss rates as a function of number and fractional hyperfine state distribution.

8.2.2 FORT loading with variable load and loss rates. The next attempt at modeling we made was to see if we could account for the variability in the terms well enough to properly fit the measured number evolution shown in figure 8.2. As we found from the evaluation of light-assisted collisions (see Chapter 6), the loss channels tend to be hyperfine level dependent [6]. While we had considered hyperfine state distribution earlier, it was only for the extraction of cross-species loss. The fact is that the two-body

loss coefficients, β and β' , are dependent upon the number of both atoms in the trap. This dependency is born from the dependency of the fractional hyperfine state distribution of an atom on the numbers of both isotopes present. The assumption that the fractional hyperfine state distribution was independent of atom number is known to be incorrect. This means that as atoms were loaded into the FORT, β and β' changed as well since the hyperfine state distribution changed with atom number. This number dependence breaks many assumptions made, such as the β in equation 8.1 and 8.2 being constant. They no longer the same under the peak loading conditions, and the values for both vary during the load. Changing the fractional hyperfine state distribution can have marked effects on the load rate into the FORT by affecting the various number and hyperfine state dependent terms for the atoms trapped in the FORT. If the variance in hyperfine level dependent losses and atom number can be mapped out, however, it would still be possible to fully characterize the FORT load and would allow us the ability to tune our atom numbers.

As such, a careful consideration of the loss rates can “unpack” the folded in loss rates due to hyperfine dependent losses and off-resonant losses. By doing this, we can write each of the two-body loss rates as:

$$\begin{aligned}
\beta_{85/85} &= \gamma_{85,uu}^{85} \kappa_{85}^2 + \gamma_{85,ul}^{85} \kappa_{85} (1 - \kappa_{85}) + \gamma_{85,ll}^{85} (1 - \kappa_{85})^2 \\
&+ \gamma_{87,uu}^{85} \kappa_{85}^2 + \gamma_{87,ul}^{85} \kappa_{85} (1 - \kappa_{85}) + \gamma_{87,ll}^{85} (1 - \kappa_{85})^2 \\
\beta_{87/87} &= \gamma_{85,uu}^{87} \kappa_{87}^2 + \gamma_{85,ul}^{87} \kappa_{87} (1 - \kappa_{87}) + \gamma_{85,ll}^{87} (1 - \kappa_{87})^2 \\
&+ \gamma_{87,uu}^{87} \kappa_{87}^2 + \gamma_{87,ul}^{87} \kappa_{87} (1 - \kappa_{87}) + \gamma_{87,ll}^{87} (1 - \kappa_{87})^2 \\
\beta_{85/87} &= \gamma_{85,uu}^{85/87} \kappa_{87} \kappa_{85} + \gamma_{85,ul}^{85/87} \kappa_{87} (1 - \kappa_{85}) + \gamma_{85,lu}^{85/87} (1 - \kappa_{87}) \kappa_{85} + \gamma_{85,ll}^{85/87} (1 - \kappa_{87}) (1 - \kappa_{85}) \\
&+ \gamma_{87,uu}^{85/87} \kappa_{87} \kappa_{85} + \gamma_{87,ul}^{85/87} \kappa_{87} (1 - \kappa_{85}) + \gamma_{87,lu}^{85/87} (1 - \kappa_{87}) \kappa_{85} + \gamma_{87,ll}^{85/87} (1 - \kappa_{87}) (1 - \kappa_{85})
\end{aligned}
\tag{8.3}$$

Here γ was used to denote the two-body loss coefficients as to avoid confusion with the β terms. The γ terms are functions of the applied light fields and hyperfine levels weighted by the hyperfine state population distribution. The superscript denotes the isotopes which are lost due to that particular term. The subscript denotes the isotope laser cooling field associated with the coefficient and the hyperfine state of the colliding atom pair. For example, in the ^{85}Rb homonuclear two-body loss rate, $\gamma_{85,uu}^{85}$ denotes the loss coefficient is associated with an ^{85}Rb pair in the presence of the ^{85}Rb cooling light and that the collision takes place between two ^{85}Rb atoms in the upper hyperfine state. Likewise in the heteronuclear loss, $\gamma_{85,ul}^{85/87}$ denotes the loss coefficient between an ^{85}Rb and ^{87}Rb atom pair in the presence of the ^{85}Rb cooling light between an ^{85}Rb atom in its upper hyperfine ground-state and an ^{87}Rb atom in its lower hyperfine ground-state. Each of these loss coefficients were then weighted by the hyperfine population. This weighting is given by κ_{85} and κ_{87} which are the fraction of ^{85}Rb in the F=3 state and the fraction of ^{87}Rb atoms in the F=2 state respectively.

In principle, if one were to measure all the various γ 's and κ 's in equation 8.3, it should still be possible to accurately model the load of the FORT. The problem which arises in contemplating how to do so, however, is that κ is not a constant. For our experimental parameters, this variation in κ doesn't affect much predicting the effective cross-species two-body loss rates near the peak simultaneous heteronuclear loading conditions. The reason for this is that the data for those loss coefficient measurements were taken under FORT loading conditions. While the fractional hyperfine state populations may change with number of atoms, because we took the cross-species loss coefficient data under normal dual load conditions such that the loss data were collected

with nearly the peak number of atoms of the isotopes loaded into the FORT, the measured value we calculated is appropriate for modeling the load evolution curves near the maximum number of ^{87}Rb and ^{85}Rb atoms. This isn't true, however, for the homonuclear two-body loss rate measurements. Since these were taken without the other species present, the hyperfine distributions under which the data was taken were different than what it would be under normal operation with both isotopes being loaded into the FORT. As such, the first fix to our FORT load model problem is to relax the approximation that the hyperfine state distribution for the measured homonuclear two-body loss coefficients is always constant.

For our measured homonuclear loss values (which were reported above in section 8.2.1), we had essentially measured:

$$\begin{aligned}\beta_{85/85} &= \gamma_{85,uu}^{85} \kappa_{85}^2 + \gamma_{85,ul}^{85} \kappa_{85} (1 - \kappa_{85}) + \gamma_{85,ll}^{85} (1 - \kappa_{85})^2 \\ \beta_{87/87} &= \gamma_{85,uu}^{87} \kappa_{87}^2 + \gamma_{85,ul}^{87} \kappa_{87} (1 - \kappa_{87}) + \gamma_{85,ll}^{87} (1 - \kappa_{87})^2\end{aligned}\tag{8.4}$$

We measured the β values for the homonuclear case, though, not the explicit values of the various γ 's. Therefore, we cannot simply insert the proper heteronuclear fractional hyperfine state distribution and extract the proper β 's for the heteronuclear case. However, since we know that the β values are dependent upon the fractional hyperfine population, we can estimate the scaling of the β 's as a function of κ . We started by modeled this dependence as $\beta \propto \kappa^n$ where n is an appropriate scaling factor. Measurements of our hyperfine state dependent losses indicate that $\gamma_{85,ll}^{85}$ and $\gamma_{87,ll}^{87}$ in equation 8.4 were negligibly small for our system and thus can be dropped. The absolute maximum scaling with κ would occur if $\gamma_{85,ul}^{85}$ and $\gamma_{87,ul}^{87}$ were zero as well, which would

give us $n=2$ for our scaling factor. However, if this were true, we would have observed a quadratic scaling of β with κ . In our measurements of FORT load optimization, this scaling was not observed.

Since we did not have the data necessary to explicitly find the appropriate value of n for our system, we picked a range of possible scalings of the homonuclear loss-rate coefficients on κ that would be appropriate for our system. The low end of the approximation was made on the assumption that $\gamma_{85,uu}^{85} = \gamma_{87,uu}^{87} = 0$. This assumption was not entirely true; the upper-upper collisions could not be totally ignored. However, the simultaneous load fractional hyperfine distribution was measured to have 10% of the ^{85}Rb atoms in the upper-state and 20% of the ^{87}Rb atoms in the upper-state. As such, the $\gamma_{85(87),ul}^{85(87)}$ terms dominated the scaling. As such, the assumption $\gamma_{85,uu}^{85} = \gamma_{87,uu}^{87} = 0$ serves well as a lower bound on the loss. On the upper end, we had already ruled out a purely quadratic scaling with κ . From the degree of linearity of measured loss coefficients as a function of hyperfine pump power we estimated an upper limit for n . That estimate was consistent with a $\beta \propto \kappa^{1.5}$ scaling, and thus this was taken as our upper limit. Since the only assumption which was relaxed for this treatment was the independent hyperfine state approximation, we still used the independent load rate approximation to generate the curves.

The results of this treatment are shown in Figure 8.2 as the solid black line and grey band. The black curve is the lower bound and the grey curve accounts for scalings of κ up to $\kappa^{1.5}$. The obvious observation is that the modeled load curve is now even further out of agreement with measure load curve. However, this is not unexpected. We had already observed that the presence of one isotope in the FORT lowered the fractional

upper-state hyperfine population of the other isotope. The lower-hyperfine state-lower hyperfine state loss rates were all relatively low for both homo- and heteronuclear collisions, given our measurements and assumptions. Thus the increased lower-state fraction would be expected to reduce our predicted homonuclear β 's. This reduction then manifested itself as a prediction from the model of greater numbers being trapped in the FORT.

While it is true that the loss rates decrease due to the change in the hyperfine state population, there was also an observed load rate reduction associated with simultaneous loading. When we relaxed the assumption on hyperfine state independence, we kept the independent load rate approximation. Thus we accounted for the decrease in the β terms but not for the reduction in load rate. As such, the model overshoots the actual load of the FORT.

The last assumption of the load rate independence was then relaxed to fit the data. The discrepancy between the predicted FORT load and the measured from the previous treatment is assumed to be due to the dependence of $R(t)$ on the number of atoms around the trap. From Chapter 7 we saw that ^{85}Rb produced a reduction in the load rate of ^{87}Rb into the trap. While we had taken a rather larger amount of data on the ^{87}Rb hyperfine distribution and its change with ^{85}Rb , the data on ^{85}Rb 's hyperfine state distribution is less complete. In this light, we assume the behavior of ^{85}Rb in the presence of the other isotope was similar to that of ^{87}Rb .

To make up for the discrepancy between the predicted and measured load, we used $R(t)$ and N_{peak} as a free parameters to fit model predictions to the data at its peak. This was done by taking the extracted $R(t)$ from previous measurements and scaling it by

a constant. The scaling constant was varied to best fit $R(t)$ at the peak of the load. The N_{peak} was varied to account for the changes in load and loss rates which depend upon atom number. We then calculated the load rate reduction necessary for each isotope to achieve the fit to determine if the reduction is appropriate for our system. However, since we had relaxed the assumption on the independence of $R(t)$, the previous determination of $R(t)$ (explained in Chapter 5) cannot be used. Because of this, we focused on fitting $R(t)$ to match the peak load numbers (while keeping the shape of $R(t)$ constant). It was reasonable to do so as the majority of our data was taken around the peak, and we know those numbers and hyperfine state distributions rather well. The peak data included 3 points (see Figure 8.2 inserts), with the $R(t)$ scaling factor and N_{peak} as fitting parameters to give a 2 parameter fit to 3 points. Additionally, at the peak the number (and thus hyperfine state distribution) changes minimally. Because of this, we can assume that $R(t)$ does not vary significantly at the peak. This procedure isolated us from some of the variability due to the number and time evolution of $R(t)$ and allowed us to calculate the $R(t)$ which would more accurately describe the loading of our system.

The results of this final approximation relaxation are shown in the inserts of Figure 8.2. Since we used $R(t)$ as a free parameter to fit the measured data, it was then guaranteed that predicted load curve would match the peak load data. The question is whether or not the load rate reduction necessary to agree with the data was reasonable. For our measurements, we calculated a drop in $R(t)$ for ^{87}Rb by 26% and for ^{85}Rb by 36%. Given our measurements, change in the hyperfine state population, and the complex and entangled nature of the load rate under a simultaneous load; the calculated reduction was reasonable. Since we matched our calculated load rate reduction under

normal FORT load conditions we have greater confidence in the calculated load rate reduction.

The fact that ^{87}Rb initially fit so well was most likely a coincidence: the fact that there was a load rate reduction for ^{87}Rb in the heteronuclear load was balanced by a drop in the overall drop in the loss rate as well. The drop in the loss rate coming from changes in the fractional hyperfine population distribution due to the number of atoms trapped in the FORT. The complex interaction could work in such a way as to make it seem that the predicted evolution curve and actual evolution curve are closer than would be justified by the accuracy of the model.

8.3 Using the model to predict FORT load.

One of the main goals for the full characterization of the simultaneous FORT load was to allow us to determine a parameter set by which we could tune the system through detuning, hyperfine power, FORT timing, etc. to tailor our isotope population to the needs of any particular experiment. However, through the course of the investigation we had found that the simple assumptions normally made for modeling a FORT load were not applicable to our system. Thus, the particulars of the experimental set up such as laser power, detuning, overlap, optical pumping, etc. have a much larger effect on the FORT load than a simple change in the loading rate and loss coefficients. This could be why differing groups had previously reported varying scalings of atom number vs. trap power [7, 8, 9]. As such, while we started with the standard assumptions for modeling the load of a FORT, we had gradually relaxed those assumptions to better match the dynamics of our system.

Since many of the loss rates are hyperfine dependent, the fact that the fractional hyperfine state distribution changes with atom number complicates the characterization of the FORT load. Perhaps a bit more surprising was the dependence of the load rate on atom number and hyperfine state distribution of atoms trapped in the FORT. The entangling of the load rate and loss coefficients with parameters of the system makes simple predictions of load number difficult at best. However, it does highlight dynamics associated with FORT loading which were previously not addressed. Because the FORT is a conservative potential, the load numbers are strongly dependent upon the sub-Doppler cooling efficiency. Disruption of that efficiency would ultimately manifest itself as disruptions to the FORT load. The presence of another isotope, even one detuned from the other by several hundred natural linewidths, is enough in and of itself to cause a change in the hyperfine state distribution and thus a change in the sub-Doppler cooling efficiency. This disruption can affect the load rate of the atoms into the FORT. Furthermore, the strongly hyperfine dependent two-body losses are also affected by this change in the hyperfine state distribution. Because the simultaneous loading equations are coupled, it's not possible to simply adjust the loss rate of one isotope without affecting the other.

Thus the FORT load is seen to be a rather complex dynamic controlled by many variables which will in all likelihood vary from system to system. While we sought to describe the load of the FORT well enough to tune our atom numbers easily, became obvious during the analysis of our data that there is no simple parameter space which could give us a convenient “knob” by which we can independently adjust the number of ^{87}Rb and ^{85}Rb in the FORT. In order to tailor the numbers of atoms in the trap to suit our

experimental needs, realistically the parameters and loading sequence will have to be found through experiment trial and error.

The complications which arose during the simultaneous load (notably, the unexpected additional loss) do not substantially impede future experimental plans. It should be noted that the current number of ^{87}Rb and ^{85}Rb which can be trapped in the FORT meet the experimental design for testing Collision Assisted Zeeman cooling.

References for Chapter 8

- ¹ S. J. M. Kuppens, K. L. Corwin, K. W. Miller, T. E. Chupp, and C. E. Wieman, Phys. Rev. A **62**, 013406 (2000)
- ² E. L. Raab, M. Prentiss, A. Cable, S. Chu, and D. E. Pritchard, Phys. Rev. Lett. **59**, 2631 (1987)
- ³ M. S. Hamilton, A. R. Gorges, and J. L. Roberts, Phys. Rev. A **79**, 013148 (2009)
- ⁴ Renee C. Nesnidal and Thad G. Walker, Phys. Rev. A **62**, 030701(R) (2000)
- ⁵ S. D. Gensemer, D. L. Gould, P. J. Leo, E. Tiesinga, and C. J. Williams, Phys. Rev. A **62**, 030702(R) (2000)
- ⁶ Anthony R. Gorges, Nicholas S. Bingham, Michael K. DeAngelo, Mathew S. Hamilton, and Jacob I. Roberts, Phys. Rev. A **78**, 033420 (2008)
- ⁷ J. Wu *et al.*, J. Appl. Phys. **100**, 054903 (2006)
- ⁸ E. J. Prime, J. A. Behr, and M. R. Pearsom, Can. J. Phys. **85**, 1 (2007)
- ⁹ P. Ahmadi, B. O. Timmons, and G. S. Sunny, Phys. Rev. A **72**, 023411 (2005)

Chapter 9

Review and Future Measurements

The previous chapters have discussed the work which has been accomplished with the current system thus far. As was the case with the work presented in this thesis, future experiments will revolve around collisions between ^{87}Rb and ^{85}Rb . The ultimate goal of this future work is to explore a technique designed to further cool atoms in an optical trap without the use of evaporative cooling. The experiments and results of this thesis were stepping stones necessary for achieving the system to explore the new cooling regime. To tailor the system to the experimental needs, the dynamics of loading dual isotopes into a Far Off Resonant Trap (FORT) in the presence of cooling light needed to be understood first.

This chapter will briefly review (in section 9.1) the results of those findings so as to explain better the plans for future experiments. In the immediate future, there are a few modifications to be made to adapt the system to meet the needs of the experiments planned. Those modifications are discussed below in section 9.2. In addition, a basic outline of the cooling that is to be pursued is presented in that section as well. Finally, a few closing remarks are included in section 9.3.

9.1 Review

The first physics we looked into was that of reabsorption, and our work was presented in Chapter 4. The goal of the work was to investigate the effects of reabsorption in optically thick clouds and investigate means by which reabsorption may

be mitigated. In brief, reabsorption is a one or two photon process by which additional heat is delivered to the atom cloud. In optically thick clouds, reabsorption can lead to a limitation in cooling efficiency. The one-photon reabsorption process involves rescattering a spontaneously emitted photon by another atom in the optically dense cloud. The two-photon reabsorption process involves a photon from the main cooling beam and a spontaneously emitted photon which couples an atom from one momentum state to another. The effects of reabsorption have been observed experimentally in studies showing a decrease in laser cooling efficiency with increasing optical depth [1-5]. Since part of this project's future work will depend on having an isotope which is potentially optically thick, reabsorption effects will be important for our future studies. The proposed cooling ultimately relies on removing entropy via optical pumping, and so inefficiencies and heating that could be part of that optical pumping likely pose an important limitation to the ultimate achievable cooling efficiency.

As such, we investigated the effects of reabsorption in an ^{85}Rb Magneto Optical Trap (MOT). We found that while the one-photon reabsorption process can be mitigated through detuning, the two-photon reabsorption process was not strongly dependent upon the detuning. Ultimately, though, we found that it was possible to disrupt the reabsorption process by disrupting the coherence of the two-photon process involved in two-photon reabsorption. To accomplish this disruption in our experiments, we had used counter-propagating beams detuned from each other by about 10 MHz. This established a rapidly varying spatial interference pattern in the light which illuminated the cloud. The detuning difference and presence of the rapid spatial interference pattern were enough to disrupt the reabsorption process. By applying optical pumping beams in the

proper configuration in the cooling cycle, we can use what we learned to reduce the amount of reabsorption and mitigate this limitation to our cooling performance.

The remainder of the experiments dealt in some way with loading and losses into the FORT. These are necessary since future experiments will utilize the FORT, requiring dual loading of both Rb isotopes into the FORT. The FORT is a beneficial trap to use for the proposed cooling scheme we wish to implement since a FORT is capable of holding onto atoms in any magnetic state without inducing heat into the atoms cloud [6]. Thus the FORT itself should not interfere with the cooling efficiency of the proposed experiment.

As such, we wished to characterize the loading of the FORT under first a homonuclear load. The goal was to optimize the load and load sequence for use in further experiments. The standard loading equation for a homonuclear FORT load given in [7] is,

$$\frac{dN}{dt} = R(t) - \beta \bar{n} N - \Gamma N . \quad (9.1)$$

This equation has been discussed in great detail in previous chapters. The goal was to find a parameter space where we could maximize the load rate ($R(t)$) while minimizing the two-body loss rate (β). We found during the investigation that loading the FORT from a molasses rather than the MOT greatly improved the load of the FORT. While the peak load rate for both a MOT and molasses load were similar, the two-body loss rate between the two was significantly different. We found that the increased detuning which can be utilized for a molasses load allowed us to operate in a regime where the loss rate was greatly reduced; thus increasing the number of atoms that could be loaded into the FORT. We were also able to explain the observed differences in MOT and molasses

loading behavior based on the magnetic field present in the FORT region during the MOT-based loading. Other research groups reported using an optical molasses for FORT loading, but a detailed characterization as to why it was better was not reported in the literature. Our explanation also indicates that the use of an optical molasses-based loading is increasingly beneficial in shallow, rather than relatively deep, FORTs.

A side benefit of the results of the homonuclear loading experiments was that they indicated to us how to construct a standard load sequence for the FORT under which we could maximize the number of atoms loaded into the FORT. While Chapter 5 detailed mostly the measurements for ^{85}Rb , ^{87}Rb was examined in a similar manner to find the detuning and laser powers appropriate to maximize its trapped atom number as well.

With the individual load of each isotope determined, we then examined the cross-isotope losses while the atoms were held in the FORT. In terms of the sympathetic cooling we ultimately wish to establish, both isotopes have to be loaded into the FORT and held there long enough for the cooling to take place. However, there are also collisions between the atoms which will induce loss. While there can be a variety of collision dynamics which could produce loss from the trap, the dominant loss mechanism during the load of the FORT is light-assisted collisions. Chapter 6 detailed our measurements of light-assisted collisions in a shallow FORT for both homonuclear and heteronuclear collisions. Much care was taken to ensure we were just measuring light-assisted collisions, and those details are discussed in Chapter 6. We found that there are interatomic potential curves, such as purely repulsive curves, which mitigate some of the loss caused by light-assisted collisions. In fact, it was discovered that the more repulsive a potential set tends to be, the less loss will be observed from that collision channel. In

terms of the heteronuclear light-assisted collisions, the lowest loss rate came from collisions involving ^{87}Rb F=2 with ^{85}Rb F=2 and ^{87}Rb F=2 with ^{85}Rb F=3.

By finding the states which produce the lowest loss, we can mitigate loss out of the trap while the atoms are being loaded into the FORT. Additionally, if it is not possible to fully set the atoms in the states we want, the measurements will allow us to account for atoms lost to light-assisted collisions during the load and hold time in the FORT. When examining the efficiency of the sympathetic cooling, we'll need to know the loss rates out of the FORT.

Having examined each isotope under homonuclear loading conditions, determining the load rate $R(t)$ and homonuclear two-body loss β for each isotope, we looked at the heteronuclear loading of the FORT. During the course of the investigation, we found something rather surprising to us. Under a dual load, the load rate of the atoms into the FORT was significantly less than in a homonuclear load. This wasn't expected as the two isotopes of Rb's resonant transitions are detuned by several hundreds of natural linewidths from each other. There is heteronuclear two-body loss that ultimately reduces the number of atoms that can be trapped in the FORT. However, that loss can be accounted for through our light-assisted collisions measurements as that is the major two-body loss process. Even taking that, we did not get the expected number into the FORT. We found that the presence of one isotope has an effect on the hyperfine state distribution and load rate of the other, and hence can interfere with processes such as sub-Doppler cooling necessary for efficient FORT load [8].

Chapter 7 details our observations about how even a low-density gas of ^{85}Rb reduces the load rate of ^{87}Rb into the FORT. A likely explanation for this involves the

disruption of ground state coherences in ^{87}Rb due to ^{85}Rb collisions via long-range induced dipole-dipole interactions. In part, the observed reduction in load rate and maximum number can be explained by a disruption in the sub-Doppler cooling efficiency. Efficient sub-Doppler cooling requires an alignment between the atom's spin state and the light polarization. At the large detuning used in our molasses load, the relationship cannot be maintained with incoherent scattering as the scattering rate is too low. Thus, coherent transitions are required between ground spin states of the atom. A disruption of this coherence will cause a decrease in the sub-Doppler cooling efficiency that ultimately manifests itself as a reduction in the load rate of the FORT. For the proposed cooling scheme we ultimately wish to investigate, the number of atoms initially loaded into the FORT is an important parameter of the performance. Additionally, the presence of light fields may influence the collision rates which form the base of the proposed cooling scheme. Thus it is important to understand the effects each isotope can have on the optical pumping and hyperfine state distribution of the other isotope.

The ultimate goal was to fully characterized the FORT loading under both heteronuclear and homonuclear conditions. A full characterization of the load rate and loss for all loading conditions should enable us to tailor our FORT load to specific experimental conditions. Since the new cooling scheme would work best when one of the isotopes is optically thin while the other optically thick; we had hoped to map out a parameter space which would give us a convenient “knob” to individually tune the relative number of atoms of each isotope loaded into the FORT. Chapter 8 details the measurements we made in this regard and describes our attempt to accurately model FORT loading that matched the measured data.

As detailed in Chapter 8, we had found a breakdown of the normal assumptions used when modeling a FORT load. Normally, it is assumed that the load rate ($R(t)$), hyperfine state population distribution of the two isotopes, and the two-body loss coefficients are independent of the number of atoms trapped in the FORT and the presence of atoms of the other isotope. Through the study of the load rates, we had found that the load rate actually depends on the number of atoms from both isotopes and in part with the hyperfine state distribution of the isotopes. To complicate matters further, the hyperfine state distribution was dependent upon the number of both isotopes present. Since the two-body loss terms were highly hyperfine state dependent, the loss terms ultimately were dependent upon number of both isotopes present as well. Ultimately, this meant that the effective homonuclear two-body loss rate calculated from homonuclear loads were not the same as the effective homonuclear two-body loss rate under heteronuclear load. Additionally, the load rate varied between the two conditions as well. In an attempt to rectify the discrepancy between our predicted load and measured load, we considered cases where we relaxed the assumptions made one at a time. This process is detailed in Chapter 8.2.2.

Unfortunately, one of the conclusions of Chapter 8 was that there was no easy adjustment of a single or even a few parameters to individually tune the number of either isotope loaded. Rather, both loads are entangled with each other, and changing one will have an effect on the other that is non-linear and difficult to model. For instance, the effect of a simple change in the detuning of one isotope's associated cooling light or its hyperfine repump power cannot easily be modeled to predict the overall behavior of the loading. Instead, to find the operating conditions appropriate for the needs of our future

experiments, we will have to look at experimentally varying the available parameters until we get the desired load and number we wish to obtain.

9.2 Future Work

Our main motivation in investigating the dual loading of a FORT is ultimately the implementation of a non-evaporative cooling process. In particular, we wish to create a Collision Assisted Zeeman (CAZ) cooling system [14]. The particulars of implementing such a system are discussed in further detail later in this chapter. Briefly, CAZ cooling as we will implemented uses two species of atoms, one optically thick and the other optically thin, in the presence of a uniform magnetic field. Collisions between the two species can induce m_F changing collisions (spin-exchange collisions) in such a way as to remove kinetic energy from the system. After the collision, optical repumping restores the atoms to their initial spin states to be ready for another collision while at the same time removing entropy (heat) from the gas through scattered photons.

9.2.1 The variable aspect ratio trap. The main change to be made to the system will be the installation of a variable aspect ratio FORT. In Chapter 3.4, we detailed the experimental set up for the FORT. Specifically, in Figure 3.6 the lenses for the FORT immediately outside and inside the chamber were shown (there are other lenses in the system not shown). In our system, the interior lens is used to image a spot size from the outside lens onto the atom cloud using nearly 1:1 imaging. This design differs slightly from other setups which use the internal lens to focus onto the cloud, which is located at the interior lens focal point [9]. For these setups, beam shaping must be done on the outside of the chamber to send the proper size and divergence of beam to

the inside lens. This set up makes it relatively difficult to change the size and placement of the focus, and was the reason why we did not employ this method for our own system.

In our system, the outside lens is on a 3-D translation stage so that we can move around the position of its focus. The first inside lens images the light at that focus onto the atom cloud inside the chamber (the final lens is there to catch the CO₂ beam exiting the chamber to blow it up so we can safely block it). In this way, we could change the position of the outside lens, and thus change the spot size which is imaged onto the cloud. It then becomes relatively easy and reproducible to change the beam parameters of our FORT. The major change which is planned to accommodate the sympathetic cooling is to insert two cylindrical lenses before the final exterior lens shown in Figure 3.6. The final lens can still be used to form an image for the inside lens, but now there would be independent control of the CO₂ laser's focus in two directions.

Of these two cylindrical lenses, one lens will be mounted statically, the other will be mounted on a fast-action linear stage. This allows us to use computer control to change the position of one of the lenses. In this manner we can change the aspect ratio of the FORT, thus changing the spatial size and peak intensity of the trap. For our FORT, the potential is given by,

$$U(x, y, z) = -\frac{\alpha P}{c \epsilon_0 \pi w_x(z) w_y(z)} \exp\left(\frac{2x^2}{w_x(z)^2} - \frac{2y^2}{w_y(z)^2}\right) \quad (9.2)$$

$$w_{x,y}(z) = w_{0x,y} \sqrt{1 + \frac{(z - z'_{x,y})^2}{z_{Rx,y}^2}}$$

P is the power of the CO₂ laser composing the FORT beam, α is the polarizability constant, $w_{0x,y}$ is the minimum waist size in the x or y axis, $z'_{x,y}$ is a constant describing the location of the minimum waist location in the x or y direction. The point of using the

two cylindrical lenses with one on a moveable translation stage is so that we can control the peak intensity and intensity gradient of the FORT trap beam. By offsetting the foci of the cylindrical lenses from the position where both foci are aligned, the trap depth can be decreased and the volume of the trap increased. Since the relative location of the two lenses can be controlled, it can be altered during the cooling sequence to control the trap depth, trap confinement, trap volume.

The reason that this is useful is that the conditions for maximum FORT loading do not match conditions for the optimal cooling. Previous studies have shown that larger atom load can be obtained in a FORT with a larger trap volume. This is because more a larger number of atoms transverse the trap volume in a given amount of time, thus allowing for more atoms to be cooled into the trap. However, increasing the volume of trap decreases the density of the atoms in the FORT. Since a higher density is an asset for the proposed cooling technique, for the cooling a more tightly confining trap is preferred. Using this two cylindrical lens system we can control the FORT trap depth and volume. This will allow us to capture more atoms into the FORT initially, while after the load is finished, one of the lenses can then move, thus compressing the FORT. This can be done adiabatically, so as to not add additional heat to the cloud. What will result is an increase in the density of the atoms in the FORT while maintaining the maximum number of atoms trapped. The increase in density will encourage a higher collision rate between the two isotopes, which will ultimately be beneficial to the proposed cooling scheme. We expect that a density increase of a factor of 3-4 can likely be achieved by using this movable lens system for our system.

Much like many of the parameters of the load sequence (laser detuning, power, turn off times, etc); the movement of the lens will be controlled by the main Lab View program. It should be possible to compress the atoms nearly adiabatically, but some heat will be imparted to them. This increase in heat will have to be examined and the ramp time adjusted to make sure the resulting heating is not prohibitively large.

9.2.2 Collision assisted Zeeman Cooling. Collision assisted Zeeman (CAZ) cooling is the sympathetic cooling scheme we will implement. CAZ cooling is an “all optical” method for cooling the atoms to temperatures below that which can be obtained with standard laser cooling of atoms. Since it is all-optical cooling technique, the loss of atoms is not required as part of the cooling.

In order to discuss the advantages of CAZ cooling, it is useful to review the current state-of-the-art technique for cooling atoms below standard laser cooling temperatures: forced evaporative cooling. Forced evaporative cooling is the way in which, for instance, the primary way to obtain a Bose-Einstein Condensate (BEC) [10, 11, 12, 13]. In most systems using evaporative cooling atoms are prepared first in a MOT using standard techniques and then moved to a magnetic or optical trap. Then the most energetic atoms are ejected from the trap though either lowering the trap depth or driving these atoms out of the trap using electromagnetic fields. As these atoms are removed, the atoms left in the trap then have a lower average energy. In this manner, a cloud can be allowed to evaporate until the desired temperature (e.g. the BEC transition temperature) is reached. Currently, this is the only means by which a BEC can be obtained. The major draw back in evaporative cooling comes from the rejection of the more energetic atoms from the trap. Evaporative cooling ejects the vast majority of

atoms from the trap in order to obtain a BEC. Thus, while you can start with a relatively large number cloud, most of those atoms are thrown away.

To avoid this number loss, other methods of cooling have been suggested which do not rely on evaporation. One such method is the CAZ cooling scheme [14]. This method is one in which entropy is removed via light-scattering (as opposed to evaporative cooling as an example). This designation is made to differentiate it from evaporative cooling which removes entropy through atom loss. Since atom loss is not required, a greater number of atoms can be cooled to the desired temperature with CAZ cooling as opposed to evaporative cooling. While there is a possibility that implementation of the CAZ cooling scheme will not be able to reach BEC itself, a first stage of all-optical cooling will mean that even if one must eventually employ evaporative cooling, the average energy of the atom cloud will be lower than it otherwise would be and less atoms will have to be lost to achieve the target temperature.

In order to implement CAZ cooling, an optical trap is required. This is because several spin states, both are required to be trapped simultaneously. The atoms must also be held in a potential long enough for the collisions to occur and the gas to cool. Because of the large detuning of the CO₂ laser from any atomic resonances in Rb, there will not be significant heating of the atoms from the FORT light. While the atoms are held in the FORT, a uniform magnetic field is applied. This field lifts the degeneracy on the energy levels of the m_F sublevels.

CAZ cooling uses this splitting at the heart of the technique. If you have two species of atoms with different energy splittings due to the Zeeman effect, then collisions between the two species can be arranged where a net energy is taken out of the thermal

energy (kinetic) of the cloud and transformed into internal energy of the atom. This is because in such a situation spin-exchange collisions occur in which the final m_F state distributions coming out of the collision are not the same as going in. In the presence of a magnetic field, the change in m_F state results in a change in the Zeeman energy of the colliding pair.

Thus we look at the energy splitting of the m_F sublevels for ^{85}Rb and ^{87}Rb .

Because of the difference in the nuclear spin of the isotopes ($I_{87}=3/2$, $I_{85}=5/2$), there is indeed a difference in the m_F sublevel energies in the presence of a magnetic field due to the Zeeman effect between the two isotopes. The difference in the energy splitting can be explained by a difference in the *g-factor* between ^{85}Rb and ^{87}Rb . The splitting can be described through the interaction of the atom's magnetic moment (μ) and the applied magnetic field (B) given by $\vec{\mu} \cdot \vec{B}$. The atom's magnetic moment can be represented by

$$\vec{\mu} = -\mu_B (g_L \vec{L} + g_S \vec{S} + g_I \vec{I}) / \hbar. \quad (9.3)$$

μ_B is the Bohr magnetron and the *g*'s are the *g-factors* associated with the various angular momentum terms. For the planned experiment, both isotopes will be set into their ground-state lower hyperfine state (F=2 for ^{85}Rb and F=1 for ^{87}Rb).

The energy of a magnetic sublevel m_F is $E_{Zeeman}^{87} = \frac{-1}{2} \mu_B B m_F$ for ^{87}Rb and

$E_{Zeeman}^{85} = -\frac{1}{3} \mu_B B m_F$ for ^{85}Rb . The Zeeman energy for an atom is proportional to the m_F

state, thus the splitting between sublevels is constant. To see where these factors of $1/2$ and $1/3$ come from, consider an atom in the stretched state in the upper hyperfine ground-state. Since the nucleus of the atoms is so much heavier than an electron, it is the electron magnetic moment that contributes almost exclusively to the net magnetic

moment of the atoms. The maximal coupling (and thus Zeeman energy shift) occurs when \vec{S} is aligned completely parallel to the magnetic field. This occurs when the projection of \mathbf{I} and \mathbf{S} are maximally along the magnetic field direction. Under those conditions, the magnetic moment of the atom will lead to a shift of $\mu_B B$. In this case for ^{85}Rb we have $I+S=5/2+1/2=3$ and for ^{87}Rb we have $I+S=3/2+1/2=2$. Since the splitting between each m_F level is constant for each isotope, we can see that to get to the a shift of $\mu_B B$ in the stretched state the energy levels are offset by a factor of 1/2 in ^{87}Rb and 1/3 in ^{85}Rb . In this way, we can understand the change in the *g-factors* between ^{87}Rb and ^{85}Rb without explicitly solving for $\vec{\mu} \cdot \vec{B}$.

The idea behind CAZ cooling is to design collisions in which the m_F level is changed by 1. For a collision that causes a $\Delta m_F = -1$ change in ^{85}Rb and a $\Delta m_F = 1$ change in ^{87}Rb , the energy gained by the reduction of Zeeman energy in the ^{85}Rb is less than the gain in Zeeman energy in the ^{87}Rb . As a result, some kinetic energy of the colliding pair is converted to internal energy of the atoms [14]. Thus these collisions result in a net loss of kinetic energy from the atom cloud, cooling it. Figure 9.1 shows a cartoon of this collision process.

The next piece for CAZ cooling is to “close the cycle”. The cooling relies on collisions between ^{85}Rb and ^{87}Rb that cause a particular change in their m_F state distribution, or in other words only collisions between certain combinations of incoming m_F states will result in a reduction of kinetic energy. Eventually, there will be a build up of atoms in states which cannot facilitate the desired collisions. At this point, the atoms will have to be pumped back into their original distribution so that the cooling cycle can continue. The trouble comes in at this point in how to pump the atoms back into their

$$\Delta E_{Zeeman}^{87} > \Delta E_{Zeeman}^{85}$$

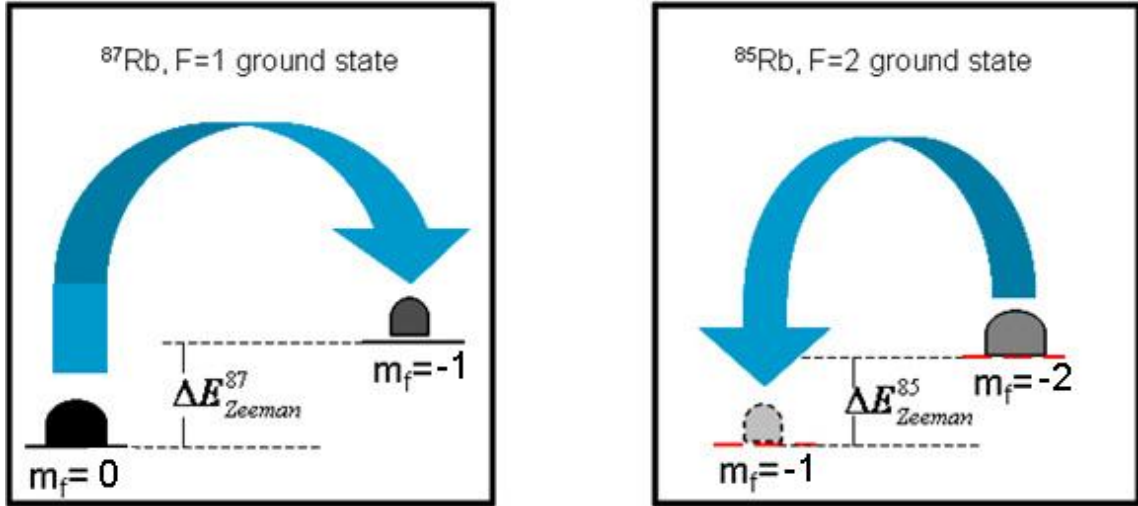


Figure 9.1 A cartoon for the CAZ cooling scheme which will be tested in future experiments. A sample of the type of collision that will be used in the cooling cycle between ^{87}Rb and ^{85}Rb in their ground-state lower hyperfine state is shown. The m_F states for each isotope are shown for this example, and the figures above them represent atom clouds. This cartoon represents a collision between ^{87}Rb in the $F=1$, $m_F=0$ state with ^{85}Rb in the $F=2$, $m_F=-2$ state. The collision drives ^{87}Rb into the $F=1$, $m_F=-1$ state and ^{85}Rb into the $F=2$, $m_F=-1$ state. For this collision the energy which can be gained from driving ^{85}Rb atoms into the $m_F=-1$ is not enough to promote the ^{87}Rb atoms into the $m_F=-1$ state. As such, for this collision to occur, kinetic energy must be taken from the system and converted into internal energy of the atoms. By repeating these collisions, the atom cloud in the FORT can ultimately be cooled further.

desired states without adding heat to the system. Any mechanism which can produce heating in the cloud has the potential of undoing any gain which is obtained through CAZ cooling. Using laser light to optically pump the atoms can cause heating through reabsorption processes and can lead to light-assisted collisional loss from the trap. To get around this, one isotope (^{85}Rb) will be kept optically thin. By using an optically thin cloud, the effects of reabsorption can be mitigated and the atoms can be pumped back into the proper m_F state to continue the cycle. Since one goal of being able to use this cooling method is increased atoms in a BEC, the other isotope (^{87}Rb) would need to be kept optically thick as to maximize the number of atoms. For this isotope, optical pumping would not necessarily be advantageous. Instead, an RF field is planned to be used. The RF-field will not add heat to the cloud, however, it also cannot pump atoms to any specific m_F level irreversibly. We will add enough noise to the RF field to randomize the m_F states of the ^{87}Rb isotope in the cloud. Instead of pumping to a specific m_F state, there will instead be an equal distribution of m_F states for that isotope in the cloud. While that means that not all the atoms will be available for the proposed collision, it does insure that there will be some fraction of the population which can continue the cycle.

9.3 Conclusion

The work presented in this thesis was made with the ultimate goal of implementing CAZ cooling to further cool atoms beyond what is attained by normal pure optical methods (i.e. sub-Doppler cooling) without resorting to evaporative cooling, which results in a significant required loss of atoms in order for the cooling to work. The work presented in this thesis has shown that an adequate number of both ^{85}Rb and ^{87}Rb atoms can be loaded into a FORT to make the proposed cooling technique a realistic

possibility. The future experiments implementing the cooling method will be investigated by Mathew Hamilton, and thus much of the detailed analysis will be addressed by him when the experiments are actually carried out.

Through the course of the experiments presented in this thesis, we found many interesting dynamics of dual loading of a FORT. This included some non-obvious results such as the presence of an off-resonant isotope having a negative effect on the load rate of the other isotope into the FORT. As a result, we have a much better understanding of the loading dynamics of a FORT.

References for Chapter 9

- ¹ D. J. Han, M. T. DePue, and D. S. Weiss, *Phys Rev. A* **63**, 023405 (2001).
- ² V. Vuletic, C. Chin, A. J. Kerman, and S. Chu, *Phys. Rev. Lett.* **81**, 5768 (1998).
- ³ H. Perrin *et al.*, *Europhys. Lett.* **46**, 141 (1999).
- ⁴ A. J. Kerman, V. Vuletic, C. Chin, and S. Chu, *Phys. Rev. Lett.* **84**, 439 (2000).
- ⁵ D. Boiron, A. Michaud, A. Lemonde, Y. Castin, C. Salomon, S. Weyers, K. Szymaniec, L. Cognet, and A. Clairon, *Phys. Rev. A* **53**, R3734 (1996).
- ⁶ J. D. Miller, R. A. Cline, and D. J. Heinzen, *Phys Rev A* **47**, R4567 (1993)
- ⁷ S. J. M. Kuppens, K. L. Corwin, K. W. Miller, T. E. Chupp, and C. E. Wieman, *Phys Rev A* **62**, 03406 (2000)
- ⁸ K. Ellinger and J. Cooper, *Phys. Rev. A* **55**, 4351 (1997)
- ⁹ A. Wax, S. Bali, and J. E. Thomas, *Opt. Lett.* **24**, 1188 (1999)
- ¹⁰ Jacob L. Roberts PhD thesis, University of Colorado (2001)
- ¹¹ M. H. Anderson, J. P. Ensher, M. R. Matthews, C. E. Wieman, and E. A. Cornell, *Science* **269**, 198 (1995)
- ¹² K. B. Davis *et al.*, *Phys. Rev. Lett.* **75**, 3969 (1995)
- ¹³ K. B. Davis, M. -O. Mewes, and W. Ketterle, *Appl. Phys. B* **60**, 155 (1995)
- ¹⁴ G. Ferrari, *Eur. Phys. J. D* **13**, 67 (2001)